DYNAMIC STRUCTURAL NETWORK MODELS OF NEURODEGENERATION: A MULTIMODAL HUMAN NEUROIMAGING APPROACH

A Dissertation

Presented to the Faculty of the Weill Cornell Graduate School

of Medical Sciences

in Partial Fulfillment of the Requirements for the Degree of

Doctor of Philosophy

by

Fontasha Janine Powell

September 2017

DYNAMIC STRUCTURAL NETWORK MODELS OF NEURODEGENERATION: A MULTIMODAL HUMAN NEUROIMAGING APPROACH

Fontasha Janine Powell, Ph.D.

Cornell University 2017

Neurodegenerative diseases are a major cause of disability and premature death worldwide (Brettschneider et al. 2015). The prevalence of neurodegenerative disorders is increasing rapidly while disease-modifying therapies remain missing (Palop et al. 2006). Hence, understanding how neurodegenerative pathology spreads throughout the brain is integral to prevention and/or the discovery of disease-modifying therapies. Hallmark patterns of disease are well-characterized from converging animal model, post mortem and human neuroimaging evidence. However, predictive whole-brain models of neurodegeneration are much less studied.

This thesis utilizes complex graph theoretic methodology and multimodal human neuroimaging data to construct and evaluate predictive models of disease spread in several debilitating disorders, including Alzheimer's Disease, Huntington's Disease and Schizophrenia. By probing the two dimensions of network neuroscience (dynamics **on** networks vs. dynamics **of** networks), the current work seeks to elucidate mechanisms of neurodegeneration.

Chapter one gives biological background to the two dimensions of network neuroscience and current hypotheses of neurodegeneration in Alzheimer's Disease (AD), Huntington's Disease (HD) and Schizophrenia (SZ). Chapter two asks if Alzheimer's Disease is a disorder encompassing dynamics **on** networks or dynamics **of** networks by using a predictive pathology spread model to assess whether the structural network undergoes degeneration or remains intact to simply serve as a conduit for degenerative pathology in AD. Chapter three expands on work presented in Chapter two by elucidating mechanisms at play atop the static structural network to determine the relationship between rate of neurodegeneration and CSF biomarkers. Chapter four focuses purely on dynamics **on** networks by constructing several models of pathology spread in Huntington's Disease in an unprecedented dataset and is the first work to empirically evaluate predictive ability of popular neurodegenerative hypotheses in vivo. Chapter five analyzes dynamics **of** networks by exploring age-related organizational changes in the WM network and the relationship to gene expression in chronic schizophrenia. Together, these distinct studies elucidate the role of structural network organization in the dynamics of neurodegeneration and suggest an umbrella approach to modeling pathology spread. Chapter six integrates findings across all three original studies and discusses the therapeutic implications of the current thesis, methodological considerations and future work.

BIOGRAPHICAL SKETCH

Fontasha Powell was born and raised in St. Louis, Missouri. Due to her never-ending curiosity, her career as a scientist was predicted by her kindergarten teacher. Fon's love for science blossomed at age 17, when she spent a summer in high school researching molecular biology in the lab of Dr. Yuqi Wang at St. Louis University. In 2013, Fon earned a bachelor's degree in Neuroscience with minors in Biology and Spanish from Duke University. After taking a class called "Inside the Disordered Brain" taught by Dr. Ahmad Hariri, she developed a fascination with abnormal brain circuits. Subsequently, Fon's passion for human neuroimaging was born while she was an undergraduate researcher in the lab of Dr. Michael Platt, the Director of the Duke Institute for Brain Sciences. For 2 years in the Platt Lab, Fon worked on behavioral EMG and resting state fMRI in subjects with Anorexia Nervosa. Fon also spent a summer as an Amgen Scholar at the University of California - San Francisco (UCSF) where she examined genetics of pediatric neurodevelopmental disorders with Dr. Eliott Sherr. Fon began her graduate work at Weill Cornell in 2013 and joined the Imaging Data Evaluation and Analytics lab (IDEAL), where Dr. Ashish Raj fostered her interest in human neuroimaging. With Dr. Raj's support, Fon also participated in many exciting collaborations, which include Dr. Michael Weiner at UCSF, the Track-HD investigators at University College of London, a schizophrenia working group at the University of Ireland- Galway and Weill Cornell's own physician scientists Dr. Marc Dubin and Dr. Conor Liston.

This thesis is dedicated to Janet Powell, whose immeasurable sacrifice enabled her little girl in the bright white shoes to make it to the top.

Dorothy Miles and Sherry Westbrook, thank you for helping build the ladder.

Nanos Gigantum Humeris Insidentes

(If I have seen further than others, it is by standing upon the shoulders of giants)

ACKNOWLEDGEMENTS

Ashish Raj: A special thanks for your knowledge and collaborative spirit.

Conor Liston, Barry Kosofsky, Amy Kuceyeski and Manu Sharma: A sincere thank you for your valuable encouragement, feedback and kindness.

Thanks to all my current and former colleagues at the Imaging Data Evaluation and Analytics Lab (IDEAL), especially Eve LoCastro.

Financial support: Ford Foundation Fellowship to FJP.

Chapter 2 - 3: NINDS grants R01 NS075425 and R01 NS092802. Data collection and sharing for this project were funded by the publicly available ADNI dataset. For full information on ADNI funding, please visit the ADNI website.

Chapter 4: TRACK-HD is supported by the CHDI Foundation, a not-for-profit organization dedicated to finding treatments for Huntington's disease.

Chapter 5: The National University of Ireland Galway Millennium Project Fund.

TABLE OF CONTENTS

LIST OF FIGURES

Chapter 5

LIST OF TABLES

Chapter 1:

An Introduction to Structural Network Dynamics and its Application to Neurodegeneration

Introduction

Neurodegenerative diseases are a major cause of disability and premature death worldwide (Bird et al., 2003; Huisman et al., 2011; Savica et al., 2013). The prevalence of neurodegenerative disorders is increasing rapidly while disease-modifying therapies remain missing (Palop et al., 2006). Hence, understanding how neurodegenerative pathology spreads throughout the brain is integral to prevention and/or the discovery of disease-modifying therapies. While hallmark patterns of specific diseases are well-characterized from converging animal model, post mortem and human neuroimaging evidence, predictive whole-brain models of neurodegeneration are largely absent.

Recent advances in non-invasive neuroimaging and the application of graph theory, a method modeling pairwise relationships between objects in a graph, to neural networks constitute a rapidly evolving field known as network neuroscience. Broadly speaking, network neuroscience pursues new ways to map, record, analyze and model the elements and interactions of neurobiological systems (Bassett and Sporns, 2017). The current thesis applies tenets of network neuroscience to build and test predictive models of disease spread, with the goal of elucidating mechanisms of neurodegeneration. This chapter will provide background to the field of network neuroscience and explain how it can be applied to evaluate popular hypotheses of disease spread in three disorders, which include Alzheimer's Disease, Huntington's Disease and Schizophrenia.

Visualizing the brain as a network

Brain systems span multiple levels of organization. Starting as a single neuron, neurons communicate to form circuits, synapses are formed between circuits that lead to systems and, collectively, distinct but interrelated systems constitute the whole brain.

Until recently, whole brain studies in humans were rare and limited in scope. Previously, neuropathological studies were the only viable approach to whole brain mapping in humans, but required large autopsy cohorts or laborious methods for whole-brain sectioning and staining (Seeley, 2017). Recent advances in non-invasive neuroimaging offer the ability to visualize and test models in vivo that have long been restricted to post mortem, mouse model and cell culture methods. The current work capitalizes on such advances by utilizing neuroimaging data to build new models.

In 2005, Sporns and colleagues coined the phrase “the connectome” as the complete description of structural connections between elements of a nervous system (Sporns et al., 2005). However, visualization of a complete nervous system was by no means a novel concept. In 1974, all 302 neurons and respective connections encompassing the nervous system was mapped in C. Elegans (Brenner, 1974). The field of connectomics is unique in that it is rooted in the tenet that brain function is contingent on brain-network interactions, and that elucidating of higher brain function requires an understanding of brain-network organization (Sporns, 2012; Sporns et al., 2005).

Quickly following the birth of the connectome came pathoconnectomics, which focuses on mapping abnormal brain networks, both elements and interaction (Rubinov and Bullmore, 2013a). As a logical extension of

connectomics, the overall goal of pathoconnectomics is “to understand brain disorders at the casual mechanistic level, to be leveraged for therapeutic intervention” (Deco and Kringelbach, 2014). Given the progressive nature of neurodegenerative disease, pathoconnectomics represents an excellent approach to further understand progressive brain changes at the whole-brain level in neurodegeneration.

The intersection of sophisticated empirical methods for mapping neurobiological data with theoretical and computational advances in data analysis and modeling of brain networks has led to rise of network neuroscience (Bassett and Sporns, 2017). In network neuroscience, the brain is visualized as a network by constructing a graph consisting of vertices representing brain regions and edges as connections between them. Edges can be constructed from a wide array of non-invasive human neuroimaging methodology to represent both structural and functional networks. Anatomical and structural networks can be constructed from magnetic resonance imaging (MRI) and diffusion MRI, respectively (Bassett et al., 2008; Wang et al., 2012). Functional networks can be visualized using functional magnetic resonance imaging (fMRI) as well as electrophysiological methods such as EEG and MEG (de Haan et al., 2009; Redcay et al., 2013). The current thesis focuses on the construction of DTI-based graphs as the basis for structural networks.

Graph theory is rooted in the physical world (Bullmore and Sporns, 2009). For example, air travel is an area where graph theory has been widely applied and further developed. Guimerra and colleagues showed that worldwide flight paths exhibit small world architecture of both simultaneous clustering and segregation, similar to that of the human brain (Guimera et al., 2005).

In network neuroscience, quantification of topological metrics such as modularity, path length, centrality and the distribution of hubs provides an understanding of brain organization (Figure 1.1) (Rubinov and Sporns, 2010; Stam and Reijneveld, 2007).

To illustrate an original example of graph theory as it applies to airport networks, JFK is an airport (vertex) in the graph that constitutes all daily flights in the United States (network). Flight path (distance) represents connections (edges) between the vertices (airports). Incidentally, JFK could be conceptualized as a hub, because, say, 70% of flights in the US stop through JFK en route to small cities and international destinations. When flying from JFK to LAX, a direct flight from JFK to LAX represents shortest path length, whereas flying from JFK to Houston to LAX represents a longer, less efficient path.

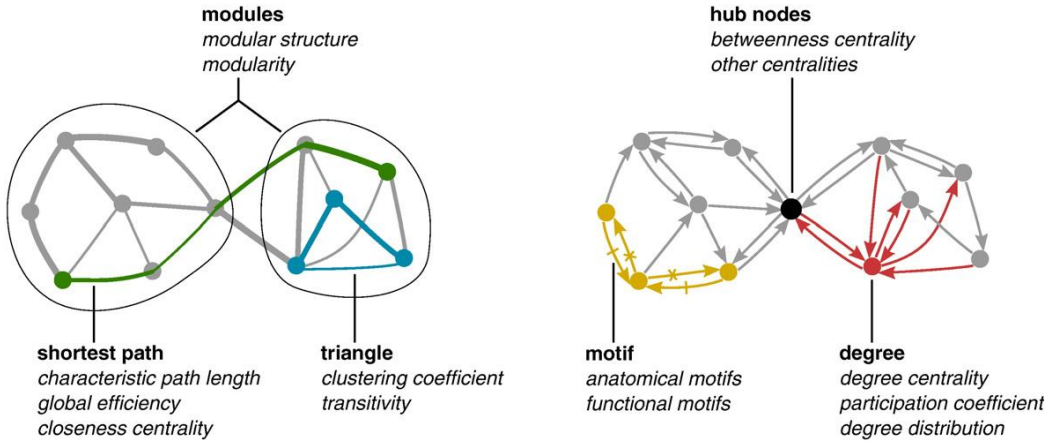

Figure 1.1. Measures of network topology. Adapted from Rubinov and Sporns, 2010. An illustration of key complex network measures (in italics) described in this thesis. These measures are typically based on basic properties of network connectivity (in bold type). Thus, measures of integration are based on shortest path lengths (green), while measures of segregation are often based on triangle counts (blue) but also include more sophisticated decomposition into modules (ovals). Measures of centrality may be based on node degree (red) or on the length and number of shortest paths between nodes. Hub nodes (black) often lie on a high number of shortest paths and consequently often have high betweenness centrality. Patterns of local connectivity are quantified by network motifs (yellow). An example three-node and four-link anatomical motif contains six possible functional motifs, of which two are shown—one motif containing dashed links, and one motif containing crossed links.

Organizational differences can be viewed both on the global level of characteristic metrics as well as the local level, which reflect the role of how individual regions fit into the larger network. Moreover, differences in global measures become more informative when supplemented by more detailed analyses that pinpoint specific network element of local measurements of network topology (Wig et al., 2011). The current thesis makes use of both global and local widespread topological properties such as path length, degree and clustering as well as additional, more complex properties of network graphs, which will be expounded upon in later chapters.

Dynamics in network neuroscience

An emerging frontier of network neuroscience is the investigation of network dynamics, which is defined as how networks change over time (Bassett and Sporns, 2017). Importantly, the mechanistic role of structural brain networks for shaping brain dynamics is a key rationale for mapping the human connectome (Sporns, 2014). The current thesis defines structural network as the interconnected system of nodes and vertices defined from white matter fiber pathways. Hence, the current work will focus on mapping structural network dynamics, which are changes involving the structural network over time, as a means to elucidate neurodegenerative processes.

Though static differences between diseased and healthy structural networks are well-characterized, the study of network dynamics is increasingly important in order to build comprehensive models of neurodegeneration. Neurodegeneration, by definition, is characterized by dynamic, progressive changes the brain (Jucker and Walker, 2013). Thus, predictive models of neurodegeneration must correspondingly capture elements of dynamicity.

Basset and Sporns identify two important dimensions of how networks change: 1) How activity patterns can change on top of a fixed structural network and 2) How structural network edges themselves can reconfigure. These dimensions are, respectively, referred to as 1) Dynamics **on** structural networks and 2) Dynamics **of** structural networks (Bassett and Sporns, 2017; Holme and Saramäki, 2012) (Figure 1.2). The current work carries out original studies that investigates dynamics **on** structural networks, dynamics **of** structural networks and also incorporates methodology to test both simultaneously. The subsequent paragraphs will provide specific examples

illustrating dynamics **on** vs. **of** structural networks and how it relates to current models of neurodegeneration.

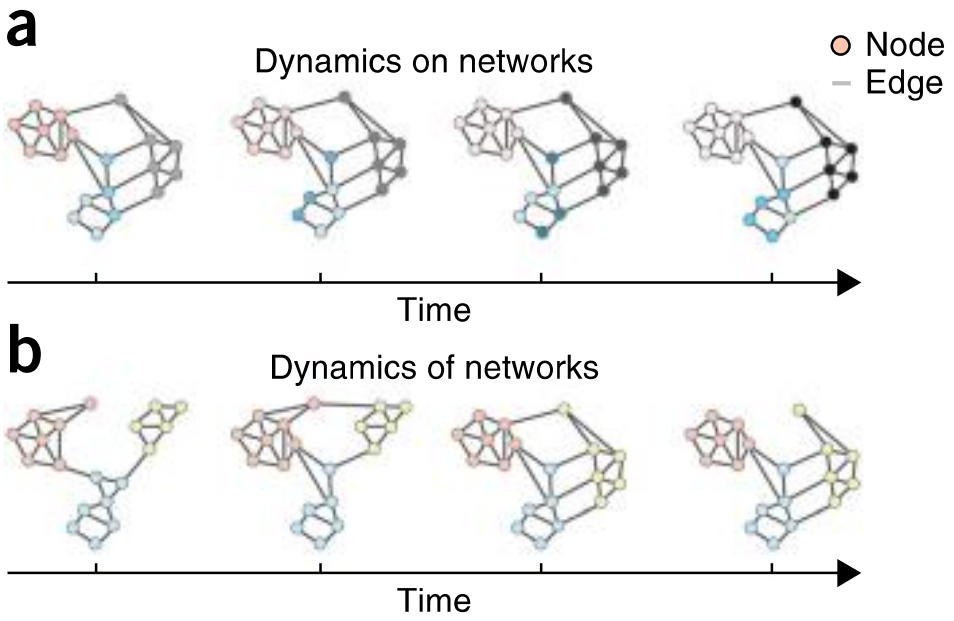

Figure 1.2. Dynamic network models. Adapted from Bassett and Sporns, 2017. In the field of network science, two types of dynamic processes are studied in some detail: dynamics on networks and dynamics of networks. (**a**) Dynamics on networks indicates that the activity (or some other property of interest) of nodes changes as a function of time. Here we illustrate decreasing activity (pink), increasing activity (gray) and changes in the pattern of activity (blue) over time in distinct network modules or communities. (**b**) Dynamics of networks indicates that the edges of the network themselves change either in their existence/absence or in their strength. Here we illustrate the coalescence of modules (blue and yellow), as well as the transfer of allegiance of a single region from one module (pink) to another (yellow) over time.

Dynamics on structural networks in neurodegeneration

Neurodegeneration is broadly classified as a progressive loss of function or structure of neurons. Nearly all neurodegenerative disorders are classified by stereotypical patterns of disease progression related to clinical symptomatology (Brettschneider et al., 2015). These patterns suggest pathology is not only simply propagated between neighboring cell bodies, but

that it also spreads along axonal pathways either away from (anterogradely) or toward (retrogradely) the cell body (Brundin et al., 2010). Though there exists heterogeneity among specific cellular and genetic mechanisms implicated in pathophysiological processes, we observe unifying patterns of broader neurodegeneration on the whole-brain scale.

A multitude of hypotheses describe the neurodegenerative process as as dynamics **on** structural networks. Such examples include the cascade hypothesis, dual-hit hypothesis, network failure hypothesis and the prion hypothesis (Heinemann et al., 2016; Jucker and Walker, 2013; Karran et al., 2011; Palop et al., 2006). When examining dynamics **on** structural networks, the current thesis will limit its scope to prion hypothesis.

The prion hypothesis posits specific proteins aggregate and misfold, propagating trans-synaptically throughout the brain in a template-directed manner (Jucker and Walker, 2013). There is considerable evidence for the prion hypothesis in several neurodegenerative disorders, including Alzheimer's Disease (AD), Frontotemporal Dementia (FTD), Amyotrophic Lateral Sclerosis (ALS), Huntington's Disease (HD) and Parkinson's Disease (PD) (Lee et al., 2001; Neumann et al., 2006; Ren et al., 2009; Spillantini et al., 1998).

However, these hypotheses have been developed and evaluated extensively in human post mortem studies, animal models and cell culture. Rarely have these models have been tested and validated in vivo on human neuroimaging data. In Chapter 2 - 4, the present thesis will evaluate and construct dynamics **on** structural network models to empirically test hypotheses of pathology spread in AD and HD as a means to elucidate mechanisms of trans-synaptic pathology spread.

The Network Diffusion Model

The Network Diffusion Model (NDM) is one of the few published predictive computational tools recapitulating the prion hypothesis in vivo and will be used as a tool in the current work. The NDM is an example of how whole-brain computational models can generate and predict dynamic brain interactions and consequences over many timescales (Rubinov and Bullmore, 2013a).

The principal investigator overseeing the current thesis developed the Network Diffusion Model in 2012 as a means to model tau pathology spread on a healthy structural connectome in Alzheimer's Disease (Raj et al., 2012). Subsequently, the model was validated, showing high predictive ability in 418 subjects on the AD spectrum from the publicly available Alzheimer's Disease Neuroimaging Initiative (ADNI) dataset (Raj et al., 2015) (Figure 1.3). The Network Diffusion Model represents dynamics **on** structural networks, as it assumes a static white matter network on which tau pathology spreads.

In the Network Diffusion Model, atrophy is used a surrogate for tau, as prior work shows a close association between the two (Attems et al., 2012; Reitz et al., 2009). From a baseline pattern of atrophy (pathology), an end state level of atrophy (pathology) can be predicted using linear algebra and complex graph theory.

To provide a more granular description, the NDM is an equation that describes the following process: From a baseline regional pattern of pathology, a diffusion kernel is calculated, which modifies pathology over time. The diffusion kernel calculation is based on eigen-decomposition of the Laplacian matrix. Eigenmode is a non-linear graph theoretic measure reflective of a region's "hubness" (Raj et al., 2012). Ultimately, the topological

metric of structural eigenmode governs disease spread. The original NDM does not assume directionality of disease spread and structural connections between regions are positive and the same in either direction.

The current thesis will evaluate the network diffusion model (NDM) on structural network associated with different disease states in AD (Chapter 2-3). In Chapter 4, several modifications to the model will be made in order to create new applications and models of pathology spread in HD.

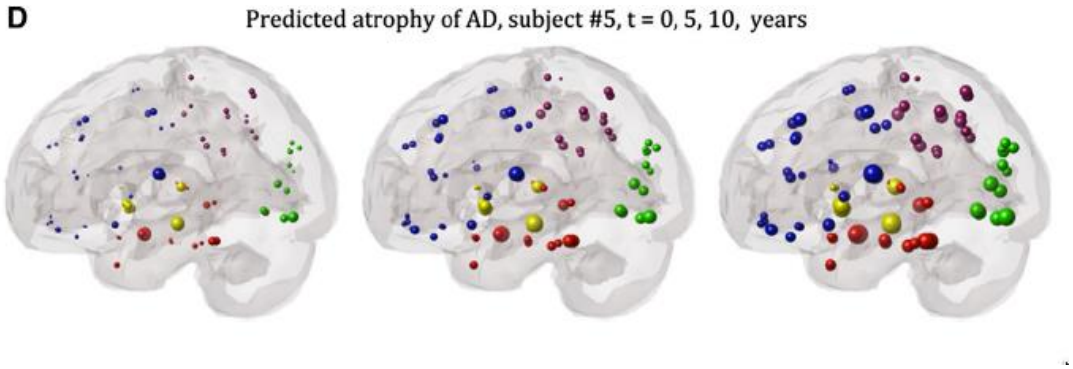

Figure 1.3. The Network Diffusion Model., adapted from Raj et al. 2012. Predicted atrophy of an AD subject, t=0, 5, 10 years from baseline. Predicted atrophy correlates strongly to observed end state atrophy (not pictured). The spheres are proportional to effect size, and color-coded by lobe: frontal = blue, parietal = purple, occipital = green, temporal = red, and subcortical = yellow.

Neurodegeneration: Dynamics of structural networks

Further hypotheses of neurodegeneration posit that because brain function is strongly linked to structure, the structural network does not remain static, but rather undergoes changes with disease progression (Seeley et al., 2009). Such hypotheses illustrate dynamics **of** structural networks.

Changes to the white matter network in neurodegeneration are studied significantly less than gray matter network changes such as atrophy, resting

and task-based fMRI and electrophysiological measures. Current hypotheses of white matter network neurodegeneration have been developed and perpetuated using tract-based spatial statistics (TBSS), which include fractional anisotropy (FA), mean diffusivity (MD), axial diffusivity (AD) and radial diffusivity (RD). While diseases such as Amyotrophic Lateral Sclerosis, Alzheimer's Disease and Schizophrenia have a moderate amount of data suggesting degeneration of the structural network, findings in Huntington's Disease and Parkinson's Disease are relatively rare (Abrahams et al., 2005; Damoiseaux et al., 2009; Mori et al., 2007).

While these findings are important to understand measures of tract integrity, they do little to elucidate changes in network organization. As such, graph theory represents a useful tool to help elucidate topological dynamics of neurodegeneration. Unfortunately, topological changes associated with neurodegeneration remain understudied. Most neurodegenerative studies of white matter organization are limited to specific patient cohorts compared to healthy controls (Lo et al., 2010; McColgan et al., 2015; van den Heuvel et al., 2010). Few studies evaluate models of structural degeneration after disease onset utilizing graph theoretic approaches, neither cross-sectionally nor longitudinally. In hopes of providing new data to this space, the current thesis seeks to model and elucidate changing brain architecture after disease onset using schizophrenia (Chapter 4).

Alzheimer's Disease

Alzheimer's disease (AD) is the most prevalent neurodegenerative disorder and is characterized by progressive memory loss in old age. It affects 1 in 100 patients and 6% of individuals over age 70 (Bird et al., 2003). Though

the disease is largely sporadic, various alleles of the APOE gene have been linked to sporadic and the rare familial AD incidence (Saunders et al., 1993).

Dynamics on structural networks in AD

The earliest histopathological human studies by Braak and Braak illustrate characteristic patterns of disease progression in AD (Braak and Braak, 1991). Briefly, it is believed pathology begins in the locus coerlus (LC) before spreading to the entorhinal cortex, the broader hippocampus, throughout the medial temporal lobe and frontal and parietal regions (68 – Brett) (Brettschneider et al., 2015). This patterning has been supported and expanded by additional post mortem, animal model and human neuroimaging evidence (Braak and Braak, 1996; de Calignon et al., 2012; Fischer et al., 2016).

Though several models of neurodegeneration exist, the current thesis will be limited to exploring the prion hypothesis. Specifically, the prion hypothesis in AD postulates that toxic tau protein misfold and aggregate first in the LC before spreading throughout the brain, transynaptically. Unknown cellular mechanisms ultimately cause tau to trigger amyloid beta pathology, which also spreads throughout the cortex to the brainstem (Thal et al., 2002). The recent advent of non-invasive PET tracers allow visualization of amyloid beta and tau in vivo recapitulate AD patterning, which recapitulate these patterns of disease in vivo (Schöll et al., 2016; Schwarz et al., 2016). Particularly, animal injection studies provide strong evidence for trans-synaptic spread, illustrating that exogenous injection of human mutant tau into the LC/EC spreads to connecting regions in a stereotypical manner (Clavaguera et al., 2009; Iba et al., 2015, 2013).

As a result of the robust converging evidence supporting the prion hypothesis, the NDM, explained above, was developed to model tau dynamics on a static healthy structural network. This model will be used in the subsequent thesis as a tool to elucidate mechanisms of disease spread in AD.

Dynamics of structural networks in AD

Tract-level differences in white matter integrity is a well-established biomarker of AD. A proliferation of studies, both in public and private datasets, show diffuse, global alterations in white matter tracts, especially in tracts connecting frontal and temporal regions (Uncinate Fasciculus) as well as tracts in the temporal region (Inferior Longitudinal Fasciculus) and tracts connecting the front and back of the brain (Superior Longitudinal Fasciculus) (Hasan et al., 2012; Lee et al., 2015; Nir et al., 2013; Rowley et al., 2013).

Despite significant changes in tract integrity, studies of structural topology in AD are inconclusive. For example, some studies report aberrant global topology across all metrics in AD, while others report disturbance of just a few topological metrics (Bai et al., 2012; Daianu et al., 2013; Lo et al., 2010). Incidentally, other studies report structural organization of the backbone is intact (Daianu et al., 2015).

Still, the extent to which disease spread is affected by well-established changes in structural integrity and inconclusive changes in topology remains poorly understood. Furthermore, it remains unknown if AD is primarily a disorder of the gray matter network (dynamics on structural networks) or the white matter network (dynamics of structural networks). To answer this question, the current study uses the Network Diffusion Model, which is independent of traditional graph summary metrics, as a mechanistic tool. By testing the Network Diffusion Model on differing static networks, results can be

synthesized to form conclusions that evaluate dimensions of both dynamics **on** structural networks as well as dynamics **of** structural networks.

Huntington's Disease

Huntington's Disease (HD) is the most common form of inherited neurodegenerative disease. The incurable disorder is caused by an autosomal dominant mutation causing CAG repeat expansion and is characterized by abnormal motor movements and personality changes. Like all neurodegenerative diseases, the age of onset begins in adulthood, with the age of onset being inversely related to the length of mutated CAG repeats. Death usually occurs 10-15 years after onset (Arrasate and Finkbeiner, 2012).

Dynamics of structural networks in HD

Relatively little whole brain preliminary evidence exists supporting dynamics **of** structural networks in HD. However, there is compelling work done in pre-HD suggesting that white matter network alterations do occur early in the disease, showing loss of white matter integrity of certain tracks, which is related to symptomatology (Rosas et al., 2006). Similarly, DTI-based studies focusing on regions of interest linked to the basal ganglia show decreased structural connectivity in HD compared to healthy controls (Kloppel et al., 2008; Marrakchi-Kacem et al., 2013; Novak et al., 2015). However, few studies illustrate whether changes to structural organization correspond to changes in structural integrity. One such study, utilizing human neuroimaging included in the current thesis, investigates global topology of HD. Vulnerability of rich club regions and loss of topological metrics reflective of network integration is reported (McColgan et al., 2015). Because dynamics **of** structural networks in HD have already been modeled in our subject cohort,

the present thesis examines dynamics **on** structural networks. Present models in the context of HD will be described below.

Dynamics on structural networks in HD

It is suggested that while structural changes in the white matter network of HD exist, substantially more evidence exists to make a case for modeling dynamics **on** structural networks in HD. For example, neuroimaging data of 657 subjects show gray matter changes are detectable in pre-HD subjects significantly sooner than white matter changes (Paulsen et al., 2010).

Unlike other neurodegenerative diseases, which are not characterized by a clear cause-and-effect mutation, CAG nucleotide repeats are linked to pathogenic expansion of glutamines on the huntingtin protein (HTT) in HD (Arrasate and Finkbeiner, 2012).

It is hypothesized that pathogenic HTT is the cause of degeneration in HD. Immunostaining of post mortem HD brains shows HTT inclusions in the nucleus as well as the cytoplasm and in neuronal processes (Becher et al., 1998; Gutekunst et al., 1999; Kim et al., 2001). Furthermore, pathogenic HTT correlates with HD symptoms in transgenic mouse models and found in neurons before the onset of behavioral symptoms (Davies et al., 1997; Ordway et al., 1997). A multitude of studies suggest mutant HTT misfolds and aggregates. For example, cell culture models show that mutant HTT is capable of oligomerizing and causing cell death (Herrera et al., 2011). Mutated HTT has been reported to diffuse into extracellular space and inside adjacent cells to act as seeds for further aggregation and neurotoxicity (Ren et al., 2009). Similarly, transgenic mouse models illustrate formation of HTT aggregations that spread throughout the brain (Ordway et al., 1997).

The striatum is believed to be the origin of pathology in HD. This is supported by converging post mortem, animal model and human neuroimaging data. For example, several post mortem studies show global atrophy of the brain, with the striatum experiencing the most drastic reductions (de la Monte et al., 1988; Vonsattel et al., 1985). Similarly, animal models utilizing genetic knock-ins report the striatum as the region of the first and most significant degeneration (Hodgson et al., 1999; Zhang et al., 2010). Classic human neuroimaging studies also illustrate extreme atrophy in striatal regions compared to the rest of the brain, which is associated with clinical phenotypes (Aylward et al., 2000; Harris et al., 1992; Starkstein et al., 1992).

The previously introduced prion hypothesis is one popular hypothesis of pathology spread in HD. In the case of HD, it proposed that mutant HD pathology begins in the striatum before diffusing before spreading both rostrally and caudally throughout the cortex (Brundin et al., 2010). Though prion hypotheses seem logical in the context of mutant HTT findings, contrary work shows mutant HTT is more actually common the cerebral cortex than the striatum (Gutekunst et al., 1999). Moreover, HTT aggregates occur in the interneurons, instead of the medium spiny projection neurons known to die first in HD (Kuemmerle et al., 1999). While it is obvious that pathology indeed spreads in HD, whether it is caused by HTT itself, or downstream inclusion bodies or deficits in cell signaling remains unclear.

Nonetheless, similar to other neurodegenerative disorders, degenerative phenomena follow stereotypical patterns in HD (Tabrizi et al., 2013, 2012, 2009). Hypotheses of HD spread have been developed in human post mortem, mouse model and cell culture work. Due to the rarity of the disorder, which affects 3 in 100,000 million people, large neuroimaging

datasets of HD are rare (Harper, 1992). Correspondingly, predictive whole brain models evaluating disease spread remain absent. The Network Diffusion Model represents an excellent tool to test neurodegenerative dynamics **on** structural networks in HD. Specifically, Chapter four of the current thesis is the first work to empirically evaluate several models of toxicity spread rooted in prion hypotheses in HD using an unprecedented human neuroimaging dataset.

Schizophrenia

Schizophrenia affects 1% of the population worldwide and is characterized by extreme heterogeneity of symptomatology both between subjects and also within a single subject (Fornito et al., 2012). Unlike other neural disorders with well characterized symptoms, clinical heterogeneity makes it increasingly difficult to pinpoint where abnormalities in neural circuitry lie and how they arise. Originally proposed by Wernicke due to the nature of symptoms, it is postulated that network disorganization in focal areas of the brain leads to global aberrant information integration (Rubinov and Bullmore, 2013b).

Similar to other neurodegenerative diseases, age of onset can be early adulthood. However, some subjects have onset beginning in the late teens and a small percentage of subjects even experience childhood onset (DeLisi, 1992). Due to several factors, including age discrepancies, human neuroimaging researchers are divided on how to classify schizophrenia (Kochunov and Hong, 2014). There is compelling evidence to suggest primary disturbance most likely from a genetic abnormality leads to a predisposition of schizophrenia, which results in a prolonged brain developmental period. Such

findings lead some researchers consider schizophrenia a neurodevelopmental disorder (Benes et al., 1994; Rapoport et al., 2012; Walsh et al., 2008). Conversely, changes in white matter integrity and gene expression cause some groups classify the disease as purely neurodegenerative (Pasternak et al., 2012; Rao et al., 2015). Still, others call it a neurodegenerative disorder with neurodevelopmental antecedents (Ashe et al., 2001). This debate is of particular relevance because determining whether a particular hallmark is a pathogenic mechanism (neurodegenerative) or a coping response (neurodevelopmental) has important therapeutic consequences (Arrasate and Finkbeiner, 2012)

As such, the current thesis seeks to shed light on progressive, possibly neurodegenerative, processes implicated in schizophrenia by modeling on-going structural brain changes. Because no pathogenic proteins have been strongly linked to schizophrenia in a manner similar to other neurodegenerative disorders, dynamics **of** network models will be emphasized. Due to strong evidence of abnormal gene expression in schizophrenia, the relationship between structural changes and gene expression will also be explored.

Dynamics of structural networks in SZ

Current models suggest SZ is a disorder of global brain dysconnectivity in the white matter network (Pettersson-Yeo et al., 2011). White matter changes as it relates to TBSS, which are metrics reflective of white matter integrity, are widespread. Though prevalent, TBSS findings are diffuse and inconsistent. Inconsistency both within and between subject cohorts in imaging protocols exacerbates inconsistency. For example, Fujino and colleagues show reduced FA in frontal, temporal, parietal and occipital lobes, a large

portion of the corpus callosum and also the corona radiata. A subset of psychosis symptoms correlate with FA in the IFOF and the anterior thalamic radiation (Fujino et al., 2014). In medication-naïve subjects, reduced FA in the the ILF and left IFOF in subjects all subjects is observed compared to controls. However, patients with audio-visual hallucinations show higher connectivity in the forceps major and IFOF than subjects with auditory hallucinations (Amad et al., 2014; Liu et al., 2014). While such work is integral in understanding changes to integrity, it does not provide significant context to dysconnectivity theories, as whole-brain organization is not probed.

A handful of studies apply graph theory to DTI networks in schizophrenia to assess a variety of global and local metrics (Fornito et al., 2012; van den Heuvel et al., 2013, 2010; Wang et al., 2012). Among these topological studies, more consistent findings emerge. Less central hubs in frontal regions and to some degree, subcortical/limbic areas is observed. Differences in metrics reflective of network integration in these same regions is also observed. These studies lend tremendous support to abnormal structural network organization, reflecting dysconnectivity.

However, such studies generally compare patients and controls at baseline. Models of how structural networks in SZ change after disease onset are lacking. Furthermore, topological abnormalities have yet to be integrated into a clinically validated model of schizophrenia; such a model would for instance allow a rational approach to the search for treatment and prevention of the disorder (Rubinov and Bullmore, 2013b). Hence, Chapter 5 of the current work seeks to understand changes dynamics **of** structural networks after SZ onset.

The current thesis

This thesis utilizes complex graph theoretic methodology and multimodal human neuroimaging data to construct and evaluate structural dynamic network models of neurodegeneration in several debilitating disorders, including Alzheimer's Disease, Huntington's Disease and Schizophrenia. **Chapter 1, "An Introduction to Structural Network Dynamics and its Application to Neurodegeneration,"** presents the field of network neuroscience and reviews literature of the current state of knowledge of neurodegenerative models in relevant disorders. The advent of non-invasive neuroimaging techniques and the application of graph theory has led to neuroscientists conceptualizing the complete brain as a network graph of nodes and edges in a field called network neuroscience. Within network neuroscience, we introduce that brain changes can be modeled according to two dimensions, which include a 1) dynamics **on** networks as well as a 2) dynamics **of** networks approach. Prior work shows that all neurodegenerative disease, show a stereotypical pattern of disease progression throughout the brain, but mechanisms underlying network spread remain unknown. Though there is much evidence supporting several different hypotheses of spread, most of these models have been developed as a result of converging post mortem, mouse model and cell culture studies. Few have been evaluated in vivo. The subsequent set of original studies seeks to test and create new models of prion-based disease spread implicating the structural connectome.

Alzheimer's Disease is perhaps the most well-studied neurodegenerative disease and represents an excellent disorder to test hypotheses of both dynamics **on** structural networks and dynamics **of** structural networks. **Chapter 2, "Preserved Overall Network Organization**

in AD Spectrum Despite Loss of White Matter Tract Integrity," examines whether the structural network is simply a conduit of pathology or also undergoes degeneration itself. Particularly, predictive performance of the Network Diffusion Model is examined on both healthy and diseased connectomes to give insight into mechanisms mediating disease spread and probe network structural topology. It is illustrated that despite measurable losses in white matter tract integrity, organization of the brain in Alzheimer's disease is preserved. Chapter 3, "**A New Network-Constrained Technique to Characterize Neurodegenerative Progression Rate in Alzheimer's Disease"** extends work conducted in Chapter 2 by presenting a new method to detect the rate of speed of pathology spread in AD using the NDM and establishing a relationship between baseline CSF biomarkers and a subject's range of speed of neurodegeneration.

After confirming the white matter network serves as a conduit for degeneration in AD, a disease that mirrors AD in many ways, but is fundamentally understudied in the context of human neuroimaging due to its extremely rare incidence, is examined. **Chapter 4, "Structural Network Model of Pathology Spread Best Predicts Neurodegeneration in Huntington's Disease,"** empirically tests several mechanisms rooted in the prion hypothesis that may mediate trans-synaptic pathology spread in HD, including genetic hypotheses, distance hypotheses, activity-dependent hypotheses and structural hypotheses. The first work to model hypotheses of pathology spread in HD, it is illustrated that a directional structural network model of neurodegeneration best predicts end state HD pathology. It is also shown that intrinsic structural architecture is important in mediating disease spread.

Having fully examined dynamics **on** networks, further elucidation involving dynamic **of** networks is required, using schizophrenia as a model disorder. Unlike AD and HD, Schizophrenia is not linked to a clear pathogenic protein species. However, hallmark patterns of neurodegeneration are still present. **Chapter 5,** "**Age-Related Changes in Topological Degradation of White Matter Networks and its Relationship to Gene Expression in Chronic Schizophrenia,"** probes changes in brain organization and corresponding relationships to gene expression with age in chronic schizophrenia. Age-related changes in the white matter network that are driven by younger subjects is observed, which suggest schizophrenia could be best viewed as a neurodevelopmental disorder and perhaps not neurodegenerative. Together, these findings point to the importance of structural network organization and feasibility of constructing topological models to capture the dynamic nature of neurodegeneration. **Chapter 6** "**Toward an Umbrella Approach to Modeling Neurodegeneration: Clinical Implications, Future Studies and Conclusions,"** integrates findings from the original studies presented in this thesis into the context or prior work on neurodegeneration. The feasibility of constructing a single umbrella model applicable to all neurodegeneration is discussed. Lastly, clinical implications of such an umbrella approach, methodological limitations of the current work and propose future advances in future research are considered.

Chapter 2:

Preserved Overall Network Organization in AD Spectrum Despite Loss of White Matter Tract Integrity

Introduction

Presence of amyloid-β plaques and tau protein-related neurodegeneration are widely accepted biomarkers of Alzheimer's Disease (AD) (Braak and Braak, 1991; Jack and Holtzman, 2013; Pearson et al., 1985). Several proposed models of AD exist, including the amyloid-cascade hypothesis, cascading network failure hypothesis and the prion hypothesis (Jones et al., 2016). The current work investigates "prion-like" transmission AD, whereby specific proteins misfold, aggregate and propagate, causing toxic gain of function and loss of function (Jucker and Walker, 2013). It is hypothesized these proteins spread trans-synaptically along neuronal pathways in specific patterns, as observed by classic clinical and anatomical progression in patients (Braak and Braak, 1991; Pearson et al., 1985; Saper et al., 1987). Converging human neuroimaging data showing stereotyped gray matter atrophy and functional connectivity impairments support this view (Apostolova et al., 2007; Pievani et al., 2011; Thompson et al., 2003). Recently published human neuroimaging of tau protein in AD recapitulate classic disease spread in vivo, which further supports trans-synaptic spread hypotheses (Schöll et al., 2016; Schwarz et al., 2016).

The brain's anatomic connectivity, given by white matter (WM) fiber pathways, is thought to play a key role in mediating regional relationships between various imaging biomarkers (Pandya et al., 2016). Anatomic connectivity appears to be impaired in AD and conversely, might serve as

conduit for progressing pathologies (Damoiseaux et al., 2009; Liu et al., 2011; Raj et al., 2012; Xie et al., 2006). Recently, our group proposed a graph theoretic model of tau pathology spread enacted on DTI-based WM connectivity networks. This model, called the network diffusion model (NDM), predicted that observed spatial patterns of degenerative diseases might be explained simply as a consequence of network spread. Subsequently, the NDM successfully predicted future atrophy patterns of AD subjects using their baseline regional atrophy (Raj et al., 2015). Thus, the NDM is based on the transmission of tau, but successfully predicts progression of regional atrophy, owing to the strong association between the two (Attems et al., 2012; Forman et al., 2002). In these models, connectivity networks were obtained from healthy subjects only, under the assumption that anatomic connectivity serves merely as a conduit for the transmission and ramification of pathologic entities, rather than itself being the primary target of those pathologies.

It is therefore emerging that both pathology and connectivity affect each other. While highly connected hub-like regions appear to have impaired connectivity in AD, they are also facilitators of pathology, and anchor epicenters or attractors into which pathology accumulates, as given by the network diffusion theory (Lo et al., 2010; Raj et al., 2012; Zhou et al., 2012). Intuitively, these hubs receive more exposition to pathogens due to their central roles in the network. Hence it is of interest to determine the causality of these processes, i.e. whether network organization governs disease transmission, or vice versa. Would lower connectivity or deteriorated microstructure impede synaptic spread or would higher pathology burden cause greater impairment of fiber tracts to pathogens and thus augment pathology propagation?

The current study uses network modeling in a multimodal dataset of 124 subjects from the Alzheimer's Disease Neuroimaging Initiative (ADNI) to investigate the impact of AD pathology on WM network organization, and the impact of WM network organization on pathology spread in the AD spectrum. We hypothesize that if WM network topology is altered prominently in AD, then it would lead to measurable change in the pattern of atrophy spread predicted by the NDM (Raj et al., 2012). To test this, we investigate 1) Global and local WM network organization changes in AD 2) The impact of thresholding on network metrics and 3) NDM performance on both canonical healthy connectomes as well as subject-specific connectomes against empirical regional longitudinal patterns.

Methods

Participants

All subject data were obtained from the Alzheimer's Disease Neuroimaging Initiative (ADNI) database (http://adni.loni.usc.edu/). ADNI is a public-private private, large multisite longitudinal study with the goal of tracking AD biomarkers and accelerate prevention and treatment of the disease. Subjects were diagnosed and grouped to Alzheimer's Disease (AD), Late Mild Cognitive Impairment (LMCI), Early Mild Cognitive Impairment (EMCI) and Control (CON) according to ADNI data description. All subjects have volumetric MRI and Diffusion MRI data. All subjects had at least one follow-up scan and there were no converters between scans. Subject demographic information is listed in Table 2.1.

Table 2.1. Demographic information of study participants.

Group	N	Age (std)	Age vs. CON	Male / Female	Gender vs. CON	Amyloid Burden (std)	Amyloid vs. CON	Time Elapsed From Baseline+
AD	19	73.5 (9.9)	p=0.64	11 M / 8 F	p=0.22	1.54 (.21)	p=5.08e-05 ***	131.3 days
EMCI	42	70.5 (7.7)	p=0.23	24 M / 18 F	p=0.03	1.35 (.23)	p=0.11	454.7 days
LMCI	26	72.6 (6.3)	p=0.86	18 M / 8 F	p=0.50	1.44 (.22)	p=0.002 **	532.8 days
CON	37	72.4 (6.1)	--	19 M / 18 M	--	1.28 (.15)	--	--

+ Denotes average time elapsed from baseline to the final longitudinal scan on which the NDM model is tested.

*** p<.001 ** p<.01

MR image acquisition

DTI and inversion-recovery spoiled gradient recalled (IR-SPGR) T1-weighted imaging data were acquired on several General Electric 3T scanners using scanner specific protocols. Briefly, DTI data were acquired with a voxel size of $1.37^2 \times 2.70$ mm^3, 41 diffusion gradients and a b-value of 1000 s/mm^2. IR-SPGR data were acquired with a voxel size of $1.02^2 \times 1.20$ mm^3. All imaging protocols and preprocessing procedures are available on the ADNI website. (http://adni.loni.usc.edu/methods/).

T1-weighted image processing

Automated cortical and subcortical volume measures were performed with FreeSurfer software package, version 5.3 (http://surfer.nmr.mgh.harvard.edu/fswiki) (Fischl et al., 2004, 2002). Automated cortical and subcortical volume measures were performed with FreeSurfer software. To reduce the confounding effect of intra-participant morphological variability, each participant's longitudinal data series was processed by FreeSurfer longitudinal workflow (http://surfer.nmr.mgh.harvard.edu/fswiki/LongitudinalProcessing). A previous test-retest study validated that the longitudinal processing provides consistent regions of interest (ROI) segmentation (Reuter et al., 2012). All images underwent standardized quality control. Participants with complete segmentation failure or gross errors throughout all brain regions were rated as complete failure. Participants with gross errors in one or more specific brain regions (i.e., temporal lobe regions, superior regions, occipital regions, and insula) were given partial pass rating. Participants with partial pass rating were included in analyses.

Raw DWIs were corrected for image artifacts including Eddy current, motion, and EPI distortions using FSL toolbox (https://fsl.fmrib.ox.ac.uk/fsl). Diffusion tensors were modeled at each voxel in the brain from the corrected DWI scans using CAMINO toolbox (http://www.camino.org.uk). Afterward, the deterministic simple whole WM streamlining has been applied on the diffusion tensor images (DTI) using CAMINO software. The tissue masks from T1 image was rigidly registered to the first frame of the DWI and used in the WM tractography. Subject-specific FreeSurfer (Desikan-Killarney) cortical and subcortical parcellations mapped in the DTI subject space is used to calculate the 86x86 ROI-ROI connectivity matrix.

Network construction and analysis

The number of resulting streamlines connecting any two gray matter regions, including from both cortical and subcortical regions were considered as edge weights in the resulting graphs. To control for inter-subject variance in total streamline count, the number of connections between each tract was divided by the total number of tracts computed on each subject's tractography data, to yield a connectivity density metric.

Characteristic graph metrics to examine differences in network topology were calculated from undirected, weighted structural connectivity matrices. Matrices were not thresholded unless otherwise noted. Network metrics including density, global efficiency, clustering coefficient, local connection strength, local efficiency and local modularity were computed in MATLAB using the Brain Connectivity Toolbox (BCT) (Rubinov and Sporns, 2010).

Network Diffusion Model

The network diffusion model (NDM) is used as described in Raj et al. 2012. The NDM was constructed and illustrated as described in Figure 2.1. Briefly, AD-related disease pattern, given by the vector x(t), is modeled as a diffusive process:

$$\mathbf{x}(t)=e^{-\beta Ht}\mathbf{x}_0, \quad \text{(Eq 1)}$$

where x_0 is the initial regional pattern of the disease, on which the term $e^{-\beta Ht}$ acts as a spatial and temporal blurring operator. We therefore call $e^{-\beta Ht}$, "the diffusion kernel." The computation of the above equation is accomplished via the eigenvalue decomposition $H = U\Lambda U^{\dagger}$, where $U = [u1 \ \ldots \ uN]$, giving:

$$\mathbf{x}(t)=Ue^{-\Lambda\beta t}U^{\dagger}\mathbf{x}_0=\sum_{i=1}^{N}(e^{-\beta\lambda_i t}\mathbf{u}_i^{\dagger}\mathbf{x}_0)\mathbf{u}_i. \quad \text{(Eq 2)}$$

In other words, the NDM is evaluated via the eigen-decomposition of the Laplacian matrix, such that the pattern of disease at any point of time is given as a linear superposition of the eigenmodes u_i's of the Laplacian. Eigenmodes are calculated, using spectral graph theory on the WM 86x86 ROI Laplacian matrix based on spectral graph theory. These eigenmodes, in turn, represent fundamental substrates upon which network spread of pathological entities is enacted. Hence, we investigated whether the prominent eigenmodes are conserved between patients' individual subject-specific connectomes and a canonical healthy connectome obtained by averaging a large number of healthy subject connectomes.

Statistical analysis

A cross-sectional design is used to evaluate topology differences in connectomes, because most subjects had a single DTI scan. Independent, two-sided t-tests were used to test for differences in characteristic graph metrics between each patient group (AD, LMCI, EMCI) compared to controls. Patient groups were not evaluated in relation to each other. Glass brains depicting magnitude of t-statistic using a previously reported method are used for visualization (LoCastro et al., 2014; Pandya et al., 2016; Raj et al., 2012). All reported significant p-values survived FDR correction for multiple comparisons and are FDR adjusted unless otherwise noted (Benjamini and Hochberg, 1995). In the case of non-Gaussian variables (measured with Anderson-Darling tests), global graph metrics were successfully replicated with non-parametric permutation testing (10,000 permutations) (Table 2.3) (Razali and Wah, 2011).

To evaluate changes in connectivity strength in the graph, the Network Based Statistic (NBS) was used. The NBS is a validated, nonparametric statistical method for performing statistical analysis on large networks, which deals with the issue of multiple comparisons by controlling for the family-wise error rate (FWER) (Bai et al., 2012; Cocchi et al., 2012; Zalesky et al., 2010). FWER-corrected p-values are calculated for each component using permutation testing (5,000 permutations). The NBS was used on weighted, non-thresholded networks, with the primary threshold for each link-based t-statistic set to 2.5, significantly more conservative than prior studies (Zalesky et al., 2011).

Figure 2.1 illustrates workflow of the NDM. The output of the NDM, x(t), is a vector of positive values at any post-baseline time t, representing

predicted pathology burden spreading from the baseline regional pattern. Results of the NDM were normalized to a Gaussian distribution via a Box-Cox transformation (Osborne, 1964). Since the NDM by itself is defined in terms of model time and not real time in years, the NDM was executed over a range of 100 arbitrary “model time” time points, until the model hit steady state.

Observed pathology, as measured by regional atrophy differences in a subject’s longitudinal scan, was logistic rescaled to a value between 0 – 1 for each subject. To evaluate predictive power of the NDM, we performed whole brain Pearson correlation analysis between predicted pathology vs. observed pathology. This analysis carried out for each of the 100 model time points. Since the model is specified in terms of model time, its relationship to a patient’s disease duration is not a priori known. Hence we compared empirical subject data with NDM output at all model times, and the model time point that yielded the best correlation was selected. For each subject, correlation analysis was performed to evaluate prediction accuracy of the NDM implemented on the template healthy connectome. Prediction accuracy was also evaluated on the subject-specific connectome. Fisher r-to-z transformations were used to compare if NDM prediction accuracy changed with connectome choice (Fisher, 1921). All analysis was performed in MATLAB.

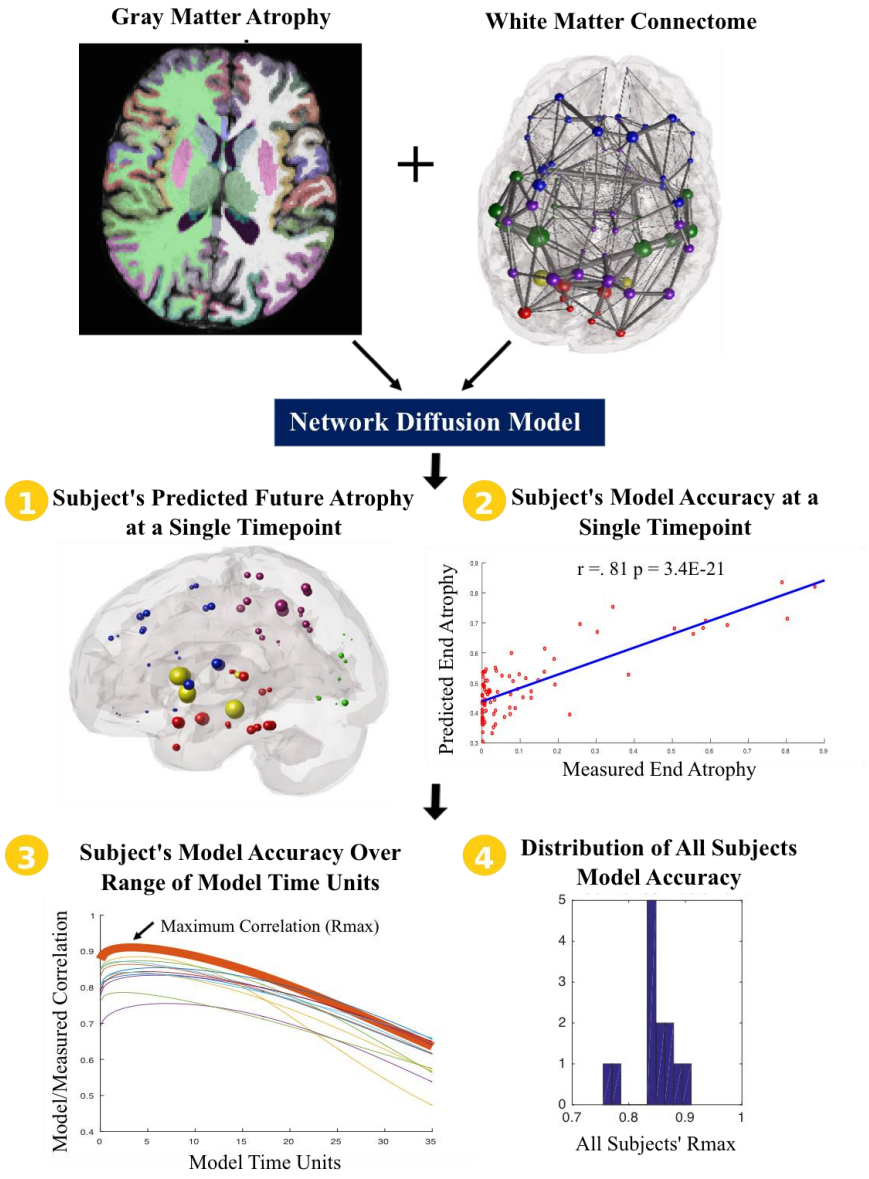

Figure 2.1. Workflow of the NDM. A subject's baseline gray matter atrophy pattern and WM connectome are used as inputs to the NDM. **(1)** The model predicts a subject's future atrophy at a single time point on a 0 - 1 scale. **(2)** Model accuracy at a single time point is determined by correlation analysis of predicted end atrophy vs. measured end atrophy. Measured end atrophy is determined by a subject's longitudinal scan. **(3)** The NDM model is modeled over a wide range of time units, until the model hits steady steady. The resulting curve is the model's prediction accuracy over a range of model time units. The highest correlation at any time, which represents the model's best prediction accuracy, is selected as R_{max}. **(4)** This analysis is carried out for each subject. Each subject's R_{max} is depicted.

Results

Cortical volume

First, it is confirmed that results from the current study's imaging pipeline reproduce numerous previously published data on this same ADNI cohort. Baseline regional cortical volume from the 86 Freesurfer ROIs are compared between patients on the AD spectrum and controls. Atrophy is corrected for intracranial volume. Figure 2.2 shows t-statistics resulting from a two-tailed student's t-test, which were obtained at each brain region. All reported regional significance in glass brains survive FDR correction for multiple comparisons. Table 2.2 depicts the full list of p-values.

Universally, patients show significantly decreased regional cortical volumes (Figure 2.2). These data showing prominent atrophy in subcortical and temporal cortices demonstrate that our imaging pipeline reproduces well-known previously reported classic features of AD topography.

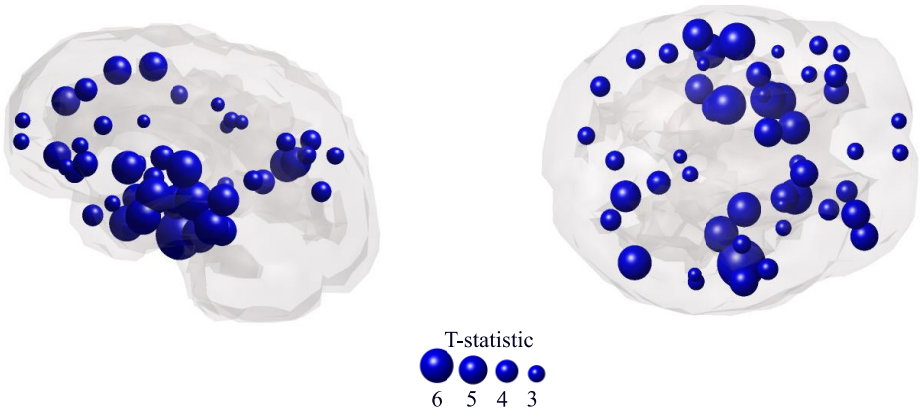

Figure 2.2. Volumetric glass brains. Glass brains displaying cortical volume in CON vs. AD. Blue denotes atrophy in AD vs. CON. Figure thresholded for significance at $p<0.05$ and all illustrated results survived FDR multiple corrections. For a full-list of p-values see Table 2.2.

Table 2.2. List of volumetric statistics.

p-value (FDR Corrected)	Region
2.02E-08	Right Inferior Temporal
2.78E-06	Left Hippocampus
3.84E-06	Right Fusiform
4.17E-06	Right Entorhinal
4.17E-06	Left Amygdala
5.97E-06	Left Superior Temporal
6.84E-06	Left Entorhinal
9.84E-06	Left Accumbens
1.64E-05	Left Inferior Temporal
1.84E-05	Right Inferior Parietal
1.84E-05	Right Hippocampus
2.03E-05	Left Middle Temporal
5.46E-05	Right Precuneus
5.73E-05	Left Fusiform
7.78E-05	Right Rostral Middle Frontal
8.29E-05	Right Parsorbitalis
8.29E-05	Left Parahippocampal
8.29E-05	Left Superior Frontal
9.30E-05	Right Middle Temporal
1.10E-04	Right Superior Frontal
1.66E-04	Right Amygdala
2.80E-04	Left Insula
3.13E-04	Left Lateral Orbitofrontal
3.86E-04	Right Isthmus Cingulate
0.001	Left Rostral Middle Frontal
0.002	Right Lateral Orbitofrontal
0.002	Right Superior Parietal
0.002	Right Temporal Pole
0.003	Right Superior Temporal
0.004	Left Inferior Parietal
0.004	Left Bankssts
0.005	Left Precuneus
0.005	Left Supramarginal
0.006	Right Precentral
0.006	Left Parstriangularis
0.009	Left Superior Parietal
0.009	Right Accumbens
0.011	Right Medial Orbitofrontal
0.011	Right Bankssts
0.011	Left Parsorbitalis
0.014	Right Posterior Cingulate
0.014	Right Frontal Pole
0.017	Right Insula
0.019	Left Frontal Pole
0.019	Left Temporal Pole
0.024	Left Putamen
0.034	Right Supramarginal
0.035	Left Precentral
0.037	Left Posterior Cingulate
0.040	Right Putamen
0.044	Left Parsopercularis

Global network analysis

Next, graph theory analysis is used to determine if commonly used metrics of global WM network organization and topology are disrupted in the AD spectrum. Specifically, we assess density, a measure of the overall number and strength of fiber connections, pathlength, a measure of network integration and efficiency, which is reflective of the ability of the network to sustain information flows (Rubinov and Sporns, 2010). Subcortical and subcortical regions constitute the graph. Connectivity matrices are not binarized, but kept as weighted values. Matrices are not thresholded.

Global metrics of density, path length and efficiency are compared between each patient group and controls. Remarkably, no global metrics are significantly different between patients and controls (Figure 2.3). Across all three groups in the AD spectrum, patients show no significant difference in density compared to control subjects (AD: p=0.65, LMCI: p=0.65, EMCI: p=0.89). Similarly, no significant difference is observed in pathlength in patients vs. controls (AD: p=0.85, LMCI: p=0.65, EMCI: p=0.65) nor global efficiency (AD: p=0.97, LMCI: p=0.82, EMCI: p=0.65). All reported p-values are FDR corrected for multiple corrections.

Due to limited sample sizes and the possibility of the summary network metrics being non-Gaussian, we performed additional analysis. First, we used the Anderson-Darling test to test for Gaussianity of each metric. Then we performed non-parametric permutation testing (10,000 permutations) for the few variables with non-Gaussian distributions (Table 2.3). In confirmation of above findings, no significant differences are found. In sum, we observe disease groups do not show significantly altered global topological properties

compared to healthy controls when weighted, non-thresholded connectivity matrices consisting of both cortical and subcortical regions are used.

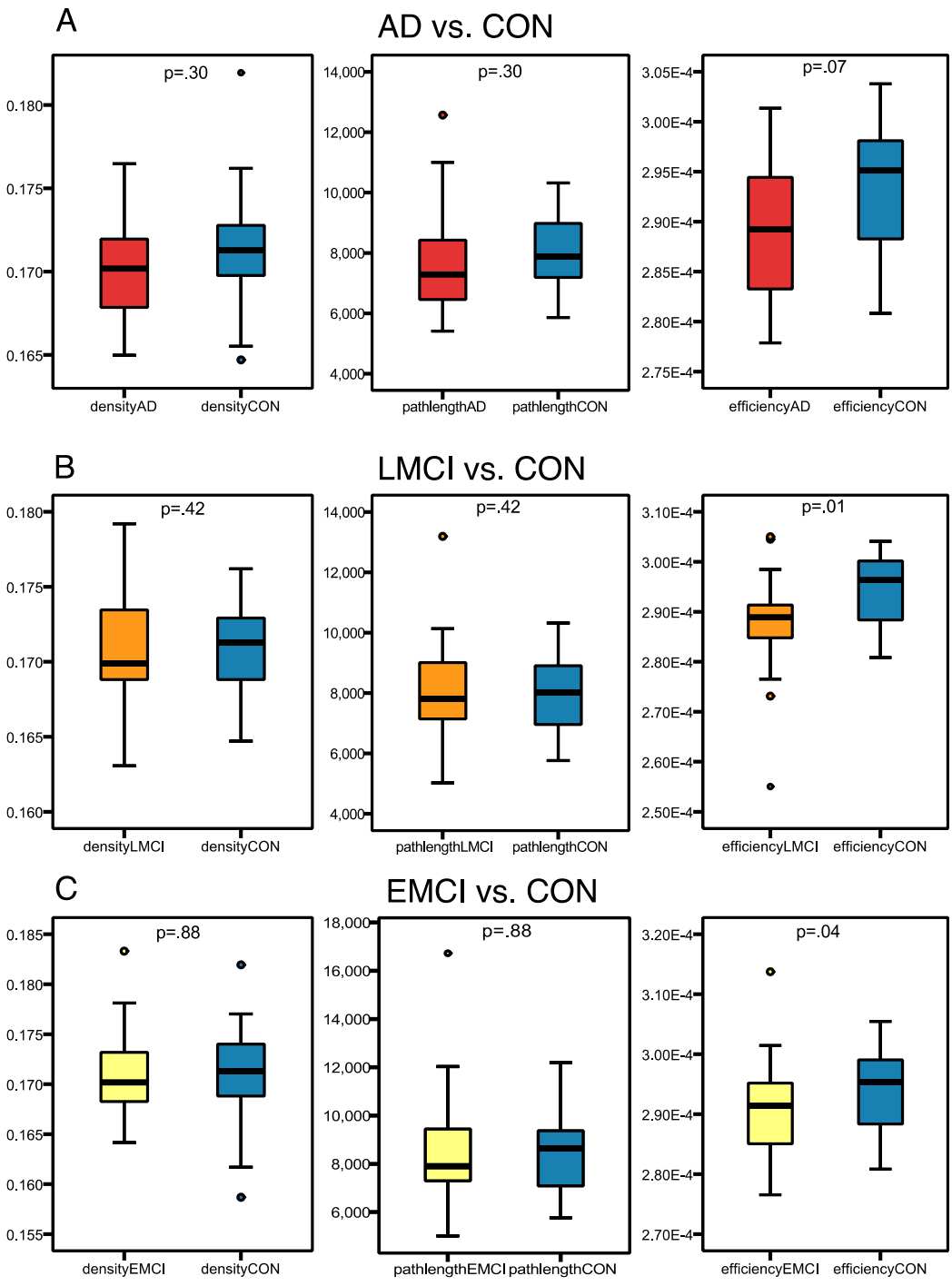

Figure 2.3. **Global network measures.** Global network measures in the AD spectrum vs. controls. All reported p-values are FDR corrected for multiple comparisons. Boxplots depict the standard t-test.

Table 2.3. **Global metric permutation testing.**

Metric	Normal Distribution	Normality test p-value	T-test vs. CON (no FDR)	Permutation Test vs CON (No FDR)
Density				
AD	Yes	p=0.66	p=0.3612	p=0.3679
LMCI	No	p < 0.001	p=0.2531	p=0.2763
EMCI	Yes	p=0.04	p=0.7958	p=0.7961
CON	Yes	p=0.27	--	--
Efficiency				
AD	No	p < 0.001	p=0.2827	p=0.3547
LMCI	Yes	p=0.30	p=0.4974	p=0.4987
EMCI	Yes	p=0.10	p=0.4828	p=0.4889
CON	No	p < 0.001	--	--
Pathlength				
AD	Yes	p < 0.03	p=0.6574	p=0.6611
LMCI	No	p=0.01	p=0.1773	p=0.1824
EMCI	Yes	p=0.15	p=0.1073	p=0.1094
CON	Yes	p=0.40	--	--

Note: The core assumption of the independent samples t-test is that variables are distributed somewhat normally. All tests of normality were carried out with the Anderson-Darling test, whose null hypothesis is that variables come from a normal distribution. A p-value of < .01 indicates that the Anderson-Darling test fails to reject the null hypothesis at the 1% significance level. Because t-tests have to be approximately normal, a cutoff of p<.01 is used. 10,000 permutations were carried out unless otherwise noted.

Local network analysis

Next, local network analysis is performed to probe distributed topological changes among specific brain regions. We examine local betweenness centrality, a measure of hub-ness, local strength, the sum of a region's connections, and local efficiency, which is a measure of local information flow (Rubinov and Sporns, 2010).

Only a handful of nodal differences, concentrated in frontal and temporal regions of all local graph metrics, are observed. However, virtually none of the differences survive FDR correction for multiple comparisons (Figure 2.4). In the AD vs. CON group, only nodal strength of the left precuneus (p=6.66e-05) survives FDR correction for multiple comparisons (Figure 2.4B). No local metrics in the LMCI vs. CON nor EMCI vs. CON group survive FDR correction. (LMCI and EMCI glass brains data not shown.)

To further probe topological differences independent of nodal summary graph metrics, we assess whether nodal strength distributions are different in AD vs. CON. For each group, we plot a distribution of the strength all nodes and fit the distribution with power law alpha. A Kolmogorov–Smirnov test reveals no significant difference between the strength distributions (p=0.98) and power law alpha values of the fitted strength distributions are virtually identical (CON: Alpha = 5.81, AD: Alpha = 5.92).

Taken together, Figure 2.4 and Figure 2.5 show local graph topology is not significantly altered between disease groups and healthy controls using weighted, non-thresholded connectivity matrices.

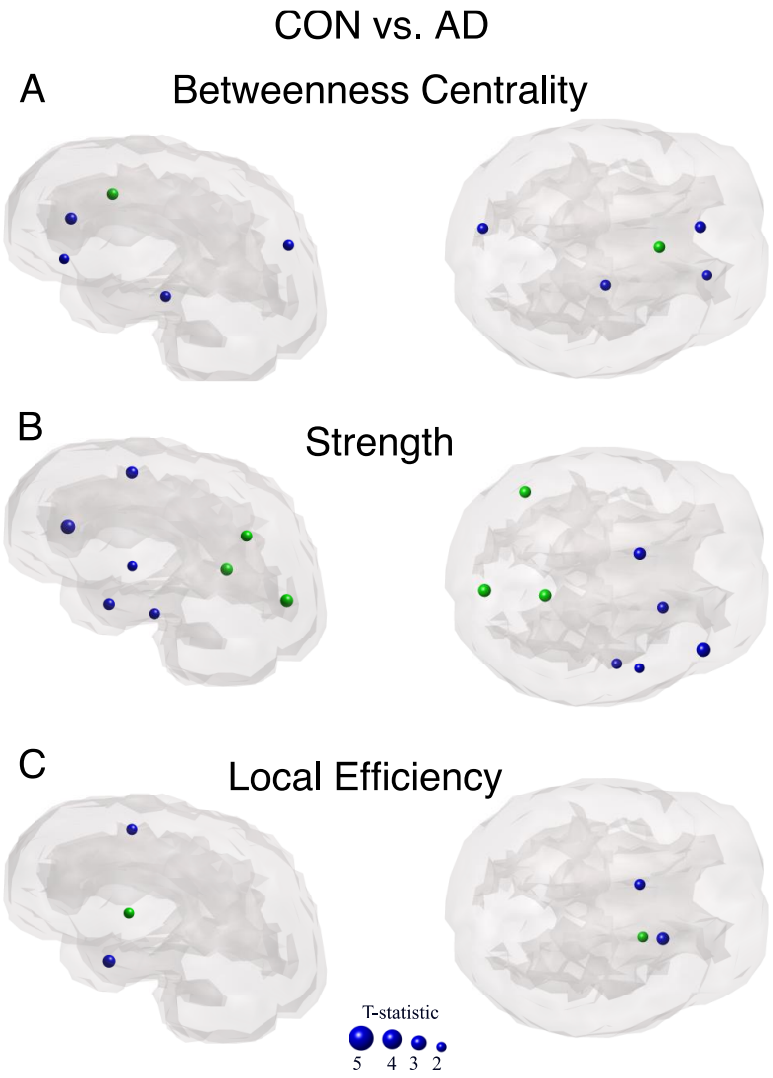

Figure 2.4. Local network metrics. Glass brains of local network measures in AD vs. CON. Images are thresholded at p<.05 significance and no reported p-values survived FDR corrections except regional strength in the left precuneus. Blue denotes decreased in AD compared to CON. Green denotes increased in AD compared to CON.

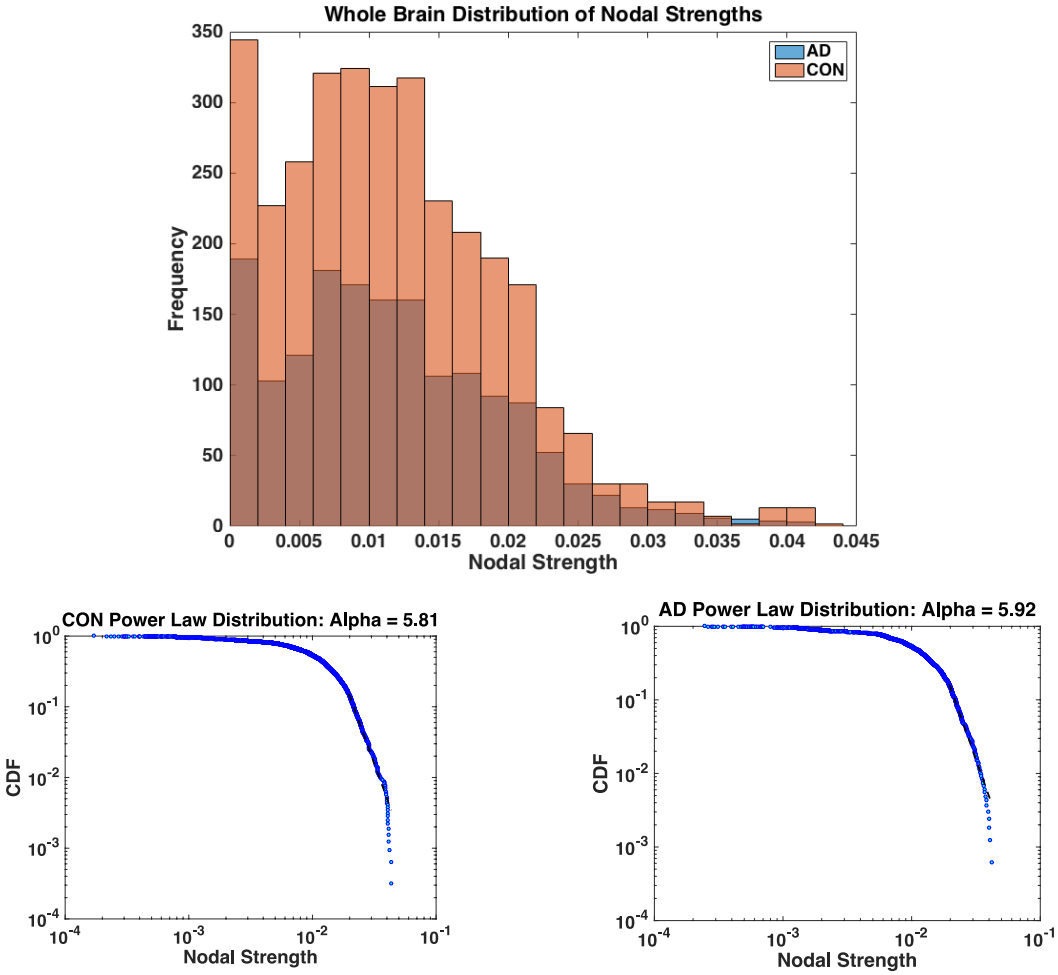

Figure 2.5. Nodal strength distributions. Histograms of the nodal strength distribution across all subjects in addition to nodal strength distribution fitted with a power law alpha function.

Tract level results

Due to prior reports of significant alterations of graph theory metrics in AD compared to control subjects, we next evaluate the possibility that our tractography and network extraction pipeline is uniquely insensitive to changes in connectivity compared to previous tract-level analyses. Thus, we assess whether the connectivity changes detected by the present methodology agreed with specific tracts reported to be disrupted in AD. To evaluate tract-level changes in fiber strength, we examine strength between every pair of GM regions in the brain (as opposed to previously, a node's sum of strengths), using the Network-Based Statistic (NBS) as detailed in Methods.

Significant alterations in a number of WM connections in ROIs along the uncinate fasciculus (UF), superior longitudinal fasciculus (SLF) and cingulum bundle (CB) (Figure 2.6, Table 2.4). Thus, in agreement with previous literature, connectivity values returned by our pipeline show significant impairment in tract-level WM changes in WM fiber count of AD compared to controls. These results confirm that the non-significant topology findings described above are not due to lack of sensitivity caused by the present study's connectivity and tractography pipelines.

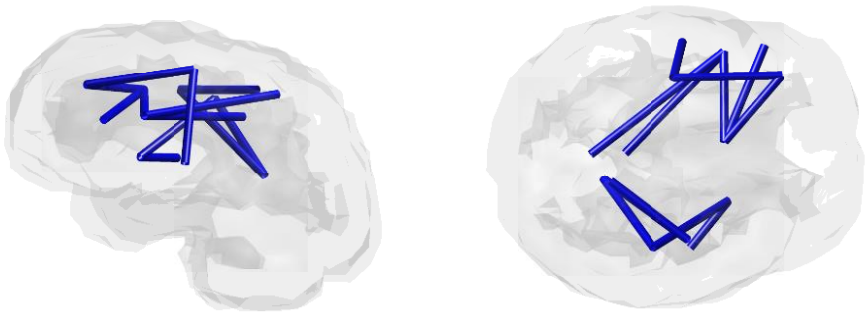

Figure 2.6. Tract-level differences. Glass brains of tract-level differences in AD vs. CON as measured by ROI-ROI connectivity strength using the NBS. Blue denotes tract decreased in AD relative to CON.

Table 2.4. List of tract-level differences. Region pairs with decreased ROI-ROI connectivity strength in AD relative to CON as measured using the NBS. Alterations depicted above in Figure 2.6.

Regions	**Tract**	**Hemisphere**
Subnetwork 1, p=.01		
Isthmus Cingulate / Post Central	CB	Right
Isthmus Cingulate / Precentral	CB	Right
Paracentral / Precentral	SLF	Right
Post Central / Putamen	--	Right
Transverse Temporal / Putamen	UF	Right
Subnetwork 2, p=.01		
Caudal Anterior Cingulate / Parsopercularis	CB	Left
Paracentral / Parsopercularis	SLF	Left
Caudal Anterior Cingulate / Parstriangularis	CB	Left
Parsopercularis / Posterior Cingulate	CB	Left
Caudal Anterior Cingulate / Rostral Middle Frontal	CB	Left
Caudal Middle Frontal / Rostral Middle Frontal	SLF	Left
Caudal Middle Frontal / Superior Temporal	--	Left

Effect of thresholding

Next, we explore whether our graph metrics appear different from previous reports due to the effect of stringent thresholding and/or binarization. To test whether these effects are responsible for observed discrepancies, we replicate previous findings by thresholding and binarizing our connectomes. Thresholding percentages are defined against raw non-zero connections.

Figure 2.7 shows thresholding in combination with binarization at a wide range of thresholds k, yields significant results across global metrics density, path length and global efficiency in AD vs. CON. Specifically, density of thresholded and binarized networks yields significance in the range of k = 5% - 65% (Figure 2.7A1), pathlength in the range 15% - 60% (Figure 2.7A2) and global efficiency in the range 5 - 65% (Figure 2.7A3).

Thresholding-only of weighted matrices (with no binarization) yields significant differences in topology for a narrow range of threshold K, which include 5%, 30% and 35% (Figure 2.7B2). Similarly, global efficiency is significantly lower in AD than controls at k=5% and k=10% (Figure 2.7B3). See Table 2.6 for a full list of p-values.

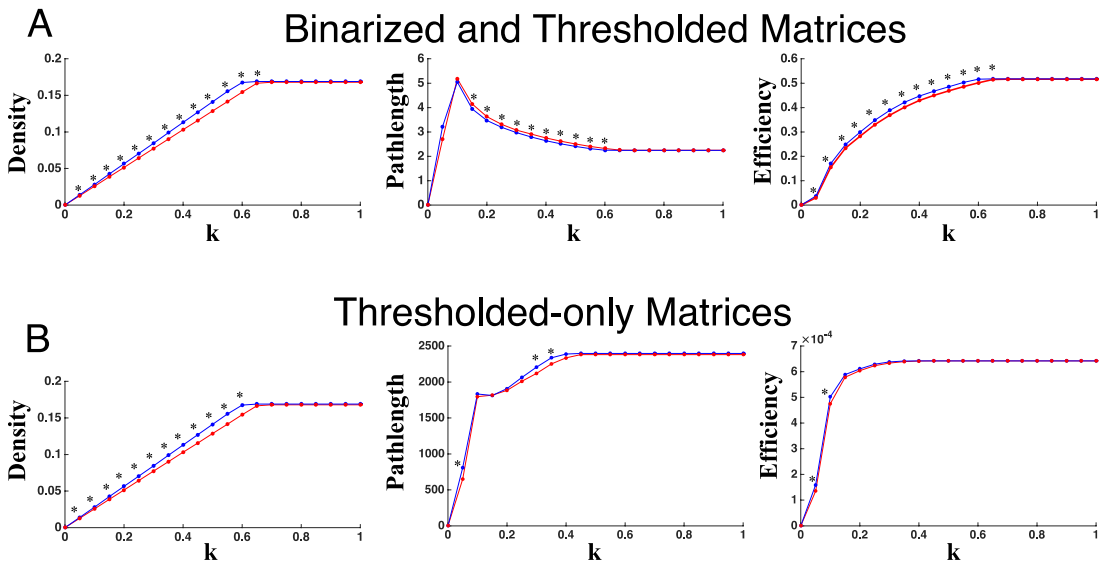

Figure 2.7. Sparsity graphs. A) Weighted matrices are binarized and thresholded at various percentages of non-zero connections, as represented by k. **B)** Weighted matrices are thresholded with no binarization, at various percentages of non-zero connections, as represented by k. * indicates significance between AD and CON. The blue line represents controls and the red line represents AD.

Table 2.5. Thresholding statistics. Global metric differences in AD vs. CON over a range of thresholds in both binarized and weighted networks.

% Threshold of Non-0 Connections	Density of Binarized Network	Global Efficiency of Binarized Network	Global Efficiency Of Network	Pathlength of Binarized Network	Pathlength of Weighted Network
5%	p<0.001***	p<0.001***	p<.01 **	p=0.07	p<.05 *
10%	p<0.001***	p<0.001***	p<.01 **	p=0.36	p=.49
15%	p<0.001***	p<0.001***	p=.14	p<0.001***	p=.90
20%	p<0.001***	p<0.001***	p=.27	p<0.001***	p=.37
25%	p<0.001***	p<0.001***	p=.39	p<0.001***	p=.08
30%	p<0.001***	p<0.001***	p=.50	p<0.001***	p<.01 **
35%	p<0.001***	p<0.001***	p=.75	p<0.001***	p<.01 **
40%	p<0.001***	p<0.001***	p=.92	p<0.001***	p=.15
45%	p<0.001***	p<0.001***	p=.97	p<0.001***	p=.68
50%	p<0.001***	p<0.001***	p=.97	p<0.001***	p=.68
55%	p<0.001***	p<0.001***	p=.97	p<0.001***	p=.68
60%	p<0.001***	p<0.001***	p=.97	p<0.001***	p=.68
65%	p<0.01**	p<.05 *	p=.97	p=0.09	p=.68
70%	p=0.30	p=0.27	p=.97	p=0.37	p=.68
75%	p=0.30	p=0.27	p=.97	p=0.37	p=.68
80%	p=0.30	p=0.27	p=.97	p=0.37	p=.68
85%	p=0.30	p=0.27	p=.97	p=0.37	p=.68
90%	p=0.30	p=0.27	p=.97	p=0.37	p=.68
95%	p=0.30	p=0.27	p=.97	p=0.37	p=.68
100%	p=0.30	p=0.27	p=.97	p=0.37	p=.68

Eigenmodes

Our prior work presents the concept of, eigenmodes, “persistent modes”, which is a topological (and linear) metric of the WM connectome governing disease spread. Eigenmodes were shown to form an effect basis on which baseline atrophy data can be projected for prediction of a subject’s future atrophy (Raj et al., 2015, 2012). We hypothesize that if the network architecture is significantly impacted by AD, as differences in tract-level changes might suggest, then the resulting eigenmodes of the diseased network will be significantly different than those in controls.

To compare eigenmodes between groups, the dot product of eigenmode from the average AD connectome is calculated in respect to that of healthy controls. Since eigenmodes are unchanged by overall sign, the absolute value of the dot product is taken. A value of 1 denotes perfect match between the eigenmodes from the two groups, and a value of zero denotes that the eigenmodes are orthogonal, hence fully dissimilar. The first three eigenmodes are presented as previous studies show the first three eigenmodes are the most stable (Raj et al., 2012; Wang et al., 2017).

We show all eigenmodes dot products are very close to 1, illustrating nearly identical eigenmodes in dementia compared to age-controlled healthy brains. (Table 2.5). Figure 2.8 presents a depiction of AD and CON network eigenmodes. Thus, despite widespread atrophy and impaired tract-level connectivity, we observe overall architecture of the diseased network does not result in measurable changes to its characteristic eigenmodes.

Table 2.6. Comparison of characteristic eigenmodes. Absolute value of dot products of group-wise comparisons of characteristic eigenmodes. A dot product of 1 denotes eigenmode equivalence.

Eigenmode	AD • CON	LMCI • CON	EMCI • CON
1	1	1	1
2	0.9986	0.9995	0.9996
3	0.9983	0.9991	0.9986

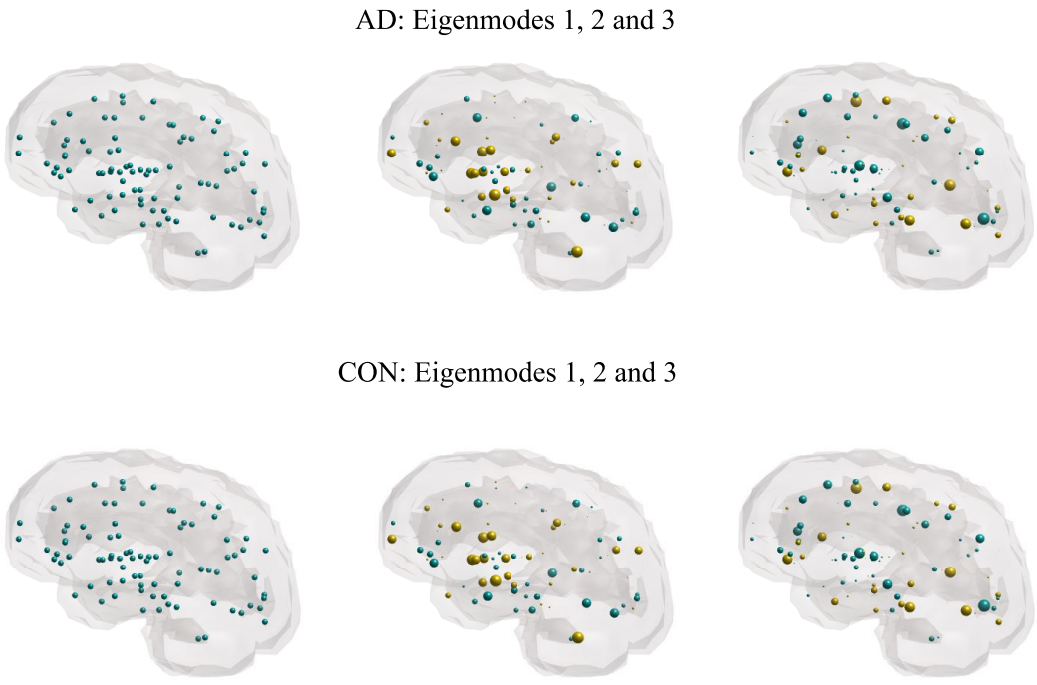

Figure 2.8. Glass brains of eigenmodes. Topology of nearly identical eigenmode 1, eigenmode 2 and eigenmode 3 of AD and CON connectomes. Blue denotes positive and yellow denotes negative; note however that eigenmodes are invariant under a global sign change.

Performance of diseased connectomes in the NDM

Given no observable AD-related differences in network organization, we examine whether models of AD progression based on WM graph topology is altered in disease. To test this, we use a network diffusion model (NDM) of pathology spread shown to provide a strong prediction of regional patterns of disease progression (Raj et al., 2015, 2012). Previously, the NDM was implemented using a healthy template connectome. The current work directly compares performance of the NDM on an age-matched connectome from ADNI controls vs. a patient's own disease-impaired connectome. We hypothesize that if overall network architecture is significantly altered in AD, then the model will give dissimilar outcomes of pathology spread.

The NDM obtains predictions of future regional patterns of atrophy ($x(t)$) from a patient's baseline volumetric scan (x_0) (see Equation 1 in Methods). To test model performance, we correlate the subject's observed end atrophy from a longitudinal scan vs. predicted atrophy as modeled by the NDM (See Methods). This procedure was carried out independently on both the healthy template connectome in addition to the subject-specific connectome. The furthest time point with the highest proportion of patients within each patient group was selected to allow for measurement of maximum disease progression.

Figure 2.9 shows that use of the diseased connectome in the NDM does not significantly increase nor decrease the high correlation between predicted future atrophy and observed end state atrophy. Specifically, Figure 2.9A1 shows overall NDM performance on the control connectome, which is obtained by correlation analysis of each subject's predicted future atrophy vs. observed end state atrophy.

Because baseline regional atrophy has been shown to highly correlate to future atrophy patterns, the degree to which the NDM improves over baseline is examined. NDM improvement is represented by the change in correlation coefficient (Δ r) between modeled-predicted atrophy vs. end state atrophy and baseline vs. end state atrophy (Eq 3).

NDM Improvement = Model Correlation to End State - Baseline Correlation to End State (Eq 3)

For example, in AD patients, on average, the NDM yields a model accuracy of r = 0.80 between predicted atrophy vs. observed end state atrophy. The correlation between baseline regional atrophy vs. observed end state atrophy is r = 0.70. Thus, the NDM offers improvement of Δ r = 0.10, on average, compared to solely using baseline atrophy as a predictor of future atrophy.

Figures 2.9B1-2 show each subject's NDM improvement from baseline on both the ADNI control connectome vs. a patient's own disease-impaired connectome. Choice of connectome does not appear to significantly impact model improvement. This confirmed by intra-subject Fisher r-to-z transformations comparing the correlation coefficients (Table 2.7). Furthermore, paired t-tests reveal no significant difference in the time it takes for model to achieve optimal diffusion on control vs. individual connectomes (AD: p=0.27, LMCI: p=0.22, EMCI p=0.42) (Figure 2.10). Thus, our results suggest that even if certain elements of the WM connectivity network are impaired by disease, they do not impair the overall network organization and topology to the extent necessary to alter the network mediation of AD pathology progression in the AD spectrum.

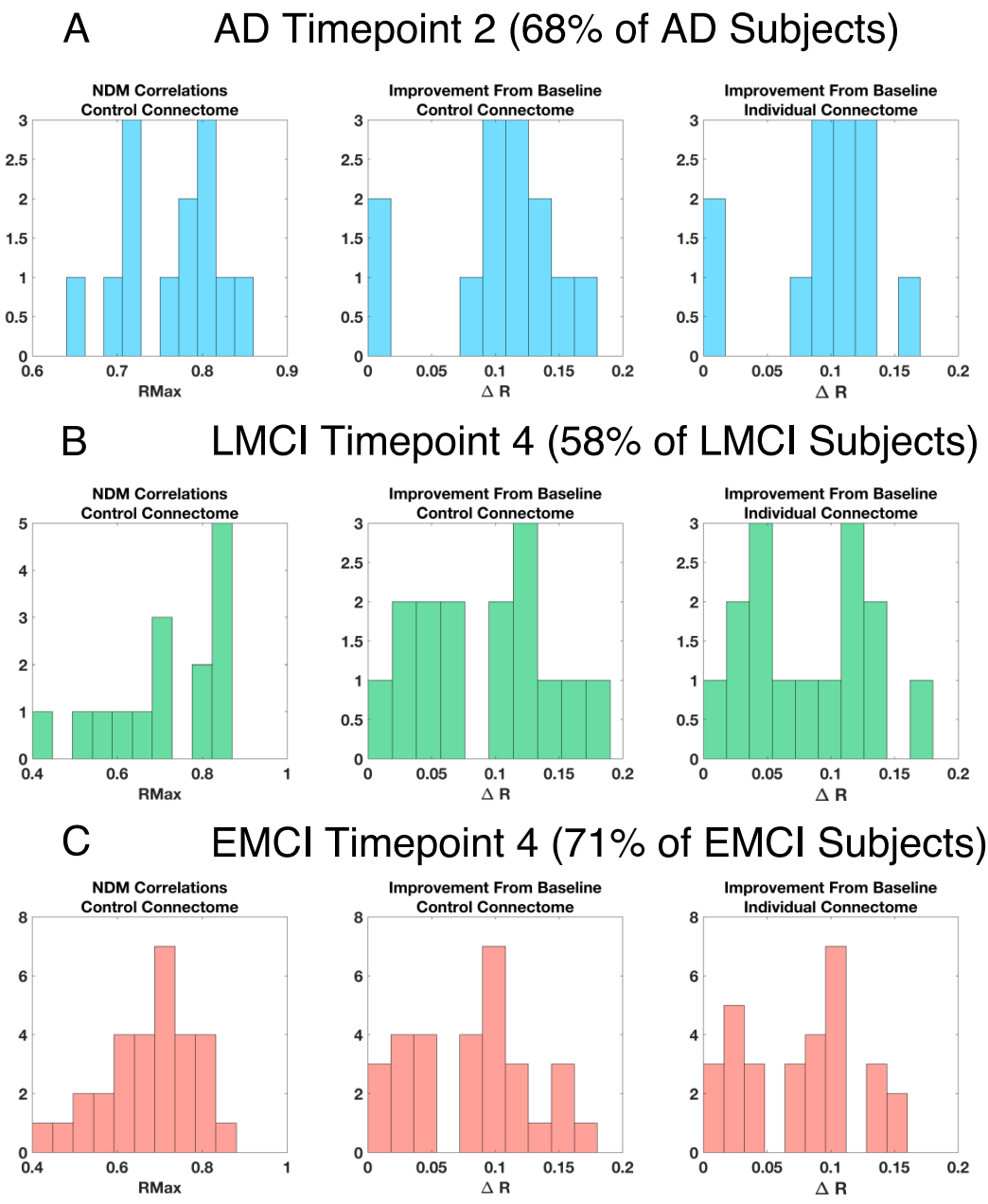

Figure 2.9. NDM performance. NDM performance on individual patient connectomes vs. age-matched control connectomes. **(A)** NDM on the control connectome, by correlating predicted future atrophy vs. measured atrophy. **(B).** Model improvement from baseline on the control connectome **(C)**. Model improvement from baseline on the individual connectome.

Table 2.7. Model performance on various connectomes. Each subject's correlation coefficient of the template connectome, Subject-Specific connectome and an independent template connectome. Blue denotes AD, green denotes LMCI and purple denotes EMCI subjects.

+ As dictated in the methods section, NDM prediction accuracy was evaluated with Pearson's correlation. There was no difference in model accuracy unless otherwise noted.

ADNI Template Connectome	ADNI Subject Connectome	Independent Template Connectome		Template Connectome	Subject Connectome	Independent Template Connectome
r = 0.8207	r = 0.8194	r = 0.8189		r = 0.7299	r = 0.7304	r = 0.7320
r = 0.8158	r = 0.8120	r = 0.8006		r = 0.8870	r = 0.8867	r = 0.8866
r = 0.8128	r = 0.8150	r = 0.8177		r = 0.6468	r = 0.6276	r = 0.7172
r = 0.7050	r = 0.6989	r = 0.6881		r = 0.7760	r = 0.7701	r = 0.7669
r = 0.7604	r = 0.7585	r = 0.7523		r = 0.7504	r = 0.7511	r = 0.7439
r = 0.7232	r = 0.7036	r = 0.7347		r = 0.7196	r = 0.7163	r = 0.7033
r = 0.7078	r = 0.7066	r = 0.7116		r = 0.6231	r = 0.6047	r = 0.6330
r = 0.8587	r = 0.8574	r = 0.8611		r = 0.6557	r = 0.6434	r = 0.6562
r = 0.6463	r = 0.6253	r = 0.7058		r = 0.5491	r = 0.5430	r = 0.5300
r = 0.8133	r = 0.8123	r = 0.8212		r = 0.5271	r = 0.5103	r = 0.5492
r = 0.7272	r = 0.7208	r = 0.7371		r = 0.7542	r = 0.7460	r = 0.7626
r = 0.7866	r = 0.7864	r = 0.7838		r = 0.5606	r = 0.5610	r = 0.5565
r = 0.7936	r = 0.7936	r = 0.7935		r = 0.9115	r = 0.9108	r = 0.8942
				r = 0.5459	r = 0.5414	r = 0.5422
r = 0.6326	r = 0.6219	r = 0.6428		r = 0.6108	r = 0.6106	r = 0.6125
r = 0.2919	r = 0.2897	r = 0.3058		r = 0.8190	r = 0.8148	r = 0.8154
r = 0.7259	r = 0.7247	r = 0.7374		r = 0.6369	r = 0.6013	r = 0.5948
r = 0.6677	r = 0.6602	r = 0.6710		r = 0.4381	r = 0.4357	r = 0.4162
r = 0.7464	r = 0.7468	r = 0.7467		r = 0.5723	r = 0.5585	r = 0.5816
r = 0.7504	r = 0.7058	r = 0.7538		r = 0.5623	r = 0.5545	r = 0.6120
r = 0.7439	r = 0.7353	r = 0.7453		r = 0.8115	r = 0.8114	r = 0.8137
r = 0.6562	r = 0.5913	r = 0.6362		r = 0.8045	r = 0.8004	r = 0.7792
r = 0.8019	r = 0.7973	r = 0.8086		r = 0.6076	r = 0.6051	r = 0.5969
r = 0.8776	r = 0.8782	r = 0.8772		r = 0.6591	r = 0.6443	r = 0.6209
r = 0.6372	r = 0.6277	r = 0.6228		r = 0.6463	r = 0.6341	r = 0.6482
r = 0.5339	r = 0.5235	r = 0.5471		r = 0.7447	r = 0.7368	r = 0.7287
r = 0.8560	r = 0.8563	r = 0.8554		r = 0.7876	r = 0.7704	r = 0.7622
r = 0.3634	r = 0.3552	r = 0.3844		r = 0.7774	r = 0.7757	r = 0.7803
r = 0.8339	r = 0.8293	r = 0.8210		r = 0.4842	r = 0.4712	r = 0.5058
r = 0.9026	r = 0.9041	r = 0.9029		r = 0.7704	r = 0.7699	r = 0.7645
r = 0.7326	r = 0.7302	r = 0.7485		r = 0.6705	r = 0.6629	r = 0.6821
r = 0.8433	r = 0.8414	r = 0.8354		r = 0.5652	r = 0.5633	r = 0.5491
r = 0.8228	r = 0.8057	r = 0.8043		r = 0.6277	r = 0.5888	r = 0.5843
r = 0.7459	r = 0.7468	r = 0.7469		r = 0.6994	r = 0.6979	r = 0.7095
r = 0.6098	r = 0.6089	r = 0.6014		r = 0.5507	r = 0.5141	r = 0.5489
r = 0.7404	r = 0.7404	r = 0.7403		r = 0.7269	r = 0.7258	r = 0.7363
r = 0.7013	r = 0.6974	r = 0.7092		r = 0.2520	r = 0.2504	r = 0.2498
r = 0.5245	r = 0.5152	r = 0.5309		r = 0.6489	r = 0.6127	r = 0.6891

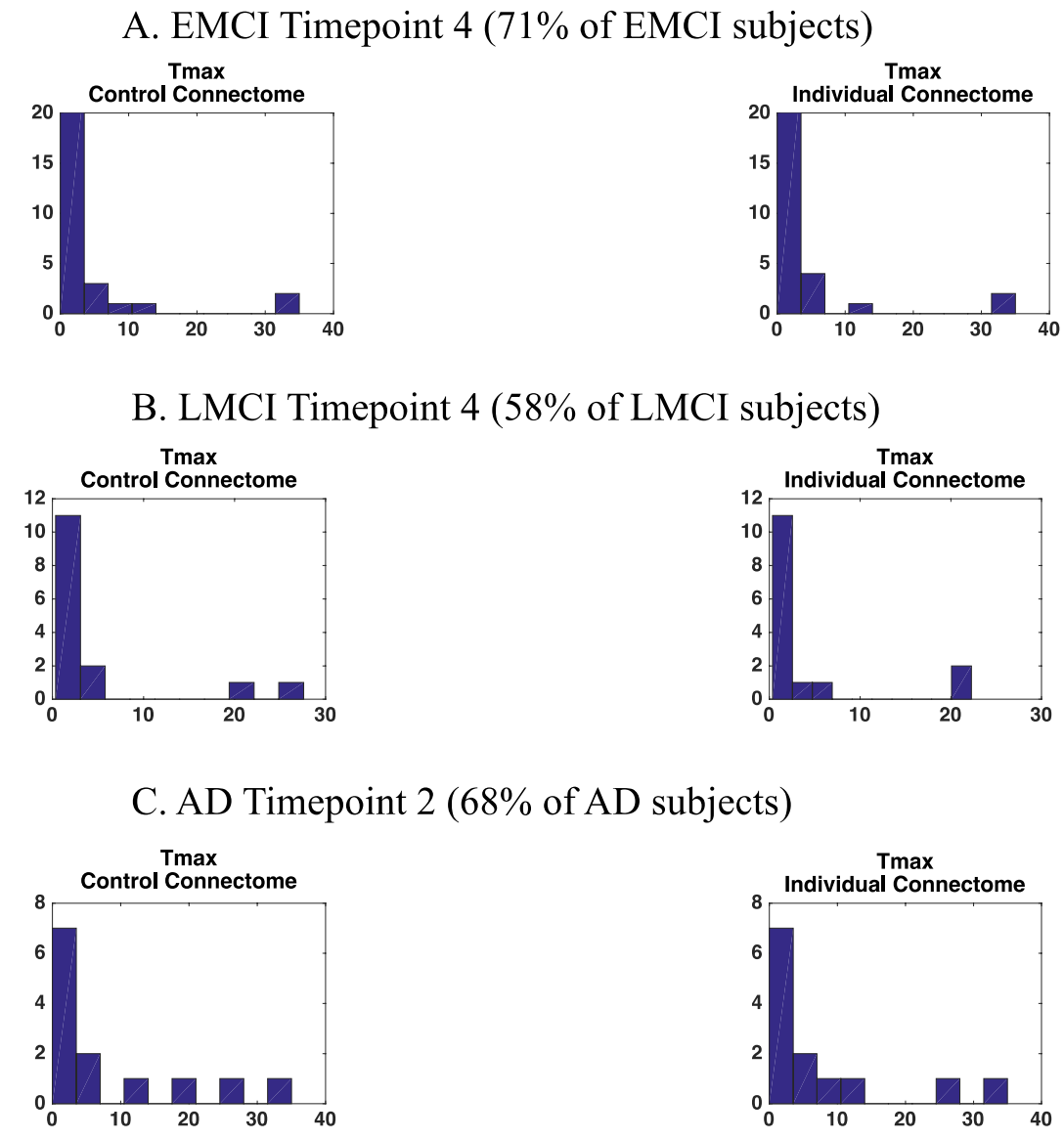

Figure 2.10. Tmax distributions. Histogram of each subject's T_{max} distribution when the NDM is tested on an individual patient connectome vs. an age-matched healthy connectome. T_{max} is the arbitrary model time it takes for optimal diffusion on the network.

To address potential concerns of ADNI tractography quality, which is an issue common in large multi-site, publicly available datasets, we assess NDM performance in AD subjects on an independent control connectome (mean age = 36.5 $\pm$ 11.8 years). Data were collected and processed as detailed in (Kuceyeski et al., 2011). Figure 2.11 illustrates NDM prediction accuracy results are unchanged when using an independent control connectome. Furthermore, Figure 2.11 shows thresholding minimally affects model performance. Weighted matrices are non-binarized and thresholded at various percentages of non-zero connections, as represented by k (Table 2.5). Fisher r-to-z transformations show no significant difference in model prediction accuracy as a result of thresholding (Table 2.7). Taken together, these data confirm previously presented results and also mitigate concerns of ADNI tractography quality.

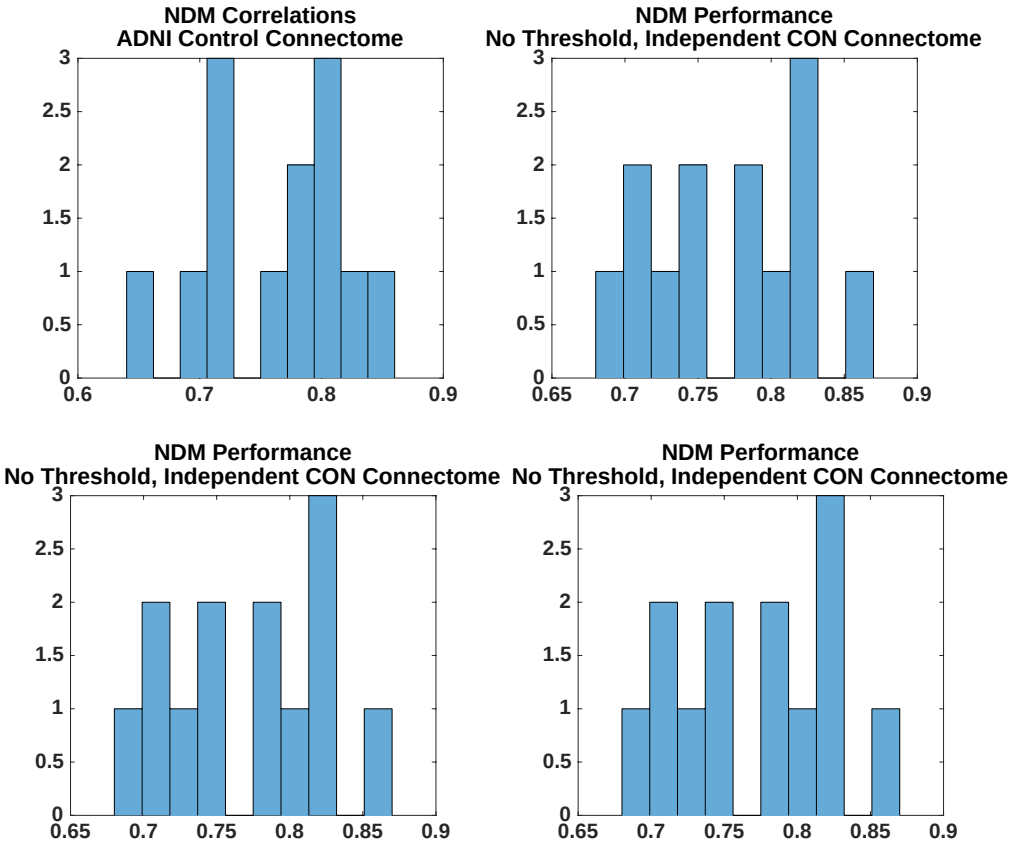

Figure 2.11. Independent template connectome. NDM performance on independent control template connectomes at various thresholds in AD.

Table 2.8. Thresholding independent connectome. Performance of the NDM on an independent control template connectome at various weighted thresholds, as represented by correlation coefficients between model predicted atrophy vs. end state measured atrophy.

Subject	K = 100% (No Threshold)	K = 80%	K = 60%	K = 40%	K = 30%	K = 20%
AD#1	0.8189	0.8189	0.8186	0.8175	0.8059	0.7690
AD #2	0.8006	0.8005	0.8003	0.7927	0.7671	0.7420
AD #3	0.8177	0.8177	0.8176	0.8173	0.8133	0.8054
AD #4	0.6881	0.6880	0.6878	0.6774	0.6718	0.6366
AD #5	0.7523	0.7523	0.7522	0.7519	0.7492	0.7486
AD #6	0.7347	0.7344	0.7266	0.7186	0.7020	0.6630
AD #7	0.7116	0.7115	0.7114	0.7104	0.7072	0.6939
AD #8	0.8611	0.8611	0.8611	0.8608	0.8567	0.8444
AD #9	0.7058	0.7048	0.7039	0.6689	0.6533	0.6217
AD #10	0.8212	0.8212	0.8211	0.8210	0.8206	0.8071
AD #11	0.7371	0.7371	0.7364	0.7194	0.7094	0.6704
AD #12	0.7838	0.7838	0.7837	0.7829	0.7813	0.7688
AD #13	0.7935	0.7935	0.7935	0.7935	0.7935	0.7932

Discussion

The present study uses network modeling to show that, despite measurable changes in integrity of specific fiber tracts, the overall topological organization of the WM network is not appreciably impaired. Most interestingly, AD does not appear to alter the ability of the network to mediate pathology spread in AD. This conclusion is supported by three main findings 1) WM network organization, as reflected by graph analysis weighted, non-thresholded graphs, is largely unchanged between patients and controls, 2) Eigenmode analysis confirms no measurable effect of disease on overall network topology and 3) Use of a patient's diseased connectome in place of a healthy connectome does not improve performance of a previously published network diffusion model (NDM).

Atrophy in the AD spectrum

First, we confirm the current imaging pipeline reproduces previously reported classic features of AD topography, specifically, gray matter volume is decreased in AD, globally and especially in subcortical and temporal regions (Figure 2.2). This finding is in agreement with published literature (Apostolova et al., 2007; Baron et al., 2001; Fischer et al., 2016; Peter et al., 2014; Thompson et al., 2003).

Global and local topology

WM disruptions are analyzed using global and local graph metrics. We show topology is not significantly different in all 3 patient groups compared to controls (Figure 2.3). Nodal results converge with global findings. Upon first survey, there are a few nodal differences between patients and controls predominately in frontal and temporal regions. These differences do not survive FDR correction (Figure 2.4). However, prior publications report

significant changes in network topology in AD vs. CON (Daianu et al., 2015a, 2015b, 2013; Lo et al., 2010; Prescott et al., 2014).

Thus, we next explore the potential causes underlying the discrepancy. We consider two possibilities: 1) Our pipelines for image processing, tractography and network extraction algorithms are different from previous work, and might be uniquely insensitive to measure changes in connectivity that are known to be present from well-established tract-level analyses *or* 2) The discrepancy is caused by lack of binarization or thresholding to our connectomes, dissimilar to methodology in previous reports.

Tract-level results

First, we consider the possibility that our connectivity pipelines are insensitive to changes in tract integrity. We assess whether connectivity changes detected by the present methodology comports with specific tracts known to be disrupted in AD. In agreement with previous literature, tract-level changes are detected in WM fiber count of AD compared to controls. We show significant alterations in a number of WM connections in ROIs along the uncinate fasciculus (UF), superior longitudinal fasciculus (SLF) and cingulum bundle (CB) (Figure 2.6, Table 2.4). These tract-level results of fiber count in AD converge with prior diffusion MRI studies reflective of tract-integrity within the ADNI dataset (Lee et al., 2015; Nir et al., 2013; Rowley et al., 2013). Taken together, our results and published findings from the ADNI dataset replicate other FA alterations reported in AD as a whole (Hasan et al., 2012; Liu et al., 2011; Mielke et al., 2009; Stricker et al., 2009).

These results confirm preserved global topology findings described above are not due to lack of sensitivity caused by the present study's connectivity and tractography pipelines. Hence, the current work suggests that

tract-level alterations in AD do not lead to significant changes in global measures of WM network organization.

Effect of thresholding

Prior work relies on binarization and/or thresholding of connectivity matrices prior to computing graph metrics (Table 2.9). Hence, we consider the possibility that discrepancy in our graph theory findings are caused by lack of binarization or thresholding being initially applied to connectomes. As previously reported, thresholding these connections can therefore lead to induced topology, an aspect of current graph theoretic approaches that we wished to avoid (Drakesmith et al., 2015; Langer et al., 2013).

When graph analyses are repeated under varying thresholds, followed by binarization, we demonstrate significant results across all three of our global graph metrics at a wide range of thresholds from 5% to 65% of all non-zero connections in the original weighted matrix (Figure 2.7A, Table 2.5). Thresholding of weighted matrices with no binarization also yields significant results across all three of our global graph metrics, but at much narrower range of thresholds (Figure 2.7B, Table 2.5). These results suggest that thresholding and binarization introduce topological constraints that may be most likely responsible for the apparent contradiction between our data and prior reports of significant topological differences in AD.

For instance, many recent reports of topological differences using graph theory within the ADNI dataset found significance after thresholding connectivity matrices based on the k-core “structural backbone” of network hubs (Daianu et al., 2015a, 2015b, 2013). Even this k-core analysis concludes that overall organization of the high-cost and high-capacity networks are relatively preserved in the AD spectrum, a finding which is in line with our

results (Daianu et al., 2015b). These results are supported by results in Figure 2.5, which showing no significant difference between hub distributions, as reflected by power alpha, in AD vs. CON.

The final methodological difference between the current study and prior work is the use of both cortical and subcortical regions in the construction of the network graph. Previous work recognizes that the addition of subcortical regions refines network organization (Daianu et al., 2015b). Few prior studies use graphs consisting of both cortical and subcortical regions (Table 2.9). Interestingly, prior work using subcortical and subcortical regions in addition to no binarization nor thresholding successfully replicate our results of no significant findings of global efficiency or path length in AD (Bai et al., 2012; Reijmer et al., 2013). Density is not assessed. Importantly, concerns of diffusion MRI quality or other study-specific bias are mitigated because these studies were replicated in AD cohorts independent of ADNI.

Table 2.9. Summary of prior work. Summary of prior studies involving AD-related topological characteristics. Highlighted studies indicate results replicated by the current study.

Study & Patient Group	ADNI	Network Construction	Include Sub cortical	D	E_{glob}	L_p	Comments
Current Study MCI & AD	✓	Weighted, Unthresholded	✓	NS	NS	NS	
Lo et al. 2010 AD		Weighted, Thresholded		--	▼	▲	
Bai et al. 2012 MCI		Weighted, Varying Thresholds	✓	--	NS	NS	Metrics reported at 0 thresholding
Reijmer et al. 2013 MCI & AD		Weighted, Unthresholded	✓	--	NS	NS	
Daianu et al. 2013 MCI & AD	✓	Binarized, Varying k-core thresholds		--	▼	▼	Created graphs by hemisphere
Prescott et al. 2014 MCI & AD	✓	Weighted, Unthresholded		--	--	--	Grouped metrics by cortical lobe
Daianu et al. 2015b MCI & AD	✓	Binarized, Varying k-core thresholds		--	▼	▲	
Daianu et al. 2015a Early-Onset AD		Binarized, 1 K-Core threshold		--	--	--	Evaluated location of hubs only
Fischer et al. 2015 Preclinical AD	✓	Weighted, Thresholded	✓	N/A	N/A	N/A	Subjects not comparable+

* D denotes density, E_{glob} denotes global efficiency and L_p denotes pathlength. ▲ denotes increased in AD vs. CON, ▼ denotes decreased in AD vs. CON, NS denotes nonsignificant . + Preclinical AD vs. Control subjects defined in cognitively healthy older adults on basis of global amyloid beta burden only, with preclinical converter status unconfirmed.

Characteristic eigenmodes

Thus far, the present study had explored global and local graph metrics, which are usually non-linear and sensitive to edge thresholding and binarization, as demonstrated above. Given this strong dependence on somewhat arbitrary parameters, we sought to determine if characteristic eigenmode, a topological (and linear) metric governing disease spread, is altered in dementia. We have previously shown that any network spread process implies a prominent role for the so-called network “eigenmodes”, which were shown to form an effective basis on which atrophy data can be projected for potential differential diagnosis. These eigenmodes are useful predictors of dementia, the spread of epilepsy and of normal brain activity (Abdelnour et al., 2015; Raj et al., 2012).

Furthermore, eigenmodes represent distinct spatial patterns that bear a strong resemblance to known patterns of various dementias and recapitulate recent findings of dissociated brain networks in dementia (Buckner et al., 2005; Du et al., 2007; Seeley et al., 2009; Zhou et al., 2010). Our prior work shows evidence that there is a one-to-one correspondence between the healthy network’s eigenmodes and atrophy patterns of normal aging and dementia (Raj et al., 2012). The first 2-3 principal network eigenmodes appear to be reproducible between healthy subjects, and the first two eigenmodes appear to be largely conserved even in patients with congenital agenesis of corpus callosum (Wang et al., 2017).

Interestingly, the current work shows eigenmodes, which are important predictors of degenerative progression, are virtually identical in AD vs. CON (Table 2.6) (Figure 2.8). This suggests that despite widespread atrophy and

clear evidence of impaired tract-level connectivity, characteristic eigenmodes, global network architecture is preserved.

Performance of the Network Diffusion Model

Given no observed significant differences in network architecture in AD vs. CON, we examine whether models of disease progression based on WM network topology is altered by disease. To do this, we utilize the NDM, a recent graph model of pathology spread that successfully predicts regional patterns of disease progression (Raj et al., 2015, 2012) (Figure 2.1). The previously published model is based on a template healthy connectome, under the assumption that the structural network serves merely as a conduit for transmitting proteinopathies, rather than being the first to be impaired itself.

In the present study, we asked whether the model would give similar outcomes if a patient's own disease-impaired connectome was used in place of a healthy connectome. Thus, by exploring the effect of individualized patient connectomes on the network diffusion model, we sought to determine indirectly whether the overall network architecture is significantly altered by disease, to the extent of causing measurable differences in how pathology might travel on the network.

Use of patient-specific connectomes in place of an age-matched, control connectome does not improve prediction of a patient's future gray matter atrophy (Figure 2.9). Personalized individual connectomes perform just as well, but not better, than healthy connectomes in capturing the longitudinal evolution of regional atrophy in AD. This finding is true across all three dementia groups of AD, LMCI and EMCI. Performance similarity between connectomes does not reflect poor predictive ability of the NDM, which gave typically high correlations ($R > 0.8$ in most cases). Furthermore, there is no

significant difference in the time it takes to achieve optimal diffusion across both connectomes (Figure 2.10). To mitigate possible concerns of DTI quality in ADNI, these results were replicated using an average connectome obtained from an independent high resolution DTI dataset of younger control subjects (Figure 2.11) (Table 2.8). Equal performance of the NDM between subject-specific diseased and healthy connectomes supports our conclusion that overall WM network organization is preserved in AD, and tract level impairments do not lead to altered mediation of pathology spread in AD.

The finding that the overall network architecture is preserved in dementia points to the possibility that neurodegenerative pathology primarily targets gray matter rather than WM network architecture, a finding widely replicated in topological studies of the GM network (Liu et al., 2012; Wang et al., 2013). Hence, either WM connectivity alteration is minor in the global brain context, or our measurement techniques are insensitive to it. There is one other possible explanation specific to the NDM results. Connectivity alterations, even if significant, might happen in a manner that does not change the topographic spread patterns the network will sustain. This is supported by the finding that thresholding weighted networks, which induces changes in graph metrics, does not result in significant changes to NDM performance (Figure 2.11, Table 2.7).

Such a finding points to an inherent strength of near-linear models like the NDM: Small changes in network connectivity will only elicit a correspondingly small change in the output of the model. This stands in stark contrast with most current graph theoretic summary metrics like path length and efficiency, which are inherently non-linear. Note that these non-linearities persist even if the metrics are redefined to utilize weighted rather than binary

connections, because these metrics are defined with respect to *implied neighbors*, which is essentially a binary decision. This point is helpful in interpreting the threshold dependence widely seen in graph theoretic concepts, and also replicated here in Figure 2.7.

We have already noted that overall network topology measured by graph theoretic metrics appears resistant to local changes in fiber integrity. Connectivity loss will, of course, change the speed of network spread according to the NDM model, but appears not to change the latter's predictive ability (maximized over all model times). The speed of network spread, encapsulated in the model parameters β and t_{max}, is a key feature of the NDM, but was not considered here because our focus is on predictive power of future atrophy patterns rather than their timeline. Fitting rate parameter of the ND model, and its neural/genetic correlates, will be the subject of our future work.

Limitations

Technical limitations of volumetric and tractography processing pipelines include HARDI spatial and angular resolution, coregistration errors, low test-retest reliability of volumetric data, and distance bias inherent in tractography. Therefore, it must be acknowledged that atrophy and connectivity results in this paper share the same sensitivity and accuracy issues common to all computational neuroanatomic data currently in public domain. However, our connectome technique successfully detected changes in tract-level connectivity, hence methodological limitations and insensitivity may not be the primary driver of our key results. To mitigate concerns of tractography quality, we illustrated reproducibility on tractography gathered and processed in an independent control dataset (Figure 2.11) (Table 2.8).

The NDM is a first-order, linear, parsimonious model of diffusive spread that assumes the structural connectivity network remains static over the duration of the longitudinal analysis. This is reasonable because the observation window (2 - 4 years) is short compared to the course of the disease. Although the model enables long-term projections of future atrophy, model validation in the current work is limited to public (ADNI) data sets of narrow time span (2 - 4 years), preventing long-term longitudinal follow-up. This is a future point of work that will be addressed as the ADNI study continues to collect additional longitudinal data.

REFERENCES

Abdelnour, F., Mueller, S., Raj, A., 2015. Relating Cortical Atrophy in Temporal Lobe Epilepsy with Graph Diffusion-Based Network Models. PLoS Comput. Biol. 11, e1004564.

Apostolova, L.G., Steiner, C.A., Akopyan, G.G., Dutton, R.A., Hayashi, K.M., Toga, A.W., Cummings, J.L., Thompson, P.M., 2007. Three-Dimensional Gray Matter Atrophy Mapping in Mild Cognitive Impairment and Mild Alzheimer Disease. Arch. Neurol. 64, 1489. doi:10.1001/archneur.64.10.1489

Attems, J., Thal, D.R., Jellinger, K.A., 2012. The relationship between subcortical tau pathology and Alzheimer's disease. Biochem. Soc. Trans. 40, 711–5.

Bai, F., Shu, N., Yuan, Y., Shi, Y., Yu, H., Wu, D., Wang, J., Xia, M., He, Y., Zhang, Z., 2012. Topologically Convergent and Divergent Structural Connectivity Patterns between Patients with Remitted Geriatric Depression and Amnestic Mild Cognitive Impairment. J. Neurosci. 32.

Baron, J.C., Chételat, G., Desgranges, B., Perchey, G., Landeau, B., de la Sayette, V., Eustache, F., 2001. In Vivo Mapping of Gray Matter Loss with Voxel-Based Morphometry in Mild Alzheimer's Disease. Neuroimage 14, 298–309. doi:10.1006/nimg.2001.0848

Benjamini, Y.H., Hochberg, Y., 1995. Controlling The False Discovery Rate - A Practical And Powerful Approach To Multiple Testing 57, 289–300. doi:10.2307/2346101

Braak, H., Braak, E., 1991. Neuropathological stageing of Alzheimer-related changes. Acta Neuropathol. 82, 239–59.

Buckner, R.L., Snyder, A.Z., Shannon, B.J., LaRossa, G., Sachs, R., Fotenos, A.F., Sheline, Y.I., Klunk, W.E., Mathis, C.A., Morris, J.C., Mintun, M.A., 2005. Molecular, Structural, and Functional Characterization of Alzheimer's Disease: Evidence for a Relationship between Default Activity, Amyloid, and Memory. J. Neurosci. 25, 7709–7717. doi:10.1523/JNEUROSCI.2177-05.2005

Cocchi, L., Bramati, I.E., Zalesky, A., Furukawa, E., Fontenelle, L.F., Moll, J., Tripp, G., Mattos, P., 2012. Altered Functional Brain Connectivity in a Non-Clinical Sample of Young Adults with Attention-Deficit/Hyperactivity Disorder. J. Neurosci. 32.

Daianu, M., Jahanshad, N., Mendez, M.F., Bartzokis, G., Jimenez, E.E., Thompson, P.M., 2015a. Communication of brain network core connections altered in behavioral variant frontotemporal dementia but possibly preserved in early-onset Alzheimer's disease, in: Ourselin, S., Styner, M.A. (Eds.), Proceedings of SPIE--the International Society for Optical Engineering. p. 941322. doi:10.1117/12.2082352

Daianu, M., Jahanshad, N., Nir, T.M., Jack, C.R., Weiner, M.W., Bernstein, M.A., Thompson, P.M., 2015b. Rich club analysis in the Alzheimer's disease connectome reveals a relatively undisturbed structural core network. Hum. Brain Mapp. 36, 3087–3103. doi:10.1002/hbm.22830

Daianu, M., Jahanshad, N., Nir, T.M., Toga, A.W., Jack, C.R., Weiner, M.W., Thompson, for the Alzheimer's Disea, P.M., Alzheimer's Disease Neuroimaging Initiative, 2013. Breakdown of Brain Connectivity Between Normal Aging and Alzheimer's Disease: A Structural *k* -Core Network Analysis. Brain Connect. 3, 407–422. doi:10.1089/brain.2012.0137

Damoiseaux, J.S., Smith, S.M., Witter, M.P., Sanz-Arigita, E.J., Barkhof, F., Scheltens, P., Stam, C.J., Zarei, M., Rombouts, S.A.R.B., 2009. White matter tract integrity in aging and Alzheimer's disease. Hum. Brain Mapp. 30, 1051–1059. doi:10.1002/hbm.20563

Drakesmith, M., Caeyenberghs, K., Dutt, A., Lewis, G., David, A.S., Jones, D.K., 2015. Overcoming the effects of false positives and threshold bias in graph theoretical analyses of neuroimaging data. Neuroimage 118, 313–333. doi:10.1016/j.neuroimage.2015.05.011

Du, A.-T., Schuff, N., Kramer, J.H., Rosen, H.J., Gorno-Tempini, M.L., Rankin, K., Miller, B.L., Weiner, M.W., 2007. Different regional patterns of cortical thinning in Alzheimer's disease and frontotemporal dementia. Brain 130, 1159–66. doi:10.1093/brain/awm016

Fischer, C.E., Ting, W.K.-C., Millikin, C.P., Ismail, Z., Schweizer, T.A., Alzheimer Disease Neuroimaging Initiative, 2016. Gray matter atrophy in patients with mild cognitive impairment/Alzheimer's disease over the course of developing delusions. Int. J. Geriatr. Psychiatry 31, 76–82. doi:10.1002/gps.4291

Fischl, B., Salat, D.H., Busa, E., Albert, M., Dieterich, M., Haselgrove, C., van der Kouwe, A., Killiany, R., Kennedy, D., Klaveness, S., Montillo, A., Makris, N., Rosen, B., Dale, A.M., 2002. Whole brain segmentation: automated labeling of neuroanatomical structures in the human brain. Neuron 33, 341–55.

Fischl, B., Salat, D.H., van der Kouwe, A.J., Makris, N., Ségonne, F., Quinn, B.T., Dale, A.M., 2004. Sequence-independent segmentation of magnetic resonance images. Neuroimage 23 Suppl 1, S69-84. doi:10.1016/j.neuroimage.2004.07.016

Fisher, 1921. On the probable error of a coefficient of correlation deduced from a small sample. Metron 1.

Forman, M.S., Zhukareva, V., Bergeron, C., Chin, S.S.-M., Grossman, M., Clark, C., Lee, V.M.-Y., Trojanowski, J.Q., 2002. Signature tau neuropathology in gray and white matter of corticobasal degeneration. Am. J. Pathol. 160, 2045–53.

Hasan, M.K., Lee, W., Park, B., Han, K., 2012. Connectivity Analysis of Hippocampus in Alzheimer's Brain Using Probabilistic Tractography. pp. 521–528. doi:10.1007/978-3-642-24553-4_69

Jack, C.R., Holtzman, D.M., 2013. Biomarker Modeling of Alzheimer's Disease. Neuron 80, 1347–1358. doi:10.1016/j.neuron.2013.12.003

Jones, D.T., Knopman, D.S., Gunter, J.L., Graff-Radford, J., Vemuri, P., Boeve, B.F., Petersen, R.C., Weiner, M.W., Jack, C.R., 2016. Cascading network failure across the Alzheimer's disease spectrum. Brain 139, 547–562. doi:10.1093/brain/awv338

Jucker, M., Walker, L.C., 2013. Self-propagation of pathogenic protein aggregates in neurodegenerative diseases. Nature 501, 45–51. doi:10.1038/nature12481

Kuceyeski, A., Maruta, J., Niogi, S., Ghajar, J., Raj, A., 2011. The generation and validation of white matter connectivity importance maps. Neuroimage.

Kuceyeski, A., Maruta, J., Relkin, N., Raj, A., 2013. The Network Modification (NeMo) Tool: elucidating the effect of white matter integrity changes on cortical and subcortical structural connectivity. Brain Connect.

Langer, N., Pedroni, A., Jäncke, L., Bullmore, E., Bassett, D., Rubinov, M., Sporns, O., et al., 2013. The Problem of Thresholding in Small-World Network Analysis. PLoS One 8, e53199. doi:10.1371/journal.pone.0053199

Lee, S.-H., Coutu, J.-P., Wilkens, P., Yendiki, A., Rosas, H.D., Salat, D.H., 2015. Tract-based analysis of white matter degeneration in Alzheimer's disease. Neuroscience 301, 79–89. doi:10.1016/j.neuroscience.2015.05.049

Liu, Y., Spulber, G., Lehtimäki, K.K., Könönen, M., Hallikainen, I., Gröhn, H., Kivipelto, M., Hallikainen, M., Vanninen, R., Soininen, H., 2011. Diffusion tensor imaging and Tract-Based Spatial Statistics in Alzheimer's disease and mild cognitive impairment. Neurobiol. Aging 32, 1558–1571. doi:10.1016/j.neurobiolaging.2009.10.006

Liu, Z., Zhang, Y., Yan, H., Bai, L., Dai, R., Wei, W., Zhong, C., Xue, T., Wang, H., Feng, Y., You, Y., Zhang, X., Tian, J., 2012. Altered topological patterns of brain networks in mild cognitive impairment and Alzheimer's disease: A resting-state fMRI study. Psychiatry Res. Neuroimaging 202, 118–125. doi:10.1016/j.pscychresns.2012.03.002

Lo, C.-Y., Wang, P.-N., Chou, K.-H., Wang, J., He, Y., Lin, C.-P., 2010. Diffusion Tensor Tractography Reveals Abnormal Topological Organization in Structural Cortical Networks in Alzheimer's Disease. J. Neurosci. 30. doi:10.1523/JNEUROSCI.4136-10.2010

LoCastro, E., Kuceyeski, A., Raj, A., 2014. Brainography: An Atlas-Independent Surface and Network Rendering Tool for Neural Connectivity Visualization. Neuroinformatics 12, 355–359. doi:10.1007/s12021-013-9206-1

Mielke, M.M., Kozauer, N.A., Chan, K.C.G., George, M., Toroney, J., Zerrate, M., Bandeen-Roche, K., Wang, M.-C., vanZijl, P., Pekar, J.J., Mori, S., Lyketsos, C.G., Albert, M., 2009. Regionally-specific diffusion tensor imaging in mild cognitive impairment and Alzheimer's disease. Neuroimage 46, 47–55. doi:10.1016/j.neuroimage.2009.01.054

Nir, T.M., Jahanshad, N., Villalon-Reina, J.E., Toga, A.W., Jack, C.R., Weiner, M.W., Thompson, P.M., Alzheimer's Disease Neuroimaging Initiative (ADNI), 2013. Effectiveness of regional DTI measures in distinguishing Alzheimer's disease, MCI, and normal aging. NeuroImage Clin. 3, 180–195. doi:10.1016/j.nicl.2013.07.006

Osborne, J.W., 1964. Improving your data transformations: Applying the Box-Cox transformation 15.

Pandya, S., Kuceyeski, A., Raj, A., 2016. The Brain's Structural Connectome Mediates the Relationship between Regional Neuroimaging Biomarkers in Alzheimer's Disease. J. Alzheimer's Dis. Preprint, 1–19. doi:10.3233/JAD-160090

Pearson, R.C., Esiri, M.M., Hiorns, R.W., Wilcock, G.K., Powell, T.P., 1985. Anatomical correlates of the distribution of the pathological changes in the neocortex in Alzheimer disease. Proc. Natl. Acad. Sci. U. S. A. 82, 4531–4.

Peter, J., Scheef, L., Abdulkadir, A., Boecker, H., Heneka, M., Wagner, M., Koppara, A., Klöppel, S., Jessen, F., Alzheimer's Disease Neuroimaging Initiative, 2014. Gray matter atrophy pattern in elderly with subjective memory impairment. Alzheimer's Dement. 10, 99–108. doi:10.1016/j.jalz.2013.05.1764

Pievani, M., de Haan, W., Wu, T., Seeley, W.W., Frisoni, G.B., 2011. Functional network disruption in the degenerative dementias. Lancet Neurol. 10, 829–843. doi:10.1016/S1474-4422(11)70158-2

Prescott, J.W., Guidon, A., Doraiswamy, P.M., Kingshuk, F., Choudhury, R., Liu, C., Petrella, J.R., 2014. The alzheimer structural connectome: Changes in Cortical Network Topology with Increased Amyloid Plaque Burden 1. Radiology 273.

Raj, A., Kuceyeski, A., Weiner, M., 2012. A Network Diffusion Model of Disease Progression in Dementia. Neuron 73, 1204–1215. doi:10.1016/j.neuron.2011.12.040

Raj, A., LoCastro, E., Kuceyeski, A., Tosun, D., Relkin, N., Weiner, M., 2015. Network Diffusion Model of Progression Predicts Longitudinal Patterns of Atrophy and Metabolism in Alzheimer's Disease. Cell Rep. 10, 359–369. doi:10.1016/j.celrep.2014.12.034

Razali, N.M., Wah, Y.B., 2011. Power comparisons of Shapiro-Wilk, Kolmogorov-Smirnov, Lilliefors and Anderson-Darling tests. J. Stat. Model. Anal. 2, 21–33.

Reijmer, Y.D., Leemans, A., Caeyenberghs, K., Heringa, S.M., Koek, H.L., Biessels, G.J., Utrecht Vascular Cognitive Impairment Study Group, 2013. Disruption of cerebral networks and cognitive impairment in Alzheimer disease. Neurology 80, 1370–1377. doi:10.1212/WNL.0b013e31828c2ee5

Reuter, M., Schmansky, N.J., Rosas, H.D., Fischl, B., 2012. Within-subject template estimation for unbiased longitudinal image analysis. Neuroimage 61, 1402–1418. doi:10.1016/j.neuroimage.2012.02.084

Rowley, J., Fonov, V., Wu, O., Eskildsen, S.F., Schoemaker, D., Wu, L., Mohades, S., Shin, M., Sziklas, V., Cheewakriengkrai, L., Shmuel, A., Dagher, A., Gauthier, S., Rosa-Neto, P., 2013. White Matter Abnormalities and Structural Hippocampal Disconnections in Amnestic Mild Cognitive Impairment and Alzheimer's Disease. PLoS One 8, e74776. doi:10.1371/journal.pone.0074776

Rubinov, M., Sporns, O., 2010. Complex network measures of brain connectivity: Uses and interpretations. Neuroimage 52, 1059–1069. doi:10.1016/j.neuroimage.2009.10.003

Saper, C.B., Wainer, B.H., German, D.C., 1987. Axonal and transneuronal transport in the transmission of neurological disease: potential role in system degenerations, including Alzheimer's disease. Neuroscience 23, 389–98.

Schöll, M., Lockhart, S.N., Schonhaut, D.R., O'Neil, J.P., Janabi, M., Ossenkoppele, R., Baker, S.L., Vogel, J.W., Faria, J., Schwimmer, H.D., Rabinovici, G.D., Jagust, W.J., 2016. PET Imaging of Tau Deposition in the Aging Human Brain. Neuron 89, 971–982. doi:10.1016/j.neuron.2016.01.028

Schwarz, A.J., Yu, P., Miller, B.B., Shcherbinin, S., Dickson, J., Navitsky, M., Joshi, A.D., Devous, M.D., Mintun, M.S., 2016. Regional profiles of the candidate tau PET ligand 18F-AV-1451 recapitulate key features of Braak histopathological stages. Brain.

Seeley, W.W., Crawford, R.K., Zhou, J., Miller, B.L., Greicius, M.D., 2009. Neurodegenerative Diseases Target Large-Scale Human Brain Networks. Neuron 62, 42–52. doi:10.1016/j.neuron.2009.03.024

Stricker, N.H., Schweinsburg, B.C., Delano-Wood, L., Wierenga, C.E., Bangen, K.J., Haaland, K.Y., Frank, L.R., Salmon, D.P., Bondi, M.W., 2009. Decreased white matter integrity in late-myelinating fiber pathways in Alzheimer's disease supports retrogenesis. Neuroimage 45, 10–16. doi:10.1016/j.neuroimage.2008.11.027

Thompson, P.M., Hayashi, K.M., de Zubicaray, G., Janke, A.L., Rose, S.E., Semple, J., Herman, D., Hong, M.S., Dittmer, S.S., Doddrell, D.M., Toga, A.W., 2003. Dynamics of gray matter loss in Alzheimer's disease. J. Neurosci. 23, 994–1005.

Wang, J., Zuo, X., Dai, Z., Xia, M., Zhao, Z., Zhao, X., Jia, J., Han, Y., He, Y., 2013. Disrupted Functional Brain Connectome in Individuals at Risk for Alzheimer's Disease. Biol. Psychiatry 73, 472–481. doi:10.1016/j.biopsych.2012.03.026

Wang, M.B., Owen, J.P., Mukherjee, P., Raj, A., Bukshpun, P., Vora, S., 2017. Brain network eigenmodes provide a robust and compact representation of the structural connectome in health and disease. PLOS Comput. Biol. 13, e1005550. doi:10.1371/journal.pcbi.1005550

Xie, S., Xiao, J.X., Gong, G.L., Zang, Y.F., Wang, Y.H., Wu, H.K., Jiang, X.X., 2006. Voxel-based detection of white matter abnormalities in mild Alzheimer disease. Neurology 66, 1845–1849. doi:10.1212/01.wnl.0000219625.77625.aa

Zalesky, A., Fornito, A., Bullmore, E.T., 2010. Network-based statistic: Identifying differences in brain networks. Neuroimage 53, 1197–1207. doi:10.1016/j.neuroimage.2010.06.041

Zalesky, A., Fornito, A., Seal, M.L., Cocchi, L., Westin, C.F., Bullmore, E.T., Egan, G.F., Pantelis, C., 2011. Disrupted axonal fiber connectivity in schizophrenia. Biol Psychiatry 69, 80–89. doi:10.1016/j.biopsych.2010.08.022

Zhou, J., Gennatas, E.D., Kramer, J.H., Miller, B.L., Seeley, W.W., 2012. Predicting Regional Neurodegeneration from the Healthy Brain Functional Connectome. Neuron 73, 1216–1227. doi:10.1016/j.neuron.2012.03.004

Zhou, J., Greicius, M.D., Gennatas, E.D., Growdon, M.E., Jang, J.Y., Rabinovici, G.D., Kramer, J.H., Weiner, M., Miller, B.L., Seeley, W.W., 2010. Divergent network connectivity changes in behavioural variant frontotemporal dementia and Alzheimer's disease. Brain 133, 1352–1367. doi:10.1093/brain/awq075

Chapter 3:
A New Network-Constrained Technique to Characterize Neurodegenerative Progression Rate in Alzheimer's Disease

Introduction

Pathological processes in the brains of Alzheimer's Disease (AD) patients start more than a decade before the first symptoms are noticed (Jack et al., 2013; Price and Morris, 1999). The long, inexorable course of progression of AD gives rise to a stereotyped pattern of regional pathology, atrophy and dysfunction. These features have led to intensive recent interest in the prognostic ability of molecular and imaging biomarkers to predict longitudinal decline and clinical outcomes for practical purposes such as differential diagnosis, therapeutic treatment and clinical trial inclusion (Ewers et al., 2015; Mattsson et al., 2014; Shaw et al., 2011; Tosun et al., 2016).

Current measures of decline rely on changes in cognitive metrics like MMSE, as well as imaging-derived measures of atrophy rates defined as changes in global brain volume of an individual (Karas et al., 2004; Schindler et al., 2017). There are two limitations with reliance on global brain volumes as measures of longitudinal changes. First, a global rate ignores the highly spatially varying patterns of AD-related atrophy. Second, the global atrophy rate measure ignores the process by which progression proceeds in the brain, which is now thought to involve network-level spread. Network spread is, in turn, undergirded by a well-studied process of "prion-like" transsynaptic transmission of misfolded pathologic proteins amyloid beta and tau (Frost and

Diamond, 2010; Jucker and Walker, 2013; Prusiner, 1998). It is possible to overcome these limitations by obtaining separate rate values for each brain region. However, such a method has limited utility for clinical applications where a single rate metric is needed for the purpose of prognosis or as a primary endpoint of clinical trials.

In order to overcome these limitations, this paper presents a new measure of disease progression rate in AD. Our previously published Network Diffusion Model (NDM) recapitulates spatial and temporal patterns of AD-related pathology spread along the brain's white matter (WM) fiber architecture (Raj et al., 2012). It also calculates longitudinal AD progression of a subject's atrophy patterns staring from their baseline MRI data (Raj et al., 2015). The strength of this approach is that it connects a biophysically realistic model of microscopic processes involving protein transmission to the macroscopically realized behavior at the whole brain regional level. Therefore, we reasoned that the NDM would serve as a robust model from which a pathology progression rate metric can be derived.

The current work makes three main contributions: First, we propose an algorithm to compute the speed of pathology spread parameter from longitudinal MRI of a subject. The NDM contains a single (*a priori* unknown) rate parameter called the diffusivity rate β, which we propose is a primary metric of disease progression rate. It gives a single number that encapsulates the entire spatiotemporal evolution of the disease and serves as a more mechanistically relevant measure of rate of progression in AD. Second, we thoroughly characterize this rate parameter on a large cohort of 810 subjects across the AD disease spectrum available in the ADNI study (Mueller et al., 2005). We describe how the rate depends on various natural stratifications of

the AD cohorts, such as diagnostic group or APOE4 allele status. Third, we explore whether it is possible to predict a subject's speed of neurodegeneration from baseline CSF and MRI biomarkers, with the ultimate goal of one-day circumventing costly and time consuming scanning procedures for prognostic application.

Methods

Participants

All subject data were obtained from the Alzheimer's Disease Neuroimaging Initiative (ADNI) database, a public-private multisite longitudinal study (http://adni.loni.usc.edu/). Subjects were diagnosed as Alzheimer's Disease (AD), Late Mild Cognitive Impairment (LMCI), Early Mild Cognitive Impairment (EMCI) or Control (CON) according to ADNI data description. All subjects have at least 2 longitudinal time points of volumetric MRI and 92% of subjects have baseline CSF, which includes Amyloid Beta, Tau and phosphorylated tau. 92% of subjects also had measures of the Mini-Mental State Exam (MMSE) and Functional Activities Questionnaire (FAQ) to assess cognitive impairment. MMSE and FAQ measurements are considered baseline as 99% of cognitive measurements were collected within 1.25 years of the baseline MRI scan (mean = .59 years, median = 0.55 years. 4 EMCI subjects had baseline cognitive metrics measured ~2 years post baseline scan).

Patients are age-matched to healthy controls (AD: $p = 0.65$, LMCI: $p=0.77$, EMCI: $p=0.10$). 40 subjects from the CON group were eliminated to age-match for LMCI and EMCI subjects. Subjects are also gender matched (AD, $p=0.06$, LMCI: $p=0.76$, EMCI: $p=0.77$). There was a moderate trend toward significant difference in age between AD and CON, but the decision to

not eliminate any subjects was made in order to include in an order to maintain the largest sample size for later machine learning techniques. There were no converters between scans. Subject demographic information is listed in Table 1.

Table 3.1. Subject demographics.

Dx	**N =**	**Age** (std)	**Sex** (% F)	**APOE4 Status** (0/1/2)	**MMSE** (std)	**FAQ** (std)	**CSF AB** (pg/mL) (std)	**CSF Tau** (pg/mL) (std)	**CSF pTau** (pg/mL) (std)
AD	117	74.9 (8.1)	38%	24/51/22 83%$^{+}$	21.6 (3.9) 85%$^{+}$	15.5 (6.9) 84%$^{+}$	134.6 (37.2) 94%$^{+}$	131.2 (64.8) 89%$^{+}$	58.9 (32.9) 94%$^{+}$
LMCI	172	72.5 (7.7)	45%	74/69/27 99%$^{+}$	26.7 (2.4) 97%$^{+}$	4.8 (5.7) 97%$^{+}$	159.4 (49) 94%$^{+}$	99.8 (54.5) 89%$^{+}$	47.6 (27.4) 94%$^{+}$
EMCI	289	71.3 (7.2)	44%	161/103/20 98%$^{+}$	28 (1.8) 95%$^{+}$	2.3 (3.5) 95%$^{+}$	183.8 (51.2) 94%$^{+}$	77.2 (47.6) 89%$^{+}$	36.8 (21.1) 94%$^{+}$
CON	232	74.5 (6.9)	53%	153/56/6 93%$^{+}$	28.9 (1.3) 91%$^{+}$	0.44 (2) 90%$^{+}$	198.1 (51.2) 94%$^{+}$	68 (33.7) 89%$^{+}$	33.1 (17.9) 89%$^{+}$

+ Denotes percentage of data available in diagnostic cohort

MR image acquisition and processing

DTI and inversion-recovery spoiled gradient recalled (IR-SPGR) T1-weighted imaging data were acquired on several General Electric 3T scanners using scanner specific protocols. Briefly, DTI data were acquired with a voxel size of 1.372 × 2.70 mm3, 41 diffusion gradients and a b-value of 1000 s/mm2. IR-SPGR data were acquired with a voxel size of 1.022 × 1.20 mm3. All imaging protocols and preprocessing procedures are available on the ADNI website. (http://adni.loni.usc.edu/methods/). Automated cortical and subcortical volume measures were performed with FreeSurfer software

package, version 5.3 (http://surfer.nmr.mgh.harvard.edu/fswiki) For details on T1-weighted data preprocessing, please see Supplementary Methods.

DTI acquisition and processing

The WM connectome was constructed by taking the mean of diffusion MRI data of normal, healthy subjects. Normal subject data were collected jointly by Weill Cornell Medical College and the Brain Trauma Foundation. Seventy-three healthy subjects (40 men, 33 women, 30.2±6.7 years) were used to create the normative connectivity information in the form of tractograms. T1-weighted structural and diffusion-weighted MR images were collected on a 3 T GE Sigma EXCITE scanner (GE Healthcare, Waukesha, WI). The High Angular Resolution Diffusion Images data were acquired with 55 isotropically distributed diffusion-encoding directions at b=1000 sec/mm^2 and one at b=0 sec/mm^2, from 72 1.8-mm thick interleaved slices (no slice gap) and 128×128 matrix size, zero-filled during reconstruction to 256×256, with a field of view (FOV) of 230 mm^2. The structural scan was an axial three dimensional inversion-recovery fast spoiled gradient-recalled echo sequence ((echo time [ET]=1.5 msec, repetition time [TR]=6.3 msec, inversion time [TI]=400 msec) flip angle of 15°) with a 256×256 matrix over a 230 mm^2 FOV and 156 1.0-mm contiguous partitions. The diffusion images were corrected for eddy current and motion artifacts using FMRIB Software Library (FSL) (Smith et al., 2004).

T1 images were processed by first segmenting the tissue into cerebrospinal fluid, WM and GM. The GM segment was subsequently parcellated into 86 different ROIs using cortical and subcortical structures from the FreeSurfer (Desikan-Killarney) gray matter parcellation. The parcellated GM was then linearly transformed and resampled to diffusion image space for

use in tractography. Briefly, the surface voxels of the parcellated cortical and subcortical structures were used to seed the tracts. Proposed and validated in Iturria-Medina and colleagues (2005), the tractography algorithm implemented here incorporates tissue classification probability and orientation distribution information in a Bayesian manner. A tract terminated when the algorithm reached the boundary of an image volume, the edge of a GM region, a voxel not in the gray or WM masks, or when the angle between subsequent steps exceeded π/3. This analysis was done using the eighth version of Statistical Parametric Mapping (SPM), (Friston et al., 2007), a software package within Matlab R2009a (The Mathworks, Inc., Natick, MA), and the Individual-Based Atlas toolbox (Aleman-Gomez, 2006) within SPM.

Further details of the image processing and tractography method are given in a previous publication (Kuceyeski et al., 2013, 2011). To control for inter-subject variance in total fiber count, a density metric was computed by dividing by the total number of tracts based on each subject's tractography data. The subsequent undirected connectomes were not thresholded and kept as weighted.

The Network Diffusion Model

Our group's previously published NDM has been shown to accurately recapitulate spread of Alzheimer's Disease pathology throughout the brain (Raj et al., 2015, 2012). Briefly, pathology transmission is modeled as a network diffusion process:

$$\mathbf{x}(t) = e^{-\beta H t}\mathbf{x_0} \qquad (1)$$

where $\mathbf{x_0}$ and $\mathbf{x}(t)$ are the initial and evolved patterns of the regional pathology respectively, expressed as 86x1 vectors, corresponding to the 86-region brain atlas. The matrix exponential $\exp(-\beta H t)$ acts as a spatial and temporal

blurring operator, called the diffusion kernel. Matrix H, called the network Laplacian, is a derivative of the connectivity matrix obtained from the WM structural organization. The parameter β represents the diffusion speed coefficient, which is considered the rate of disease progression/speed of neurodegeneration in the current study.

Relationship to atrophy. The measurable phenotype (regional MRI-derived atrophy) in region k is assumed to be the consequence of and thus proportional to the *accumulation* of pathology. Hence, it is modeled as the integral:

$$\phi_k(t) = \int_0^t x_k(\tau)\ d\tau \qquad (2)$$

On the whole brain this gives:

$$\mathbf{\Phi}(t) = \int_0^t \mathbf{x}(\tau)\ d\tau \qquad (3)$$

Relationship between baseline atrophy and its rate of change. It was shown in (Raj et al., 2015a) that the relationship at baseline scan between atrophy and its rate of change (as modeled by NDM) under the integral relationship above is given by

$\frac{d\mathbf{\Phi}}{dt}|_{t=t_{base}} = \beta\widetilde{H}(\beta t_{base})\mathbf{\Phi_{base}}$ (4) where we define a new variant of the Laplacian $\widetilde{H}(\beta,t) = diag\left(\begin{Bmatrix} \frac{1}{\beta t}, & i=1 \\ \frac{\lambda_i e^{-\lambda_i \beta t}}{1-e^{-\lambda_i \beta t}}, & i>1 \end{Bmatrix}\right)U^{\dagger}$ involving the eigendecomposition $H = U\lambda U^{\dagger}$, with eigenvalues λ_i. Please see Raj et al., 2015 for details. Thus, the network diffusion model deterministically predicts that the atrophy at baseline and its rate of change are related via the matrix $\widetilde{H}(\beta,t)$. Note the relationship involves an unknown time between onset and baseline scan t_{base}.

where we define a new variant of the Laplacian

$$\widetilde{H}(\beta,t) = diag\left(\begin{Bmatrix} \frac{1}{\beta t}, & i=1 \\ \frac{\lambda_i e^{-\lambda_i \beta t}}{1-e^{-\lambda_i \beta t}}, & i>1 \end{Bmatrix}\right)U^{\dagger} \qquad (5)$$

involving the eigendecomposition $H = U\Lambda U^{\dagger}$, with eigenvalues λ_i. Please see Raj et al. 2015 for details. Thus, the NDM deterministically predicts that the atrophy at baseline and its rate of change are related via the matrix $\widetilde{H}(\beta, t)$. Note the relationship involves an unknown time between onset and baseline scan t_{base}.

Algorithm for fitting β to individual subjects' longitudinal scans

For each subject, the beta parameter is computed using the subject's longitudinal atrophy patterns. The algorithm has the following steps:

1. First, the atrophy slope of each region is calculated independently, using the time elapsed between each scan. Let t_{long} be a vector of timestamps (length *nt*) of a patient's longitudinal visits, in years and their volumetric-processed regional atrophy patterns be contained in the (*nt x 1*) vector for any given region, $\boldsymbol{\phi}$. A fitted estimate of slope of atrophy for that region is calculated from this longitudinal data, as per:

$$\boldsymbol{\phi} = \begin{pmatrix}\mathbf{1} & t_{long}\end{pmatrix}\begin{pmatrix}a\\ b\end{pmatrix}; \quad \Delta\phi = b \qquad (6)$$

In our implementation, the above fitting was performed using MATLAB's pseudoinverse function. Regions with negative atrophy slopes are set to 0, as thickening of the cortex is a rare and unlikely event in AD, and most likely is a result of measurement or analysis noise.

Since the rate relationship Eq (4) involves two unknowns, β and t_{base}, we need to achieve joint fitting to measured regional slope data. However, given that the two parameters appear together in the matrix relationship, instead of a joint fitting approach we conduct a two-step process detailed in steps 2 and steps 3:

2. Set $\beta = \beta_0$. Then minimize over t_{base}:

$$\widehat{t_{base}} = argmax_{t_{base}} \{corr(\beta_0 \widetilde{H}(\beta_0 t_{base})\boldsymbol{\Phi}_{\mathbf{base}}, \frac{\Delta\boldsymbol{\Phi}}{\Delta t})\}$$

where $corr(\cdot,\cdot)$ refers to the Pearson correlation coefficient between two vectors, and recall that $\frac{\Delta\mathbf{\Phi}}{\Delta t}$ is the measured slope from step 1.

3. Then the optimal rate $\hat{\beta}$ is given by least squares fitting of β in the linear system:

$$\frac{1}{\beta_0}\frac{\Delta\mathbf{\Phi}}{\Delta t} = \beta\widetilde{H}(\beta_0\widehat{t_{base}})\mathbf{\Phi_{base}}$$

Statistical analysis

Following calculation of each subject's beta parameter from baseline and subsequent longitudinal volumetric scans, beta outliers were removed. Outliers are defined as 1.5 times greater or less than the inter-quartile range separately for each diagnostic group.

Differences in subject characteristics across diagnostic groups, APOE status categories and clusters were assessed with the Kruskal Wallis H-test, a non-parametric one-way ANOVA on ranks (Kruskal and Wallis, 1952). Wilcoxon rank sum tests were used in the case of comparing 2 groups directly (Wilcoxon, 1950). Differences in frequencies were assessed with classic chi square analysis. Due to the non-parametric nature of the data, correlations were assessed with the Kendall rank correlation coefficient (Bolboaca and Jäntschi, 2006). Independent, two-sided t-tests were used to test for differences in local brain volume. Glass brains depicting magnitude and t-statistic are used for visualization (LoCastro et al. 2014). Multivariate linear regression analysis was used to examine the relationship between multiple CSF biomarkers, cortical/subcortical volumes and beta. The coefficient of determination, R^2 was used to evaluate model fit.

Z-scores of CSF metrics were computed relative to age-matched controls to normalize features for hierarchical clustering analysis and K

nearest neighbors (KNN) classification. Hierarchical clustering analysis was used to delineate clusters of subjects in a 6 dimensional space defined by baseline CSF biomarkers of AB, Tau, pTau and their respective ratios. 3 was selected as the cluster size because the variance ratio criterion (Calinski-Harabasz index), defined as the ratio of between-cluster variance to within-cluster variance, is maximized at 3 clusters (Maulik and Bandyopadhyay, 2002).

With cluster labels obtained from hierarchical clustering, a KNN classifier assigned subjects to clusters based on the Euclidean distance from k nearest neighbors. Classifier performance was tested over a wide range of k nearest neighbors. Classification performance was evaluated by calculating classification error by 5-fold cross validation. 490 patients on the AD spectrum of 578 patients (excluding outliers) had complete data on all 6 CSF biomarkers of interest in the current study and were used in clustering analysis and KNN classification. All analysis was carried out in MATLAB.

Results

We propose the beta parameter modeled in the current study is reflective of pathology spread. We hypothesize there will be a strong relationship between beta and global atrophy as well as a strong relationship between beta and slope of cognitive decline. First, we show a high correlation between the modeled beta parameter and global rate of atrophy (r=0.42, p=3.7e-48) (Figure 3.1A). We also show a moderate correlation between the modeled beta parameter and slope of cognitive decline as measured by MMSE (r=0.22, p=0.0003) (Figure 3.1B).

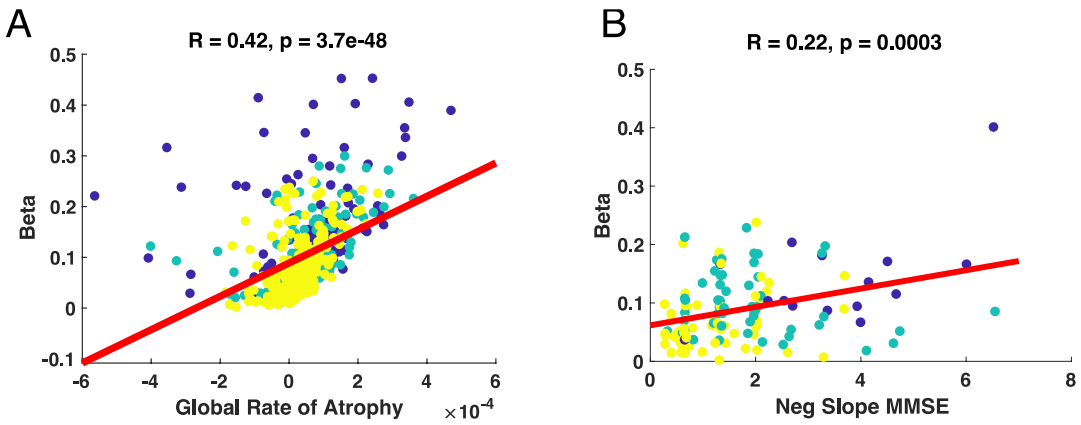

Figure 3.1. Beta vs. global atrophy and MMSE. A) Correlation between each subject's modeled speed of pathology spread (beta) and global atrophy rate. **B)** Correlation between each subject's beta and slope of cognitive decline as measured by MMSE. Blue represents AD, teal represents LMCI and yellow represents EMCI.

Prion AD hypotheses suggest the disease spreads in an exponential, viral-like manner, with the disease spreading faster with increased disease severity (Prusiner, 1998). Thus, we hypothesized subjects later in clinical progression have a higher rate of disease spread than subjects early in the disease. To test this hypothesis, each subject's beta parameter (speed of disease spread) was calculated and the effect of beta across each of the 3 diagnostic groups was assessed using a non-parametric Kruskal Wallis H test. We observe a significant effect of beta across diagnoses on the AD spectrum ($p=6.67e-18$). Furthermore, when directly comparing the earliest stage EMCI group to the AD group, we show a significant difference in beta between EMCI and AD patients ($p=5.72e-18$) (Figure 3.2A).

A wide body of literature implicates the role amyloid beta in clinical deterioration, suggesting clinical trajectories of subjects with higher amyloid burden worsen faster than subjects without high amyloid beta burden (Okello et al., 2009; Tosun et al., 2016). Because amyloid positivity is highly associated with the number of putative APOE4 alleles, we examined the relationship between beta and APOE4 allele status (Morris et al., 2010; Sunderland et al., 2004). 266 patients have 0 APOE4 alleles, 195 patients have 1 allele and 66 have 2 APOE4 alleles. Thus, we hypothesized beta is higher in subjects with the pathogenic APOE4 allele compared to subjects without the APOE4 allele. A one way Kruskal-Wallis test confirms this, illustrating a significant effect of beta across subjects with 0 , 1 and 2 APOE4 alleles ($p=0.0006$) Specifically, we observe beta in subjects with the E4/E4 allele is significantly higher than subjects without the E4 allele ($p= 7.50e-04$) (Figure 3.2B).

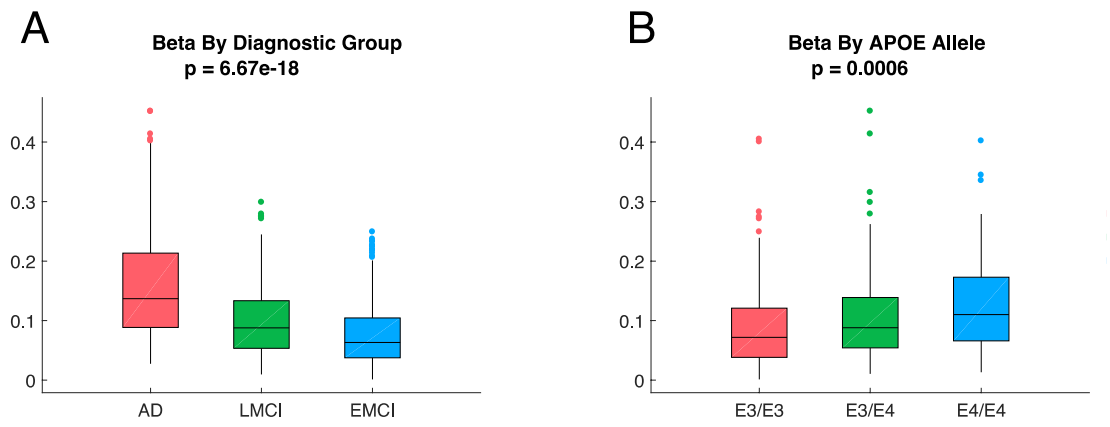

Figure 3.2. Beta by diagnostic group and APOE allele. A) Significant effect of beta by diagnostic group across the AD spectrum. **B)** Significant effect of beta by APOE4 allele status across the AD spectrum.

Next, we conduct an exploratory correlation analysis to examine the relationship between each subject's baseline CSF biomarker and rate of pathology progression. We individually probe baseline CSF amyloid beta, tau, ptau, ratio of AB/tau, AB/pTau and pTau/tau. We hypothesize a significant relationship between at least one of baseline CSF biomarkers and speed of pathology spread, both within all subjects and within individually diagnostic groups.

Contrary to our hypothesis, correlation analysis reveals weak relationships between beta and baseline CSF measurements (Figure 3.3A). Though baseline CSF values are highly correlated with one another, correlation to speed of disease diffusion is overall poor (Figure 3.3B). Additional linear, quadratic and power models did not reveal significant relationships between CSF biomarkers and beta (data not shown). Multivariate linear regression using multiple CSF biomarkers as predictor variables for beta

also yielded poor predictive ability as assessed by the coefficient of determination (data not shown).

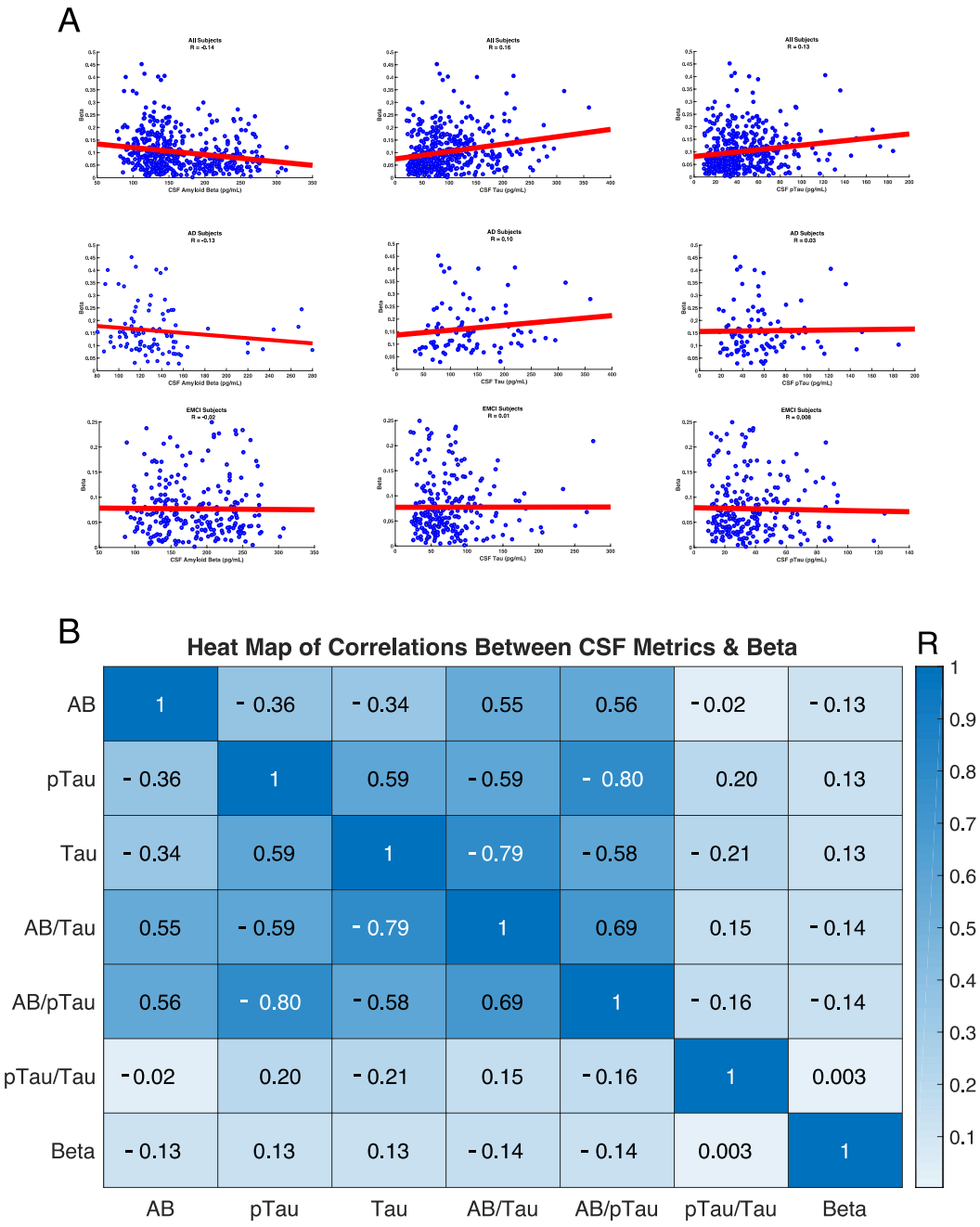

Figure 3.3. **Beta vs. CSF biomarkers. A)** Scatterplots depicting lack of strong correlations between baseline CSF AB, Tau, pTau and their ratios vs. beta in all subjects, AD-subjects only and EMCI-subjects only. **B)** Heat map illustrating correlations of baseline CSF measurements with one another and beta.

At this point in the investigation, we hypothesized efforts to predict a patient's precise beta from baseline CSF metrics were unsuccessful due to potential subject heterogeneity in CSF profile. There is precedent for this hypothesis, as prior work shows CSF biomarker profile across the AD spectrum is variable, with clusters of subjects present (Iqbal et al., 2005). Hierarchical clustering analysis was utilized to understand potential subject heterogeneity in baseline CSF biomarker profile. We show subjects are clearly delineated into 3 clusters, which are defined by the z-scores of 6 baseline CSF biomarkers (Figure 3.4A). There is no significant effect of age across cluster ($p=0.20$, Cluster 1: 71.3 years, Cluster 2: 72.9 years, Cluster 3: 72.7 years).

Because subjects fall into clearly delineated clusters based on baseline CSF biomarker profile, we hypothesized we could predict a subject's cluster based on baseline CSF characteristics. To test this hypothesis, a K nearest neighbor (KNN) classifier sorted the 490 subjects with complete data into clusters based on Euclidean distance from k nearest neighbors. Cluster 1 consists of 108 subjects, cluster 2 is comprised of 207 subjects and 175 subjects are in cluster 3. The KNN classifier predicts cluster identity at a rate of more than 90% of the time in a 5 k-fold cross validated model over a wide range of 1 – 90 nearest neighbors. As expected, classifier performance drops below chance as more than 350 neighbors are added, an action which adds significant variance to the model (Figure 3.4B).

Next, we examine CSF biomarker signatures that define each of the 3 identified clusters. First, we plot z-scores of the 6 CSF biomarkers computed relative to age-matched, healthy controls, as a function of cluster identity.

Then, we examine concentration of the three CSF biomarkers, amyloid beta, tau and ptau, of each of the clusters in relation to each other.

We observe cluster 1 is characterized by the least pathogenic biomarker profile as it shows very little difference relative to controls across all 6 biomarkers. Conversely, cluster 3 appears to be the most pathogenic cluster, as it shows the most remarkable differences in CSF biomarkers compared to controls. Specifically, cluster 3 mirrors the pathogenic biomarker signature of typical of AD, which includes decreased CSF AB and increased Tau and pTau compared to controls. Cluster 2 falls between cluster 1 and 2 in terms of pathogenic profile. (Figure 3.4C)

When compared directly to each other, we observe Cluster 3 appears significantly more pathogenic than Cluster 1. Specifically, Cluster 3 exhibits significantly less baseline CSF AB compared to cluster 1 as well as significantly higher pTau and Tau (AB: p=1.93e-43, pTau: p= 5.63e-45, Tau: p=1.79e-44) (Figure 3.4D).

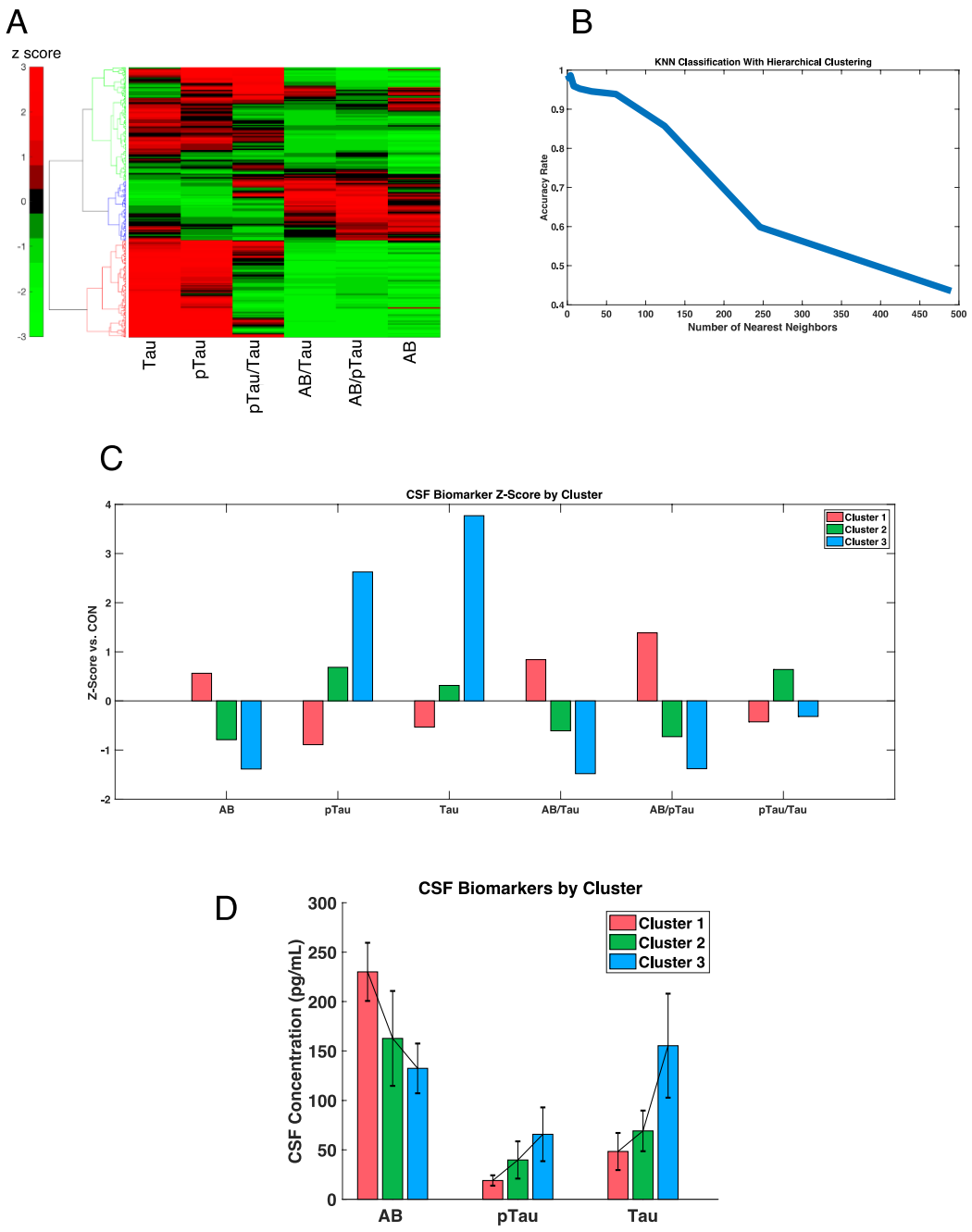

Figure 3.4. CSF biomarker clustering and classification. A) Dendrogram depicting 3 clusters defined by z-scores of baseline CSF biomarkers. **B)** KNN classifier accuracy over a wide range of nearest neighbors in a 5 k-fold cross validation model. **C)** Average z-score of CSF metrics vs. age-matched controls **D)** CSF metrics across clusters. Error bars represent one standard deviation.

Following successful identification, prediction and characterization of baseline CSF profile, which define the disparate clusters, we examine baseline volume differences and the speed of disease spread across clusters. Volumetric differences in each cluster was calculated with respect to the same group of age-matched controls. We observe that baseline atrophy patterns correspond to baseline CSF profiles. Specifically, cluster 3 is characterized by the most pathogenic atrophy, while cluster 1 is the least. Cluster 2 falls squarely in the middle (Figure 3.5A).

Evaluation of beta across clusters shows a significant effect of beta across clusters ($p=3.89e-6$). Specifically, the cluster defined by the most AD-related CSF biomarkers, cluster 3, shows the highest speed of disease progression (Figure 3.5B). Conversely, cluster 1, which is characterized by the least pathogenic biomarkers, has the lowest speed of disease progression. As depicted in the boxplots of Figure 3.5B, the 25^{th} and 75^{th} percentile range of cluster 1 is 0.0349 - 0.1044, the equivalent range for cluster 2 is 0.0509 - 0.1380 and lastly, 0.0598 - 0.1542 for cluster 3.

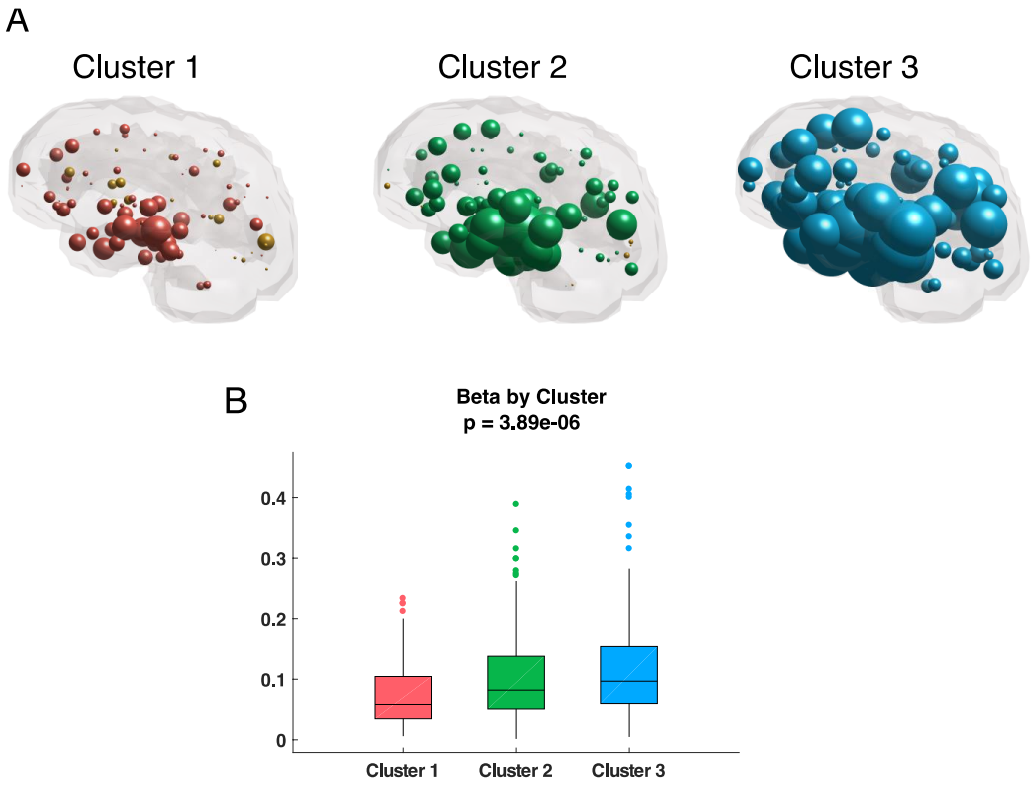

Figure 3.5. Baseline volumetric and degeneration speed by cluster. A) Glass brains depict t-statistics of differences in baseline volumetric by cluster compared to age-matched controls Gold represents hyperatrophy, all other colors represent atrophy. **B)** Boxplot of beta by cluster.

We also observe a significant effect of baseline FAQ and baseline MMSE cognitive scores across clusters, with cognitive score as the subject's earliest cognitive time point (FAQ: p=9.01e-7) (MMSE: 7.23e-5) (Figure 3.6A-B). Clinical measures are most compromised in cluster 3 vs. cluster 1 (FAQ: p=7.98e-07, MMSE: p=1.69e-05), a finding that converges with each cluster's biomarker profile and speed of disease spread. Correspondingly, we observe the more pathogenic cluster 3 has a higher, but non-significant, percentage of APOE4 allele carriers compared to the least pathogenic cluster (Figure 3.6C).

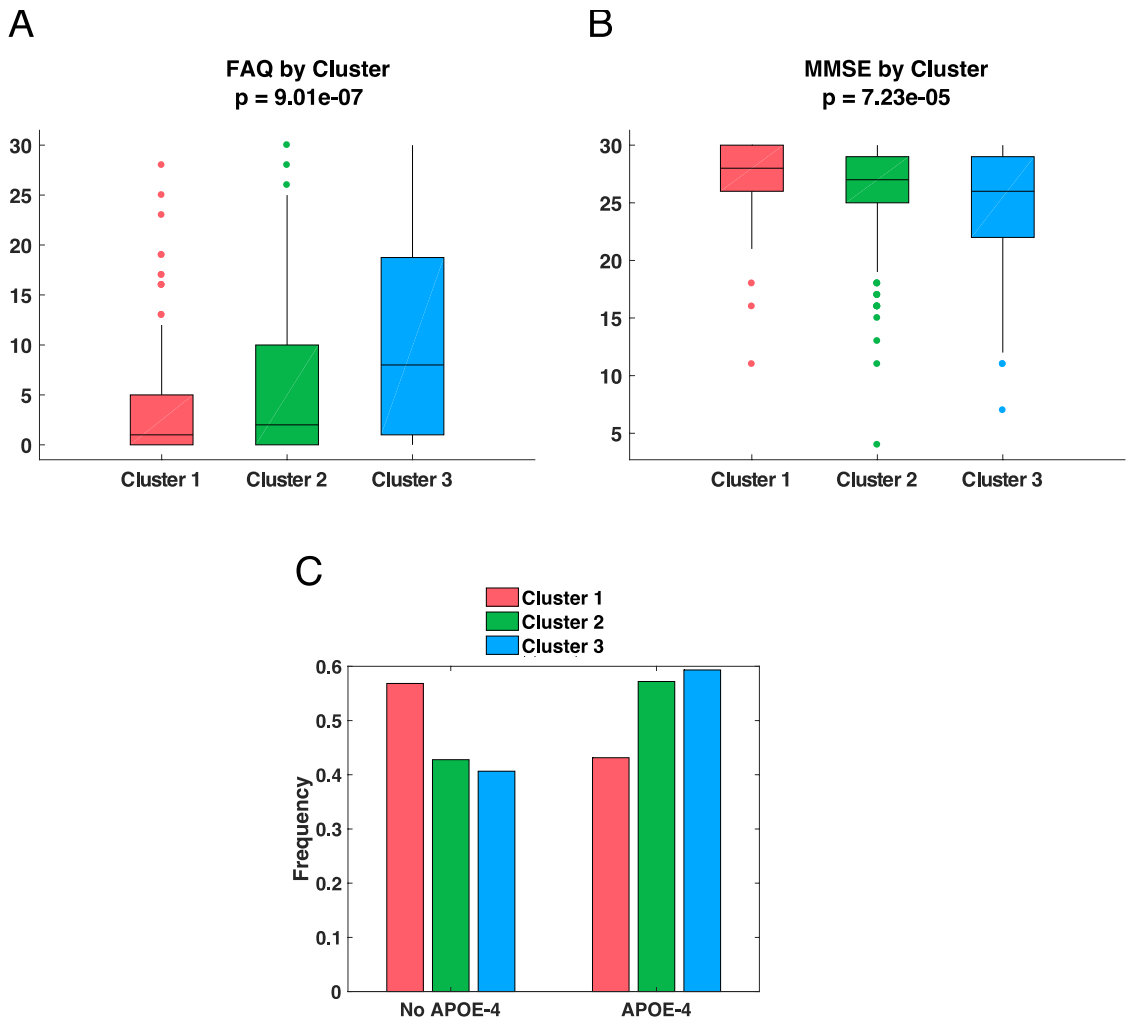

Figure 3.6. Cognitive scores and APOE by cluster. A-B) Differences in baseline cognitive score FAQ and MMSE across cluster. **C)** Frequencies in APOE4 across clusters. Pink represents cluster 1, green represents cluster 2 and blue represents cluster 3.

Lastly, we show significant correlations between a subject's speed of disease spread and baseline cognitive score, which differ across clusters. Examining baseline MMSE, we observe cluster 2 has the strongest

relationship between beta and the cognitive metric (r=-0.28, p=2.5e-8), followed by cluster 1 (r=0.20, p=0.004) and a relatively weak cluster 3 (r=-0.14, p=0.02) (Figure 3.7A). Interestingly, the FAQ survey shows the strong relationship with beta in cluster 1 (r=0.28, p=8.7e-05), followed by cluster 3 (r=0.20, p=.0003) and is the weakest in cluster 2 (r=0.15, p=0.002) (Figure 3.7B).

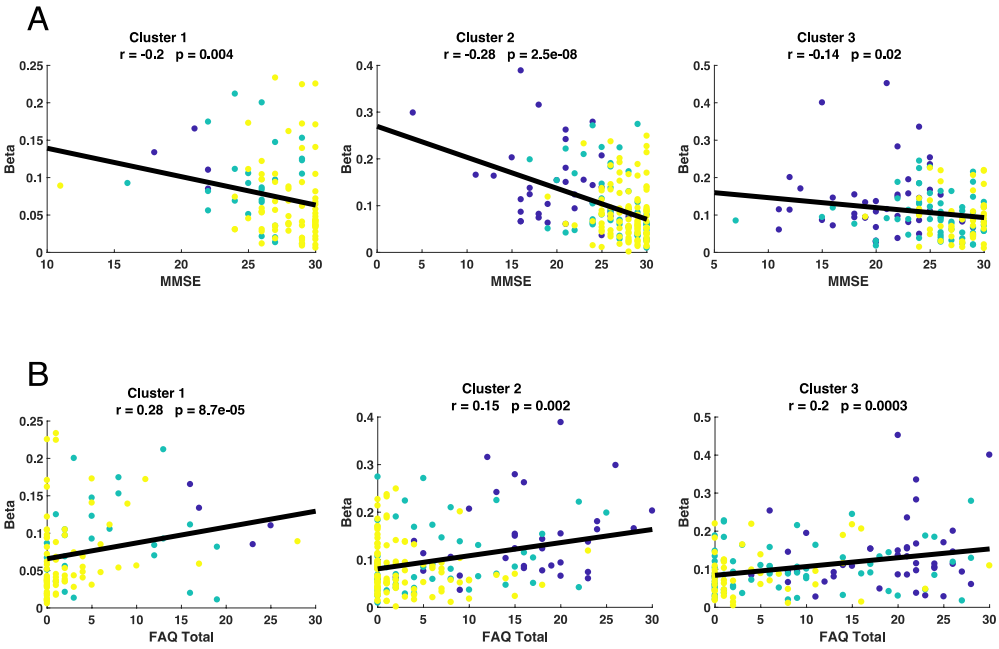

Figure 3.7. Cluster-specific beta vs. cognitive score. A) Correlation between rate of disease progression and baseline MMSE cognitive score across each of the three clusters. **B)** Correlation between beta and baseline FAQ cognitive score across each of the three clusters. Blue represents AD, turquoise represents LMCI and yellow represents EMCI.

Though we were able to predict a narrow range of beta based on cluster assignment from CSF biomarker profiles, we strived to obtain a more accurate prediction of beta. To do this, we integrated neuroimaging with our cluster analysis. Though the initial goal of the study was to circumvent neuroimaging all together, the use of one neuroimaging biomarker as opposed to several longitudinal ones still represents an improvement in regards to clinical efficiency. We hypothesized the regression model of cluster 3, the cluster exhibiting the most pathogenic characteristics, would yield the highest prediction as reflected by R^2.

To test this hypothesis, we created a regression model using the top 10 most atrophied regions characteristic of AD pathology. ROIs were obtained by independent t-tests in the AD group vs. age-matched controls. ROIs were all in the middle temporal lobe and include: Left hippocampus, right hippocampus, left amygdala, left entorhinal, right amygdala, left middle temporal gyrus, left inferior temporal gyrus, right entorhinal cortex, right inferior temporal and right middle temporal gyrus. These top 10 most atrophied ROIs were used in conjunction with the three baseline CSF biomarkers, AB, tau and pTau to form a 13 variable multivariate linear regression for beta prediction. We observe that the least pathologically severe cluster, cluster 1, gives a relatively weak R^2 of 0.15, the middle cluster yields a moderately strong R^2 of 0.26 and the most pathologically severe cluster 3 yields a relatively week R^2 of 0.12. In cluster 2's linear regression, which yielded the highest coefficient of determination, CSF Amyloid Beta was the most significant predictor (p=.0006) followed by volume of the right amygdala (p=.005), right hippocampus volume (p=.002) and left hippocampus volume (p=.01).

Next, we conducted the same regression analysis using global atrophy rate as the respone variable in order to directly compare the performance of our modeled beta parameter to global atrophy rate. Dissimilar to beta regression results, we observe that prediction of global atrophy rate using the same regressors yields the strongest R^2 in the least pathologically severe cluster 1 (Figure 3.8D). Cluster 2 and cluster 3 yield relatively poor predictive ability of global atrophy rate with R^2=0.12 and R^2=0.06, respectively (Figure 3.8E-F).

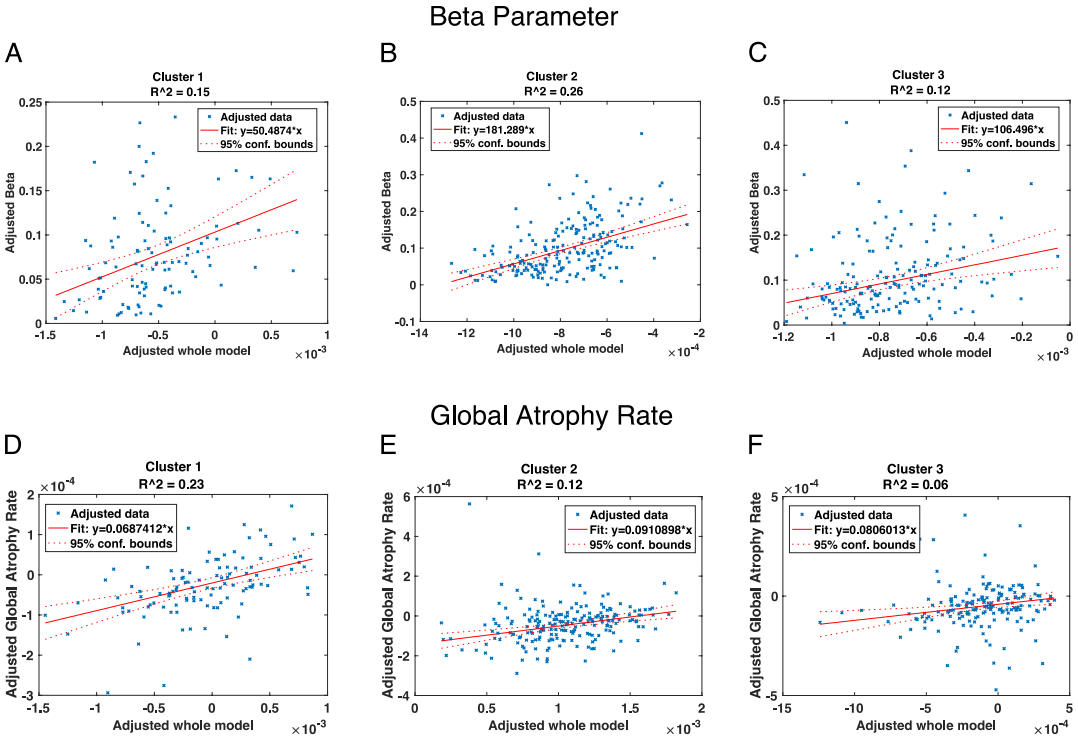

Figure 3.8. Linear regressions predicting beta by cluster. Regressions include the top 10 most atrophied regions characteristic of AD pathology and 3 CSF metrics. **A)** To predict beta in Cluster 1 **B)** To predict beta in Cluster 2 **C)** To predict beta in Cluster 3 **D)** To predict global atrophy rate in Cluster 1 **E)** To predict global atrophy rate in Cluster 2 **F)** To predict global atrophy rate in Cluster 3.

Discussion

The present study applies graph theoretic approaches and machine learning in a multimodal dataset of 810 subjects to obtain a new measure of rate of progression. Using our group's previously published Network Diffusion Model of AD spread (Raj et al., 2015, 2012), we derive a single neurodegeneration rate, given by the model's diffusivity parameter β, from each subject's longitudinal MRI data. This rate measure depends on various natural stratifications of the AD cohorts. At the group level it is highest for AD patients, lower for LMCI and lowest for EMCI, indicating that the degenerative process speeds up over time. The rate is higher for subjects with 2 putative APOE4 alleles compared to subjects with no putative APOE4 alleles.

However, these group differences mask substantial individual variability, which is shown in cluster analysis based on baseline CSF metrics. We demonstrate that 3 separate clustered emerge, which are characterized by differing degrees of AD-related pathology as reflected by cognitive scores, APOE allele status, beta parameter and baseline atrophy patterns. We then focused on the clinically relevant problem of predicting the rate parameter from a subject's baseline data only. We found that baseline CSF biomarkers, even within clusters, were not able to predict individual rate parameters. However, a combination of CSF and MRI biomarkers at baseline can predict a narrow range of rate values, and this prediction is most accurate in those subjects who happen to be in the middle of their degenerative course. This is the first study to propose a rate metric derived from the known mechanism of progression in AD, and the first to successfully model a narrow range of a subject's rate of brain degeneration from baseline CSF and MRI biomarkers.

Characterizing the rate parameter

We observed a highly significant correlation between our proposed rate of pathology spread and global rate of atrophy, suggesting that the former can serve as a mechanistically realistic surrogate of the latter (Figure 3.1A). We also show a moderately significant correlation between rate of pathology spread and cognitive decline as measured by the MMSE (Figure 3.1B). Although it is not expected that the proposed rate measure will completely track the established global atrophy rate measure, it is comforting that the two are closely associated. To confirm that proposed beta measure converges with current hypotheses of neurological decline, we tested the effect of modeled beta parameters across diagnostic groups and APOE allele status. AD subjects had the highest speed of pathology spread compared to LMCI and EMCI subjects (Figure 3.2A).

Because AD is reported to spread faster in a prion-like manner with disease progression, it is expected that AD subjects have higher rates of disease spread compared to LMCI and EMCI (Brundin et al., 2010; Jucker and Walker, 2013; Prusiner, 1998). Similarly, the highest speed of pathology spread was present in APOE E4/E4 subjects compared to E4/E3 and E3/E3 (Figure 3.2B). This result is in accordance with prior work, as the effect of APOE and amyloid beta burden on accelerated cognitive and clinical decline in both AD and cognitively normal subjects is well-established (Doraiswamy et al., 2014; Lim et al., 2014; Tosun et al., 2016). These results robustly characterize the proposed rate measure, and demonstrate that it agrees with current literature and hypotheses.

Predicting rate parameter from baseline CSF biomarkers

The ability to predict a subject's speed of neurodegeneration from baseline CSF and MRI biomarkers will be critical to approach the ultimate goal of one-day circumventing costly and time consuming scanning procedures for prognostic application. Simple correlation analysis reveals no significant, straightforward relationship between baseline CSF biomarker and speed of neurodegeneration (Figure 3.3). Though this result is contrary to our original hypothesis, it is not entirely surprising, as current molecular biomarker models posit the relationship between disease spread and CSF biomarker is dynamic and changes with stage of disease, suggesting more sophisticated modeling is necessary (Jack et al., 2013; Jack and Holtzman, 2013).

Therefore, we employed machine learning, specifically hierarchical clustering and K nearest neighbors (KNN) classification of 490 patients on 6 baseline CSF profiles, to establish a relationship between a subject's baseline CSF biomarkers and rate of AD progression. The 6 baseline CSF metrics include AB, pTau, Tau, AB/tau, AB/pTau, pTau/Tau. Hierarchical clustering revealed 3 distinct clusters (Figure 3.4A). CSF profiles across clusters are roughly arranged in order of pathological severity, going from cluster 1 (highest Ab42, lowest tau) to cluster 3 (lowest Ab42, highest tau), see Figure 3.4C-D. Although there is no one-to-one mapping between CSF clusters and AD stage, we found that cluster 1 was most enriched with EMCI and cluster 3 by AD, suggesting a clear order of severity, both pathologically and clinically. KNN classification successfully assigned subjects to clusters with >90% in a 5 k-fold validation approach (Figure 3.4B). These results are consistent with previous work, particularly (Iqbal et al., 2005) (Wallin et al., 2010), which demonstrated existence of similar clusters from non-ADNI AD patients. The 3

clusters are also arranged in order of increasing atrophy burden (Figure 3.5A). Mirroring the variability in CSF biomarkers and atrophy between clusters, we found that each cluster also displays a distinct range of the beta rate parameter (Figure 3.5B). Notably, the more pathogenic clusters also show higher rates of disease spread, cognitive impairments and frequency of putative APOE alleles (Figure 3.4-6). Within clusters, patients have differing relationships to cognitive metrics (Figure 3.7).

However, it is clear that CSF biomarkers alone are insufficient to correctly estimate an individual patient's rate parameter. Partly this reflects the well-known heterogeneity amongst AD cohorts (Iqbal et al., 2005) (Wallin et al., 2010). Visual inspection of our 3 CSF-based clusters reveals a mix of AD, LMCI and EMCI (Figure 3.7). Prior classification work in large datasets, in particular a CSF classification study in 675 subjects showed that while CSF profile was able to discriminate between neural disorders such as depression and AD, it performed poorly at classifying across different dementias, suggested dementias have intertwined pathophysiology (Ewers et al., 2015). Therefore we reasoned that MRI-derived biomarkers might be necessary to further improve predictive ability.

MRI-derived atrophy and CSF biomarkers predict rate of progression

When baseline neuroimaging biomarkers were introduced along with CSF biomarkers into a linear regression model, a subject's beta parameter could be predicted with a relatively high coefficient of determination in cluster 2 ($R^2 = 0.26$), and moderately predictive in clusters 1 and 3 (R^2 ~0.15) (Figure 3.8A-C). At first, it would appear more plausible that cluster 3, the most pathologically severe cluster, would yield the best linear regression results. A closer inspection revealed that cluster 3 is highly enriched with mature AD

patients, and cluster 1 for early or mild cases (Figure 3.7). In contrast, cluster 2 may be considered a middle phase that is most active pathologically. Previous studies have frequently observed this behavior, which has been accommodated by considering a non-linear model of progression (Jack et al., 2010).

This model expects that progression rates increase initially until an inflection point is reached. Thereafter a plateau effect becomes operational, such that further rate increases are constrained by resource challenged environments corresponding to mature disease (Jack et al., 2010, 2013; Jack and Holtzman, 2013). In this respect, our result showing the highest rate of progression in middle pathological stages (cluster 2) is consistent with the literature. In contrast, Figures 3.8D-F show the highest predictive ability using these same regressors to predict global atrophy rate is highest in the least pathogenic cluster 1. Predictive ability is poor for subjects in the middle and end of their degenerative courses, which provides further support for the use of modeled beta parameter, as global atrophy is shown not to be sensitive enough to detect network constrained AD-pathology spread.

Clinical implications

There has been recent interest and remarkable progress in prognostic neuroimaging and molecular biomarkers (Ba et al., 2017; Tosun et al., 2016). Notwithstanding, the relationship between baseline and longitudinal progression is inconsistently described (Mattsson et al., 2009; Schindler et al., 2017). Moreover, overall accuracy of clinical diagnosis based on cognitive metric is shown to be low (Beach et al., 2012). Dependence on cognitive score as a metric of disease spread is problematic, because some individuals clinically diagnosed with MCI and AD dementia later are discovered to have

non-AD etiologies and cognitively normal controls may have preclinical AD (Hassenstab et al., 2016). Prior work shows baseline biomarker profiles can distinguish AD from other neurological diseases, assess risk for progression from Mild Cognitive Impairment (MCI) to AD as well as predict progressors from non progressors in clinical trial environments (Ewers et al., 2015; Mattsson et al., 2014; Shaw et al., 2011; Tosun et al., 2016). However, the majority of this work has been done by neuroimaging protein biomarkers in vivo. Unfortunately, neuroimaging equipment and analysis are expensive, time consuming and not readily available in all clinical settings. A practical, inexpensive tool to predict speed of neurodegeneration has not yet been developed. Brain imaging with MRI, FDG-PET, and amyloid PET often require advanced imaging analyses, which may not be easily accessible in all clinical environments.

A lumbar puncture, in contrast, may be done in many different clinical settings and CSF samples can easily be shipped to a central laboratory for analysis (Herukka et al., 2017). Over the past 6 years, diagnostic criteria for Alzheimer's Disease (AD) has evolved to include molecular biomarkers (McKhann et al., 2011). A wide body of literature corroborates that AD pathology is accompanied by a stereotypical decrease in CSF Amyloid-beta (AB) in addition to increased CSF tau and phosphorylated tau (pTau) (Andreasen et al., 2003, 2001; Hulstaert et al., 1999; Rosén et al., 2013; Tapiola et al., 2009). CSF biomarkers influence decision making depending on the extent to which biomarkers reflect AD pathology, consistency between clinical–pathologic information, and the ambiguity of protein values (Gooblar et al., 2015).

Hence, we focused on predicting a subject's progression rate from CSF biomarkers from a single lumbar puncture. It was found necessary to include MRI regional atrophy, which we feel is clinically acceptable, as most patients will have had at least a standard-of-care MRI exam. We demonstrated that the rate of progression can be reasonably predicted from baseline CSF and MRI in a large class of subjects falling within an intermediate pathological cluster. In clinical terms, this is perhaps also the group that can most benefit from a prognostic indicator of longitudinal progression. To our knowledge, this is the first study to propose a network-based measure of progression rate and to predict it from baseline CSF and MRI biomarkers, see, e.g. (Herukka et al., 2017). It is our hope that the proposed rate measure will be used in a prognostic manner as a screening tool for differential diagnosis, clinical trial inclusion and therapeutic treatments. In order to facilitate adoption we are making the computer code available freely on our website (www.ideal-cornell.com).

Limitations

There exists concern that lack of standardization of CSF protocols to detect AB42 and tau is common across sites, with different commercial kits utilizing their own standards, anti-bodies, ranges and cut-offs (Lehmann et al., 2015). However, the University of Pennsylvania (UPenn) ADNI Biomarker Core laboratory has thoroughly studied and published methodology regarding measurement of $A\beta_{1–42}$, t-tau and p-tau_{181} in highly clinically annotated ADNI CSF samples to identify and attempt to control key sources of analytical variability (Shaw et al., 2011). Furthermore, it has been suggested that longitudinal CSF data is necessary for prognostic application as biomarkers can change linearly with time, exponetially, sigmoidally, etc (Fagan et al.,

2014; Jack and Holtzman, 2013). The current study mitigates that issue as 90% of the CSF data included was collected within a year of each subject's baseline scan, reducing the need for extensive modeling of biomarker dynamics. An additional limitation is that the NDM is a first-order, linear, parsimonious model of diffusive spread that assumes that the structural connectivity network remains static and unchanged over the duration of the longitudinal analysis. This is reasonable because the observation window (2-4 years) is short compared to the course of the disease. Additionally, although the model enables long-term projections of future atrophy, model validation in the current work is limited to public (ADNI) data sets of rather narrow time span (2–4 years), precluding long-term longitudinal follow-up.

Acknowledgments

The authors declare no conflict of interest. This research was supported in part by grants from the Ford Foundation, NINDS grants R01 NS075425 and R01 NS092802. Data collection and sharing for this project were funded by the ADNI (NIH grant U01 AG024904) and DOD ADNI (Department of Defense award number W81XWH-12-2-0012). ADNI is funded by the National Institute on Aging, the National Institute of Biomedical Imaging and Bioengineering, and through generous contributions from the following: Abbott, AstraZeneca AB, Bayer Schering Pharma AG, Bristol-Myers Squibb, Eisai Global Clinical Development, Elan Corporation, Genentech, GE Healthcare, GlaxoSmithKline, Innogenetics, Johnson and Johnson, Eli Lilly and Co., Medpace, Inc., Merck and Co., Inc., Novartis AG, Pfizer Inc., F. Hoffman-La Roche, Schering-Plough, Synarc, Inc., as well as non-profit partners the Alzheimer's Association and Alzheimer's Drug Discovery Foundation, with participation from the U.S. Food and Drug Administration. Private sector contributions to ADNI are facilitated by the Foundation for the National Institutes of Health (http://www.fnih.org). The grantee organization is the Northern California Institute for Research and Education, and the study is coordinated by the Alzheimer's Disease Cooperative Study at the University of California, San Diego. ADNI data are disseminated by the Laboratory for Neuro Imaging at the University of California, Los Angeles.

REFERENCES

Aleman-Gomez, Y., 2006. IBASPM: toolbox for automatic parcellation of brain structures. 12th Annu. Meet. Organ. Hum.

Andreasen, N., Minthon, L., Davidsson, P., Vanmechelen, E., Vanderstichele, H., Winblad, B., Blennow, K., 2001. Evaluation of CSF-tau and CSF-Abeta42 as diagnostic markers for Alzheimer disease in clinical practice. Arch. Neurol. 58, 373–9.

Andreasen, N., Sjögren, M., Blennow, K., 2003. CSF markers for Alzheimer's disease: total tau, phospho-tau and Abeta42. World J. Biol. Psychiatry 4, 147–55.

Ba, M., Li, X., Ng, K.P., Pascoal, T.A., Mathotaarachchi, S., Rosa-Neto, P., Gauthier, S., 2017. The prevalence and biomarkers' characteristic of rapidly progressive Alzheimer's disease from the Alzheimer's Disease Neuroimaging Initiative database. Alzheimer's Dement. Transl. Res. Clin. Interv. 3, 107–113. doi:10.1016/j.trci.2016.12.005

Beach, T.G., Monsell, S.E., Phillips, L.E., Kukull, W., 2012. Accuracy of the Clinical Diagnosis of Alzheimer Disease at National Institute on Aging Alzheimer Disease Centers, 2005–2010. J. Neuropathol. Exp. Neurol. 71, 266–273. doi:10.1097/NEN.0b013e31824b211b

Bolboaca, S., Jäntschi, L., 2006. Pearson versus Spearman, Kendall's tau correlation analysis on structure-activity relationships of biologic active compounds. Leonardo J. Sci.

Brundin, P., Melki, R., Kopito, R., 2010. Prion-like transmission of protein aggregates in neurodegenerative diseases. Nat. Rev. Mol. Cell Biol.

Doraiswamy, P.M., Sperling, R.A., Johnson, K., Reiman, E.M., Wong, T.Z., Sabbagh, M.N., Sadowsky, C.H., Fleisher, A.S., Carpenter, A., Joshi, A.D., Lu, M., Grundman, M., Mintun, M.A., Skovronsky, D.M., Pontecorvo, M.J., AV45-A11 Study Group, A.-A.S., AV45-A11 Study Group, 2014. Florbetapir F 18 amyloid PET and 36-month cognitive decline: a prospective multicenter study. Mol. Psychiatry 19, 1044–51. doi:10.1038/mp.2014.9

Ewers, M., Mattsson, N., Minthon, L., Molinuevo, J.L., Antonell, A., Popp, J., Jessen, F., Herukka, S.-K., Soininen, H., Maetzler, W., Leyhe, T., Bürger, K., Taniguchi, M., Urakami, K., Lista, S., Dubois, B., Blennow, K., Hampel, H., 2015. CSF biomarkers for the differential diagnosis of Alzheimer's disease: A large-scale international multicenter study. Alzheimer's Dement. 11, 1306–1315. doi:10.1016/j.jalz.2014.12.006

Fagan, A.M., Xiong, C., Jasielec, M.S., Bateman, R.J., Goate, A.M., Benzinger, T.L.S., Ghetti, B., Martins, R.N., Masters, C.L., Mayeux, R., Ringman, J.M., Rossor, M.N., Salloway, S., Schofield, P.R., Sperling, R.A., Marcus, D., Cairns, N.J., Buckles, V.D., Ladenson, J.H., Morris, J.C., Holtzman, D.M., Dominantly Inherited Alzheimer Network, 2014. Longitudinal change in CSF biomarkers in autosomal-dominant Alzheimer's disease. Sci. Transl. Med. 6, 226ra30. doi:10.1126/scitranslmed.3007901

Friston, K.J. (Karl J.., Ashburner, J., Kiebel, S., Nichols, T., Penny, W.D., 2007. Statistical parametric mapping : the analysis of funtional brain images. Elsevier/Academic Press.

Frost, B., Diamond, M.I., 2010. Prion-like mechanisms in neurodegenerative diseases. Nat. Rev. Neurosci. 11, 155–9. doi:10.1038/nrn2786

Gooblar, J., Carpenter, B.D., Coats, M.A., Morris, J.C., Snider, B.J., 2015. The influence of cerebrospinal fluid (CSF) biomarkers on clinical dementia evaluations. Alzheimer's Dement. 11, 533–540.e2. doi:10.1016/j.jalz.2014.04.517

Hassenstab, J., Chasse, R., Grabow, P., Benzinger, T., 2016. Certified normal: Alzheimer's disease biomarkers and normative estimates of cognitive functioning. Neurobiol.

Herukka, S.-K., Simonsen, A.H., Andreasen, N., Baldeiras, I., Bjerke, M., Blennow, K., Engelborghs, S., Frisoni, G.B., Gabryelewicz, T., Galluzzi, S., Handels, R., Kramberger, M.G., Kulczyńska, A., Molinuevo, J.L., Mroczko, B., Nordberg, A., Oliveira, C.R., Otto, M., Rinne, J.O., Rot, U., Saka, E., Soininen, H., Struyfs, H., Suardi, S., Visser, P.J., Winblad, B., Zetterberg, H., Waldemar, G., 2017. Recommendations for cerebrospinal fluid Alzheimer's disease biomarkers in the diagnostic evaluation of mild cognitive impairment. Alzheimer's Dement. 13, 285–295. doi:10.1016/j.jalz.2016.09.009

Hulstaert, F., Blennow, K., Ivanoiu, A., Schoonderwaldt, H.C., Riemenschneider, M., De Deyn, P.P., Bancher, C., Cras, P., Wiltfang, J., Mehta, P.D., Iqbal, K., Pottel, H., Vanmechelen, E., Vanderstichele, H., 1999. Improved discrimination of AD patients using beta-amyloid(1-42) and tau levels in CSF. Neurology 52, 1555–62.

Iqbal, K., Flory, M., Khatoon, S., Soininen, H., Pirttila, T., Lehtovirta, M., Alafuzoff, I., Blennow, K., Andreasen, N., Vanmechelen, E., Grundke-Iqbal, I., 2005. Subgroups of Alzheimer's disease based on cerebrospinal fluid molecular markers. Ann. Neurol. 58, 748–757. doi:10.1002/ana.20639

Jack, C., Knopman, D., Jagust, W., Shaw, L., 2010. Hypothetical model of dynamic biomarkers of the Alzheimer's pathological cascade. Lancet.

Jack, C.R., Holtzman, D.M., 2013. Biomarker Modeling of Alzheimer's Disease. Neuron 80, 1347–1358. doi:10.1016/j.neuron.2013.12.003

Jack, C.R., Knopman, D.S., Jagust, W.J., Petersen, R.C., Weiner, M.W., Aisen, P.S., Shaw, L.M., Vemuri, P., Wiste, H.J., Weigand, S.D., Lesnick, T.G., Pankratz, V.S., Donohue, M.C., Trojanowski, J.Q., 2013. Tracking pathophysiological processes in Alzheimer's disease: an updated hypothetical model of dynamic biomarkers. Lancet Neurol. 12, 207–216. doi:10.1016/S1474-4422(12)70291-0

Jucker, M., Walker, L.C., 2013. Self-propagation of pathogenic protein aggregates in neurodegenerative diseases. Nature 501, 45–51. doi:10.1038/nature12481

Karas, G.B., Scheltens, P., Rombouts, S.A.R.B., Visser, P.J., van Schijndel, R.A., Fox, N.C., Barkhof, F., 2004. Global and local gray matter loss in mild cognitive impairment and Alzheimer's disease. Neuroimage 23, 708–716. doi:10.1016/j.neuroimage.2004.07.006

Kruskal, W.H., Wallis, W.A., 1952. Use of Ranks in One-Criterion Variance Analysis. J. Am. Stat. Assoc. 47, 583–621. doi:10.1080/01621459.1952.10483441

Kuceyeski, A., Maruta, J., Niogi, S., Ghajar, J., Raj, A., 2011. The generation and validation of white matter connectivity importance maps. Neuroimage.

Kuceyeski, A., Maruta, J., Relkin, N., Raj, A., 2013. The Network Modification (NeMo) Tool: Elucidating the Effect of White Matter Integrity Changes on Cortical and Subcortical Structural Connectivity. Brain Connect. 3, 451–463. doi:10.1089/brain.2013.0147

Lehmann, S., Gabelle, A., Paquet, C., 2015. Can we rely only on ratios of cerebrospinal fluid biomarkers for AD biological diagnosis? Alzheimer's Dement. 11, 1125–1126. doi:10.1016/j.jalz.2014.09.003

Lim, Y.Y., Maruff, P., Pietrzak, R.H., Ames, D., Ellis, K.A., Harrington, K., Lautenschlager, N.T., Szoeke, C., Martins, R.N., Masters, C.L., Villemagne, V.L., Rowe, C.C., AIBL Research Group, 2014. Effect of amyloid on memory and non-memory decline from preclinical to clinical Alzheimer's disease. Brain 137, 221–231. doi:10.1093/brain/awt286

Mattsson, N., Insel, P.S., Landau, S., Jagust, W., Donohue, M., Shaw, L.M., Trojanowski, J.Q., Zetterberg, H., Blennow, K., Weiner, M., 2014. Diagnostic accuracy of CSF Ab42 and florbetapir PET for Alzheimer's disease. Ann. Clin. Transl. Neurol. 1, 534–543. doi:10.1002/acn3.81

Mattsson, N., Zetterberg, H., Hansson, O., Andreasen, N., Parnetti, L., Jonsson, M., Herukka, S.-K., van der Flier, W.M., Blankenstein, M.A., Ewers, M., Rich, K., Kaiser, E., Verbeek, M., Tsolaki, M., Mulugeta, E., Rosén, E., Aarsland, D., Visser, P.J., Schröder, J., Marcusson, J., de Leon, M., Hampel, H., Scheltens, P., Pirttilä, T., Wallin, A., Jönhagen, M.E., Minthon, L., Winblad, B., Blennow, K., 2009. CSF Biomarkers and Incipient Alzheimer Disease in Patients With Mild Cognitive Impairment. JAMA 302, 385. doi:10.1001/jama.2009.1064

Maulik, U., Bandyopadhyay, S., 2002. Performance evaluation of some clustering algorithms and validity indices. IEEE Trans. Pattern.

McKhann, G.M., Knopman, D.S., Chertkow, H., Hyman, B.T., Jack, C.R., Kawas, C.H., Klunk, W.E., Koroshetz, W.J., Manly, J.J., Mayeux, R., Mohs, R.C., Morris, J.C., Rossor, M.N., Scheltens, P., Carrillo, M.C., Thies, B., Weintraub, S., Phelps, C.H., 2011. The diagnosis of dementia due to Alzheimer's disease: Recommendations from the National Institute on Aging-Alzheimer's Association workgroups on diagnostic guidelines for Alzheimer's disease. Alzheimer's Dement. 7, 263–269. doi:10.1016/j.jalz.2011.03.005

Morris, J., Roe, C., Xiong, C., Fagan, A., 2010. APOE predicts amyloid-beta but not tau Alzheimer pathology in cognitively normal aging. Ann.

Mueller, S.G., Weiner, M.W., Thal, L.J., Petersen, R.C., Jack, C.R., Jagust, W., Trojanowski, J.Q., Toga, A.W., Beckett, L., 2005. Ways toward an early diagnosis in Alzheimer's disease: The Alzheimer's Disease Neuroimaging Initiative (ADNI). Alzheimer's Dement. 1, 55–66. doi:10.1016/j.jalz.2005.06.003

Okello, A., Koivunen, J., Edison, P., Archer, H.A., Turkheimer, F.E., Någren, K., Bullock, R., Walker, Z., Kennedy, A., Fox, N.C., Rossor, M.N., Rinne, J.O., Brooks, D.J., 2009. Conversion of amyloid positive and negative MCI to AD over 3 years: an 11C-PIB PET study. Neurology 73, 754–60. doi:10.1212/WNL.0b013e3181b23564

Price, J., Morris, J., 1999. Tangles and plaques in nondemented aging & preclinical Alzheimer's disease. Ann. Neurol.

Prusiner, S.B., 1998. Prions. Proc. Natl. Acad. Sci. U. S. A. 95, 13363–83. doi:10.1073/PNAS.95.23.13363

Raj, A., Kuceyeski, A., Weiner, M., 2012. A Network Diffusion Model of Disease Progression in Dementia. Neuron 73, 1204–1215. doi:10.1016/j.neuron.2011.12.040

Raj, A., LoCastro, E., Kuceyeski, A., Tosun, D., Relkin, N., Weiner, M., 2015. Network Diffusion Model of Progression Predicts Longitudinal Patterns of Atrophy and Metabolism in Alzheimer's Disease. Cell Rep. 10, 359–369. doi:10.1016/j.celrep.2014.12.034

Rosén, C., Hansson, O., Blennow, K., Zetterberg, H., Rowe, C., McLean, C., Masters, C., Evin, G., Li, Q., Lovestone, S., Resnick, S., 2013. Fluid biomarkers in Alzheimer's disease – current concepts. Mol. Neurodegener. 8, 20. doi:10.1186/1750-1326-8-20

Schindler, S.E., Jasielec, M.S., Weng, H., Hassenstab, J.J., Grober, E., McCue, L.M., Morris, J.C., Holtzman, D.M., Xiong, C., Fagan, A.M., 2017. Neuropsychological measures that detect early impairment and decline in preclinical Alzheimer disease. Neurobiol. Aging 56, 25–32. doi:10.1016/j.neurobiolaging.2017.04.004

Shaw, L.M., Vanderstichele, H., Knapik-Czajka, M., Figurski, M., Coart, E., Blennow, K., Soares, H., Simon, A.J., Lewczuk, P., Dean, R.A., Siemers, E., Potter, W., Lee, V.M.-Y., Trojanowski, J.Q., Initiative, the A.D.N., 2011. Qualification of the analytical and clinical performance of CSF biomarker analyses in ADNI. Acta Neuropathol. 121, 597–609. doi:10.1007/s00401-011-0808-0

Smith, S., Jenkinson, M., Woolrich, M., Beckmann, C., 2004. Advances in functional and structural MR image analysis and implementation as FSL. Neuroimage.

Sunderland, T., Mirza, N., Putnam, K., Linker, G., 2004. Cerebrospinal fluid β-amyloid 1–42 and tau in control subjects at risk for Alzheimer's disease: The effect of APOE ε4 allele. Biological.

Tapiola, T., Alafuzoff, I., Herukka, S.-K., Parkkinen, L., Hartikainen, P., Soininen, H., Pirttilä, T., 2009. Cerebrospinal Fluid β-Amyloid 42 and Tau Proteins as Biomarkers of Alzheimer-Type Pathologic Changes in the Brain. Arch. Neurol. 66, 382–9. doi:10.1001/archneurol.2008.596

Tosun, D., Chen, Y.-F., Yu, P., Sundell, K.L., Suhy, J., Siemers, E., Schwarz, A.J., Weiner, M.W., 2016. Amyloid status imputed from a multimodal classifier including structural MRI distinguishes progressors from nonprogressors in a mild Alzheimer's disease clinical trial cohort. Alzheimer's Dement. 12, 977–986. doi:10.1016/j.jalz.2016.03.009

Wallin, A.K., Blennow, K., Zetterberg, H., Londos, E., Minthon, L., Hansson, O., 2010. CSF biomarkers predict a more malignant outcome in Alzheimer disease. Neurology 74, 1531–7. doi:10.1212/WNL.0b013e3181dd4dd8

Wilcoxon, F., 1950. Some rapid approximate statistical procedures. Ann. N. Y. Acad. Sci.

Chapter 4:

Structural Network Model of Pathology Spread Predicts Neurodegeneration in Huntington's Disease

Introduction

Huntington's Disease (HD) is an autosomal dominant genetic disorder caused by a mutation (CAG repeat expansion) in the Huntingtin gene (HTT). The topography of HD in the human brain displays a well characterized and stereotyped regional pattern and progression. Disease pathology initially appears in the striatum, followed by striatal neighbors and connected cortical areas (Brettschneider et al., 2015)

The mechanisms underlying stereotyped patterning and progression are not fully understood. It is suggested that both cell-cell communications governed by anatomical and functional connections, and cell autonomous molecular factors characterized by gene expression signatures, play a role in vulnerability to disease spread (Brettschneider et al., 2015; Frost and Diamond, 2010; Jucker and Walker, 2013; Lee et al., 2010; Prusiner, 1984; Seeley, 2017). It is less clear whether cell type and molecular factors are the main source of regional vulnerability in HD, or whether non-cell autonomous factors, of which network connectivity is a canonical example, are the key driver of vulnerability. It is possible that both sets of factors play a role, however their relative contribution and interactions remain unknown.

Previous studies of selective regional vulnerability in HD have generally focused on cellular toxic effects involving cell autonomous mechanisms, such as proteolytic and post translational modifications (Ross and Tabrizi, 2011). Recently, it is emerging that non-autonomous mechanisms, likely involving the

brain's anatomic or functional connectivity patterns, might also be responsible for selective vulnerability in HD. Indeed, mutant HTT is pathogenic, has a tendency to aggregate and potentially diffuse to extracellular space and thence to neighboring cells to act as a seed for further aggregation (Lee et al., 2001; Tan et al., 2015). This process is reminiscent of the well-studied prion model of neurodegeneration, which hypothesize that misfolded proteins spread trans-synaptically along neuronal pathways in specific patterns. Several neurodegenerative disorders including Alzheimer's Disease (AD), Frontotemporal Dementia (FTD), Parkinson's Disease (PD), Amyotrophic Lateral Sclerosis (ALS) and Huntington's Disease (HD) report aggregation and transmission of pathogenic proteins between cells in addition to stereotypical patterns of disease progression (Hansen et al., 2011; Herrera et al., 2011; Jack and Holtzman, 2013; Lee et al., 2001; Neumann et al., 2006; Spillantini et al., 1998).

Given that trans-synaptic transmission must proceed along axonal projections, the spatiotemporal dynamics of pathology spread can be quantitatively and deterministically captured once the inter-regional anatomic connectivity patterns are known. Recently, our group proved tested this hypothesis with a mathematical model of prion-like spread on diffusion MRI-based structural networks. We proposed a mathematical model of prion-like trans-synaptic spread of neurodegenerative pathology called the network diffusion model (NDM). This model demonstrated that observed spatial patterns of neurodegeneration in common degenerative diseases like Alzheimer's and frontotemporal dementia can be explained simply as a consequence of network spread (Raj et al., 2012). This model also gives an explanation of selective regional vulnerability in terms of disease epicenters,

called eigenmodes, associated with pathology. The model was successfully validated to predict future atrophy patterns of AD subjects from baseline atrophy patterns on a single template connectome (Raj et al., 2015).

The current study explores two of the potential mechanisms underlying selective regional vulnerability in HD: 1) Molecular factors characterized by innate regional gene expression patterns of HD-related genes; and 2) Prion-like spread of HTT and downstream protein products along connectivity. In addition to structural connectivity, the current study also assesses a distanced-model connectivity model as well as a functional connectivity model. To assess regional gene expression models of HD, regional gene expression is used from of 6 healthy brains published by the Allen Institute, with a set of genes selected on the basis of their relevance to HD. For connectivity-based model, a previously published NDM to a variety of connectomes quantitatively assesses whether trans-synaptic transmission of HD pathology can recapitulate observed HD topography. Empirical data to test various models comes from an unprecedented dataset of 231 subjects with HD from the Track-HD study, a multinational prospective observation study of HD that examines clinical and biological findings of disease progression in individuals with pre-manifest HD and early-stage HD (Tabrizi et al., 2012, 2011, 2009). This is the first published study to systematically test multiple hypotheses of pathology spread in living human subjects with HD.

Methods

Participants

Track-HD is a multinational prospective observational study of Huntington's disease (HD) that examines clinical and biological findings of disease progression in individuals with pre-manifest HD and early-stage HD. Inclusion criteria, procedures, data collection and data storage have been described previously (Tabrizi et al., 2012, 2011, 2009). Subjects were assessed at four study sites in the Netherlands, the UK, France, and Canada. The study was approved by local ethics committees and written informed consent was obtained from each participant before enrollment.

Individuals without HD but carrying the mutant huntingtin gene (classed as preHD-A if ≥10.8 years and preHD-B if <10.8 years from predicted onset), participants with early HD (classed as HD1 if they had a total functional capacity score of 11–13 and HD2 if they had a score of 7–10), and healthy controls. Controls were selected from the spouses or partners of individuals with premanifest or early Huntington's disease or were gene-negative siblings, to ensure consistency of environments. All control groups were age-matched and gender matched with patient group (Table 4.1).

Table 4.1. Study participants.

Patient Group	Patient N	Patient Age (std)	Patient Gender	Control N	Control Age (std)	Control Gender	Age p-value	Gender p-value
preHD-A	62	41.05 (8.63)	33 (F) 29 (M)	100	43.34 (8.77)	57 (F) 43 (M)	p=.11	p=.28
preHD-B	54	40.65 (8.73)	33 (F) 21 (M)	93	42.27 (8.11)	53 (F) 40 (M)	p=.26	p=.39
HD1	72	46.69 (10.37)	42 (F) 30 (M)	119	46.20 (10.42)	68 (F) 51 (M)	p=.75	p=.73
HD2	43	51.98 (8.55)	19 (F) 24 (M)	92	50.23 (7.94)	54 (F) 38 (M)	p=.25	p=.63

MR image processing

MRI was collected and processed as described in (Tabrizi et al., 2013). The brain was parcellated into 86 different ROIs using cortical and subcortical structures from the FreeSurfer (Desikan-Killarney) gray matter parcellation.

White matter connectome

The white matter (WM) connectome was constructed by taking the mean of diffusion MRI data of normal, healthy subjects. Normal subject data were collected jointly by Weill Cornell Medical College and the Brain Trauma Foundation. Seventy-three healthy subjects (40 men, 33 women, 30.2 ± 6.7 years) were used to create the normative connectivity information in the form of tractograms. T1-weighted structural and diffusion-weighted MR images were collected on a 3 T GE Sigma EXCITE scanner (GE Healthcare, Waukesha, WI). The High Angular Resolution Diffusion Images data were acquired with 55 isotropically distributed diffusion-encoding directions at b=1000 sec/mm^2 and one at b=0 sec/mm^2, from 72 1.8-mm thick interleaved slices (no slice gap) and 128×128 matrix size, zero-filled during reconstruction to 256×256, with a field of view (FOV) of 230 mm^2. The structural scan was an axial three dimensional inversion-recovery fast spoiled gradient-recalled echo sequence ((echo time [ET]=1.5 msec, repetition time [TR]=6.3 msec, inversion time [TI]=400 msec) flip angle of 15°) with a 256×256 matrix over a 230 mm^2 FOV and 156 1.0-mm contiguous partitions. The diffusion images were corrected for eddy current and motion artifacts using FMRIB Software Library (FSL) (Smith et al., 2004).

T1 images were processed by first segmenting the tissue into cerebrospinal fluid, WM and GM. The GM segment was subsequently parcellated into 86 different ROIs using cortical and subcortical structures from

the FreeSurfer (Desikan-Killarney) gray matter parcellation. The parcellated GM was then linearly transformed and resampled to diffusion image space for use in tractography. Briefly, the surface voxels of the parcellated cortical and subcortical structures were used to seed the tracts. Proposed and validated in Iturria-Medina and colleagues (2005), the tractography algorithm implemented here incorporates tissue classification probability and orientation distribution information in a Bayesian manner. A tract terminated when the algorithm reached the boundary of an image volume, the edge of a GM region, a voxel not in the gray or WM masks, or when the angle between subsequent steps exceeded π/3. This analysis was done using the eighth version of Statistical Parametric Mapping (SPM), (Friston et al., 2007), a software package within Matlab R2009a (The Mathworks, Inc., Natick, MA), and the Individual-Based Atlas toolbox (Aleman-Gomez, 2006) within SPM.

Further details of the image processing and tractography method are given in a previous publication (Kuceyeski et al., 2013; Kuceyeski et al., 2011). To control for inter-subject variance in total fiber count, the number of connections between each tract was divided by the total number of tracts based on each subject's tractography data. Because DTI cannot provide directionality, the connectome was symmetric. The subsequent undirected connectomes were not thresholded and kept as weighted. Functional connectivity acquisition and preprocessing are also available in (Kuceyeski et al., 2013). Similarly, functional connectivity matrices were kept as weighted, non-thresholded and directionality was maintained.

Directional connectivity networks

Mesoscale mouse connectome data was used from the Allen Brain Institute (Oh et al., 2014). Total projection volume between regions was generated by multiplying element-wise by the rows the connectivity matrix times the number of voxels in each seeding region. As the MBCA connectivity matrix, retrieved from Oh et al. 2014, gave per-voxel normalized connectivity strength, our adjustment of connectivity to the size of each region approximates total connectivity. This procedure for approximating total axon volume or connectivity between regions is laid out in detail in SI.5 in Oh, et.al., 2014. Following this, we applied a thresholding criteria of getting rid of all values that were less than 0.05 the standard deviation of the nonzero entries of the mouse connectivity matrix, resulting in a network density < 0.14. The network derived from the Allen Institute is directed and the matrix representing the mouse connectivity network is therefore not symmetric over its diagonal. The above generated network is arranged such that per-region outgoing connectivity is given by each row and per-region incoming connectivity is given by each column.

Genetic data

Microarray gene expression data from post-mortem healthy human brains were downloaded from the Allen Brain Atlas Institute and obtained as described in (Hawrylycz et al., 2012). Microarray data were composed of 926 regions of the brain, each one belonging to a set of 58,692 probes that correspond to 29,181 distinct genes. Unique probe ID’s often represented the same gene and were all used for analysis of the gene, as done by (Freer et al., 2016). For analysis, the 926 regions in the microarray data were mapped to 86 regions of the Desikan Atlas. Data points that were unable to be mapped

to the Desikan Atlas included WM tracks and were excluded from analysis. The exclusion of WM tracks should have little impact on analysis due to its large composition of myelinated axons and its expendable role in research that successfully links expression signature to vulnerability in neurodegeneration (Freer et al., 2016). If multiple probes existed for a single gene, expression was averaged together for each ROI. Genes of interest were selected from a DisGeNET database, which generates integrates human gene-disease associations from curated databases and text mining (Piñero et al., 2015).

Network Diffusion Model (NDM)

The network diffusion model is used as described in Raj et al. 2012. Briefly, HD-related disease pattern, given by the vector x(t), is modeled as a diffusive process:

$$\mathbf{x}(t)=e^{-\beta H t}\mathbf{x}_0, \text{(Eq 1)}$$

where x_0 is the initial regional pattern of the disease, on which the term $e^{-\beta H t}$ acts as a spatial and temporal blurring operator. We therefore call $e^{-\beta H t}$, "the diffusion kernel." The computation of the above equation is accomplished via the eigenvalue decomposition $H = U\Lambda U^{\dagger}$, where $U = [u1 \ \ldots \ uN]$, giving:

$$\mathbf{x}(t)=Ue^{-\Lambda\beta t}U^{\top}\mathbf{x}_0=\sum_{i=1}(e^{-\beta\lambda_i t}\mathbf{u}_i^{\dagger}\mathbf{x}_0)\mathbf{u}_i. \text{(Eq 2)}$$

In other words, the network diffusion model is evaluated via the eigen-decomposition of the Laplacian matrix, such that the pattern of disease at any point of time is given as a linear superposition of the eigenmodes u_i's of the Laplacian. Eigenmodes are calculated, using spectral graph theory on the WM 86x86 ROI Laplacian matrix based on spectral graph theory. See Raj et al.

2012 for a full description of the network diffusion model. These eigenmodes, in turn, represent fundamental substrates upon which network spread of pathological entities is enacted. Hence, we investigated whether the prominent eigenmodes are conserved between patients and healthy subjects.

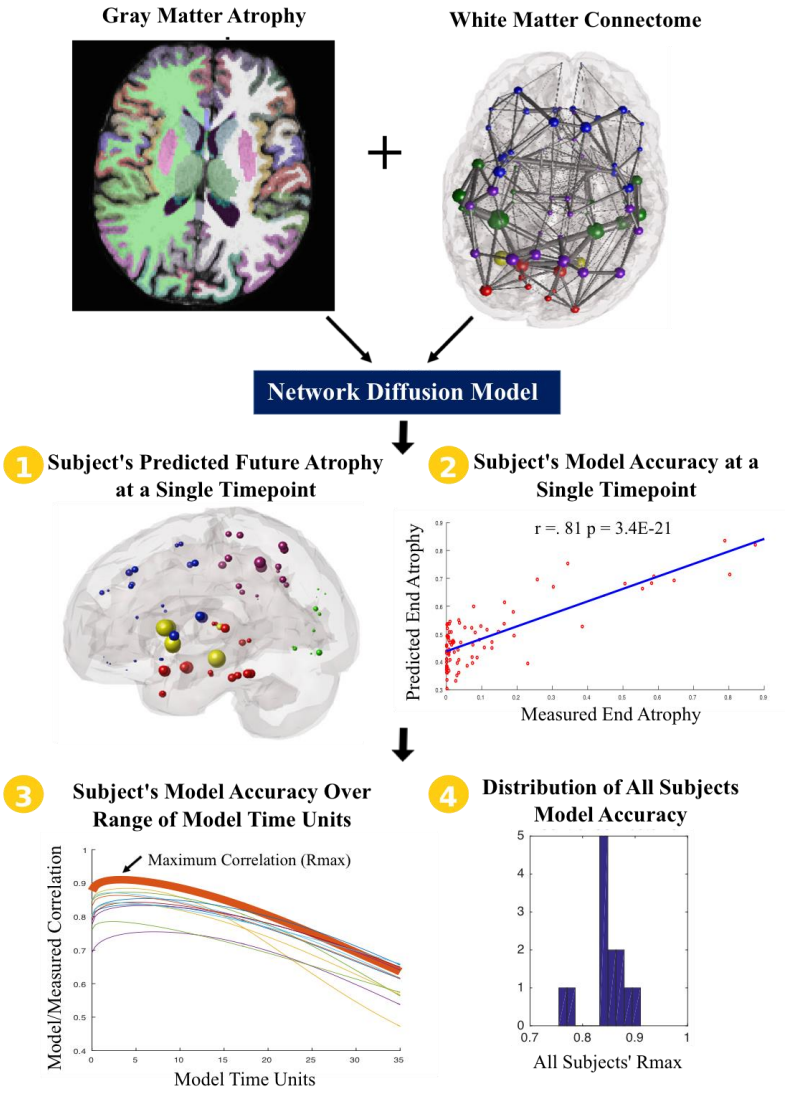

Figure 4.1. NDM construction. Using our established neuroimaging pipeline the regional atrophy vector for a patient is obtained; a "glass brain" rendering of regional atrophy is shown in panel **1.)** For each model time t, the vector x(t) is correlated against empirical atrophy vector; an example scatter plot is shown in panel **2.**) The Pearson's R statistic is plotted over all model times t, giving what we call the "R-t curve" shown in panel **3.)** This process is repeated for all possible single regional seed locations, and the maximum R, denoted as R_{max} here, for each is recorded. **4)** A histogram of R_{max} for all 86 brain regions serving as seed.

The steps leading up to NDM model construction are illustrated in Figure 4.1. To evaluate predictive power of the NDM, the correlation between simulated and observed atrophy was plotted over a wide array of model time units, giving what we call the R(t) curve (Figure 4.1.3,). The time unit with the highest correlation coefficient was selected as reflective of model performance. All analysis was performed in MATLAB.

Results

Atrophy patterns by disease stage

First, we illustrate that the regional atrophy patterns of the Track-HD subjects measured by our pipeline across the four disease severity (preHD-A, preHD-B, HD-1, HD-2) in a cross-sectional design reflects classic patterning of HD (Figure 4.2). Specifically, the earliest pre-disease subjects (preHD-A) show significant striatal atrophy in relation to the rest of the brain. Atrophy worsens with disease severity, ultimately reaching a state of global brain degeneration in HD-2 subjects. Throughout all stages, the striatum remains the region with the most atrophy. Other significant areas exhibiting atrophy are in the occipital cortex, but only in advanced subjects (HD-1 and HD-2). Regional atrophy remains bilateral in all groups.

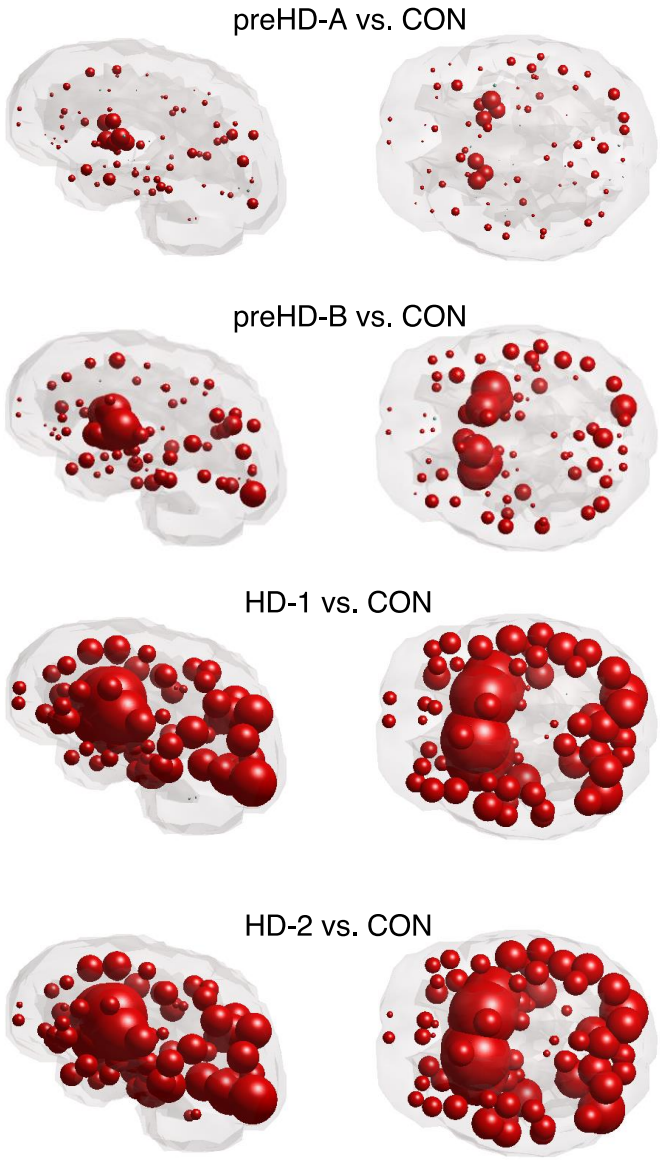

Figure 4.2. HD volumetrics. Glass brains displaying differences in cortical thickness and subcortical volumes in HD vs. CON. Red denotes atrophy in HD patients compared to age-matched, gender-matched controls. Nodes across all four stages are drawn to the same proportion.

Bivariate associations between regional atrophy and healthy gene expression

To test the hypothesis that innate molecular factors are responsible for the observed regional patterns of HD atrophy, we utilize post mortem microarray data from 6 healthy subjects published by the Allen Brain Institute (Oh et al., 2014). We examine correlations between regional expression of selected genes and regional group-level atrophy. We observe no correlation between HTT expression and atrophy at any stage of HD (Figure 4.3A1-2). Hence, we examine the relationship between atrophy and gene expression of 12 additional highly implicated genes in HD. We observed that PPAR has a significant positive correlation with pathology at the latest stage of HD (r=0.37, p=4.51e-04) (Figure 4.3B1-2). This correlation appears to be related to disease severity, as there is no correlation in the earliest stage of pre-HD (r=0.01, p=NS). Similarly, we observe a correlation in DRD2 expression that appears to be severity-related. DRD2 has a significant correlation with pre-HDA atrophy (r=0.37, p=5.45e-04), that increases at HD-2 (r=0.54, p=8.31e-08) (Figure 4.3C1-2). For a full list of observed genes and p-values, see Table 4.2.

To probe the collective effect of the most highly implicated genes in HD, we perform principal components analysis (PCA) on gene expression of all 12 genes of interest. Similar to PPAR and DRD2, the first principal component of gene expression appears to be pathology related, as the relationship increases in the later stages of the disease (preHD-A: r=0.42, p=5.30e-05 and HD-2: r=0.65, p=1.24e-11) (Figure 4.3D).

HTT production followed by network spread does not predict HD atrophy

Subsequently, we test the hypothesis that a network spread model initiated by HTT gene expression, will successfully recapitulate HD topography. Our group's previously published NDM is used to model network spread from baseline HTT gene expression patterns. Atrophy data from subjects in HD-2 was utilized as the model's observed end state to allow for maximal disease-related effect size. The NDM was evaluated on a healthy structural network, under the assumption that the WM network serves as a conduit for pathology and does not undergo significant degeneration itself.

With HTT expression pattern as the vector x_0 in the NDM equation, we correlated the NDM model prediction vector x(t) at all model times t against HD-2 atrophy vector. The model appears to give negative Pearson's R, implying that a network spread process seeded with HTT expression would not explain HD atrophy at any model time t. This suggests that baseline HTT patterns do not significantly mediate network-based spread in HD (Figure 4.3A3).

Although PPAR, DRD2 and PCA #1 had moderately high correlation with atrophy as described above, we saw virtually no evidence that subsequent NDM-based network spread would give better fit with HD-2 atrophy. Diffusing PPAR from its baseline state does not offer any improvement over the baseline correlation (Figure 4.3B3), with correlation curve being strictly monotonically decreasing from a high value at t=0. Similarly, DRD2 and PCA #1 have high correlation values at t=0, and further network diffusion gives only a miniscule improvement (<0.007) (Figure 4.3C3, Figure 4.3D3). These results suggest that while regional gene expression may be related to pathology production associated with regional atrophy, network

models of trans-synaptic spread rooted in gene expression do not recapitulate HD topography.

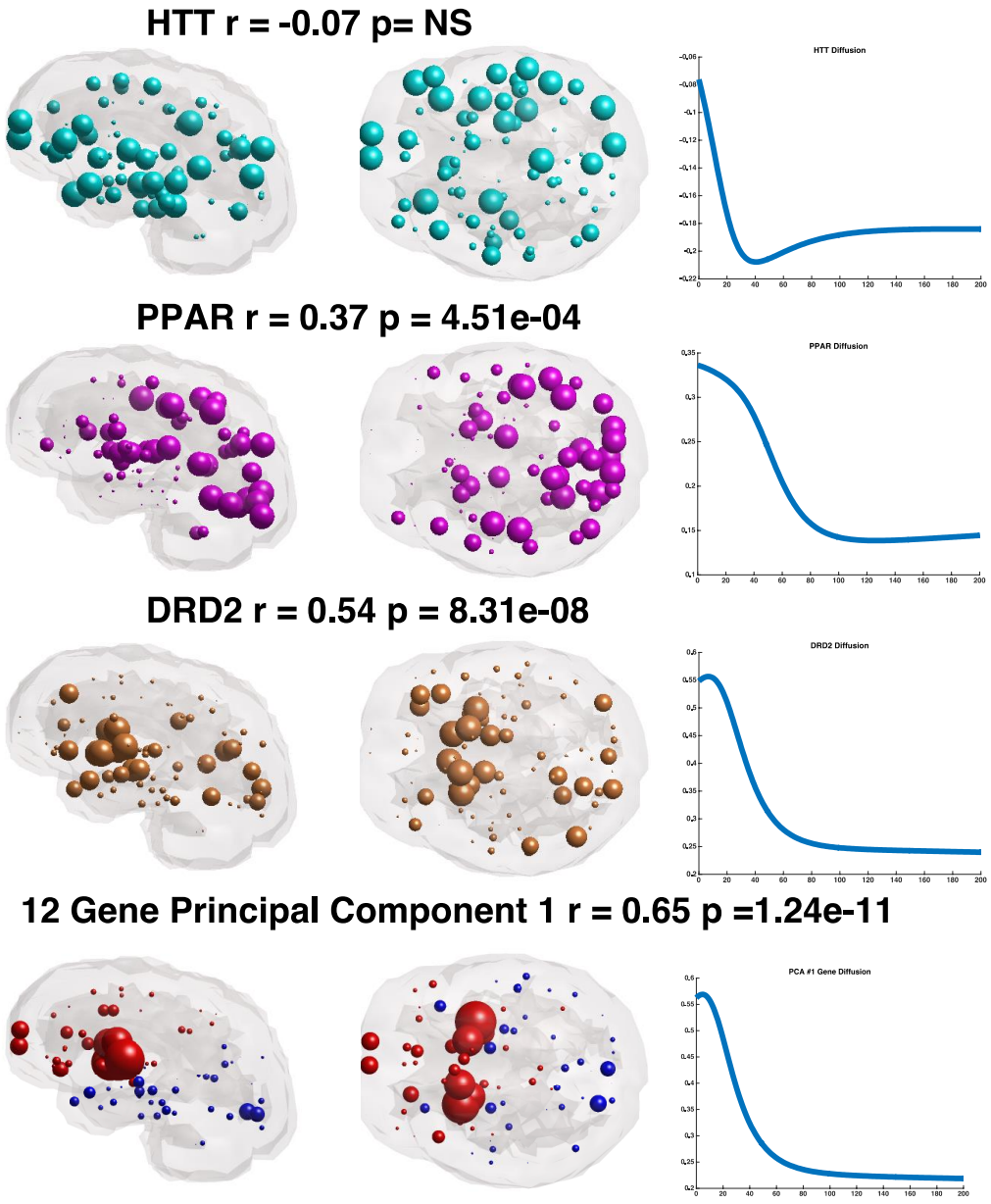

Figure 4.3. Gene diffusion. A, B, C, D1-2) Glass brains showing gene expression of post mortem healthy human brains from the Allen Brain Institute. Correlation coefficients and p-values depict the association between healthy gene expression and HD atrophy at HD-2. **A-D3)** Graphs of NDM accuracy over time, using healthy gene expression as the baseline state on a healthy structural network.

Table 4.2. Genetic correlations to atrophy. Correlations between nodal atrophy and gene expression in the latest (HD-2) and earliest (preHD-A) stage of HD.

	Correlation to HD-2 Atrophy		Correlation to preHD-A Atrophy	
Gene	r value	p value	r value	p value
HTT	-0.07	0.48	0.07	0.52
PPAR	0.37	4.51E-04 *	0.01	0.32
BDNF	-0.42	4.91E-05 *	-0.10	0.35
DRD2	0.54	8.31E-08 *	0.37	5.45E-04 *
GRIN2A	-0.18	0.10	-0.19	0.09
GRIN2B	-0.04	0.69	0.13	0.23
GRIN3A	-0.47	5.26E-06 *	-0.16	0.12
HAP1	0.10	0.38	0.09	0.39
PARK7	-0.27	0.01 *	-0.11	0.28
SLC6A4	0.10	0.34	0.05	0.64
SLC18A2	0.11	0.30	0.12	0.28
TBP	-0.28	0.008 *	-0.28	0.10
PCA #1	.65	1.24E-11 *	.42	5.30E-05 *

* denotes significance

Connectivity-based network spread from a single seed region

Distance hypotheses of neurodegeneration postulate that distance between infected nodes mediates pathology spread. Similarly, activity-dependent models hypothesize neurons that fire together in distinct regions are integral to trans-synaptic disease spread. Other models premise structural connectivity mediates the travel of toxic proteins across the brain (Brettschneider et al., 2015). Thus, we sought to empirically test if distance, functional or structural connectivity-based network models best recapitulate pathology spread in human subjects living with HD. This did not require us to develop different NDM models; the same NDM equation was applied to different adjacency matrices. A DTI-based connectivity matrix was used to test structural connectivity hypotheses, a Euclidean distance between all region-pairs to test distance hypotheses, and a resting state functional connectivity matrix to test activity-dependent hypotheses.

Since the initial seed configuration of the baseline patterns of HD pathology (x_0) is unknown, we empirically tested all seeds, separately, for all possible seed locations. For each model run, we simulated pathology spread from a single brain region, and recorded the maximum correlation coefficient (Pearson's R) between the simulated NDM vector and the empirical HD atrophy vector over a wide range of model time. We hypothesized that the best seed location will give the highest Pearson's R.

Results from empirically testing all three models from all seeds in the brain are illustrated in Figure 4.3. The R(t) curves corresponding to NDM model accuracy over time are shown in the top row (Figure 4.4A1-3). Each curve corresponds to a single site acting as a seed for NDM. Across all three models, the highest correlations are seen in striatal seeds (shown in bold red) for all thee adjacency models. Histograms of the maximum R for all seed locations are shown in Figure 4.4B1-3. Across all three models, we observe striatum is the most likely place of pathology origin, as it is the seed yielding the highest correlation to observed state atrophy. Specifically, we identify three regions of the striatum: Caudate, Putamen and Nucleus Accumbens. Moreover, these data show that both structural and functional connectivity serve as equally good substrates for network diffusion, whereas Euclidean distance does not. There is no evidence of network diffusion in the distance-based model, as maximum correlation achieved by model stimulation is less than a .01 improvement from baseline.

Figure 4.4C1-3 lends further support to NDM results, as we observe there is no relationship between regional distance from the striatum and atrophy ($r=-0.09$, $p=NS$) nor between functional connectivity to the striatum and atrophy ($r=0.11$, $p=NS$). However, we observe a significant relationship

between a region's structural connectivity to the striatum and its HD atrophy ($r=0.24$ $p=0.03$). Taken together, these data show striatal-seeding on a structural connectivity-based network model best recapitulates HD spread in vivo and suggest structural connectivity to the striatum may be implicated in trans-synaptic pathology spread in HD.

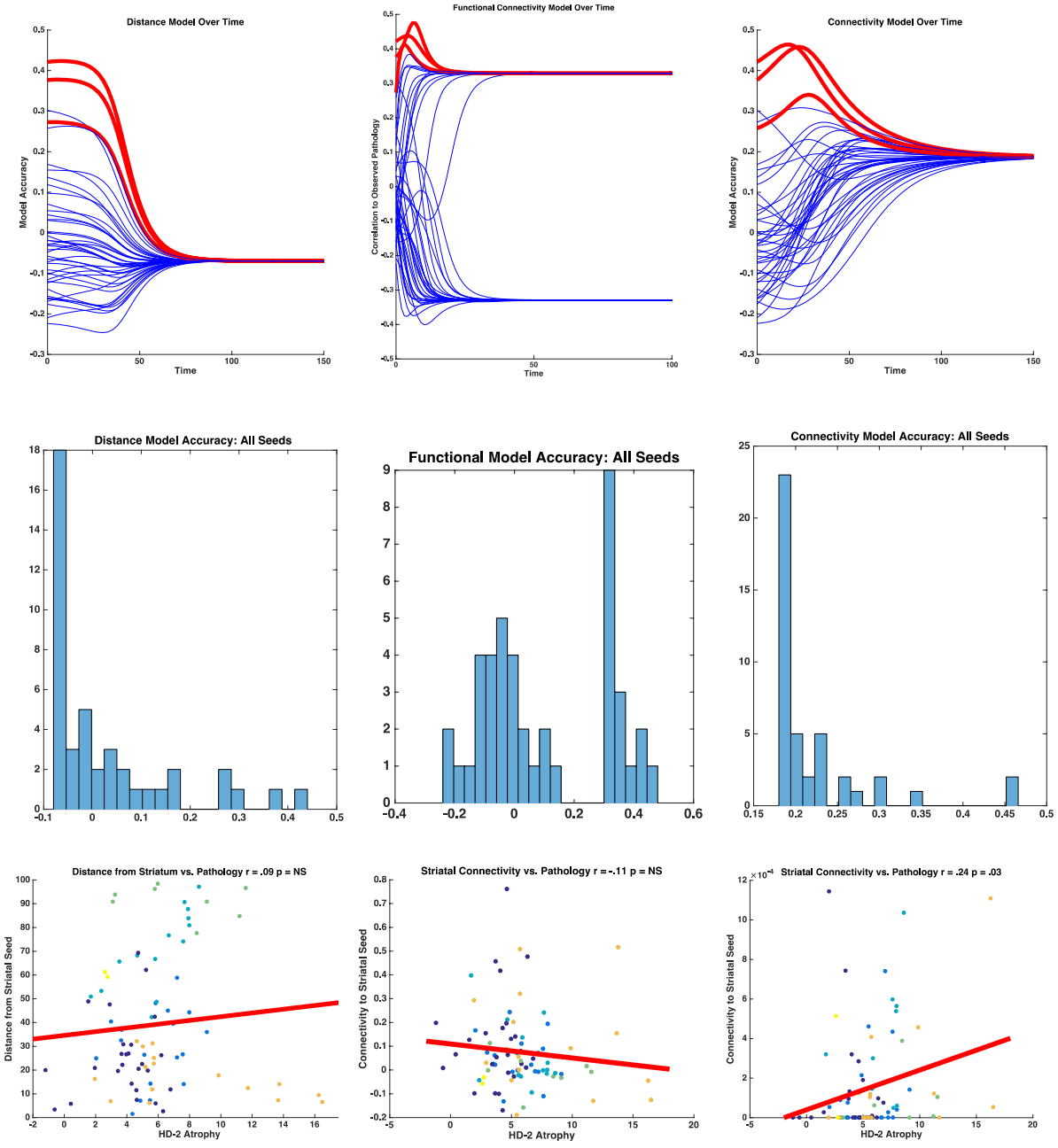

Figure 4.4. Distance, functional and structural NDM. Evaluating distance, activity-dependent and structural connectivity models of disease spread in HD. **A1-3)** Model accuracy over time of the model being simulated separately from each seed in the brain. **B1-3)** Histograms of the highest accuracy achieved by each seed. **C1-3)** Association between the model characteristic and regional pathology.

Directional network diffusion

A limitation of the NDM approach is that it is based on bidirectional DTI connectivity networks, which assumes connections are the same in both direction. This could limit NDM predictive ability, because trans-synaptic transmission may have a distinct directional bias, such that misfolded protein species may follow anterograde transport or signaling pathways. This is especially true in subcortical and striatal connections, which are known to be highly directional in comparison to corticocortical connections.

Thus, we hypothesized a directional (anterograde) process of spread along a structural connectivity network will further improve model performance. We use a directional human connectome obtained from blending non-directional human DTI and directional viral tracing connectomes of the mouse (see Methods).

We observe the directional structural connectome greatly improves model performance compared to the original, non-directional structural connectome. Similar to Figure 4.4, the striatum is again the most likely source of pathology origin (Figure 4.5A). Unlike the non-directional case, network diffusion does not dissipate into non-predictive patterns with low R. Instead, they seem to settle into highly predictive patterns with high R at large model times t, suggesting presence of a stable network attractor, a hypothesis that this will be interrogated in more detail below.

Figure 4.5B-C illustrate model accuracy over time and improvement over the baseline state when anterograde pathology diffusion is simulated from striatal seeds. The Nucleus Accumbens is suggested as the most likely origin of pathology. Further supporting the NDM results, Figure 4.5D shows a

significant relationship between anterograde connectivity to the Nucleus Accumbens and nodal degeneration ($r=0.66$, $p=7.38e-12$).

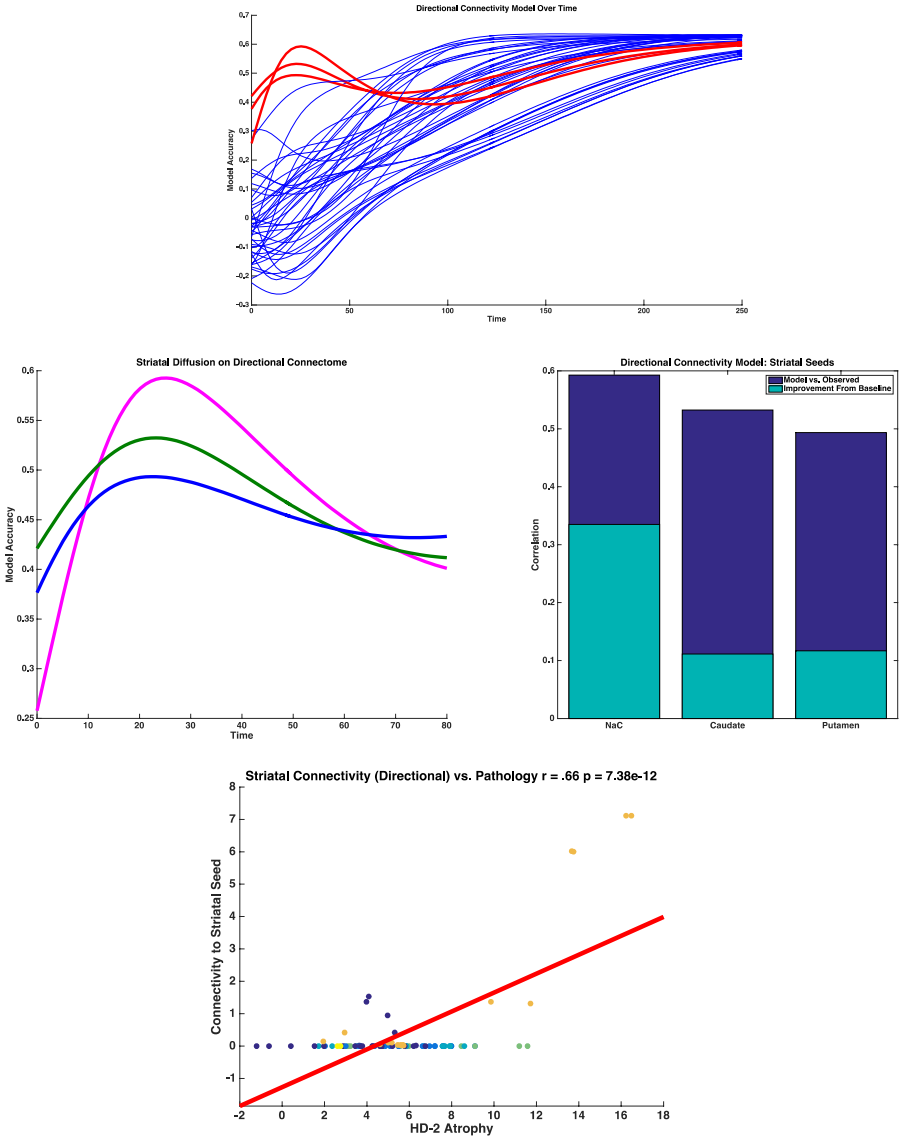

Figure 4.5. Striatal directional NDM. Accuracy of the directional, structural NDM in predicting HD disease spread when pathology is simulated from each of the striatal seeds. **A)** Model accuracy over time of all seeds. **B)** Zooming in on diffusion of striatal seeds over time. **C)** Ultimate model accuracy achieved (highest correlation) in blue and in teal, the improvement the model offers compared to just using the baseline atrophy to predict. **D)** Correlation between local degeneration and striatal connectivity.

Having established the striatum as the best seed from which to simulate pathology spread in all the models, we compiled model performance from the striatum across select models (Figure 4.6.) However, it remains unclear if the striatum performs as the best seed due to high baseline regional atrophy or characteristics of the tested models such as distance, functional connectivity or structural connectivity. To elucidate a possible confounding effect of striatal atrophy, we seed the NDM at the striatum, but randomly scramble the directional structural connectome as a negative control. We show that when the directional structural connectome is scrambled, the model does not perform. No diffusion occurs as the model simply falls to steady state (Figure 4.6A-B).

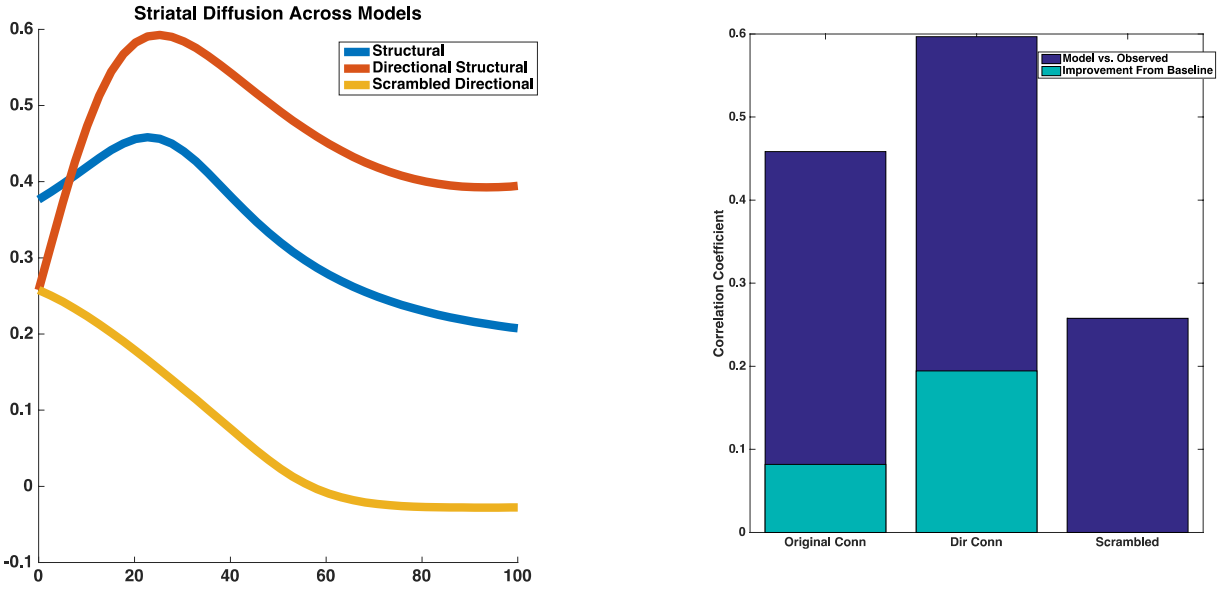

Figure 4.6. Scrambled directional NDM. Performance across several models including the striatal seeded directional structural connectome, original structural connectome, scrambled directional connectome. **A**) Accuracy as various models diffuse over time. **B)** Highest accuracy attained for each model and its improvement from baseline.

Seeded directional NDM of individual subjects

All results so far were obtained by correlating NDM prediction against group atrophy patterns. In order to assess inter-subject variability and consistency of our results, we examined NDM model performance at individual subjects basis. The maximum correlation of each subject against the anterograde NDM model, for all possible seed regions, was obtained, and the seed that gave the highest R value was recorded. The distribution of best seeds in all individuals is shown in the histograms of Figure 4.7, stratified by lobe. The striatum is again the most frequent origin of pathology in individual subjects. The parietal lobe was second highest, third was subcortical regions and we also observed 2 occipital regions. No frontal regions were identified as pathology seeds in any subjects (Figure 4.7). A majority of subjects show a maximum model accuracy of r = 0.50 or more, and the highest correlation we observed was r = 0.84. For a full list of individual subject data, see Table 4.3.

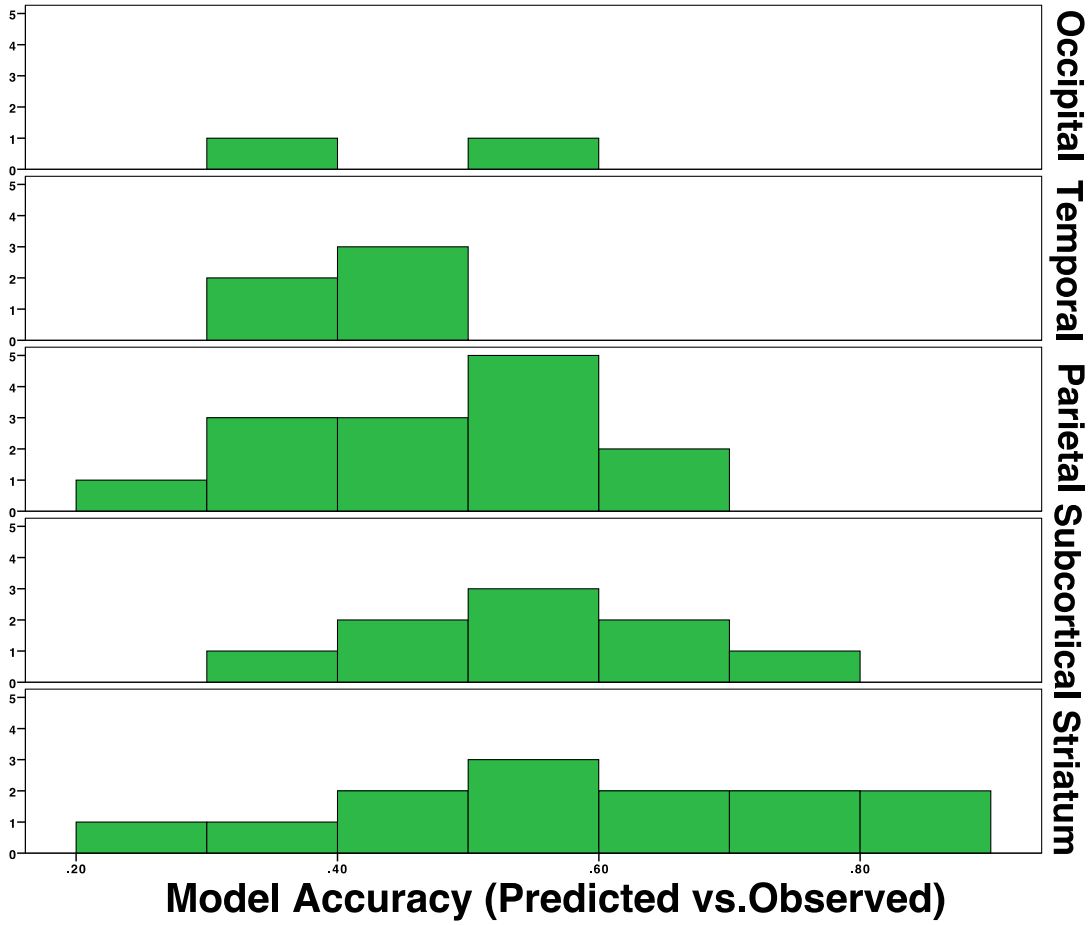

Figure 4.7. **Individual directional NDM.** Histograms illustrating the most likely place of disease origin and the models best predictive accuracy when the directional structural NDM is simulated on subject-specific atrophy patterns in HD-2.

Table 4.3. Individual subject seeds. Best seeds for individual subjects using the directional anterograde structural connectivity NDM.

R max	T max	Best Seed		R max	T max	Best Seed
0.86	30.30	NaC		0.52	65.66	Amygdala
0.80	32.83	NaC		0.50	250.00	Supramarginal
0.78	32.83	NaC		0.47	143.94	Superior Parietal
0.76	40.40	NaC		0.47	27.78	NaC
0.76	85.86	Thalamus		0.46	22.73	Caudate
0.67	30.30	NaC		0.46	30.30	Thalamus
0.65	22.73	Superior Parietal		0.44	121.21	Ventral DC
0.64	35.35	NaC		0.42	78.28	Entorhinal
0.63	250.00	Postcentral		0.42	35.35	Superior Parietal
0.61	88.38	Amygdala		0.41	179.29	Temporal Pole
0.60	90.91	Thalamus		0.40	15.15	Inferior Temporal
0.59	98.48	Ventral DC		0.38	55.56	Post Central
0.58	25.25	NaC		0.37	27.78	Inferior Parietal
0.57	27.78	NaC		0.36	103.54	Transv. Temporal
0.57	90.91	Supramarginal		0.34	35.35	Cuneus
0.57	106.06	Amygdala		0.34	20.20	Inferior Temporal
0.55	32.83	Inferior Parietal		0.33	15.15	NaC
0.54	73.23	Supramarginal		0.32	20.20	Insula
0.54	27.78	NaC		0.31	20.20	Inf. Parietal
0.54	50.51	Postcentral		0.30	25.25	Superior Parietal
0.53	78.28	Postcentral		0.27	20.20	NaC
0.53	136.36	Precuneus				

Non-seeded anterograde NDM

Although results thus far support a key role for anterograde network transmission in HD patterning, they require the extraneous assumption of a originating or seeding site. There is little evidence in the literature indicating that the striatum and specifically the nucleus accumbens has an etiologically or mechanistically privileged place in HD pathophysiology. In comparison, our non-network analyses involving the role of gene expression do not require such extraneous assumptions.

Therefore, we sought to address whether focal seeding was a necessary condition for anterograde transmission in HD, or whether diffuse or random seeding would perform just as well. An indication that this might be so was already observed in Figure 4.5A, where almost all seed locations produced R(t) curves that eventually settled into a steady state with a high R value. As mentioned, this is indicative of a potential network attractor. Using graph theory, we had previously demonstrated that any network diffusion process will eventually be dominated by the most persistent eigenmodes of the network, specifically the smallest eigenmodes of the graph Laplacian (Raj et al. 2012).

Our group's prior work with the NDM shows eigenmodes are epicenters from which disease vulnerability can be predicted and future pathology patterns can be projected. Therefore, we hypothesized that the anterograde network Laplacian's primary eigenmode (whose eigenvalue is zero) would resemble the topography of regional HD atrophy. The resulting glass brain rendering of the eigenmode is shown in Figure 4.8A1. Intriguingly, the eigenmode's spatial pattern is highly suggestive of HD topography, with high values in the striatum and cuneus. There is a significant relationship between

HD atrophy pattern and the first eigenmode that appears to be related to disease severity. In pre-HD-A this relationship is significant (r=0.53 p=1.96e-07) and the relationship strengthens as the highest disease severity group, HD-2 (r=0.64 p=1.98e-11) (Figure 4.8A1-2). This pattern is echoed, but to a much weaker extent in functional networks (Figure 4.8B1-3).

Mathematically, the first eigenmode is a linear network attractor, a state into which any anterogradely diffusing pathology will increasingly accumulate, even if pathology seeding was random, diffuse or uniform. The above result therefore supports the idea that the prominent sites of HD atrophy may not be imitating sites, but rather the sites at which early pathology first accumulates beyond some threshold. Subsequent network transmission will continue to exhibit similar topography, as shown earlier in Figure 4.5A on anterograde NDM from striatal seeding.

To confirm accumulation of anterogradely diffusing pathology from non-focal seeding predicts HD regional atrophy, we perform simulations of anterograde NDM from three diffuse seeding processes on the directional structural connectome: 1) Seeding in proportion to HTT regional expression; 2) uniform seeding in every location; 3) Seeding in proportion to the 12- gene PCA regional gene expression. In each case, the NDM model was evaluated at a range of model times $t>0$, and the corresponding $R(t)$ curve was plotted.

These results, contained in Figure 4.9, show that although there are subtle differences in the intermediate time behavior of each seeding strategy, the eventual, steady state R value was very similar ($r = 0.59$, $p < 1e\text{-}10$). This result supports the notion that a focal or specific regional seed is not required for HD pathology, and that most kinds of diffuse seeding patterns will

eventually result in observed HD atrophy pattern, purely as a result of anterograde network diffusion.

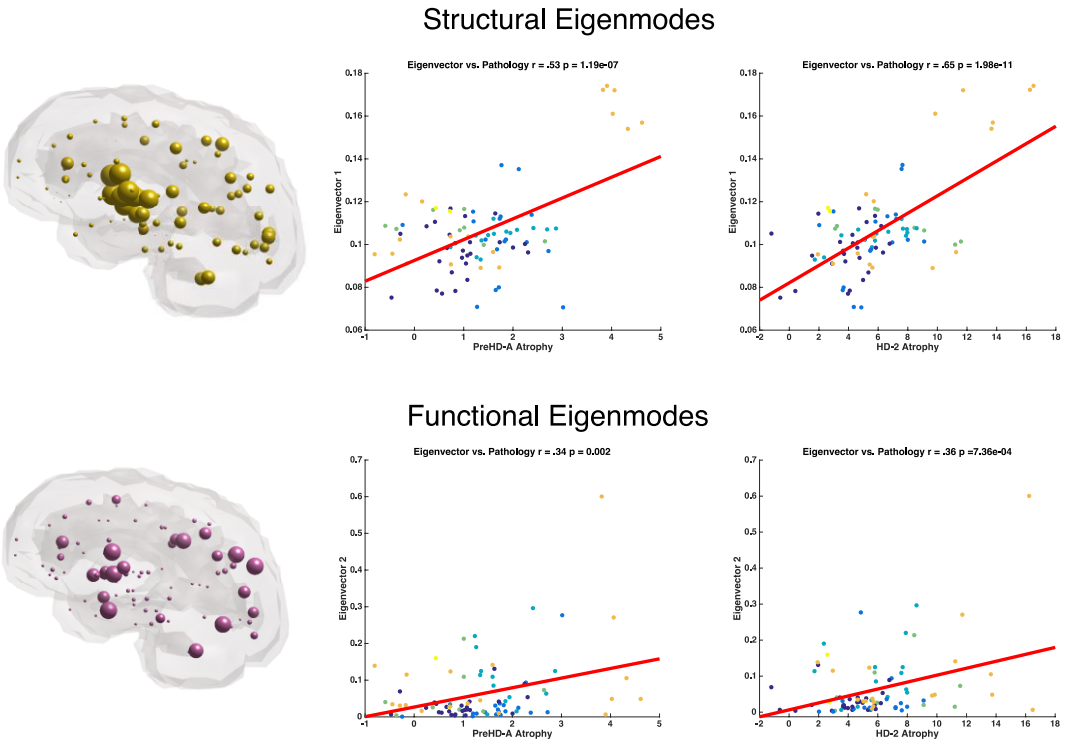

Figure 4.8. Structural and functional eigenmodes. A1, B1) Structural and functional eigenmodes, respectively. **A2, B2)** Relationship between local degeneration and eigenmode of the earliest pre Huntington's stage. **A3, B3)** Relationship between local degeneration and eigenmode at the latest stage of the disease.

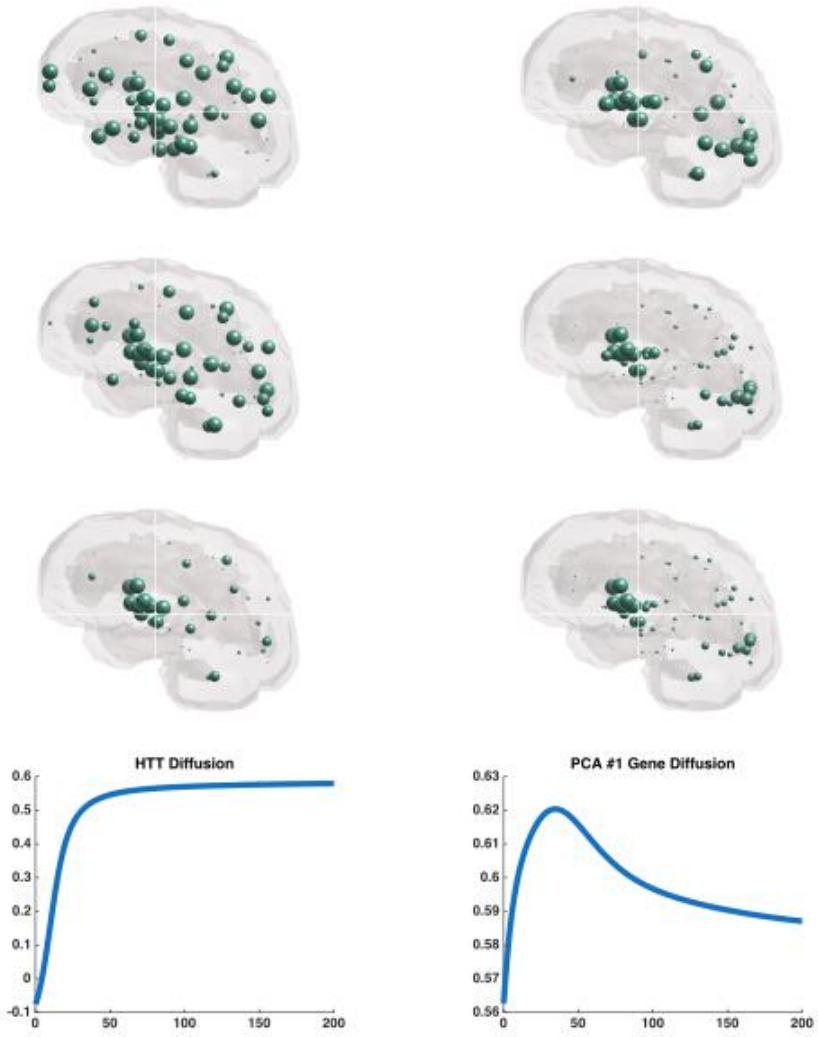

Figure 4.9. Anterograde NDM glass brains. Anterograde network diffusion starting from HTT (left) and gene PCA (right) seeding. Both seeding strategies give similar results, each undergoing anterograde transmission and accumulating increasingly in a striatal-dominant pattern governed by the first network Laplacian eigenmode. Increasing model time t is depicted from top to bottom. The bottom row shows the corresponding R(t) curves, indicating that each seeded pattern settles into a steady state pattern around r = 0.59.

Discussion

The current study applies network modeling to a rare disease as the first to systematically test hypotheses of disease spread in human subjects living with HD. Other neurodegenerative diseases like FTD, AD and ALS syndromes have been well-studied from a human brain network perspective, and have received more attention than equally important and related disorders such as HD (Seeley, 2017), due to a lack of available human data on this rare disorder, which affects approximately 3 to 7 in 100,000 individuals in western populations (Harper, 1992). The present analysis takes advantage of an unprecedented dataset of 231 subjects with HD from Track-HD, a multinational prospective observation study of HD. Our key results are described below.

Observed Pathology Across HD Stages

Across 4 stages of HD severity, the striatum suffers the most atrophy, followed by generally diffuse moderate atrophy everywhere – even in subjects who are more than 10.8 years before disease onset. These are well established findings (Tabrizi et al., 2013, 2011, 2009). The occipital cortex is the only other area showing enhanced atrophy, but only in advanced subjects. As the disease progresses, the brain ultimately reaches a state of global degeneration, with the striatum the most significant (Figure 4.2). Our replication of this result converges with characteristic features of HD as classic Human neuroimaging and post-mortem report significant global brain atrophy, with the striatum as the region of most atrophy (de la Monte et al., 1988; Kuhl et al., 1982; Vonsattel et al., 1985). These data point to the lack of regional discrimination in HD, except for the striatum.

Regional gene expression is a moderate to weak predictor of HD topography

We sought to understand whether innate regional expression of HD-implicated genes can predict above described HD topography. WT HTT has been illustrated to generate oligomers by itself and oligomerize with mutant HTT, causing additional aggregation and apoptosis (Herrera et al., 2011). Surprisingly, we found that HTT expression in the healthy human brain has almost no association with the regional pattern of atrophy seen in HD patients at any stage (Figure 4.2A1-2). This finding is at odds with the overwhelming support of the key role of mutant HTT in HD pathogenesis (Bradford et al., 2009; Chou et al., 2008; Herrera et al., 2011; Lee et al., 2001; Ren et al., 2009; Tan et al., 2015).

Next, we hypothesized that while there may not be direct relationship between HTT expression and local degeneration, perhaps mutant HTT had downstream effects on other genes. To test this hypothesis, we evaluated the relationship between HD atrophy and gene expression of 12 additional highly implicated genes in HD. PPAR had a significant positive correlation atrophy at the latest stage of HD ($r = 0.37$, $p=4.51e-04$) (Figure 4.3B1-2). This correlation appears to be related to disease severity, as there is no correlation in the earliest stage of pre-HD ($r = 0.01$ p=NS). We observed a correlation in DRD2 expression that appears to be disease-severity-related. DRD2 has a significant correlation with pre-HDA atrophy ($r = 0.37$, $p=5.45e-04$), that increases at HD-2 ($r = 0.54$, $p=8.31e-08$) (Figure 4.3C1-2). Disease-severity-related correlations of PPAR, DRD2, BDNF and GRIN3A support prior evidence implicating abnormality of these genes in metabolism, dopamine vulnerability,

neuronal growth, and excitatory synapse signaling and their roles in HD (Duan et al., 2003; Marco et al., 2013; Quintanilla et al., 2008; Zuccato et al., 2005).

To probe the collective effect of the most highly implicated genes in HD, we performed principal components analysis (PCA) on gene expression of all 12 genes. Similar to PPAR and DRD2, the first principal component of gene expression appears to be pathology related, as the relationship increases in more severe disease (preHD-A: r=0.42, p=5.30e-05 and HD-2: r=0.65, p=1.24e-11) (Figure 4.3D). Interestingly, associated genes reflect a predominantly striatum pattern.

A visual inspection shows that all significant genes and their combinations described above in fact reflect a strong dominance of the striatum (Figure 4.3). DRD2 codes for dopamine receptors which are predominantly found in striatal structures, and PPAR and BDNF are also highly expressed there, and this pattern also continues in PCA of these genes. Therefore, we considered whether the above gene results are simply a reflection of the fact that the striatum is selectively vulnerable to HD atrophy, and that the implicated genes simply reflect that, with no other mechanistic basis. This notion is strengthened by the fact that HTT, which is known to be the etiological culprit, does not in fact show any resemblance to HD atrophy patterns.

HTT aggregation and propagation in HD does not recapitulate HD atrophy

Mutated HTT is a pathogenic protein linked to network degeneration via trans-synaptic spread in a manner similar to pathogenic proteins implicated in other neurodegenerative disorders, such as tau (AD), amyloid beta (AD), alpha-synuclein (PD) and SOD1 (ALS) (Nagai et al., 2007; Schwarz et al., 2016; Spillantini et al., 1998). Current hypotheses of pathology spread in neurodegeneration are centered on the prion hypothesis, which posits that toxic proteins spread trans-synaptically along neuronal pathways in specific patterns. This hypothesis has been particularly well-studied in tauopathies such as AD (Jucker and Walker, 2013). Converging neuroimaging, post-mortem and mouse injection site studies all point to mutated tau aggregating and spreading stereotypically throughout the neural network in AD (Braak and Braak, 1996; Clavaguera et al., 2009; Schwarz et al., 2016).

There is mounting evidence that mutant aggregated HTT is capable of prion-like spread between cells. Wildtype HTT can generate oligomers by itself and oligomerize with mutant HTT, causing additional aggregation and apoptosis (Herrera et al., 2011). Mutated HTT has been reported to diffuse into extracellular space and inside adjacent cells to act as seeds for further aggregation and neurotoxicity (Ren et al., 2009). Glial cells are another purported mechanism of mutant HTT spread in HD, as glial cells can transport mutant HTT without undergoing apoptosis themselves, but still cause neuronal death (Bradford et al., 2009; Chou et al., 2008). A non-cell anonymous, synaptic vesicle mediated transport of pathology in *ex vivo* and *in vivo* models of HD was demonstrated in (Pecho-Vrieseling et al., 2014).

Hence, we hypothesized that network spread would recapitulate HD topography when seeded with the baseline pattern of regional HTT gene expression. To our knowledge, such a network model of disease propagation has not been reported before. To achieve this, we utilized a computational Network Diffusion model (NDM) which we had previously proposed as a means of modeling tau propagation in the AD brain (Raj et al., 2012a). As in previous work, the NDM used here was evaluated on a healthy structural network, under the assumption that the WM network serves as a conduit for pathology and does not undergo significant degeneration itself.

We found that disease spread simulated from baseline HTT patterns does not successfully recapitulate HD progression (Figure 4.3A3). It is of course possible that HTT aggregation may not necessarily mimic baseline wild type HTT expression. Prior work shows that medium spiny neurons in the striatum contain few HTT nuclear aggregates, but nonetheless undergo the most extensive damage, experiencing significant apoptosis (Gutekunst et al., 1999). However, in our analysis, we expect that over the whole brain, wild type HTT expression should have regional association with atrophy. Our results suggest that neither HTT regional expression by itself, nor its subsequent network transmission, is capable of recapitulating HD topography. This is surprising in view of the key role of mutant HTT in HD pathogenesis.

Evaluating associated genes as a starting point for network transmission

We also simulated the NDM initiated from 12 of the implicated gene's expression patterns, but found no evidence that post-production network spread via NDM contributes to HD atrophy patterns. Neither PPAR nor DRD2, nor PCA exhibited evidence of diffusion through the structural network, as model performance improvement is less than .01 from baseline (Figure 4.3). BDNF and GRIN3A were also significantly correlated with atrophy, but did not demonstrate diffusion. Collectively these data suggest that while certain genes may play a role in mediating tissue vulnerability to disease spread, network models of trans-synaptic spread rooted in gene expression do not recapitulate HD topography.

Focal seeding followed by network spread recapitulates HD atrophy

Since network spread following baseline gene expression did not recapitulate HD atrophy, we tested whether network spread from focal seed sites would perform better. Although trans-synaptic transmission appears the most likely candidate, the exact mode of transmission is unknown. Hence to minimize model bias we simulated spread between regions in a number of ways: spread mediated by inter-regional distance; spread mediated by functional connectivity between brain regions; and spread mediated by WM fiber connectivity. We found that for each model, striatal seeding, specifically Caudate, Putamen and Nucleus Accumbens, gave the best results (Figure 4.4). Converging post mortem and neuroimaging studies showing the striatum is the most likely region of pathology origin in HD (de la Monte et al., 1988; Kuhl et al., 1982; Vonsattel et al., 1985).

No evidence of distance-based spread

Interestingly, the Euclidean distance-based model does not give any evidence of spreading (since its R(t) curve in Figure 4.4 is monotonically decreasing). There was also no relationship between regional distance from the striatum and regional atrophy (r=-0.09, p=NS). These results appear to rule out a primarily distance-based model of spread – an important finding since conventional understanding of cell-cell transmission involves the uptake of pathological proteins via endocytosis and exocytosis (Brettschneider et al., 2015) into extracellular spaces where pathology must diffuse spatially via the extracellular diffusion of transcripts, proteins, growth factors and other cues.

Absence of a distance-based effect in our results suggests that pathology spread must require long-range fiber projections rather than extracellular diffusion. In this, HD resembles Alzheimer's and Parkinson's disease, which too do not show strong evidence of distance-based spread. However, it is at odds with prior *ex vivo* cell culture work done in ALS, which shows that pathogenic proteins can diffuse into extracellular space without synaptic contact (Freundt et al., 2012).

Spread along structural versus functional connections

Both structural and functional connectivity serve as equally good substrates for network diffusion, as their NDM models seeded at striatal regions achieve both high ultimate model performance and model improvement from baseline. Whether neurodegenerative pathology patterns are mediated by structural or functional connections is controversial (Brettschneider et al., 2015; Jones et al., 2016; Raj et al., 2012; Zhou et al., 2012). Although misfolded proteins are known to spread along long range fiber projections (Jucker and Walker, 2013), it is also plausible that pathology

follows network dysfunction or cascading failures in brain activity (Jones et al., 2016). Our NDM results do not favor either hypothesis over the other (4.4A).

However, we observe a significant relationship between a region's structural connectivity to the striatum and its HD atrophy (r=0.24 p=0.03) (Figure 4.4C), but did not find similar effect for functional connectivity to the striatum (r=0.11, p=NS). Given that functional and structural connectivity in themselves are highly correlated, the most economical interpretation of our results is that the structural network mediates disease spread in HD (Greicius et al., 2009; Honey et al., 2009). The apparent mediation by the functional network might be a secondary, perhaps epi-phenomenon, a consequence of underlying structural topology. However, we think this notion warrants further investigation, as there could be additional underlying factors mediating functional network diffusion.

There is certainly mounting evidence from related cell culture and mouse studies that support our assertion that the structural network mediates pathology spread in HD. For example, both in-vitro and in-vivo transmission of pathology only occurred when a functioning synaptic network was in place (Gutekunst et al., 1999). Converging work in AD supports models of trans-synaptic pathology spread mediated by structural connectivity. For example, classic studies identify the Locus Coereulus (LC) as the location where tau pathology is initially identified. However, the entorhinal region (EC), which is anatomically distant, but receives direct axonal projections from the LC, is the second region to develop tau pathology (Braak and Braak, 1996) (Pearson et al., 1985). Mouse studies using immunohistochemistry demonstrated relocation of tau from axons between the two regions to dendrites in the EC to lend further support to the notion of disease spread mediated by anatomical

connectivity (Liu et al., 2012). Overall, empirical data does not give overwhelming support to either cell autonomous or non-autonomous hypotheses explored so far in the investigation.

Directional structural connectivity model

Having identified structural connectivity as the most likely mechanism of transynaptic pathology spread in HD, we sought to further improve our model by adding directionality. Trans-synaptic transmission can have a distinct directional bias, such that misfolded protein species might follow anterograde transport or signaling pathways. This is especially true in subcortical and striatal connections, which are known to be highly directional in comparison to corticocortical connections. Although little work has been done in HD, tau pathology in AD differentiates between efferent and afferent connections (Iba et al., 2015).

Hence, we tested the hypothesis that directional (specifically anterograde) process of spread along structural connectivity network will further improve model performance. The directional NDM results are shown in Figure 4.5. Overall, use of the directional structural connectome greatly improves model performance. As before, the striatum is again the most likely source of pathology origin (Figure 4.5A), but unlike the non-directional case, directional network diffusion does not dissipate into non-predictive patterns with low R; instead they seem to settle into highly predictive patterns with high R at large model times t, suggesting presence of a stable network attractor.

The model performance is highly significant ($r=0.59$, $p < 1e\text{-}10$), especially in comparison with random network scrambling of the directional structural connectome (Figure 4.6), confirming that network organization is integral to disease spread in HD. The Nucleus Accumbens is the most likely

region of pathology origin, and a significant relationship exists between anterograde connectivity to the Nucleus Accumbens and regional atrophy (r=0.66, p=7.38e-12). These results are superior to almost all previous models we have tested so far, save for PCA gene expression.

These data are complemented by strong evidence for heterogeneity of seeding and pathology origin in individual subjects. Although the majority of subjects give the striatum as the most likely region of origin, several subjects show occipital, parietal and temporal regions as seeds. This data converges with the emerging notion, especially in FTD, that a single disorder may have diverse anatomical and clinical manifestations, and uncertainty surrounds which aspect of proteinopathy drives that protein to select its unique anatomy in an individual patient (Seeley, 2017).

Non-seeded anterograde NDM

Having established that directional structural connectivity is the network model that best recapitulates trans-synaptic HD progression, we sought to further elucidate the relationship between degeneration and intrinsic structural architecture. So far, the NDM model requires the extraneous assumption of an originating or seeding site. There is little evidence in the literature indicating that the striatum and specifically the Nucleus Accumbens has an etiologically or mechanistically privileged place in HD pathophysiology. Certainly, some of our gene expression results show moderate association with atrophy, but their striatal dominance is less a proof of striatal involvement than a tautology. The question remains: why is the striatum such a strong location for HD atrophy, even though HTT is not expressed especially strongly there, nor is there evidence of its network transmission to the striatum?

To address this, we sought to understand whether focal seeding was a necessary condition for anterograde transmission in HD, or whether diffuse or random seeding would perform just as well. We hypothesized the existence of intrinsic structural network epicenters or attractors, into which propagating HD pathology might accumulate. An indication that this might be so was already observed in the above directional NDM results (Figure 4.4A), where almost all seed locations produced R-t curves that eventually settled into a steady state with a high R value. As mentioned, this is indicative of a potential network attractor.

Using graph theory, previous work demonstrates that any (non-directional) network diffusion process will eventually be dominated by the most persistent eigenmodes of the network, specifically the smallest eigenmodes of the graph Laplacian (Raj et al. 2012). Furthermore, eigenmodes were shown to form an effective basis on which baseline neurodegenerative atrophy data can be projected for prediction of a subject's future atrophy.

Therefore, we hypothesized that the anterograde network Laplacian's primary eigenmode (whose eigenvalue is zero) would resemble the topography of regional HD atrophy. This eigenmode hypothesis is independent of any specific starting or seed site. Intriguingly, the eigenmode's spatial pattern was found to be strikingly similar to HD topography, with high values in the striatum and cuneus (Figure 4.8A). There was a significant relationship that appears to be related to disease severity. In pre-HD-A, this relationship is significant ($r=0.53$ $p=1.96e-07$) and the relationship strengthens as the highest disease severity group, HD-2 ($r=0.64$ $p=1.98e-11$) (Figure 4.8A1-2). This pattern is echoed, but to a much weaker extent in functional networks (Figure

4.8B1-3). To our knowledge, this is the first report of a directional human network eigenmode, and its link to anterograde pathology transmission.

As previously mentioned, the first anterograde eigenmode is a mathematically linear network attractor, a state into which any anterogradely diffusing pathology will increasingly accumulate, even if pathology seeding was random, diffuse or uniform. The above result therefore supports the idea that the prominent sites of HD atrophy may not be initiating sites, but rather the sites at which early pathology first accumulates beyond some threshold.

Subsequent network transmission will continue to exhibit similar topography, as shown earlier in Figure 4.4A on anterograde NDM from striatal seeding. Thus, network eigenmode presents a simple explanation of vulnerable “epicenters” whose healthy connectivity serve as a template for template-directed misfolding (Zhou et al., 2012). Eigenmodes anchor distinct networks and are hypothesized to give rise to different clinicoanatomical presentations in neurodegeneration (Seeley, 2017).

If this is so, then stereotyped progression in HD must imply stable primary eigenmode across individuals. Indeed, it was recently reported that the first few structural brain eigenmodes are stable across healthy subjects, and are relatively preserved even in diseases of extreme brain malformation such as agenesis of the corpus callosum (Wang et al., 2017).

Previous proposals involving network epicenters used resting state functional networks, which suggest that intrinsic topology of the functional network mediates template directed misfolding (Zhou et al., 2012). Our data somewhat replicate this in HD, as our functional eigenmodes also show a significant correlation with local degeneration in HD, which increases with disease progression (Figure 4.8B). However, this correlation is only about half

as strong as that of the structural eigenmode, which confirms our earlier conclusion that HD transmission is underpinned by structural rather than functional connectivity.

Network-based anterograde accumulation of pathology from diffuse seeding

In order to confirm that accumulation of anterogradely diffusing pathology from non-focal seeding does indeed predict HD regional atrophy, we performed simulations of anterograde NDM from three diffuse seeding processes: a) seeding in proportion to HTT regional expression; b) uniform seeding in every location; c) random seeding. The results, contained in Figure 4.9, show that although there are subtle differences in the intermediate time behavior of each seeding strategy, the eventual, steady state R value of around 0.59, as well as the spatial pattern, was very similar. The best result was obtained for seeding by PCA of all 12 HD-implicated genes, giving $r=0.62$, $p < 1e\text{-}10$. This result supports the notion that a focal or specific regional seed is not required for HD pathology, and that most kinds of diffuse seeding patterns will eventually result in observed HD atrophy pattern, purely as a result of anterograde network diffusion. In particular, HTT or gene PCA seeding of the anterograde NDM yields very strong correlations with atrophy, representing the closest match with empirical data contained in this paper.

Concluding remarks

Collectively, these data show that the intrinsic architecture of the structural network mediates disease spread in HD, most likely via a process of trans-synaptic transmission. The success of the anterograde network model suggests a simple process whereby local production of HTT starts off a

process of pathology accumulation, followed by anterograde network transmission, which due to the nature of the network eigenmode, increasingly accumulates in striatal and occipital areas. The apparent selective vulnerability and early seeding of HD pathology in these areas might be explained purely in these terms, without requiring a privileged status for any brain region.

Limitations

Several methodological considerations should be taken into account when interpreting the current study. The first are limitations of the NDM. The NDM is a first-order, linear, parsimonious model of diffusive spread that assumes that the structural connectivity network remains unchanged over the duration of the longitudinal analysis. Though this assumption DTI data for individual subjects was not available in the current study, previous cross-sectional analysis in a subset of the current cohort shows rich club organizational changes in comparison to controls (McColgan et al., 2015). However, connectivity between HD stages and longitudinal connectivity remains unassessed. Similarly, the NDM model may not be the best fit for a resting state functional connectivity network, as neuroimaging work suggests the functional network is impeded by the presence of pathogenic proteins (Filippini et al., 2009). Moreover, individual subject genetic repeat length, medication history and age of symptom onset was not available. These variables could have implications in the individual group wise analysis, when identifying each subject's seed region or determining individual rate of disease diffusion. Because this is the first study to empirically test multiple network models of pathology spread in HD, it will benefit from independent replication. Future work elucidating striatal vulnerability as well as the effect of repeat length on disease spread is necessary.

Aleman-Gomez, Y., 2006. IBASPM: toolbox for automatic parcellation of brain structures. 12th Annu. Meet. Organ. Hum.

Braak, H., Braak, E., 1996. Evolution of the neuropathology of Alzheimer's disease. Acta Neurol. Scand. Suppl. 165, 3–12.

Bradford, J., Shin, J.-Y., Roberts, M., Wang, C.-E., Li, X.-J., Li, S., 2009. Expression of mutant huntingtin in mouse brain astrocytes causes age-dependent neurological symptoms. Proc. Natl. Acad. Sci. U. S. A. 106, 22480–5. doi:10.1073/pnas.0911503106

Brettschneider, J., Tredici, K. Del, Lee, V., 2015. Spreading of pathology in neurodegenerative diseases: a focus on human studies. Nat. Rev.

Chou, S., Weng, J., Lai, H., Liao, F., Sun, S., 2008. Expanded-polyglutamine huntingtin protein suppresses the secretion and production of a chemokine (CCL5/RANTES) by astrocytes. J.

Clavaguera, F., Bolmont, T., Crowther, R.A., Abramowski, D., Frank, S., Probst, A., Fraser, G., Stalder, A.K., Beibel, M., Staufenbiel, M., Jucker, M., Goedert, M., Tolnay, M., 2009. Transmission and spreading of tauopathy in transgenic mouse brain. Nat. Cell Biol. 11, 909–913. doi:10.1038/ncb1901

de la Monte, S.M., Vonsattel, J.-P., Richardson, E.P., 1988. Morphometric Demonstration of Atrophic Changes in the Cerebral Cortex, White Matter, and Neostriatum in Huntington's Disease. J. Neuropathol. Exp. Neurol. 47, 516–525. doi:10.1097/00005072-198809000-00003

Duan, J., Wainwright, M.S., Comeron, J.M., Saitou, N., Sanders, A.R., Gelernter, J., Gejman, P. V., 2003. Synonymous mutations in the human dopamine receptor D2 (DRD2) affect mRNA stability and synthesis of the receptor. Hum. Mol. Genet. 12, 205–216. doi:10.1093/hmg/ddg055

Filippini, N., MacIntosh, B.J., Hough, M.G., Goodwin, G.M., Frisoni, G.B., Smith, S.M., Matthews, P.M., Beckmann, C.F., Mackay, C.E., 2009. Distinct patterns of brain activity in young carriers of the APOE-epsilon4 allele. Proc. Natl. Acad. Sci. U. S. A. 106, 7209–14. doi:10.1073/pnas.0811879106

Freer, R., Sormanni, P., Vecchi, G., Ciryam, P., Dobson, C.M., Vendruscolo, M., 2016. A protein homeostasis signature in healthy brains recapitulates tissue vulnerability to Alzheimer's disease. Sci. Adv. 2, e1600947. doi:10.1126/sciadv.1600947

Freundt, E.C., Maynard, N., Clancy, E.K., Roy, S., Bousset, L., Sourigues, Y., Covert, M., Melki, R., Kirkegaard, K., Brahic, M., 2012. Neuron-to-neuron transmission of ?-synuclein fibrils through axonal transport. Ann. Neurol. 72, 517–524. doi:10.1002/ana.23747

Friston, K.J. (Karl J.., Ashburner, J., Kiebel, S., Nichols, T., Penny, W.D., 2007. Statistical parametric mapping : the analysis of funtional brain images. Elsevier/Academic Press.

Frost, B., Diamond, M.I., 2010. Prion-like mechanisms in neurodegenerative diseases. Nat. Rev. Neurosci. 11, 155–9. doi:10.1038/nrn2786

Greicius, M.D., Supekar, K., Menon, V., Dougherty, R.F., 2009. Resting-State Functional Connectivity Reflects Structural Connectivity in the Default Mode Network. Cereb. Cortex 19, 72–78. doi:10.1093/cercor/bhn059

Gutekunst, C.-A., Li, S.-H., Yi, H., Mulroy, J.S., Kuemmerle, S., Jones, R., Rye, D., Ferrante, R.J., Hersch, S.M., Li, X.-J., 1999. Nuclear and Neuropil Aggregates in Huntington's Disease: Relationship to Neuropathology. J. Neurosci. 19.

Hansen, C., Angot, E., Bergström, A.-L., Steiner, J.A., Pieri, L., Paul, G., Outeiro, T.F., Melki, R., Kallunki, P., Fog, K., Li, J.-Y., Brundin, P., 2011. α-Synuclein propagates from mouse brain to grafted dopaminergic neurons and seeds aggregation in cultured human cells. J. Clin. Invest. 121, 715–25. doi:10.1172/JCI43366

Harper, P., 1992. The epidemiology of Huntington's disease. Hum. Genet. 89, 365–376. doi:10.1007/BF00194305

Hawrylycz, M.J., Lein, E.S., Guillozet-Bongaarts, A.L., Shen, E.H., Ng, L., Miller, J.A., van de Lagemaat, L.N., et al., 2012. An anatomically comprehensive atlas of the adult human brain transcriptome. Nature 489, 391–399. doi:10.1038/nature11405

Herrera, F., Tenreiro, S., Miller-Fleming, L., 2011. Visualization of cell-to-cell transmission of mutant huntingtin oligomers. PLOS Curr.

Honey, C.J., Sporns, O., Cammoun, L., Gigandet, X., Thiran, J.P., Meuli, R., Hagmann, P., 2009. Predicting human resting-state functional connectivity from structural connectivity. Proc. Natl. Acad. Sci. 106, 2035–2040. doi:10.1073/pnas.0811168106

Iba, M., McBride, J.D., Guo, J.L., Zhang, B., Trojanowski, J.Q., Lee, V.M.-Y., 2015. Tau pathology spread in PS19 tau transgenic mice following locus coeruleus (LC) injections of synthetic tau fibrils is determined by the LC's afferent and efferent connections. Acta Neuropathol. 130, 349–62.

Jack, C.R., Holtzman, D.M., 2013. Biomarker Modeling of Alzheimer's Disease. Neuron 80, 1347–1358. doi:10.1016/j.neuron.2013.12.003

Jones, D.T., Knopman, D.S., Gunter, J.L., Graff-Radford, J., Vemuri, P., Boeve, B.F., Petersen, R.C., Weiner, M.W., Jack, C.R., 2016. Cascading network failure across the Alzheimer's disease spectrum. Brain 139, 547–562. doi:10.1093/brain/awv338

Jucker, M., Walker, L.C., 2013. Self-propagation of pathogenic protein aggregates in neurodegenerative diseases. Nature 501, 45–51. doi:10.1038/nature12481

Kuceyeski, A., Maruta, J., Niogi, S., Ghajar, J., Raj, A., 2011. The generation and validation of white matter connectivity importance maps. Neuroimage.

Kuceyeski, A., Maruta, J., Relkin, N., Raj, A., 2013. The Network Modification (NeMo) Tool: Elucidating the Effect of White Matter Integrity Changes on Cortical and Subcortical Structural Connectivity. Brain Connect. 3, 451–463. doi:10.1089/brain.2013.0147

Kuhl, D.E., Phelps, M.E., Markham, C.H., Metter, E.J., Riege, W.H., Winter, J., 1982. Cerebral metabolism and atrophy in huntington's disease determined by18FDG and computed tomographic scan. Ann. Neurol. 12, 425–434. doi:10.1002/ana.410120504

Lee, S.-J., Desplats, P., Sigurdson, C., Tsigelny, I., Masliah, E., 2010. Cell-to-cell transmission of non-prion protein aggregates. Nat. Rev. Neurol. 6, 702–706. doi:10.1038/nrneurol.2010.145

Lee, V.M.-Y., Goedert, M., Trojanowski, J.Q., 2001. Neurodegenerative Tauopathies. Annu. Rev. Neurosci. 24, 1121–1159. doi:10.1146/annurev.neuro.24.1.1121

Liu, L., Drouet, V., Wu, J.W., Witter, M.P., Small, S.A., Clelland, C., Duff, K., 2012. Trans-synaptic spread of tau pathology in vivo. PLoS One 7, e31302.

Marco, S., Giralt, A., Petrovic, M.M., Pouladi, M.A., Martínez-Turrillas, R., Martínez-Hernández, J., Kaltenbach, L.S., Torres-Peraza, J., Graham, R.K., Watanabe, M., Luján, R., Nakanishi, N., Lipton, S.A., Lo, D.C., Hayden, M.R., Alberch, J., Wesseling, J.F., Pérez-Otaño, I., 2013. Suppressing aberrant GluN3A expression rescues synaptic and behavioral impairments in Huntington's disease models. Nat. Med. 19, 1030–8. doi:10.1038/nm.3246

McColgan, P., Seunarine, K.K., Razi, A., Cole, J.H., Gregory, S., Durr, A., Roos, R.A.C., Stout, J.C., Landwehrmeyer, B., Scahill, R.I., Clark, C.A., Rees, G., Tabrizi, S.J., 2015. Selective vulnerability of Rich Club brain regions is an organizational principle of structural connectivity loss in Huntington's disease. Brain 138, 3327–3344. doi:10.1093/brain/awv259

Nagai, M., Re, D., Nagata, T., Chalazonitis, A., 2007. Astrocytes expressing ALS-linked mutated SOD1 release factors selectively toxic to motor neurons. Nature.

Neumann, M., Sampathu, D.M., Kwong, L.K., Truax, A.C., Micsenyi, M.C., Chou, T.T., Bruce, J., Schuck, T., Grossman, M., Clark, C.M., McCluskey, L.F., Miller, B.L., Masliah, E., Mackenzie, I.R., Feldman, H., Feiden, W., Kretzschmar, H.A., Trojanowski, J.Q., Lee, V.M.-Y., 2006. Ubiquitinated TDP-43 in Frontotemporal Lobar Degeneration and Amyotrophic Lateral Sclerosis. Science (80-.). 314, 130–133. doi:10.1126/science.1134108

Oh, S., Harris, J., Ng, L., Winslow, B., Cain, N., Mihalas, S., 2014. A mesoscale connectome of the mouse brain. Nature.

Pearson, R.C., Esiri, M.M., Hiorns, R.W., Wilcock, G.K., Powell, T.P., 1985. Anatomical correlates of the distribution of the pathological changes in the neocortex in Alzheimer disease. Proc. Natl. Acad. Sci. U. S. A. 82, 4531–4.

Pecho-Vrieseling, E., Rieker, C., Fuchs, S., 2014. Transneuronal propagation of mutant huntingtin contributes to non-cell autonomous pathology in neurons. Nature.

Piñero, J., Queralt-Rosinach, N., Bravo, À., Deu-Pons, J., Bauer-Mehren, A., Baron, M., Sanz, F., Furlong, L.I., 2015. DisGeNET: a discovery platform for the dynamical exploration of human diseases and their genes. Database (Oxford). 2015, bav028. doi:10.1093/database/bav028

Prusiner, S., 1984. Some speculations about prions, amyloid, and Alzheimer's disease.

Quintanilla, R.A., Jin, Y.N., Fuenzalida, K., Bronfman, M., Johnson, G.V.W., 2008. Rosiglitazone treatment prevents mitochondrial dysfunction in mutant huntingtin-expressing cells: possible role of peroxisome proliferator-activated receptor-gamma (PPARgamma) in the pathogenesis of Huntington disease. J. Biol. Chem. 283, 25628–37. doi:10.1074/jbc.M804291200

Raj, A., Kuceyeski, A., Weiner, M., 2012. A Network Diffusion Model of Disease Progression in Dementia. Neuron 73, 1204–1215. doi:10.1016/j.neuron.2011.12.040

Raj, A., LoCastro, E., Kuceyeski, A., Tosun, D., Relkin, N., Weiner, M., 2015. Network Diffusion Model of Progression Predicts Longitudinal Patterns of Atrophy and Metabolism in Alzheimer's Disease. Cell Rep. 10, 359–369. doi:10.1016/j.celrep.2014.12.034

Ren, P.-H., Lauckner, J.E., Kachirskaia, I., Heuser, J.E., Melki, R., Kopito, R.R., 2009. Cytoplasmic penetration and persistent infection of mammalian cells by polyglutamine aggregates. Nat. Cell Biol. 11, 219–225. doi:10.1038/ncb1830

Ross, C.A., Tabrizi, S.J., 2011. Huntington's disease: from molecular pathogenesis to clinical treatment. Lancet Neurol. 10, 83–98. doi:10.1016/S1474-4422(10)70245-3

Schwarz, A.J., Yu, P., Miller, B.B., Shcherbinin, S., Dickson, J., Navitsky, M., Joshi, A.D., Devous, M.D., Mintun, M.S., 2016. Regional profiles of the candidate tau PET ligand 18F-AV-1451 recapitulate key features of Braak histopathological stages. Brain.

Seeley, W., 2017. Mapping Neurodegenerative Disease Onset and Progression. Cold Spring Harb. Perspect.

Smith, S., Jenkinson, M., Woolrich, M., Beckmann, C., 2004. Advances in functional and structural MR image analysis and implementation as FSL. Neuroimage.

Spillantini, M., Crowther, R., Jakes, R., 1998. α-Synuclein in filamentous inclusions of Lewy bodies from Parkinson's disease and dementia with Lewy bodies. Proc.

Tabrizi, S., Langbehn, D., Leavitt, B., Roos, R., 2009. Biological and clinical manifestations of Huntington's disease in the longitudinal TRACK-HD study: cross-sectional analysis of baseline data. Lancet.

Tabrizi, S., Reilmann, R., Roos, R., Durr, A., 2012. Potential endpoints for clinical trials in premanifest and early Huntington's disease in the TRACK-HD study: analysis of 24 month observational data. Lancet.

Tabrizi, S., Scahill, R., Durr, A., Roos, R., Leavitt, B., 2011. Biological and clinical changes in premanifest and early stage Huntington's disease in the TRACK-HD study: the 12-month longitudinal analysis. Lancet.

Tabrizi, S., Scahill, R., Owen, G., Durr, A., Leavitt, B., 2013. Predictors of phenotypic progression and disease onset in premanifest and early-stage Huntington's disease in the TRACK-HD study: analysis of 36-month. Lancet.

Tan, Z., Dai, W., Erp, T. van, Overman, J., Demuro, A., 2015. Huntington's disease cerebrospinal fluid seeds aggregation of mutant huntingtin. Molecular.

Vonsattel, J.P., Myers, R.H., Stevens, T.J., Ferrante, R.J., Bird, E.D., Richardson, E.P., 1985. Neuropathological classification of Huntington's disease. J. Neuropathol. Exp. Neurol. 44, 559–77.

Wang, M.B., Owen, J.P., Mukherjee, P., Raj, A., Bukshpun, P., Vora, S., 2017. Brain network eigenmodes provide a robust and compact representation of the structural connectome in health and disease. PLOS Comput. Biol. 13, e1005550. doi:10.1371/journal.pcbi.1005550

Zhou, J., Gennatas, E., Kramer, J., Miller, B., Seeley, W., Bangaru, S., Grzadzinski, R., Evans, A.C., Zang, Y.F., Castellanos, F.X., Milham, M.P., 2012. Predicting Regional Neurodegeneration from the Healthy Brain Functional Connectome. Neuron 73, 1216–1227. doi:10.1016/j.neuron.2012.03.004

Zuccato, C., Liber, D., Ramos, C., Tarditi, A., Rigamonti, D., Tartari, M., Valenza, M., Cattaneo, E., 2005. Progressive loss of BDNF in a mouse model of Huntington's disease and rescue by BDNF delivery. Pharmacol. Res. 52, 133–139. doi:10.1016/j.phrs.2005.01.001

Chapter 5:

Age-Related Changes in Topological Degradation of White Matter Networks and Gene Expression in Chronic Schizophrenia

Introduction

Current models stipulate schizophrenia (SZ), a psychiatric disease characterized by hallucinations, flattened affect and cognitive disturbances, is a disorder of dysconnectivity arising not from focal pathophysiology, but rather from impaired neuroanatomical integration across the brain (O'Donoghue et al., 2017). Converging neuroimaging, physiological and molecular evidence suggest core symptoms of the disease are related to altered connectivity between distinct brain regions, causing inefficient information integration in the network (Pettersson-Yeo et al., 2011; van den Heuvel et al., 2010). Importantly, longitudinal evidence suggests SZ is not a static neurodevelopmental disorder, but rather an alteration in cortical plasticity that occurs over the lifetime of an individual (DeLisi et al., 1997).

A large number of diffusion MRI studies examining tract-level changes report findings reflective of altered white matter (WM) integrity in SZ (Kubicki et al., 2011, 2002; Luck et al., 2011; Price et al., 2008; Szeszko et al., 2008). Prior studies applying graph theory analysis to diffusion MRI data show abnormal pathlength, centrality and efficiency in frontal and temporal network structure as well as impaired efficiency and clustering coefficient in medial frontal, parietal/occipital and left temporal lobes (van den Heuvel et al., 2010; Wang et al., 2012; Zalesky et al., 2011). While such studies elucidate

macrostructural changes in disease pathophysiology, age-related changes within and between WM networks with SZ progression remain incompletely understood (Gogtay, 2008). Furthermore, though WM abnormalities in SZ are shown to be highly heritable, the relationship between changes in network topology with age and its relationship to gene expression is largely uninvestigated (Ripke et al., 2014; Skudlarski et al., 2013).

The current study uses a cross-sectional design to test network models based on DTI and genetic expression data. We hypothesize network topology will degrade faster in SZ compared to controls, with a significant association between gene expression and topological abnormalities. To test this hypothesis, graph theory analysis is utilized to examine age-related patterns of global and local topological degradation. Additionally, we model the topological relationship to gene expression as measured by microarray data from healthy human brains from the Allen Brain Institute. The combination of multiple graph metrics in conjunction with gene expression data to examine questions of age-related organizational disturbances in SZ is unprecedented.

Methods

Subjects

DTI data were acquired from 24 individuals with chronic, treatment-resistant SZ and 51 healthy controls. Patients were recruited from inpatient and outpatient units at the University College Hospital Galway (UCHG) and in the catchment area of HSE West of Ireland. All patients were diagnosed by experienced psychiatrists, using the Structured Clinical Interview for DSM disorders (SCID) (First and Pincus, 2002), as meeting the criteria for SZ per

the DSM-IV-TR [Diagnostic and Statistical Manual of Mental Disorders, Fourth Edition].

Patients and control subjects were age and gender-matched (Table 4.1). All patients with chronic SZ were treatment resistant at the time of scanning and being considered for treatment with clozapine, an atypical antipsychotic medication for treatment resistance. Treatment resistance was defined as failure to respond to at least 2 antipsychotic medications, one of which an atypical, with a prolonged period of moderate to severe positive and/or negative symptoms. At time of scanning, all patients were medicated with atypical antipsychotics, with some on 2 or more medications (Table 4.1). Mean Chlorpromazine equivalent dose was 247 mg. The control group consisted of 51 participants with no current or past axis I or II disorders (DSM-IV-TR) and was screened using the SCID-Non-Patient Version (First and Pincus, 2002). Both the University College Hospital Galway and the National University of Ireland Galway Ethics committees granted ethical approval and written informed consent was obtained from each participant.

Table 5.1. Study participants. Demographic information of study participants.

Characteristic	Patients n=24 Mean ± SD, range	Controls n=31 Mean ± SD, range	t-test /x^2 vs. CON
Age (years)	36.2 ± 10.02 20-59	34.4 ± 11.31 19-57	p=0.48
Male/female (% male)	35/16 (46%)	17/7 (41%)	p=0.41
Duration of illness (years)	14.42 ± 8.16 4-39		
# psychotic episodes	4.8 ± 3.38 2-20		
Medications			
Typical antipsychotics	12		
Atypical antipsychotics	24		
Clozapine	0		
Clinical scales			
Total PANSS	53.9(17.2)		
SAPS	27.9 (16.3)		
SANS	42.5(20.6)		
GAF	46.8(10.8)		

Abbreviations: PANSS, Positive and Negative Syndrome Scale (Scored on the 0-6 scale); SANS, Scale for the Assessment of Negative Symptoms, SAPS, Scales for the Assessment of Positive; GAF, Global Assessment of Functioning.

Younger vs. Older

For reasons detailed in the results section, subjects were split into a "younger adult" or "older adult" group. For the younger adult group, there was no significant difference in gender composition between patients (n=14) and controls (n=30) (p=0.79). Furthermore, there was no significant difference in age between patients and controls in the younger adult group (p=0.11). The average age of a control subject in the younger adult group was 26.3 (standard deviation: 5.45) and the average age of a patient in the same group was 29.1 (standard deviation: 5.18). For older adult subjects, there was no significant difference in gender composition between patients (n=10) and controls (n=21) (p=0.92). Similarly, there was no significant difference in age between patients and controls in the older adult group (p=0.90). The average age of a control subject in the older adult group was 45.9 (standard deviation: 5.4) and the average age of a patient in the same group was 46.2 (standard deviation: 6.3).

Image acquisition

Structural MR images were acquired on a 1.5T Siemens Magnetom Symphony MRI scanner, as detailed in (Holleran et al., 2014). For each individual, a two-dimensional midsagittal scan was used to position the subject so that the floor of the fourth ventricle was parallel to the y axis of the scanner coordinates system. The anterior–posterior (AP) axis was determined on the midsagittal slice using the anterior commisure–posterior commisure (AC-PC) line. Detailed high-resolution, wholehead contiguous axial slices (thickness 0.9 mm, field of view 230x 230 mm) parallel to this axis were acquired using a set of three-dimensional (3D) T1-weighted magnetization prepared rapid gradient-echo (MPRAGE) sequences (relaxation time (TR): 1140 ms; echo time (TE):

4.38 ms; inversion time (TI): 600 ms; flip angle 15°; acquisition matrix 256 x 256, interpolated to 512 Å~ 512, pixel resolution of 0.45mm x 0.45 mm).

The diffusion sequence utilized Echo Planar Imaging (EPI)-based diffusion, 64 independent diffusion gradient directions at a b-value of 1300 s/mm^2 and 7 undirected images, TR=8100 ms, TE=95 ms, in-plane voxel resolution of 2.5 x 2.5 mm, slice thickness of 2.5 mm and SNR of b=1000 s/mm^2 images >20. After scout images, the total imaging time was 10.24 min for the diffusion MRI sequence. Diffusion parameters are further described in Holleran et al. 2014 utilizing methodologies recommended by (Jones et al., 1999).

Image preprocessing: Structural and diffusion MRI

Whole brain networks were constructed from 51 control and 24 schizophrenic subjects, using previously described methodology (Iturria-Medina et al., 2008; Raj and Chen, 2011). Briefly: T1-weighted MR images were processed using the FreeSurfer automatic volumetric pipeline to map and construct cortical volumes (Dale et al., 1999; Fischl et al., 2004a, 2004b, 2002, 2001, 1999; Ségonne et al., 2004), (http://surfer.nmr.mgh.harvard.edu). Inspection of T1 data revealed 7 subjects (5 patients and 2 controls) had motion artifacts. These were excluded from analysis and not included in subject demographics.

Primary visual inspection did not indicate presence of major artifacts in any of the diffusion MRI data. Slice-by-slice inspection showed motion was most evident in the frontal pole, but no major artifacts were detected that would result in additional exclusion from the study. Any potential confounding motion artifact was successfully addressed by eddy current and motion

distortion correction using methodology detailed in (Leemans and Jones, 2009).

Cortical and subcortical volume mappings from the FreeSurfer aparc+aseg parcellation atlas were used to establish 86 region-of-interest nodes for tractography. The processed tissue segmentation defined the white-gray matter interface, which was used to seed points for probabilistic tractography with 1000 streamlines drawn per seed voxel (Behrens et al., 2007). Each streamline is assigned a probability score according to established criteria (Iturria-Medina et al., 2008). WM tracts are estimated by the connection strength of each ROI, which is obtained by summing the probabilities of the streamlines terminating between 2 regions.

Graph theory analysis

Characteristic graph metrics to examine differences in network topology were calculated from undirected, weighted, non-thresholded structural connectivity matrices. Figure 5.1 depicts network construction. Network metrics including density, global efficiency, clustering coefficient, smallworldness, local connection strength, local efficiency and local modularity were computed in MATLAB using the Brain Connectivity Toolbox (BCT) as described in (Rubinov and Sporns, 2010). Additional metrics including power law alpha and largest eigenvalue of adjacency matrix were not available in the BCT and calculated using the *igraph* tool (Csardi et al., 2006). See below for definitions of additional network properties:

Consider a network/graph $\mathcal{G} = (\mathcal{V}, \mathcal{E})$, with a set of $\mathcal{N}_\mathcal{V}$ nodes $\mathcal{V} = \{(\mathcal{v}_i)|i \epsilon 1, \ldots., \mathcal{N}_\mathcal{V}\}$ and the set of $\mathcal{N}_\mathcal{E}$ edges where $\mathcal{E} = \{(e_{i,j})|\ i\epsilon\mathcal{V},\ j\epsilon\mathcal{V}\}$. $\mathcal{N}_\mathcal{V}$ and $\mathcal{N}_\mathcal{E}$ are notations for total number of nodes and edges in $\mathcal{G}$ respectively. $e_{i,j}$ is the edge connecting the nodes $i\epsilon\mathcal{V}$ and $j\epsilon\mathcal{V}$. $w_{ij} \epsilon [0, \infty)$ is the weight associated with the edge $e_{i,j}$, computed through fiber pathways measured through tractography.

Weight of the path $P = < \mathcal{v}_1, \mathcal{v}_2, \ldots\ldots\ldots, \mathcal{v}_k >$ is $w(P) = \sum_{i=1}^{k} w_{\mathcal{v}_i, \mathcal{v}_{i+1}}$. Shortest path $\delta_{\mathcal{v}_a, \mathcal{v}_b}$ between the nodes $\mathcal{v}_a$ to $\mathcal{v}_b$ has the weight:

$$\delta_{\mathcal{v}_a, \mathcal{v}_b} = \begin{cases} \min\{w(P)|\ P \text{ is the path from } \mathcal{v}_a \text{ to } \mathcal{v}_b\}, & \text{If path exists} \\ \infty, & \text{otherwise} \end{cases}$$

Adjacency matrix $\mathcal{A}_\mathcal{G}$ is defined as the $\mathcal{N}_\mathcal{V} \times \mathcal{N}_\mathcal{V}$ matrix where the non-diagonal entry is equal to w_{ij}, where $i\epsilon\mathcal{V}$ and $j\epsilon\mathcal{V}$. In the current study we work with undirected simple graphs, therefore diagonal elements of $\mathcal{A}_\mathcal{G}$ is equal to 0 and $w_{ij} = w_{ji}$.

Power Law Alpha is the slope of the straight line that fits the log frequency distribution of node degree in the network. It is calculated by fitting the line to the equation:

$$\mathcal{Y} = \beta\chi^{-\alpha}$$

Here, $\mathcal{Y}$ is the degree distribution, β is the fitting constant and α is the value of power law alpha.

Largest Eigenvalue of Adjacency Matrix $\mathcal{A}_\mathcal{G}$ can be calculated with $\mathcal{v}$ as a nonzero $\mathcal{N}_\mathcal{V} \times 1$ column vector, $I_{\mathcal{N}_\mathcal{V}}$ as the $\mathcal{N}_\mathcal{V} \times \mathcal{N}_\mathcal{V}$ identity matrix. Given $\mathcal{A}_\mathcal{G}$, an eigenvalue λ and its associated eigenvector $\mathcal{v}$ are a pair obeying the relationship:

$$(\mathcal{A}_\mathcal{G} - \lambda\, I_{\mathcal{N}_\mathcal{V}})\mathcal{v} = 0$$

From the spectra of all the obtained values of λ, largest computed value in magnitude is called as largest eigenvalue.

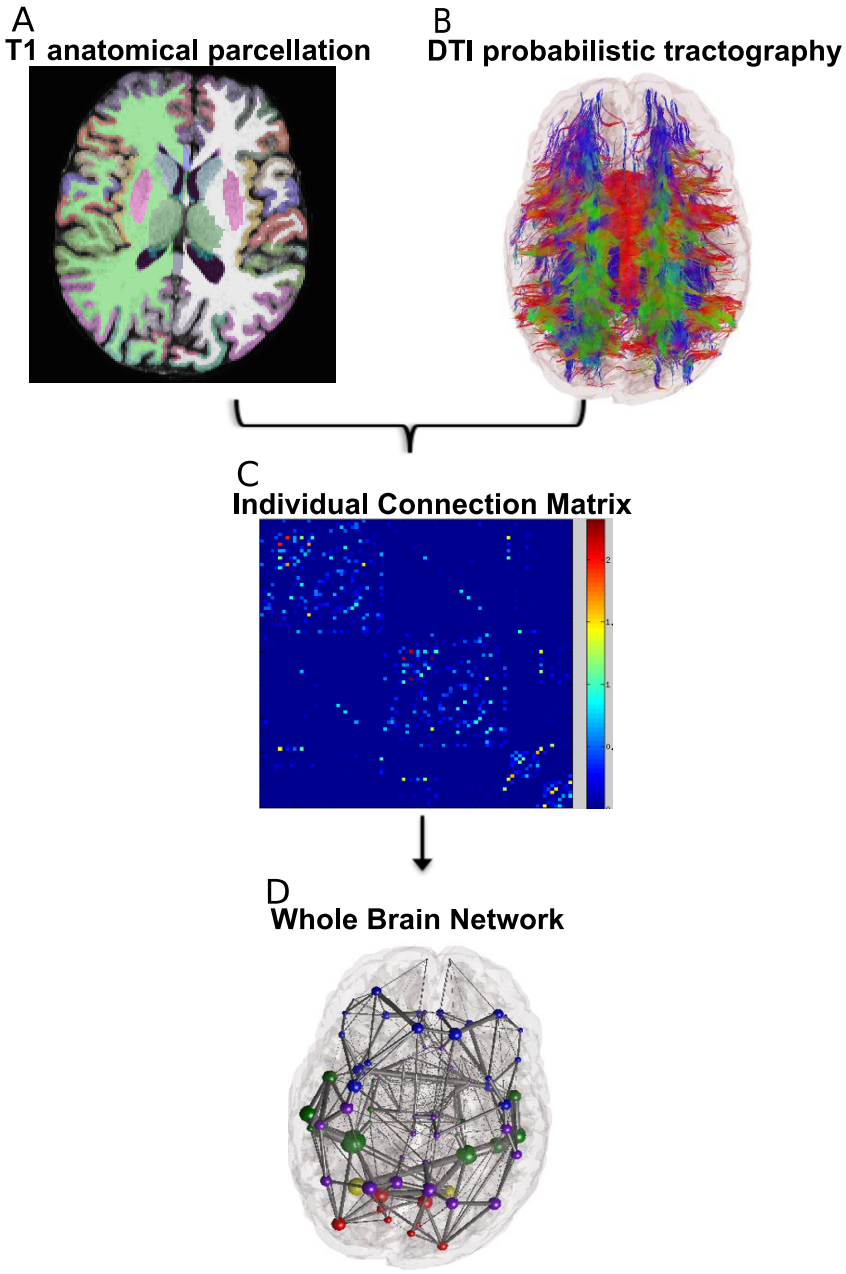

Figure 5.1. Brain network construction. A) T1 images were used to partition the brain into 86 cortical and subcortical areas with FreeSurfer **B)** WM fibers were arranged as determined by probabilistic tractography. Colors indicate directionality. Green is dorsal to ventral, red is left to right and blue is anterior to posterior. **C**) Individual structural connectivity matrices were created from probabilistic tractography **D**) Graph network analysis performed with nodes representing brain regions and edges representing the strength of WM tract connections

Genetic data

Microarray gene expression data from post-mortem healthy human brains were downloaded from the Allen Brain Atlas Institute and obtained as described in (Hawrylycz et al., 2012). The microarray data is composed of 926 regions of the brain, each one belonging to a set of 58,692 probes that correspond to 29,181 distinct genes. Unique probe ID's often represented the same gene and the average as used for analysis of the gene, as done by (Freer et al., 2016). For analysis, the 926 regions in the microarray data were mapped to 86 regions of the Desikan Atlas. Genes of interest implicated in SZ were selected from a DisGeNET database, which generates human gene-disease associations from curated databases and text mining (Piñero et al., 2015).

Statistical analysis

Independent, two-sided t-tests were used to test for differences in characteristic graph metrics. All reported significant global p-values survived FDR correction for multiple comparisons and are FDR adjusted (Benjamini and Hochberg, 1995). When noted, permutation testing, randomly mixing group assignment, was performed to obtain a null-distribution of component size, independent of group status (5,000 permutations). Permutation tests for group differences in global network metrics were FDR corrected for multiple comparisons. Local metrics did not survive FDR corrections and local reported p-values are uncorrected. Using global metrics as dependent variables and age as independent variables, network degradation was modeled using regression analysis. The significance of regression model fits was evaluated using the F-statistic.

Correlation analyses were carried out to determine whether identified brain topological changes were associated with gene expression. Correlations between a specific gene's expression and a local graph metric were Bonferroni corrected across all three tested age ranges ($p < 0.05/3$). This Bonferonni correction method was applied in a manner suggested by (Mayo and Cox, 2006), which urges each experiment's goals be considered when applying Bonferroni correction. Specifically, the current study considers each gene and its relationship to age to represent its own experiment. Within each experiment exist 3 hypotheses (1 hypothesis for younger subjects, 1 hypothesis for older subjects and 1 hypothesis for all subjects).

Results

White matter network topology in all subjects

First, we confirm results from our imaging pipeline reproduces numerous previously published data on altered global WM topology in SZ. We observe patients show significantly decreased density ($p=0.02$), global efficiency ($p=0.01$), clustering coefficient ($p=0.01$), largest eigenvalue of the adjacency matrix ($p=0.02$) and power law alpha ($p=0.02$) compared to controls. No significant difference in smallworldness is observed between patients and controls ($p=0.38$) (Figure 5.2). All reported global p-values survived FDR correction for multiple comparisons. To mitigate concerns of small sample, p-values were replicated with permutation testing (5,000 permutations - FDR corrected, in Table 4.2).

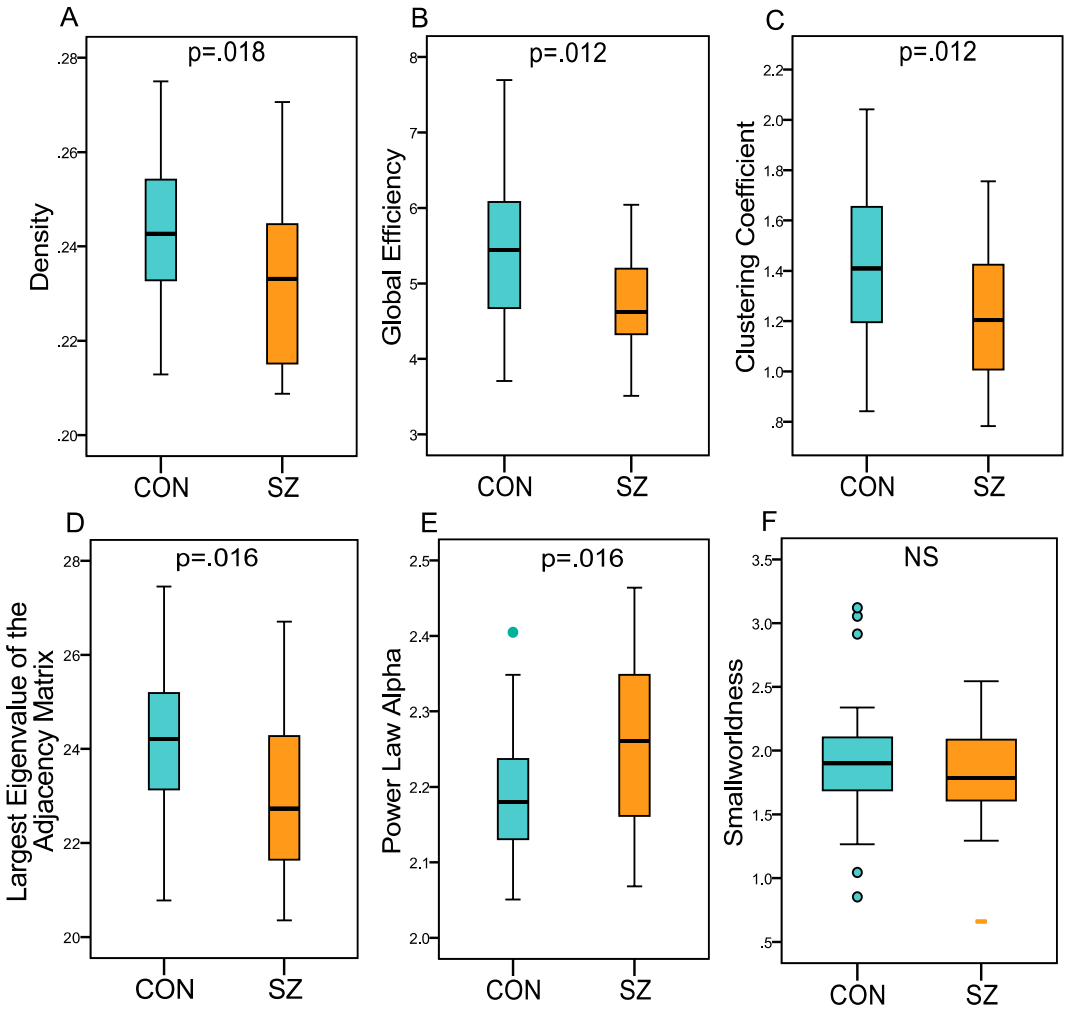

Figure 5.2. Global metrics across all subjects. Boxplots of **A**) density, significant, p=0.018 **B)** global efficiency, significant, p=0.012 **C)** clustering coefficient, significant, p=0.012 **D)** largest eigenvalue of the adjacency matrix, p=0.016 **E)** power law alpha, p=.016 and **F)** smallworldness, not significant. Errors bars express standard deviation.

Table 5.2 Permutation testing of global metrics. Permutation tests of group differences in summary metrics (5,000 permutations).

All Subjects

Metric	FDR Corrected Raw P Value	Raw P value	Permutation P Value
Density	p=0.018	p=0.0077	p=0.0078
Global Efficiency	p=0.012	p=0.0039	p=0.0044
Clustering Coefficient	p=0.012	p=0.0032	p=0.0044
Largest Eigen Adj	p=0.016	p=0.0029	p=0.0038
Power Law Alpha	p=0.016	p=0.0016	p=0.0016
Small Worldness	p=NS	p=0.3861	p=0.3934

Younger Subjects Under 37

Metric	FDR Corrected Raw P Value	Raw P value	Permutation P value
Density	NS	p=0.045	p=0.0474
Global Efficiency	p=0.0018	p=0.002	p=0.0022
Clustering Coefficient	p=0.0018	p=0.0009	p=0.0014
Small Worldness	NS	p=0.53	p=0.54

Older Subjects Over 37

Metric	FDR Corrected Raw P Value	Raw P value	Permutation P Value
Density	NS	p=0.07	p=0.0678
Global Efficiency	NS	p=0.33	p=0.3368
Clustering Coefficient	NS	p=0.62	p=0.6098
Small Worldness	NS	p=0.08	P=0.0842

Age-dependent network degradation

To quantify changes in network topology with age, regression models were fit to each global metric over the age range of all subjects. Graphs fitting global network metric as a function age are hereby referred to as “age-resolved” graphs and are depicted in Figure 5.3. Linear models were tested because prior work shows WM microstructure changes linearly with age in healthy control subjects (Hagmann et al., 2010). In addition, we hypothesized quadratic models may also capture network degradation as the current study encompasses a later, wider age range than prior work. To test these hypotheses, models fits were evaluated using significance of the F-statistic. We observe that in control subjects, all metrics degraded in a stereotyped manner. Density ($p=0.02$), efficiency ($p=0.002$), clustering coefficient ($p=0.005$) and power law alpha ($p=0.05$) degrade linearly with age (Figure 5.3) (Table 5.3). Interestingly, largest eigenvalue of the adjacency matrix degrades quadratically with age in controls ($p=0.007$).

In contrast, age-related network degradation patterns in patients do not follow similar, stereotyped trends trends. Density ($p=0.076$) and global efficiency ($p=0.075$) degrade in a moderate quadratic trend toward significance with age in patients (Figure 5.3A-B). However, neither linear nor quadratic fits accurately model age degradation patterns in clustering coefficient, power law alpha and largest eigenvalue of the adjacency matrix. The best regression equations for these age-resolved graphs are over-fitted, fifth degree polynomials, which are likely not generalizable (Table 5.3) (Figure 5.3C). (Power law alpha and largest eigenvalue of the adjacency matrix not shown). Taken together, these data show that while controls show stereotyped, linear degradation of network organization with age, a

stereotyped network model for SZ is overall poor, as the best result shows merely a moderate trend toward significance (Figure 5.3A-B). Subsequent analysis splits patients into 2 separate age groups with the goal of elucidating the abnormal degradation trajectory observed in SZ.

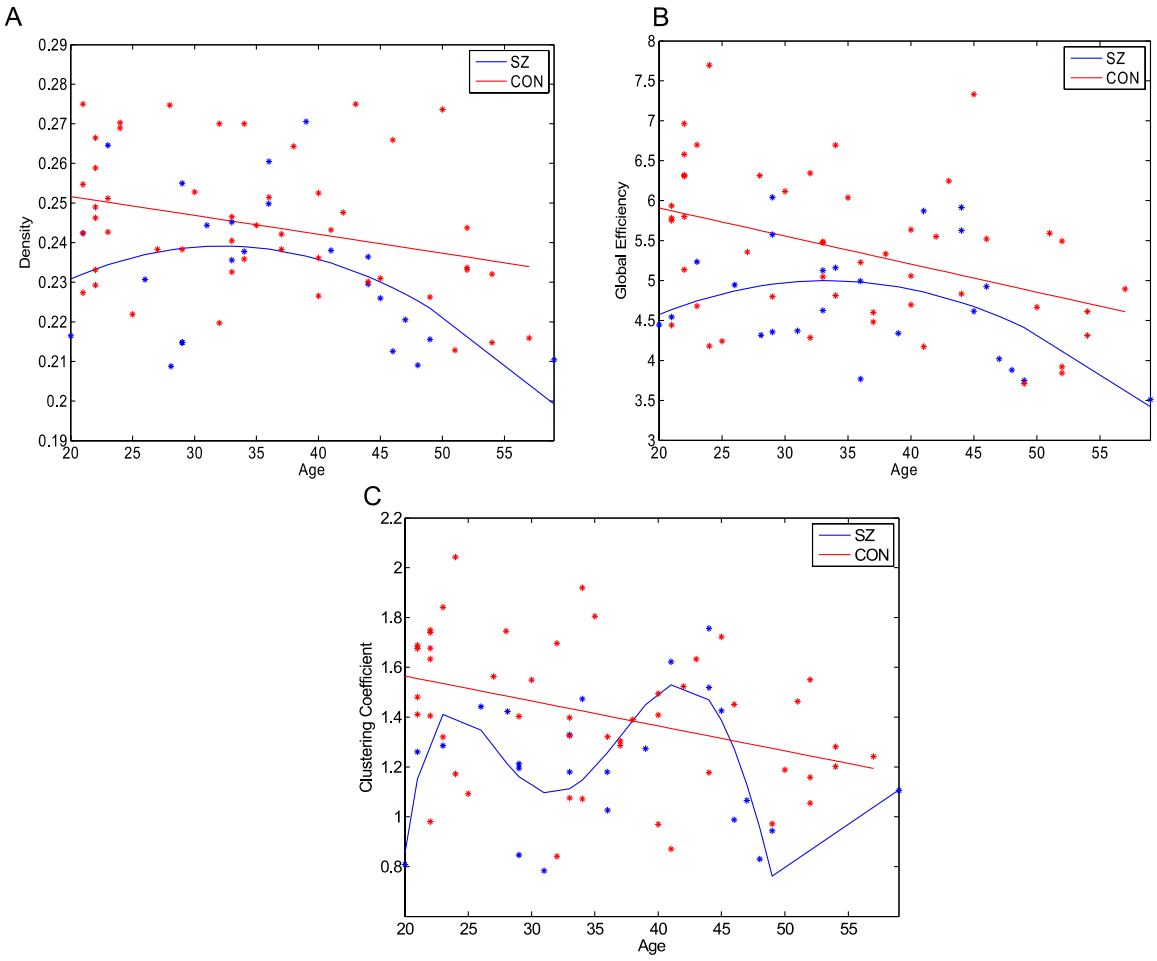

Figure 5.3. Age-resolved graphs. Best regression fits for age-resolved graphs of network metrics in all controls and patients. Global metrics in control subjects degrade in a significant linear, stereotyped manner. Patient networks do not exhibit the same trends.

Table 5.3. **Model fits.** p-values of F-statistics evaluating linear and quadratic regression model fit of global graph metrics vs. age.

Metric	Age (CON)	Age^2 (CON)	Age (SZ)	Age^2 (SZ)
Density	p=0.024 *	p=0.03	p=0.12	p=0.076 *
Global Efficiency	p=0.002 *	p=0.01	p=0.18	p=0.075 *
Clustering Coefficient	p=0.005 *	p=0.02	p=0.91	p=0.47
Power Law Alpha	p=0.05 *	p=0.06	p=0.32	p=0.28
Largest Eigenvalue of Adjacency Matrix	p=0.018	p=0.007 *	p=0.11	p=0.13

* indicates significant and moderate trends toward significance.

To further investigate age-related network degradation within SZ, regression was performed with patients split into a “younger adult” or “older adult” group. Age 37 was selected as the cut-off between “older” and “younger” subjects because visual inspection of SZ age-resolved graphs shows age 37 represents the peak of the parabolic age effect. Specifically, it is evident in Figure 5.3A-B that density and global efficiency continue to grow in the younger age range, before reaching a peak at age 37 then declining. This finding suggests a possible age-related topological change that warranted further analysis. Hence, to test this hypothesis, regression analysis was carried out separately in each age group. These individual regression fits are depicted in Figure 5.4. Due to the small sample size in each age group, permutation testing consisting of 5,000 iterations was carried out after the initial regression. In the younger adult group, degradation slopes of density, global efficiency, power law and largest eigenvalue of the adjacency matrix slopes do not significantly differ from 0. This result survived permutation testing (Table 4.4). In contrast, preliminary regression analysis shows all 4 of

those metrics degrade in a significant, linear manner in older adults (Figure 5.4). However, only between the age effect of global efficiency and largest eigenvalue of the adjacency matrix survived permutation testing (Table 4.4). Clustering Coefficient did not follow this trend and does not degrade at a slope significantly different in either age group, suggesting a more sophisticated model may be necessary (data not shown).

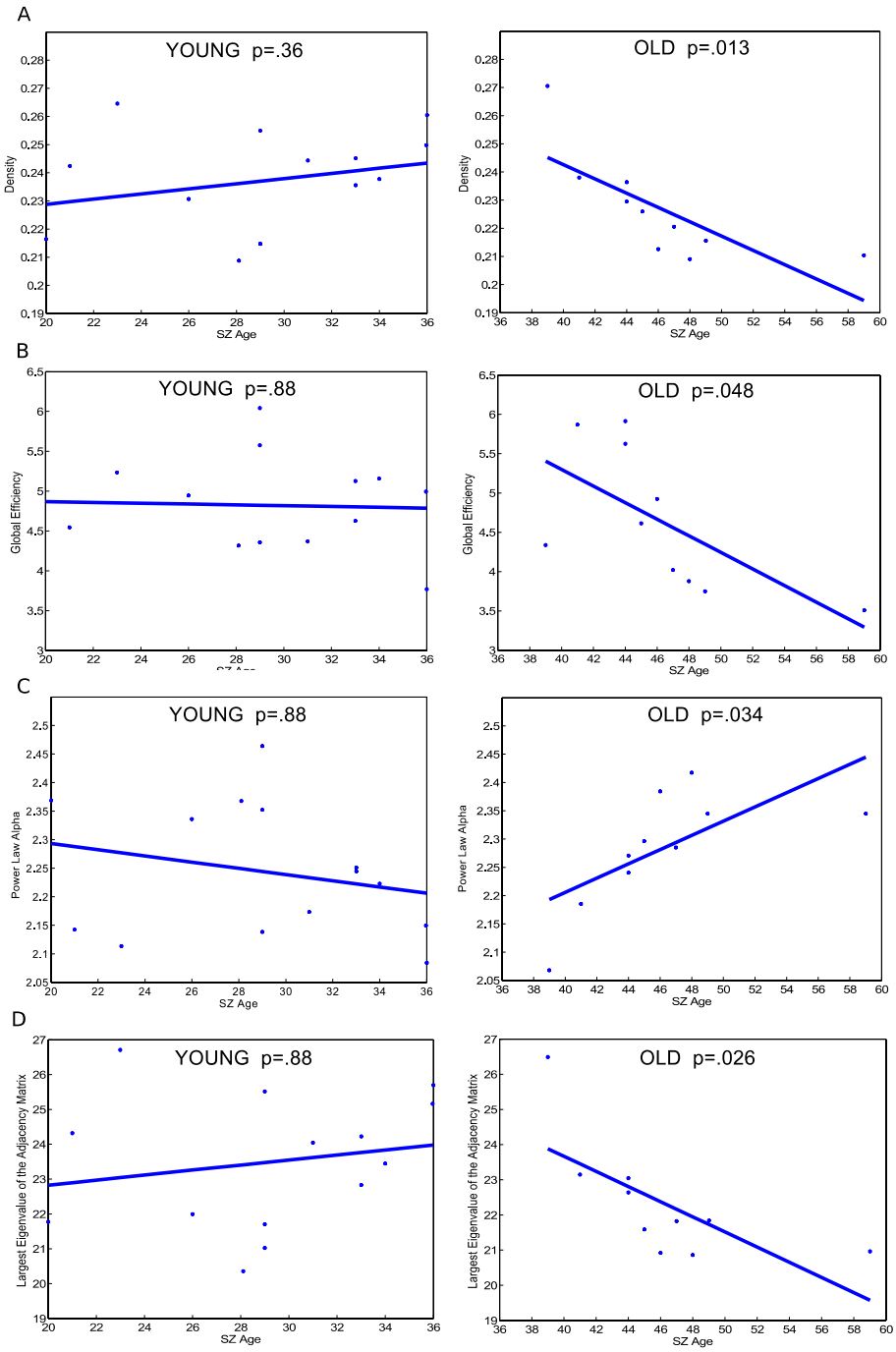

Figure 5.4. Young vs. old age regression. p-values of linear regression fits for age-resolved graphs of global metrics for patients, divided into young (under age 37) and old (over age 37). A non-significant linear fit indicates the slope is not significantly different from 0.

Table 5.4. Regression permutations. Permutation analysis of age-resolved models.

Metric	Regression Young	Regression Young 5000 Permutations	Regression Old	Regression Old 5000 Permutations
Density	F = 0.898 p=0.362	p=0.300	F = 9.97 p=0.013 *	p=1
Global Efficiency	F = 0.24 p=0.88	p=0.745	F = 5.45 p=0.048 *	p=0.002 *
Power Law Alpha	F = 0.744 p=0.405	p=0.423	F = 6.53 p=0.034 *	p=1
Largest Eigen Adj	p=0.507	p=0.396	F = 7.40 p=0.026 *	p=0.010 *

+ F represents F-statistic and p represents p-value.

Note: Permutation tests do not calculate F-statistics, instead, calculates p-value based on unique sums of squares (Type III SS)

Younger adult vs. older adult global network analysis

Next, we examine network organization between patients and controls within the two age groups. Younger adult patients show significantly decreased global efficiency (p=0.002) and clustering coefficient (p=0.002) compared to age-matched controls (Figure 5.5B-C). Density (p=0.11) shows significant before multiple corrections, but does not survive FDR correction (Figure 5.5A). Similarly, power law alpha (p=0.11), largest eigenvalue of the adjacency matrix (p=0.11) also show significance before multiple corrections, but do not survive FDR correction (Data not shown). Smallworldness (p=0.55) is preserved between younger patients and controls (Figure 5.5D). No global graphic metrics are significantly different between older adult patients and age-matched controls (Figure 5.5E-H).

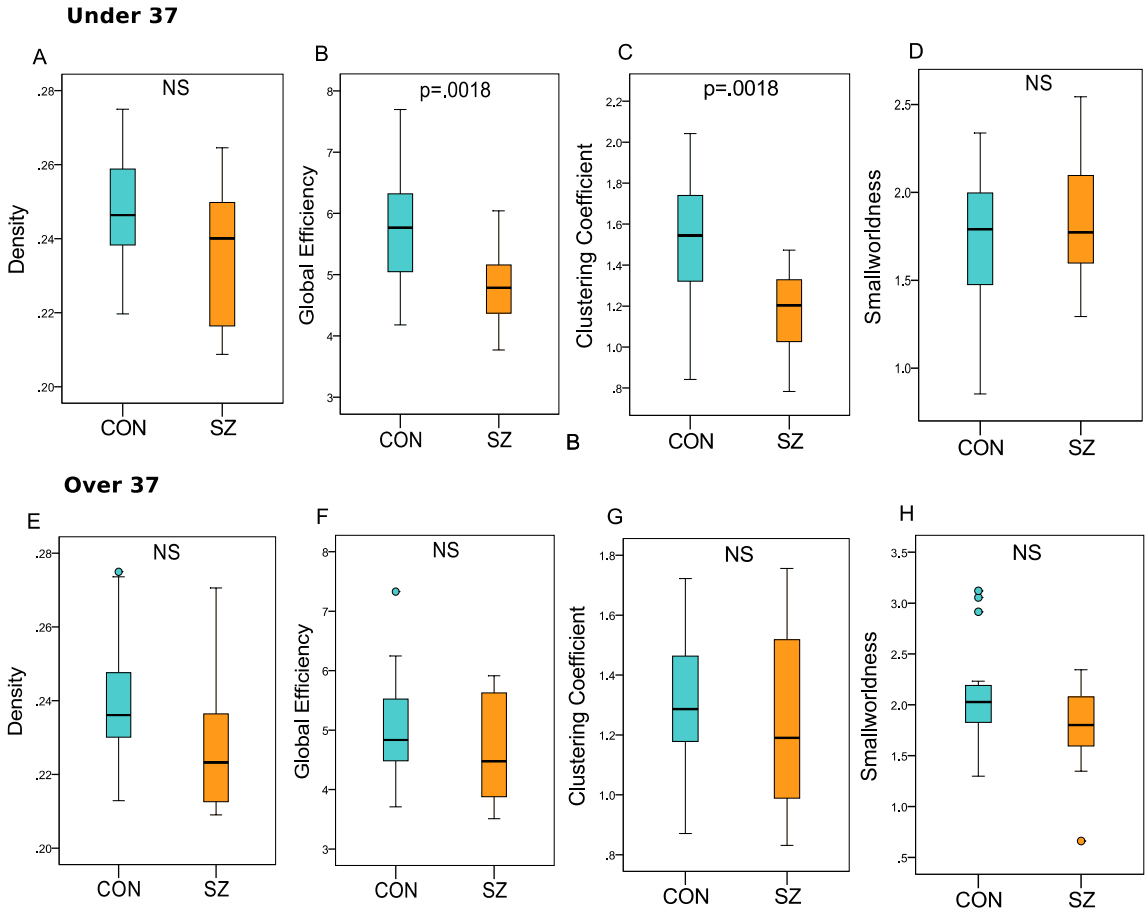

Figure 5.5. Young vs. old global metrics. Boxplots under age 37 of **A)** density, not-significant (NS) **B)** global efficiency, significant, p=.0018 **C)** clustering coefficient, significant, p=.0018 **D)** smallworldness, NS. Over age 37 boxplots of **E)** density, NS **F)** global efficiency, NS **G)** clustering coefficient, NS **F)** Smallworldness, NS. Errors bars express standard deviation.

Relationship between gene expression & local network analysis

Due to the highly heritable nature of WM abnormalities in SZ, we investigated the relationship between changes in topological degradation and gene expression in both younger adult and older adult subjects. The current study's 6 genes of interest include DISC1, DRD2, DTNB1, GRM3, COMT and BDNF. These genes were identified as the top genes reported to be associated with SZ from a GWAS database. Glass brains of healthy gene expression of DISC1 from post mortem brains are illustrated, as DISC1 the literature reports it as most associated with SZ (Figure 5.6). Figure 5.7 depicts glass brains of the additional regions of interest.

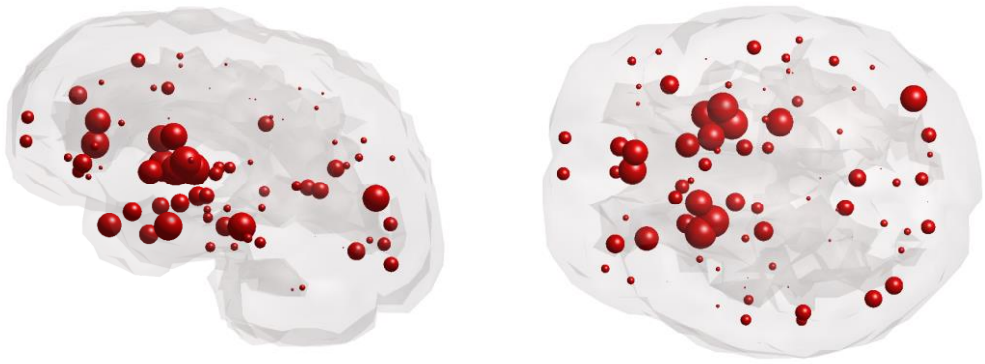

Figure 5.6. DISC1 expression. Sagittal and axial glass brains of gene expression of DISC1 from post-mortem brains of healthy subjects. Gene expression data is logistic rescaled on a scale from 0 – 1 and nodal sizes are depicted to the same scale.

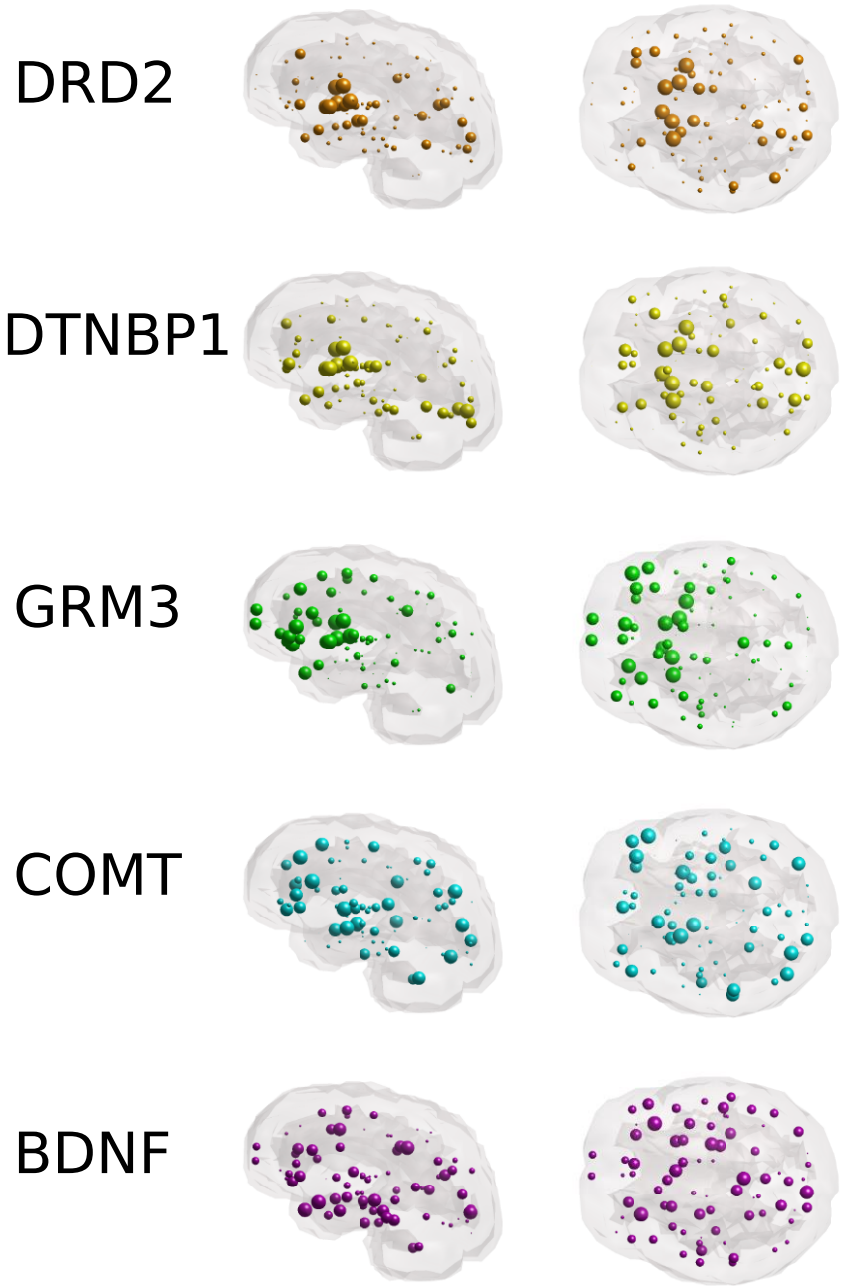

Figure 5.7. Expression of additional genes. Sagittal and axial glass brains of gene expression from healthy brains of additional genes of interest. All gene expression data is logistic rescaled on a scale from 0 – 1 and nodal sizes are depicted to the same scale.

To pinpoint regional abnormalities, local network analysis of connection strength, efficiency and modularity was performed. Reported local effects did not survive FDR correction. Group analyses reveal reduced local connection strength between younger adult patients and age-matched controls in frontal, temporal and cingulate regions (Figure 5.8A). Specifically, the most drastic reductions in local connection strength of these regions are observed in the left caudal anterior cingulate cortex (p=0.00005), bilaterally in the superior temporal gyrus (p=0.0008, p=0.04), left pars triangularis (p=0.005), left transverse temporal gyrus (p=0.01) and right precentral gyrus (p=0.01) (Table 4.5).

Older adult patients show only 3 nodes with altered local connection strength compared to age-matched controls, which include the right middle temporal gyrus (p=0.004), right hippocampus (p=0.009) and left nucleus accumbens (p=0.02) (Figure 5.8B) (Table 4.5). Interestingly, DISC1, DRD2, DTNBP1 and GRM3 show an age-related change in association between local connection strength and gene expression (Table 4.6). Age-related differences in the relationship between DISC1 and local connection strength disturbances appear to be driven by a significant correlation in younger subjects, an effect absent in older subjects (Figure 5.8C). Conversely, age-related differences in the relationship between DRD2 and DTNBP1 are driven by a significant correlation in older subjects and absent in younger subjects. We observe no age-related effect of connection strength disturbances and BDNF nor COMT expression.

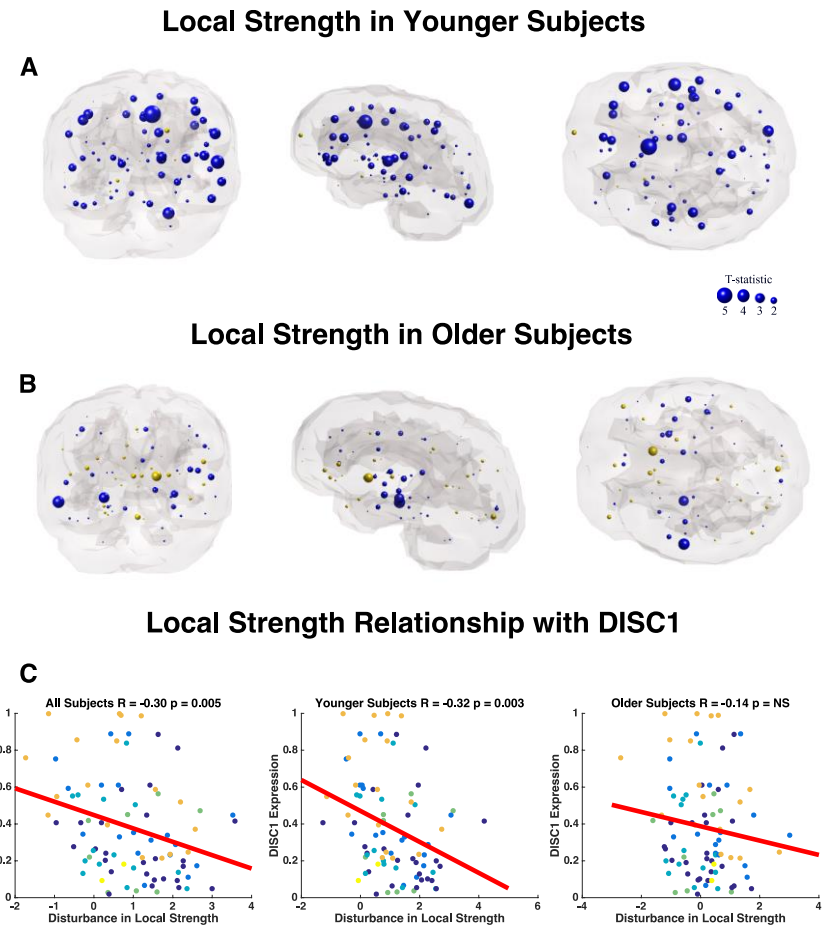

Figure 5.8. Local connection strength. Coronal, sagittal and axial glass brains with decreased local connection strength in patients (blue nodes) and increased connection strength in patients (gold nodes) vs. controls. **A)** Younger subjects under age 37 and **B)** Older subjects over age 37. Node size represents t-statistic. Effects did not survive FDR correction. **C)** Correlation between differences in local connection strength (t-statistic) vs. healthy DISC1 expression. Colors correspond to lobe.

Table 5.5. Local strength statistics. Nodes with significant (uncorrected) group effects in local connection strength. + denotes nodal metric is increased in SZ, lack of symbol denotes metric is decreased in SZ vs. CON.

Region	Lobe	p value (uncorrected)
Under Age 37		
Caudal Anterior Cingulate (L)	Cingulate	F=.00005
Superior Temporal Gyrus (L), (R)	Temporal	p=0.0008, p=0.04
Lateral Occipital Cortex (L)	Occipital	p=0.003
Pars Triangularis (L)	Frontal	p=0.005
Postcentral Gyrus (R), (L)	Parietal	p=0.007, p=0.02
Thalamus (L)	Subcortical	p=0.01
Transverse Temporal Gyrus (L)	Temporal	p=0.01
Precentral Gyrus (R)	Frontal	p=0.01
Rostral Middle Frontal Gyrus (L)	Frontal	p=0.02
Medial Orbitofrontal Cortex (L)	Frontal	p=0.02
Rostral Anterior Cingulate (L)	Frontal	p=0.02
Lateral Orbitofrontal Cortex (L), (R)	Frontal	p=0.02, p=0.03
Middle Temporal Gyrus (L)	Temporal	p=0.02
Paracentral Lobule (L), (R)	Frontal	p=0.02, p=0.05
Inferior Temporal Gyrus (L)	Temporal	p=0.03
Caudal Middle Frontal Gyrus (L)	Frontal	p=0.04
Over Age 37		
Middle Temporal Gyrus (R)	Temporal	p=0.004 +
Hippocampus (R)	MTL	p=0.009 +
Nucleus Accumbens (L)	Medial Temporal	p=0.02

Table 5.6. **Gene expression and connection strength.** Age-related differences in the relationship between gene expression & local connection strength.

Gene	All Subjects	Younger Subjects	Older Subjects	Age Effect
BDNF	R = 0.05 p=0.61	R = 0.04 p=0.71	R = 0.19 p=0.08	--
DISC1	R = -0.30 p=0.005 *	R = -0.32 p=0.003 *	R = -0.14 p=0.21	Driven by younger subjects
COMT	R = 0.07 p=0.50	R = 0.08 p=0.47	R = 0.03 p=0.79	--
DRD2	R = -0.33 p=0.002 *	R = -0.26 p=0.02	R = -0.31 p=0.004 *	Driven by older subjects
DTNBP1	R = -0.26 p=0.02	R = 0.16 p=0.15	R = -0.30 p=0.005 *	Driven by older subjects
GRM3	R = -0.22 p=0.04	R = -0.09 p=0.39	R = -.30 p=0.006 *	Driven by older subjects

* Survived Bonferroni correction significance threshold of p=0.05/3
+ Blue highlight indicates age-related changes in the relationship between gene expression and WM fiber connection strength

Next, we examine local efficiency. We observe local efficiency is also reduced in younger adult patients compared to age-matched controls in frontal, temporal and cingulate regions (Figure 5.9A). The most significant reductions in local efficiency is observed bilaterally in the superior frontal gyrus (p=0.0005, p=0.003), bilateral caudal anterior cingulate (p=0.003, p=0.02), bilateral rostral middle frontal gyrus (p=0.004, p=0.02), left pars triangularis (p=0.01) and bilateral precentral gyrus (p=0.03, p=0.04) (Table 4.7). In contrast, older adult patients reveal only 2 nodes with abnormal local efficiency compared to age-matched controls, which include the right pars orbitalis (p=0.02) and left pericalcarine cortex (p=0.05) (Figure 5.9B) (Table 5.7).

Age-related differences in the relationship between DISC1 and local efficiency alterations appear to be driven by a significant correlation in younger subjects, an effect that is absent in older subjects (Figure 5.9C). There is no

relationship between DRD2, DTNBP1 and GRM3 (Table 4.8). BDNF and COMT were omitted from analysis due to lack of relationship to connection strength disturbance.

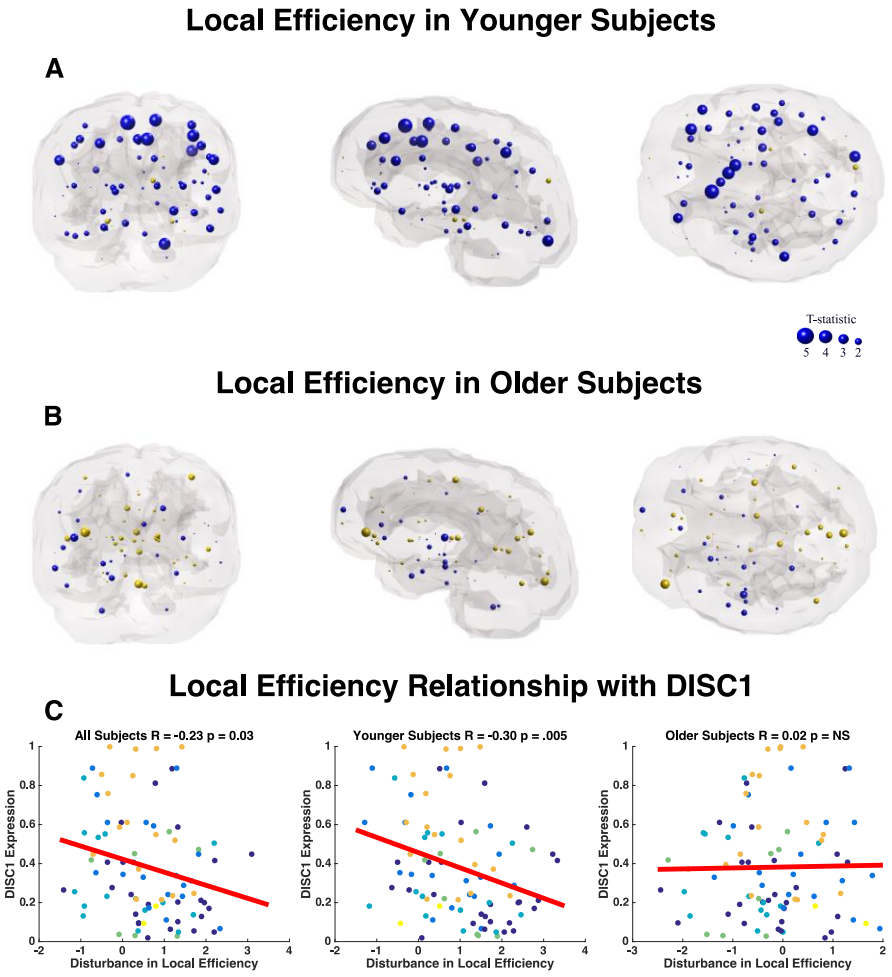

Figure 5.9. Local efficiency. Coronal, sagittal and axial glass brains with decreased local efficiency in patients (blue nodes) and increased efficiency in patients (gold nodes) vs. controls. **A)** Younger subjects under age 37 and **B)** Older subjects over age 37. Node size represents t-statistic. Effects did not survive FDR correction. **C)** Correlation between differences in local efficiency (t-statistic) vs. healthy DISC1 expression. Colors correspond to lobe.

Table 5.7. Local efficiency statistics. Nodes with significant (uncorrected) group effects in local efficiency. + denotes nodal metric is increased in SZ, lack of symbol denotes metric is decreased in SZ vs. CON.

Region	Lobe	p value (uncorrected)
Under Age 37		
Superior Frontal Gyrus (R,L)	Frontal	p=0.0005, p=.003
Caudal Anterior Cingulate (L), (R)	Cingulate	p=0.003, p=0.02
Rostral Middle Frontal Gyrus (L), (R)	Frontal	p=0.004, p=0.02
Lateral Occipital Cortex (L)	Occipital	p=0.005
Postcentral Gyrus (L)	Parietal	p=0.005
Pars Triangularis (L)	Frontal	p=0.01
Supramarginal Gyrus (R)	Parietal	p=0.01
Precentral Gyrus (L), (R)	Frontal	p=0.03, p=0.04
Hippocampus (L)	Subcortical	p=0.03
Caudal Middle Frontal Gyrus (L)	Frontal	p=0.03
Superior Temporal Gyrus (L)	Temporal	p=0.03
Over Age 37		
Pars Orbitalis (R)	Frontal	p=.02 +
Pericalcarine cortex (L)	Occipital	p=.05 +

Table 5.8. **Gene expression and local efficiency**. Age-related differences in the relationship between gene expression & local efficiency.

Gene	All Subjects	Younger Subjects	Older Subjects	Age Effect
DISC1	R = -0.23 p=0.03	R = -0.30 p=0.005 *	R = 0.02 p=0.88	Driven by younger subjects
DRD2	R = -0.20 p=0.06	NS	NS	--
DTNBP1	R = -0.21 p=0.05	NS	NS	--
GRM3	R = -0.08 p=0.49	NS	NS	--

* Survived Bonferroni correction significance threshold of p=.05/3
+ Blue highlight indicates age-related changes in the relationship between gene expression and local efficiency

Lastly, we investigate local modularity. Similarly, we observe decreased modularity in frontal, cingulate and temporal regions between younger adult patients and age-matched controls (Figure 5.10A). The most significant reductions in modularity occur bilaterally in the supramarginal gyrus (p=0.01, p=0.02), bilateral rostral middle frontal gyrus (p=0.01, p=0.03), bilateral frontal pole (p=0.01, p=0.03), bilateral caudal anterior cingulate (p=0.01, p=0.02) and bilateral transverse temporal gyrus (p=0.02, p=0.03) (Table 4.9). Older adult subjects display only 3 nodes with abnormal local modularity compared to age-matched controls, which include the right pars orbitalis (p=0.04) and bilateral nucleus accumbens (p=0.03) (Figure 5.10B) (Table 4.9). Older adult patients exhibit trends of increased modularity compared to controls. Age-related differences in the relationship between DISC1, DRD2, DTNBP1and local modularity appear to be driven by a significant correlation in older subjects, an effect that is absent in younger subjects (Figure 5.10C, Table 4.10). BDNF and COMT were omitted from analysis due to lack of relationship to connection strength. Interestingly, there is an an age-related effect in the association between GRM3 expression and local modularity alterations. Specifically, younger subjects show a significant positive correlation between SZ disturbances in modularity and GRM3 expression, while older subjects show a significant negative relationship (Table 4.10).

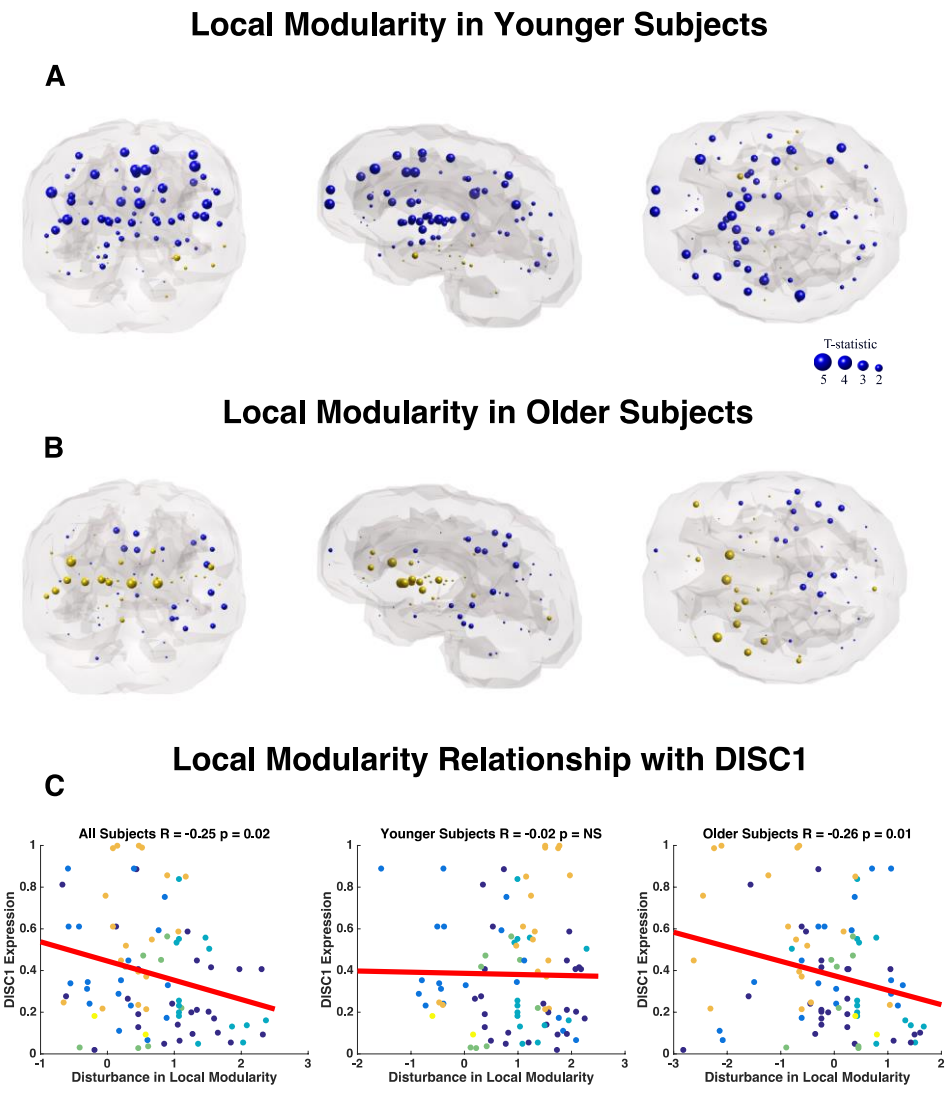

Figure 5.10. Local modularity. Coronal, sagittal and axial glass brains with decreased local modularity in patients (blue nodes) and increased modularity in patients (gold nodes) vs. controls. **A)** Younger subjects under age 37 and **B)** Older subjects over age 37. Node size represents t-statistic. Effects did not survive FDR correction. **C)** Correlation between differences in local efficiency (t-statistic) vs. healthy DISC1 expression. Colors correspond to lobe.

Table 5.9. Local modularity statistics. Nodes with significant (uncorrected) group effects in local modularity. + denotes nodal metric is increased in SZ, lack of symbol denotes metric is decreased in SZ vs. CON.

Region	Lobe	p value (uncorrected)
Under Age 37		
Supramarginal Gyrus (R), (L)	Parietal	p=0.01, p=0.02
Rostral Middle Frontal Gyrus (L), (R)	Frontal	p=0.01, p=0.03
Frontal Pole (R), (L)	Frontal	p=0.01, p=0.03
Caudal Anterior Cingulate (L), (R)	Cingulate	p=0.01, p=0.02
Transverse Temporal Gyrus (R), (L)	Temporal	p=0.02, p=0.03
Caudate Nucleus (R)	Subcortical	p=0.03
Superior Parietal Lobule (R)	Parietal	p=0.03
Caudal Middle Frontal Gyrus (L)	Frontal	p=0.03
Superior Frontal Gyrus (L)	Frontal	p=0.03
Paracentral Lobule (L)	Frontal	p=0.04
Superior Temporal Gyrus (R)	Temporal	p=0.045
Pars Opercularis (R)	Frontal	p=0.046
Over Age 37		
Pars opercularis (R)	Frontal	p=.04 +
Nucleus Accumbens (R), (L)	Medial Temporal	p=.03 +, p=.03 +

Table 5.10. Gene expression and local modularity. Age-related differences in the relationship between gene expression & local modularity.

Gene	All Subjects	Younger Subjects	Older Subjects	Age Effect
DISC1	R = -0.25 p=0.02	R = -0.02 p=0.87	R = -0.26 p=0.01 *	Driven by older subjects
DRD2	R = -0.06 p=0.57	R = 0.18 p=0.10	R = -0.27 p=0.009 *	Driven by older subjects
DTNBP1	R = -0.23 p=0.03	R = 0.02 p=0.85	R = -0.31 p=0.004 *	Driven by older subjects
GRM3	R = 0.11 p=0.33	R = 0.33 p=0.002 *	R = -0.26 p=0.01 *	Sign of relationship changes with age

* Survived Bonferroni correction significance threshold of p=.05/3
+ Blue highlight indicates age-related changes in the relationship between gene expression and local modularity

Discussion

The present study uses DTI, advanced graph theory and post-mortem microarray data in a cross-sectional design to show novel alterations in age-related topological network degradation and its relationship to gene expression in SZ. These findings support popular disconnection models suggesting WM disruptions underlie pathophysiology in SZ, which compromise network integration throughout the lifespan.

First, we replicate prior findings of disrupted global topology in SZ and preserved smallworldness between patients and controls across all subjects (Figure 5.2). Previous diffusion MRI and graph theory studies support these findings, which suggest a limited capacity of brain information integration in SZ (Bassett et al., 2008; Filippi et al., 2013; Pettersson-Yeo et al., 2011; van den Heuvel et al., 2010; Zalesky et al., 2011). It is believed such topological differences may be due to the outcome of different growth processes and that neurodevelopmental abnormalities in SZ that specifically impact large multimodal cortical organization (Bassett et al., 2008).

Because largest eigenvalue of the adjacency matrix (Figure 5.2D) and power law alpha (Figure 5.2E) are novel metrics in the context of DTI and SZ, they will be briefly discussed. Power law alpha is a derivative of degree, and follows previously published results of decreased degree in SZ compared to patients (Fornito et al., 2012). Eigenvalues are a set of characteristic roots associated with a system. Thus, reduced largest eigenvalue of the adjacency matrix (Figure 5.2D) across all patients compared to controls suggest a network more vulnerable to insult with decreased information flow and robustness (Navlakha et al., 2014; Restrepo et al., 2007). Because our study

is the first examining these metrics in the present context, these results will benefit from independent replication.

Regression analysis reveals control network topology degrades in a stereotyped manner, while corresponding patient networks do not (Figure 5.3, Table 4.3). Due to the small sample size arising from splitting up the patient group, permutation testing was carried out. Age-effects survived permutation testing with FDR correction in metrics largest eigenvalue of the adjacency matrix and global efficiency.

Prior graph theory analysis of network topology on diffusion MRI data in healthy networks shows a significant positive stereotyped, linear effect of age on network costs (Gong et al., 2009). This suggests the aging network experiences a linear reduction in overall cortical connectivity, causing it to become less connected. This result converges with our findings of linear degradation in global efficiency in control subjects because networks with higher costs tend to have lower efficiencies (Figure 5.3A).

Additional network modeling shows absence of significant network degradation in younger adult patients. In contrast, significant linear network degradation, which more closely resembles control networks, is observed in older adult patients (Figure 5.4). Interestingly, global network topology of younger adult patients is significantly compromised when compared to age-matched controls (Figure 5.5A-D). This effect is not observed in older patients (Figure 5.5E-H). Local analysis reveals global network abnormalities in younger adult patients are driven by changes in frontal, temporal and cingulate regions (Figure 5.8A, Figure 5.9A, Figure 5.10A). These regional differences become markedly less pronounced in older patients when compared to age-matched controls (Figure 5.8B, Figure 5.9B, Figure 5.10B).

Observed local topology disruptions in younger patients converge with DTI studies examining WM integrity, as reflected by Fractional Anisotropy (FA). It is reported that patients with SZ show globally reduced FA, including in frontal, temporal and cingulate regions compared to controls (Kochunov and Hong, 2014; Kubicki et al., 2002; Luck et al., 2011; Mori et al., 2007; Price et al., 2008; Szeszko et al., 2008). Indeed, many of these changes are observed at the earliest stages of illness (Kuswanto et al., 2012; Samartzis et al., 2014).

Model of age-related topological degradation in schizophrenia

Our age model of disrupted topology, presented in Figure 5.11 supports neurodevelopmental hypotheses of SZ, which postulate a neurodevelopment risk factor of SZ acts during adolescence, disrupting the synaptic reorganization and pruning stages later in life (Kochunov and Hong, 2014)). The current work shows younger adult patients (ages 20-37), show compromised topology but lack of network degradation, which we believe is evidence of compensatory rewriting, reflective of the dynamic nature of brain networks.

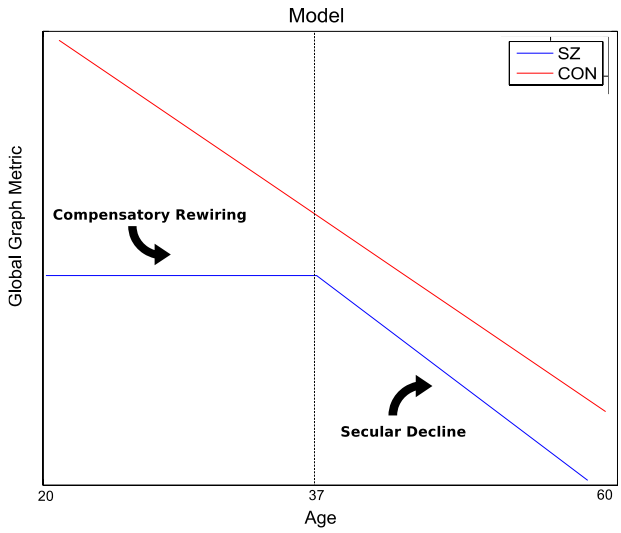

Figure 5.11. Model of topological degradation. Control networks degrade in a constant, linear manner. In SZ, network metrics are stagnant at a significantly compromised level throughout younger adulthood and begin to degrade linearly in old age.

There is support for rewiring and extended development into the third decade of life (Petanjek et al., 2011). Further evidence suggests homeostatic mechanisms can often compensate for one insult by shifting weights in parallel pathways (Marder and Goaillard, 2006; Tononi et al., 1999). Subsequently, older adult patients (ages 38-68) show linear degradation of global networks and less pronounced network differences between patients and controls. There is evidence for structural brain changes at different stages of the illness. In line with our results, several cross-sectional studies show WM deficits in chronic patients are either absent or less severe than in first episode patients (Friedman, et al., 2008; Kong et al., 2011).

Prior anatomical studies in SZ also support our age model. Graph network findings of anatomical architecture suggest topological differences

between divisions of normal cortex may represent the outcome of different growth processes in SZ, which impact cortical organization (Bassett et al., 2008). Furthermore, in a 19-year longitudinal study of cortical thickness, brain developmental trajectory in patients normalizes with age in posterior regions, while remaining divergent in frontal and temporal regions (Greenstein et al., 2006). Specifically, the diminished posterior anatomical differences represent attenuation of loss with age, and as a result healthy controls appear to 'catch up' with patients, as controls also have a parietal-frontal 'wave of loss' that characterizes normal development (Gogtay et al., 2004).

Similarly, diffusion MRI studies examining WM integrity (FA), support our age-related WM degradation model. It it is suggested that progressive brain abnormalities exist early in the disease and that ongoing brain changes occur in the initial years of diagnosis (Karlsgodt et al., 2008; Kyriakopoulos and Frangou, 2009; Pantelis et al., 2005). Patients early in the SZ disease process show decreased connectivity in structural networks compared to controls, with structural connectivity negatively correlating with illness duration (Zhang et al., 2015).

Prior literature shows differences in WM integrity (FA) of the frontal cortex between SZ patients and controls. Differences are most pronounced in the youngest subjects and disappear with increasing age, suggesting age-related differences in WM maturation between groups (Jones et al., 2006). This result was recently replicated and extended in a 300-subject study examining the impact of age on WM integrity in SZ, the largest study of its kind to-date. It is reported that FA differences do not appear to progress with age. Converging with our data, controls show a gradual FA decline while patients

show a flat relationship in FA decline. Younger patients show lower FA than controls, a difference which disappears with age (Kanaan et al., 2017).

Relationship between age-related topological changes and gene expression

Correlation analysis reveals age-related differences in the relationship between gene expression in our genes of interest and disturbances in logical topology. Though more than 108 common associated loci have been identified with schizophrenia, we specifically tested a priori hypotheses of the six most highly published genes associated with the disease (Ripke et al., 2014).

Remarkably, we show DISC1, a gene discovered and named for its causative implications in SZ, has an age-related effect across all three metrics of local connection strength, efficiency and modularity (Figure 5.8C, Figure 5.9C, Figure 5.10C.) Though gene expression data was collected from healthy post-mortem brains, analysis was carried out on nodal metric t-statistics of patients vs. controls, suggesting DISC1 has a relationship with organizational disturbances. Though DISC1 was the only gene with a significant, age-related topological association with local efficiency, we observe DISC1, DRD2, DTNBP1 and GRM3 all show significant relationships with disturbances in modularity (Table 4.10).

Younger patients show decreased modularity compared to controls, a segregation metric similar to clustering coefficient, and a result replicated in other studies (van den Heuvel et al., 2010). Interestingly, later in the disease, this trend changes in older patients, showing increases in modularity. The corresponding significant relationships to gene expression experiences the same sign flip between younger and older subjects (Table 4.10). Because this

is the first study examining the relationship between modularity and gene expression in schizophrenia, this result will benefit from independent replication.

Because COMT and BDNF is reported to mediate WM microstructure disconnectivity in SZ, the lack of relationship between connection strength disturbance in COMT and BDNF is surprising (Table 4.6) (Chen et al., 2017; Poletti et al., 2016). However, it is not wholly unexpected as FA changes in the same subjects are not reported to be identical to connection strength measurements in SZ (van den Heuvel et al., 2010).

Prior work establishes a precedent that gene networks show associations with regional structural connectivity (Forest et al., 2017). Similarly, a recently published survey of 20,000 genes shows the average transcriptional profile of 85 SZ risk genes is associated with WM connectome disconnectivity (Romme et al., 2017). Dissecting these 85 risk genes into six functional classes such as neurodevelopment, synaptic function and glutamatergic neurotransmission illustrates only one gene class (calcium signaling) shows a significant relationship between connection strength in SZ. This study did not test age effects. Upon first survey of the entire subject age range of our genes of interest, we similarly observe nonexistent or weak correlations that didn't survive Bonferroni correction. However, significant associations emerge when subjects are separated into the older and younger age range. Together, these results support age-related models of WM topological degradation in SZ while also informing genetic underpinnings of age-related changes in connectivity.

Limitations

Some points should be taken into account when interpreting our results. The first is that we acknowledge the possible confounding factor of antipsychotic medications on the observed findings. The current study includes a relatively homogenous group with a clinical profile of severe enduring schizophrenia despite being medicated with atypical antipsychotics. However, it remains possible that long term use of antipsychotic medications contributes to effects observed in older subjects. While the effect of antipsychotic medications on gray matter volume are well-documented, there is relatively little evidence to suggest antipsychotics changes WM microstructure (Navari and Dazzan, 2009). Additional analysis examining the relationship between medication strength and graphics metrics was not performed in the current study because prior work in these subjects suggests no relationship between medication strength and WM microstructure. Specifically, previous analysis carried out in this subject cohort shows no correlation between patient FA and chlorpromazine equivalents for each patient's medication status (Holleran et al., 2014). The second point to take into account is that global graph metrics are not independent. Graph theory measures depend on the network density and thresholding of weak connections. In this study we chose not to vary the threshold to test for robustness because weak synaptic connections have been suggested to be critical for the expression of plasticity within a network (Poirazi and Mel, 2001).

Additional limitations of the study include the small patient sample size and that reported local effects did not survive FDR correction. The issue of small sample size was addressed by extensive permutation testing, which is applicable to very small sample sizes (Legendre et al. 2012). Due to the

multiple thousands of voxels that are tested, lack of survival of FDR correction is a frequently reported phenomenon in structural connectomics (Dennis et al., 2013; van den Heuvel et al., 2010; Verstraete et al., 2011; Zou et al., 2008). While alternative correction methods to reduce family-wise error rate have been proposed, none have been extensively adopted (Zalesky et al., 2010). An additional limitation of the current study is its cross-sectional design, which does not control for age of onset and medication history between patients. However, all subjects were relatively homogenous with SZ diagnosis. All patients were chronic and treatment resistant, being considered for a trial of clozapine. It is our hope that these findings provide a basis for future studies involving a longitudinal experimental design.

REFERENCES

Bassett, D.S., Bullmore, E., Verchinski, B.A., Mattay, V.S., Weinberger, D.R., Meyer-Lindenberg, A., 2008. Hierarchical organization of human cortical networks in health and schizophrenia. J Neurosci 28, 9239–9248. doi:10.1523/JNEUROSCI.1929-08.2008

Behrens, T.E.J., Berg, H.J., Jbabdi, S., Rushworth, M.F.S., Woolrich, M.W., 2007. Probabilistic diffusion tractography with multiple fibre orientations: What can we gain? Neuroimage 34, 144–155. doi:10.1016/j.neuroimage.2006.09.018

Benjamini, Y., Hochberg, Y., 1995. Controlling the false discovery rate: a practical and powerful approach to multiple testing. J. R. Stat. Soc. Ser. B 289–300.

Chen, J., Calhoun, V.D., Wu, L., Caprihan, A., Perrone-Bizzozero, N.I., Bustillo, J.R., Turner, J.A., et al., 2017. 628. Polygenic Risk Score for Schizophrenia of CREB1 and BDNF Associated with Structural Brain Dysconnectivity. Biol. Psychiatry 81, S254–S255. doi:10.1016/j.biopsych.2017.02.498

Dale, A.M., Fischl, B., Sereno, M.I., 1999. Cortical surface-based analysis. I. Segmentation and surface reconstruction. Neuroimage 9, 179–194. doi:10.1006/nimg.1998.0395

DeLisi, L.E., Sakuma, M., Tew, W., Kushner, M., Hoff, A.L., Grimson, R., 1997. Schizophrenia as a chronic active brain process: a study of progressive brain structural change subsequent to the onset of schizophrenia. Psychiatry Res. Neuroimaging 74, 129–140. doi:10.1016/S0925-4927(97)00012-7

Dennis, E.L., Jahanshad, N., McMahon, K.L., de Zubicaray, G.I., Martin, N.G., Hickie, I.B., Toga, A.W., Wright, M.J., Thompson, P.M., 2013. Development of brain structural connectivity between ages 12 and 30: a 4-Tesla diffusion imaging study in 439 adolescents and adults. Neuroimage 64, 671–684. doi:10.1016/j.neuroimage.2012.09.004

Filippi, M., van den Heuvel, M.P., Fornito, A., He, Y., Hulshoff Pol, H.E., Agosta, F., Comi, G., Rocca, M.A., 2013. Assessment of system dysfunction in the brain through MRI-based connectomics. Lancet Neurol 12, 1189–1199. doi:10.1016/S1474-4422(13)70144-3

First, M.B., Pincus, H.A., 2002. The DSM-IV Text Revision: rationale and potential impact on clinical practice. Psychiatr Serv 53, 288–292.

Fischl, B., Liu, A., Dale, A.M., 2001. Automated manifold surgery: constructing geometrically accurate and topologically correct models of the human cerebral cortex. IEEE Trans Med Imaging 20, 70–80. doi:10.1109/42.906426

Fischl, B., Salat, D.H., Busa, E., Albert, M., Dieterich, M., Haselgrove, C., van der Kouwe, A., Killiany, R., Kennedy, D., Klaveness, S., Montillo, A., Makris, N., Rosen, B., Dale, A.M., 2002. Whole brain segmentation: automated labeling of neuroanatomical structures in the human brain. Neuron 33, 341–55.

Fischl, B., Salat, D.H., van der Kouwe, A.J., Makris, N., Ségonne, F., Quinn, B.T., Dale, A.M., 2004a. Sequence-independent segmentation of magnetic resonance images. Neuroimage 23 Suppl 1, S69-84. doi:10.1016/j.neuroimage.2004.07.016

Fischl, B., Sereno, M.I., Tootell, R.B., Dale, A.M., 1999. High-resolution intersubject averaging and a coordinate system for the cortical surface. Hum Brain Mapp 8, 272–284.

Fischl, B., van der Kouwe, A., Destrieux, C., Halgren, E., Ségonne, F., Salat, D.H., Busa, E., Seidman, L.J., Goldstein, J., Kennedy, D., Caviness, V., Makris, N., Rosen, B., Dale, A.M., 2004b. Automatically parcellating the human cerebral cortex. Cereb Cortex 14, 11–22.

Forest, M., Iturria-Medina, Y., Goldman, J.S., Kleinman, C.L., Lovato, A., Oros Klein, K., Evans, A., Ciampi, A., Labbe, A., Greenwood, C.M.T., 2017. Gene networks show associations with seed region connectivity. Hum. Brain Mapp. 38, 3126–3140. doi:10.1002/hbm.23579

Fornito, A., Zalesky, A., Pantelis, C., Bullmore, E.T., 2012. Schizophrenia, neuroimaging and connectomics. Neuroimage 62, 2296–2314. doi:10.1016/j.neuroimage.2011.12.090

Freer, R., Sormanni, P., Vecchi, G., Ciryam, P., Dobson, C.M., Vendruscolo, M., 2016. A protein homeostasis signature in healthy brains recapitulates tissue vulnerability to Alzheimer's disease. Sci. Adv. 2.

Friedman, J.I., Tang, C., Carpenter, D., Buchsbaum, M., Schmeidler, J., Flanagan, L., Golembo, S., Kanellopoulou, I., Ng, J., Hof, P.R., Harvey, P.D., Tsopelas, N.D., Stewart, D., Davis, K.L., 2008. Diffusion Tensor Imaging Findings in First-Episode and Chronic Schizophrenia Patients. Am. J. Psychiatry 165, 1024–1032. doi:10.1176/appi.ajp.2008.07101640

Gogtay, N., 2008. Cortical brain development in schizophrenia: insights from neuroimaging studies in childhood-onset schizophrenia. Schizophr Bull 34, 30–36. doi:10.1093/schbul/sbm103

Gogtay, N., Giedd, J.N., Lusk, L., Hayashi, K.M., Greenstein, D., Vaituzis, A.C., Nugent, T.F., Herman, D.H., Clasen, L.S., Toga, A.W., Rapoport, J.L., Thompson, P.M., 2004. Dynamic mapping of human cortical development during childhood through early adulthood. Proc. Natl. Acad. Sci. U. S. A. 101, 8174–9. doi:10.1073/pnas.0402680101

Gong, G., Rosa-Neto, P., Carbonell, F., Chen, Z.J., He, Y., Evans, A.C., 2009. Age- and gender-related differences in the cortical anatomical network. J Neurosci 29, 15684–15693. doi:10.1523/JNEUROSCI.2308-09.2009
Greenstein, D., Lerch, J., Shaw, P., Clasen, L., Giedd, J., Gochman, P., Rapoport, J., Gogtay, N., 2006. Childhood onset schizophrenia: cortical brain abnormalities as young adults. J Child Psychol Psychiatry 47, 1003–1012. doi:10.1111/j.1469-7610.2006.01658.x

Hagmann, P., Sporns, O., Madan, N., Cammoun, L., Pienaar, R., Wedeen, V.J., Meuli, R., Thiran, J.-P., Grant, P.E., 2010. White matter maturation reshapes structural connectivity in the late developing human brain. Proc. Natl. Acad. Sci. U. S. A. 107, 19067–72. doi:10.1073/pnas.1009073107

Hawrylycz, M.J., Lein, E.S., Guillozet-Bongaarts, A.L., Shen, E.H., Ng, L., Miller, J.A., van de Lagemaat, L.N., et al., 2014. Altered interhemispheric and temporal lobe white matter microstructural organization in severe chronic schizophrenia. Neuropsychopharmacology 39, 944–954. doi:10.1038/npp.2013.294

Iturria-Medina, Y., Canales-Rodriguez, E.J., Aleman-Gomez, Y., Sotero, R.C., Melie-Garcia, L., 2008. Studying the human brain anatomical network via diffusion-weighted MRI and Graph Theory. Neuroimage 40, 1064–76. doi:10.1016/j.neuroimage.2007.10.060

Jones, D.K., Catani, M., Pierpaoli, C., Reeves, S.J., Shergill, S.S., O'Sullivan, M., Golesworthy, P., et al., 2006. Age effects on diffusion tensor magnetic resonance imaging tractography measures of frontal cortex connections in schizophrenia. Hum Brain Mapp 27, 230–238. doi:10.1002/hbm.20179

Jones, D.K., Horsfield, M.A., Simmons, A., 1999. Optimal strategies for measuring diffusion in anisotropic systems by magnetic resonance imaging. Magn. Reson. Med. 42, 515–25.

Kanaan, R.A., Picchioni, M.M., McDonald, C., Shergill, S.S., McGuire, P.K., 2017. White matter deficits in schizophrenia are global and don't progress with age. Aust. New Zeal. J. Psychiatry 486741770072. doi:10.1177/0004867417700729

Karlsgodt, K.H., van Erp, T.G., Poldrack, R.A., Bearden, C.E., Nuechterlein, K.H., Cannon, T.D., 2008. Diffusion tensor imaging of the superior longitudinal fasciculus and working memory in recent-onset schizophrenia. Biol Psychiatry 63, 512–518. doi:10.1016/j.biopsych.2007.06.017

Kochunov, P., Hong, L.E., 2014. Neurodevelopmental and neurodegenerative models of schizophrenia: white matter at the center stage. Schizophr Bull 40, 721–728. doi:10.1093/schbul/sbu070

Kong, X., Ouyang, X., Tao, H., Liu, H., Li, L., Zhao, J., Xue, Z., Wang, F., Jiang, S., Shan, B., Liu, Z., 2011. Complementary diffusion tensor imaging study of the corpus callosum in patients with first-episode and chronic schizophrenia. J. Psychiatry Neurosci. 36, 120–5. doi:10.1503/jpn.100041

Kubicki, M., Alvarado, J.L., Westin, C.F., Tate, D.F., Markant, D., Terry, D.P., Whitford, T.J., et al., 2011. Stochastic tractography study of Inferior Frontal Gyrus anatomical connectivity in schizophrenia. Neuroimage 55, 1657–1664. doi:10.1016/j.neuroimage.2011.01.047

Kubicki, M., Westin, C.F., Maier, S.E., Frumin, M., Nestor, P.G., Salisbury, D.F., Kikinis, R., Jolesz, F.A., McCarley, R.W., Shenton, M.E., 2002. Uncinate fasciculus findings in schizophrenia: a magnetic resonance diffusion tensor imaging study. Am J Psychiatry 159, 813–820.

Kuswanto, C.N., Teh, I., Lee, T.-S., Sim, K., 2012. Diffusion Tensor Imaging Findings of White Matter Changes in First Episode Schizophrenia: A Systematic Review. Clin. Psychopharmacol. Neurosci. 10, 13–24. doi:10.9758/cpn.2012.10.1.13

Kyriakopoulos, M., Frangou, S., 2009. Recent diffusion tensor imaging findings in early stages of schizophrenia. Curr Opin Psychiatry 22, 168–176. doi:10.1097/YCO.0b013e328325aa23

Leemans, A., Jones, D.K., 2009. The B-matrix must be rotated when correcting for subject motion in DTI data. Magn. Reson. Med. 61, 1336–49. doi:10.1002/mrm.21890

Luck, D., Buchy, L., Czechowska, Y., Bodnar, M., Pike, G.B., Campbell, J.S., Achim, A., Malla, A., Joober, R., Lepage, M., 2011. Fronto-temporal disconnectivity and clinical short-term outcome in first episode psychosis: a DTI-tractography study. J Psychiatr Res 45, 369–377. doi:10.1016/j.jpsychires.2010.07.007

Marder, E., Goaillard, J.M., 2006. Variability, compensation and homeostasis in neuron and network function. Nat Rev Neurosci 7, 563–574. doi:10.1038/nrn1949

Mayo, D.G., Cox, D.R., 2006. Frequentist Statistics as a Theory of Inductive Inference. Lect. Notes-Monograph Ser. doi:10.2307/4356393

Mori, T., Ohnishi, T., Hashimoto, R., Nemoto, K., Moriguchi, Y., Noguchi, H., Nakabayashi, T., Hori, H., Harada, S., Saitoh, O., Matsuda, H., Kunugi, H., 2007. Progressive changes of white matter integrity in schizophrenia revealed by diffusion tensor imaging. Psychiatry Res 154, 133–145. doi:10.1016/j.pscychresns.2006.09.004

Navari, S., Dazzan, P., 2009. Do antipsychotic drugs affect brain structure? A systematic and critical review of MRI findings. Psychol. Med. 39, 1763–77. doi:10.1017/S0033291709005315

Navlakha, S., He, X., Faloutsos, C., Bar-Joseph, Z., 2014. Topological properties of robust biological and computational networks. J R Soc Interface 11, 20140283. doi:10.1098/rsif.2014.0283

O'Donoghue, S., Holleran, L., Cannon, D.M., McDonald, C., 2017. Anatomical dysconnectivity in bipolar disorder compared with schizophrenia: A selective review of structural network analyses using diffusion MRI. J. Affect. Disord. 209, 217–228. doi:10.1016/j.jad.2016.11.015

Pantelis, C., Yücel, M., Wood, S.J., Velakoulis, D., Sun, D., Berger, G., Stuart, G.W., Yung, A., Phillips, L., McGorry, P.D., 2005. Structural brain imaging evidence for multiple pathological processes at different stages of brain development in schizophrenia. Schizophr Bull 31, 672–696. doi:10.1093/schbul/sbi034

Petanjek, Z., Judaš, M., Šimic, G., Rasin, M.R., Uylings, H.B.M., Rakic, P., Kostovic, I., 2011. Extraordinary neoteny of synaptic spines in the human prefrontal cortex. Proc. Natl. Acad. Sci. U. S. A. 108, 13281–6. doi:10.1073/pnas.1105108108

Pettersson-Yeo, W., Allen, P., Benetti, S., McGuire, P., Mechelli, A., 2011. Dysconnectivity in schizophrenia: where are we now? Neurosci Biobehav Rev 35, 1110–1124. doi:10.1016/j.neubiorev.2010.11.004

Piñero, J., Queralt-Rosinach, N., Bravo, À., Deu-Pons, J., Bauer-Mehren, A., Baron, M., Sanz, F., Furlong, L.I., 2015. DisGeNET: a discovery platform for the dynamical exploration of human diseases and their genes. Database (Oxford). 2015, bav028. doi:10.1093/database/bav028

Poirazi, P., Mel, B.W., 2001. Impact of active dendrites and structural plasticity on the memory capacity of neural tissue. Neuron 29, 779–796.

Poletti, S., Mazza, E., Bollettini, I., Falini, A., Smeraldi, E., Cavallaro, R., Benedetti, F., 2016. The COMT Val158Met polymorphism moderates the association between cognitive functions and white matter microstructure in schizophrenia. Psychiatr. Genet. 26, 193–202. doi:10.1097/YPG.0000000000000130

Price, G., Cercignani, M., Parker, G.J., Altmann, D.R., Barnes, T.R., Barker, G.J., Joyce, E.M., Ron, M.A., 2008. White matter tracts in first-episode psychosis: a DTI tractography study of the uncinate fasciculus. Neuroimage 39, 949–955. doi:10.1016/j.neuroimage.2007.09.012

Raj, A., Chen, Y.H., 2011. The wiring economy principle: connectivity determines anatomy in the human brain. PLoS One 6, e14832. doi:10.1371/journal.pone.0014832

Restrepo, J.G., Ott, E., Hunt, B.R., 2007. Approximating the largest eigenvalue of network adjacency matrices. Phys Rev E Stat Nonlin Soft Matter Phys 76, 56119.

Ripke, S., Neale, B.M., Corvin, A., Walters, J.T.R., Farh, K.-H., Holmans, P.A., Lee, P., et al, 2014. Biological insights from 108 schizophrenia-associated genetic loci. Nature 511, 421–427. doi:10.1038/nature13595

Romme, I.A.C., de Reus, M.A., Ophoff, R.A., Kahn, R.S., van den Heuvel, M.P., 2017. Connectome Disconnectivity and Cortical Gene Expression in Patients With Schizophrenia. Biol. Psychiatry 81, 495–502. doi:10.1016/j.biopsych.2016.07.012

Rubinov, M., Sporns, O., 2010. Complex network measures of brain connectivity: Uses and interpretations. Neuroimage 52, 1059–1069. doi:10.1016/j.neuroimage.2009.10.003

Samartzis, L., Dima, D., Fusar-Poli, P., Kyriakopoulos, M., 2014. White Matter Alterations in Early Stages of Schizophrenia: A Systematic Review of Diffusion

Tensor Imaging Studies. J. Neuroimaging 24, 101–110. doi:10.1111/j.1552-6569.2012.00779.x

Ségonne, F., Dale, A.M., Busa, E., Glessner, M., Salat, D., Hahn, H.K., Fischl, B., 2004. A hybrid approach to the skull stripping problem in MRI. Neuroimage 22, 1060–1075. doi:10.1016/j.neuroimage.2004.03.032

Skudlarski, P., Schretlen, D.J., Thaker, G.K., Stevens, M.C., Keshavan, M.S., Sweeney, J.A., Tamminga, C.A.,et al., 2013. Diffusion tensor imaging white matter endophenotypes in patients with schizophrenia or psychotic bipolar disorder and their relatives. Am J Psychiatry 170, 886–898. doi:10.1176/appi.ajp.2013.12111448

Szeszko, P.R., Robinson, D.G., Ashtari, M., Vogel, J., Betensky, J., Sevy, S., Ardekani, B.A., et al., 2008. Clinical and neuropsychological correlates of white matter abnormalities in recent onset schizophrenia. Neuropsychopharmacology 33, 976–984. doi:10.1038/sj.npp.1301480

Tononi, G., Sporns, O., Edelman, G.M., 1999. Measures of degeneracy and redundancy in biological networks. Proc Natl Acad Sci U S A 96, 3257–3262.

van den Heuvel, M.P., Mandl, R.C., Stam, C.J., Kahn, R.S., Hulshoff Pol, H.E., 2010. Aberrant frontal and temporal complex network structure in schizophrenia: a graph theoretical analysis. J Neurosci 30, 15915–15926. doi:10.1523/JNEUROSCI.2874-10.2010

Verstraete, E., Veldink, J.H., Mandl, R.C., van den Berg, L.H., van den Heuvel, M.P., 2011. Impaired structural motor connectome in amyotrophic lateral sclerosis. PLoS One 6, e24239. doi:10.1371/journal.pone.0024239

Wang, Q., Su, T.-P., Zhou, Y., Chou, K.-H., Chen, I.-Y., Jiang, T., Lin, C.-P., 2012. Anatomical insights into disrupted small-world networks in schizophrenia. Neuroimage 59, 1085–1093. doi:10.1016/j.neuroimage.2011.09.035

Zalesky, A., Fornito, A., Bullmore, E.T., 2010. Network-based statistic: Identifying differences in brain networks. Neuroimage 53, 1197–1207. doi:10.1016/j.neuroimage.2010.06.041

Zalesky, A., Fornito, A., Seal, M.L., Cocchi, L., Westin, C.F., Bullmore, E.T., Egan, G.F., Pantelis, C., 2011. Disrupted axonal fiber connectivity in schizophrenia. Biol Psychiatry 69, 80–89. doi:10.1016/j.biopsych.2010.08.022

Zhang, R., Wei, Q., Kang, Z., Zalesky, A., Li, M., Xu, Y., Li, L.,et al., 2015. Disrupted brain anatomical connectivity in medication-naïve patients with first-episode schizophrenia. Brain Struct. Funct. 220, 1145–1159. doi:10.1007/s00429-014-0706-z

Zou, K., Huang, X., Li, T., Gong, Q., Li, Z., Ou-yang, L., Deng, W., Chen, Q., Li, C., Ding, Y., Sun, X., 2008. Alterations of white matter integrity in adults with major depressive disorder: a magnetic resonance imaging study. J Psychiatry Neurosci 33, 525–530.

Chapter 6:
Toward an Umbrella Approach to Modeling Neurodegeneration: Clinical Implications, Future Studies and Conclusions

Recent advances in non-invasive neuroimaging technology and the application of graph theory to neural networks constitute a rapidly evolving field known as network neuroscience (Bassett and Sporns, 2017). Motivation behind the study of network neuroscience is rooted in the principle that illumination of higher brain function requires an understanding of brain network organization (Sporns, 2012; Sporns et al., 2005). A proliferation of studies have begun to unpack static states of brain network organization, both in healthy subjects and across a wide range of neural disorders (Bassett et al., 2008; de Haan et al., 2009; Redcay et al., 2013; Wang et al., 2012).

A recent focus has been placed on the mechanistic role that structural brain networks have in shaping brain dynamics, which is broadly defined as how the brain changes with time (Sporns, 2014). Given the progressive, stereotypical patterns of disease progression related to clinical symptomatology, mapping brain dynamics of neurodegeneration is a critical area of research (Brettschneider et al., 2015). In line with the core tenets of network neuroscience, the brain can change on two previously described dimensions: 1) Dynamics **on** brain networks (functional and pathological consequences taking place atop a static structural network) and 2) Dynamics **of** brain networks (changing structural networks).

The current thesis applies graph theoretic approaches and machine learning to multimodal human neuroimaging data with the central aim of

constructing predictive models to elucidate mechanisms of neurodegeneration. To achieve this aim, four distinct, but related, studies were performed. In Chapter two, we examined both dynamics **on** networks and dynamics **of** networks using a predictive pathology spread model to assess whether the structural network undergoes degeneration in Alzheimer's Disease (AD). Subsequently, in Chapter three, we showed a relationship between protein cerebrospinal fluid (CSF) biomarkers and atrophy and speed of disease progression. Chapter four focuses purely upon dynamics **on** networks by constructing several predictive models of pathology spread in Huntington's Disease (HD) as the first work to empirically test HD neurodegeneration hypotheses in vivo. In Chapter five, we switched gears to analyze dynamics **of** networks by exploring age-related organizational structural changes and the relationship to gene expression in chronic schizophrenia (SZ). This final chapter integrates findings across all four original studies and discusses the therapeutic implications of the current thesis, methodological considerations and future work.

Structural network mediates neurodegeneration and is preserved in Alzheimer's Disease

The first study that we presented sought to test hypotheses of both 1) Dynamics **on** networks as well as 2) Dynamics **of** networks in AD. Popular models of AD hypothesize stereotyped disease progression occurs via white matter (WM) fiber connections, most likely through trans-synaptic transmission of toxic proteins (Jucker and Walker, 2013). Hence, an important question in the field is whether and how organization of fiber pathways is affected by disease. It remains unknown whether fibers act as mere conduits of

degenerative pathologies, or if they also degenerate with the gray matter network.

Because a large body of evidence shows that WM integrity is weakened in AD, we tested the hypothesis that a compromised WM network mediates neurodegeneration (Hasan et al., 2012; Lee et al., 2015; Nir et al., 2013; Rowley et al., 2013). In Chapter 2, **Preserved Overall Network Organization in AD Spectrum Despite Loss of White Matter Tract Integrity**, we tested our hypothesis using our group's previously published Network Diffusion Model (NDM) as a tool. Graph theoretic analysis and the NDM were used in a longitudinal design of 124 subjects. We found that despite significant loss of WM integrity, the overall organization of the structural network remains intact.

Specifically, graph theory analysis showed preserved network organization in patients compared to controls. Topology is preserved on the global level (Figure 2.3), local level (Figure 2.4) and between distribution of hubs (Figure 2.5) in AD vs. age-matched controls. However, such results seemed to conflict with prior work, which report disturbances in AD structural network organization (Daianu et al., 2013; Lo et al., 2010; Prescott et al., 2014). Puzzled, we sought to find the source of our conflicting results. We replicated well-published differences in tract-level density (Figure 2.6), confirming there was no issue in our subject data or preprocessing pipelines.

Examination of our thresholding strategy revealed that the fact that we did not perform previously employed thresholding and binarization steps was likely the source of our discordant results (Figure 2.7). A literature search also showed that prior studies used smaller network graphs, most of which did not include subcortical regions (Table 2.8). To probe the effect of a potentially compromised WM network on disease spread, we examined local

eigenmodes, a structural characteristic previously shown to govern disease spread (Raj et al., 2015a, 2012). We found eigenmodes were virtually identical in patients compared to controls (Figure 2.8). Furthermore, use of a diseased connectome in place of a template connectome did not improve prediction accuracy of the NDM (Figure 2.9).

These results suggest that, despite measurable changes in integrity of specific fiber tracts, overall WM network organization in AD is preserved. Further, there is no difference in the mediation of putative pathology spread between healthy and AD-impaired networks. This conclusion is somewhat at variance with previous graph theory results, which report global topological disturbances in AD (Daianu et al., 2013; Lo et al., 2010; Prescott et al., 2014). Our data indicate that the combined effect of edge thresholding, binarization and inclusion of subcortical regions to network graphs may be responsible for alterations found in previous reports. Taken together, data presented in Chapter 2 support hypotheses encompassing dynamics **on** networks in AD. We showed that the WM network, which has been previously shown to mediate disease spread, is not significantly compromised in AD. Our conclusion is that the static WM network does not undergo change as a result of disease and may likely simply serve as a conduit for neurodegenerative pathology.

CSF biomarkers predict range of speed of neurodegeneration in AD

Having established that AD is indeed a disorder reflecting dynamics **on** networks, our next study sought to further understand the dynamics at play atop the static, preserved structural AD network. Biomarker hypotheses postulate that progression of AD pathology in the brain is related to and

proceded by protein biomarker changes in CSF (Jack and Holtzman, 2013) (Rosén et al., 2013). Numerous studies support this hypothesis, showing biomarker profiles related to AD, such as low AB and high Tau and pTau in CSF, are related to increased rates of global atrophy and cognitive decline (Barnes et al., 2013; Dickerson et al., 2012; Ewers et al., 2012; Schott et al., 2010; Stomrud et al., 2010; Young et al., 2014).

Hence, we turned our attention to examining the relationship between CSF biomarkers and the speed of degenerative pathology spread. A recent focus has been placed on the prognostic ability of molecular biomarkers to predict clinical outcomes for practical purposes such as differential diagnosis, therapeutic treatment and clinical trial inclusion (Ewers et al., 2015; Mattsson et al., 2014; Shaw et al., 2011; Tosun et al., 2016). Still, current methods to assess rate of degeneration often require multiple, expensive brain scans that may not be readily available in all clinical settings. Current measures of atrophy rates further relies on global brain volumes, without regard to the process by which progression proceeds in the brain. Therefore, we proposed that the rate parameter in our NDM model would serve as a more effective and more mechanistically relevant measure of rate of progression in AD. We hypothesized a subject's speed of degeneration could be predicted by baseline CSF metrics. In Chapter 3, **"A New Network-Constrained Technique to Characterize Neurodegenerative Progression Rate in Alzheimer's Disease,"** we tested our hypothesis using graph theory and machine learning in longitudinal data from 810 ADNI subjects. Our group's previously validated Network Diffusion Model (NDM), shown to accurately recapitulate patterns of AD spread, models a single parameter of disease progression rate based on a subject's longitudinal MRI data.

First, we show a significant correlation between a subject's global atrophy speed and speed of degeneration as modeled from the NDM (Figure 3.1). This suggests that our modeled beta parameter is indeed reflective of degeneration. Furthermore, we observe a significant effect of degeneration rate across diagnostic groups on the AD spectrum (Figure 3.2) in addition to an effect of APOE4 allele on degeneration rate (Figure 3.3). Interestingly, no significant relationships are found when modeling degeneration speed from baseline CSF metrics using regression or correlation analysis (Figure 3.4). However, hierarchical clustering shows three separate clusters emerge (Figure 3.5A), with significantly different rates of neurodegeneration as well as clinical severity across clusters (Figure 3.7). A K nearest neighbor classifier assigns subjects to clusters based on baseline CSF measurements with >90% high accuracy (Figure 3.5B). A range of degeneration speed can be inferred from cluster assignment. Furthermore, we illustrate that clusters have different profiles, with more pathogenic clusters characterized by classic disease-related CSF biomarker profiles (Figure 3.6). The more pathogenic clusters show higher rates of pathology spread, cognitive impairments and frequency of putative APOE4 alleles (Figure 3.7) (Figure 3.8).

Together, our results demonstrate a subject's range of degeneration speed can be predicted from baseline CSF biomarkers, which may be a practical, inexpensive screening tool for future prognostic applications. Note however that despite the predictability of range, it is still not currently possible to accurately predict the rate of an individual purely from baseline data. The addition of baseline atrophy somewhat improves the prediction of rate. Prediction accuracy is particularly high for the group of patients belonging to cluster 2, who are in the middle of their degenerative course. Overall, Chapter

3 lends further support to dynamics **on** networks, by elucidating the mechanisms atop the static structural network, further implicating the role of abnormal protein accumulation on the gray matter network, in neurodegeneration.

Structural network mediates neurodegeneration in Huntington's Disease

Thus far in the thesis, we have shown that a preserved structural network mediates disease spread in AD. We have also provided further data supporting the modeling of rate of degeneration from candidate CSF biomarkers. Next, we turn our attention to Huntington's Disease (HD). HD is different than AD in that the two diseases show different aetiologies, histopathological hallmarks and clinical phenotypes. However, they are similar in that they both exhibit a progressive, stereotyped nature of brain changes and clinical phenotypes associated with disease severity (Brettschneider et al., 2015).

Similar to AD, HD has a candidate misfolded protein species, mutant Huntingtin (HTT), which is hypothesized to flow trans-synaptically and pathologically throughout the network (Herrera et al., 2011; Lee et al., 2001; Tabrizi et al., 2016; Tan et al., 2015). Though several hypotheses of HD spread have been proposed, including distanced-based, activity-based and structural connectivity-based hypotheses, none have been evaluated empirically in vivo (Brettschneider et al., 2015). In Chapter 4, **Structural Network Model of Pathology Spread Predicts Neurodegeneration in Huntington's Disease**, we test several proposed, but to-date untested, models of how HD pathology initiates and spreads throughout the human brain. A large dataset of 231 subjects from the Track-HD study is used to build

and evaluate the following hypotheses in a cross-sectional manner: **1)** Different brain regions are selectively vulnerable to HD owing to the regional molecular composition patterns assessed via gene expression profiles (Figure 4.3B-E); **2)** HTT and downstream gene products are produced at local sites in proportion to their innate regional expression, but subsequently transmitted to remote sites via connectivity networks (Figure 4.3A); **3)** HD pathology seeding is focal and independent of gene expression, but subsequently ramify throughout the brain via network connections (Figure 4.4A3); **4)** HD pathology seeding is diffuse or random throughout the brain, but subsequent network transmission along a directional (anterograde) network can recapitulate both seeding and spread (Figure 4.5).

Since the process of trans-synaptic transmission of HTT is not conclusive in the literature, we also assessed a model of spatial spread, whereby **5)** spread between brain regions is governed by the distance (rather than connectivity) between them (Figure 4.4A1). Following recent proposals that neurodegenerative vulnerability is a result of neuronal activity between brain regions, we also assessed whether **6)** the NDM model of spread along the functional connectivity would fit empirical patterns better than NDM evolved on structural connectivity (Figure 4.4A) (Figure 4.8B).

Overall, our data show that even if HD pathology is diffuse or random throughout the brain, subsequent network transmission along a directional, anterograde structural network can recapitulate both seeding and spread (Figure 4.5). Specifically, we illustrate the striatum is the most likely source of pathology seeding in HD (Figure 4.6). Taken together, data presented in Chapter 4 utilizes graph theoretic approaches and predictive modeling as the first study to shed light on mechanisms of disease spread in HD using

hypotheses tested in vivo. Our data support models encompassing dynamics **on** networks implicated HD neurodegeneration, suggesting that, similar to AD, intrinsic structural architecture mediates disease spread in HD.

Structural network organization changes with disease progression in Schizophrenia

After successfully constructing and evaluating models encompassing dynamics **on** networks in AD and HD, we switched gears to dynamics **of** networks. Though not traditionally characterized as a neurodegenerative disorder, Schizophrenia (SZ) represented an excellent disorder to model dynamics **of** networks due to the ongoing gray and WM brain changes associated with the disease, which some scientists in the field classify as a neurodegenerative process (DeLisi et al., 1997; Kochunov et al., 2013; Kochunov and Hong, 2014). Unlike AD and HD, a candidate protein is not implicated in SZ pathology spread and there is no homogenous clinical phenotype nor progressive nature of symptomatology (O'Donoghue et al., 2017). Hence, it logically followed to evaluate SZ from a dynamics **of** network, rather than dynamics **on** network, perspective.

We hypothesized that we could recapitulate structural network degradation of SZ in a network model. The last presented study in the current thesis, Chapter 5, **Age-Related Changes in Topological Degradation of White Matter Networks and Gene Expression in Chronic Schizophrenia,** tests our hypothesis by modeling the change in structural brain architecture after disease onset and its relationship to gene expression in SZ. We apply graph theory analysis to diffusion MRI data from 75 subjects, including 24 clinically heterogeneous subjects with chronic SZ. Genetic analyses were

performed with microarray data collected from healthy brains by the Allen Brain Institute (Oh et al., 2014).

First, we replicated prior work illustrating overall differences in global structural organization in patients vs. age-matched controls (Figure 5.2). Novel results show significantly altered age-related network degradation patterns in patients compared to controls. Specifically, controls show stereotyped, linear global network decline with age. In contrast, patients show non-linear network decline with age (Figure 5.3). Further analysis reveals lack of significant topological decline in younger adult patients, which is subsequently followed by stereotyped linear decline in older adult patients (Figure 5.4). Local and global analyses show significant topological differences in frontal and limbic regions of younger adult patients compared to age-matched controls, which become less pronounced with age in older adult patients (Figure 5.5) (Figure 5.8A-B) (Figure 5.9A-B) (Figure 5.10A-B). Lastly, we show several gene expression profiles, including DISC1, are associated with age-related changes in WM disconnectivity (Figure 5.8C) (Figure 5.9C) (Figure 5.10C).

These findings provide novel WM topological and genetic support to neurodevelopmental hypotheses of SZ, suggesting network remodeling continues throughout the third decade of life before stabilizing. Overall, Chapter five offers additional evidence for the notion that structural networks in schizophrenia are dynamic. However, contrary to our hypothesis, structural architecture in schizophrenia appears to recapitulate a neurodevelopmental process, rather than neurodegeneration.

Treatment implications and future directions: Toward an umbrella model of neurodegeneration

The central aim of this thesis has been to build predictive models of neurodegenerative pathology spread. We examined models illustrating dynamics **on** networks as well as dynamics **of** structural networks. The last portion of this thesis will discuss treatment implications and future directions, with a dynamics **on** networks focus.

Treatment implications: Dynamics on structural networks

In Chapter 2, we used the NDM to show that despite extensive neurodegeneration on the gray matter network, AD pathology spread is mediated by a preserved structural network. Similarly, in Chapter 4, we tested six separate versions of the NDM to show that HD disease spread was also mediated by the, likely preserved, structural network. Because the NDM is based on eigen decomposition of the connectome, we note the structural eigenmode plays a crucial role in governing disease spread from a baseline state. Eigenfunctions are omnipresent in classical mechanics, where for example, standing waves in continuous media are eigenfunctions. In structural biology, the “normal modes” that describe the degrees of freedom of large molecules are the eigenfunctions of the equations that capture the relationship between the atoms of the molecule (Heller, 1981). Furthermore, many phenomena related to graphs or networks can be described in terms of the constituent graph eigenmodes, a field known as spectral graph theory, which has thus far had limited application in network neuroscience (Ng et al., 2002; Wang et al., 2017).

Conceptually, eigenmodes represent the orthogonal sub-networks of brain connectivity. Our lab has previously shown that the brain graph's low eigenmodes act as network attractors (AD, Chapter 2) or sinks (HD, Chapter 4) for neurodegenerative pathologies, brain activity and the spread of hyperactivity in epilepsy (Abdelnour et al., 2015a; Abdelnour et al., 2015b; Raj et al., 2015). Since these eigenmodes, or epicenters, have the lowest eigenvalues, linear dynamics will settle into those few modes.

Work conducted on both AD and HD leads us to conclude that disease spread in the two neurodegenerative pathologies is mediated by intrinsic structural network architecture, which remains the same, even in the diseased state. The discovery of preserved eigenmodes in the disordered brain is a result replicated outside of the present thesis. Recently, it was shown that structural eigenmodes are nearly identical between healthy subjects and even to a large extent conserved in severe neurodevelopmental brain malformations such as agenesis of the corpus callosum (Wang et al., 2017).

Our studies implicating the critical role of structural eigenmodes converge with prior work, which suggest neurodegenerative-associated networks contain vulnerable "epicenters" whose healthy connectivity serve as a template for template-directed misfolding (Zhou et al., 2012). These epicenters anchor distinct networks and are hypothesized to give rise to different clinicoanatomical presentations in neurodegeneration (Seeley, 2017). The connection between eigenmodes and brain epicenters is cemented by the high correlation between eigemode importance maps and structural edge density maps presented in Wang et al. 2017, which is a well-replicated result (Owen et al., 2016, 2015).

Taken together, we conclude that intrinsic structural brain architecture can be used, in conjunction with a scan capturing baseline state, to construct predictive network models of the dynamic process of neurodegeneration. We propose our model can be extended outside of just AD and HD to perhaps all neurodegenerative disorders, which exhibit characteristics of dynamics **on** structural networks, such as stereotyped gray matter network brain changes linked to candidate misfolded proteins. From a treatment perspective, this conclusion has substantial treatment implications. Prior network studies have focused on detecting differences between groups of patients and controls at discrete time points (Bassett et al., 2008; de Haan et al., 2009; Redcay et al., 2013; Wang et al., 2012).

While these studies are valuable in terms of finding relevant disease biomarkers, they are not sufficient for direct clinical diagnostic/prognostic adoption. The main reason is that many of these findings are statistically significant at the group level, but the individual discrimination ability of the proposed biomarkers is not typically evaluated (Arbabshirani et al., 2017; Rüb et al., 2001).

The NDM is a tool that can predict a single subject's future state of neurodegeneration. Eventual clinical adoption of the NDM could have widespread diagnostic and prognostic implications on differential diagnosis, treatment interventions and clinical trial inclusion. Furthermore, the ability to predict a subject's rate of pathology using CSF biomarkers, as performed in Chapter 3, could one day eliminate the need for multiple, time-consuming brain scans that require expensive equipment and processing. Clinical translation of work performed in Chapter 3 could result in the development of a

practical, inexpensive tool to predict neurodegeneration from a lumbar puncture, which could be used widely in all clinical settings.

Future directions: Dynamics on structural networks

Future directions for expanding the NDM as a clinically relevant prognostic tool include expansion of current work within AD and HD as well as development of the model in other neurodegenerative disorders, such as Parkinson's Disease (PD) and Amyotrophic Lateral Sclerosis (ALS). A future point of work as it relates to AD is to model protein biomarker dynamics of the disease. Chapter 3 shed light on the relationship between baseline protein biomarkers and prediction of a range of speed of neurodegeneration. The role of protein biomarkers in the etiology of AD is well-established (Andreasen et al., 2003, 2001; Hulstaert et al., 1999; Rosén et al., 2013; Tapiola et al., 2009). Specifically, it is known that the pathological processes in the brains of AD patients start more than a decade before the first symptoms are noticed (Jack et al., 2013; Price and Morris, 1999). However, biomarker data in the current subjects was gathered within a year of the baseline MRI scan, after subjects had already been diagnosed with dementia. Future work should focus on gathering CSF biomarker data in a longitudinal manner, before clinical manifestations of disease. Mapping the rate of neurodegeneration predicted by the NDM as a function of temporal dynamics of CSF biomarker profiles is critical. Such a work could potentially detect dementia long before clinical onset and could potentially lead to the development of preventative treatments.

In Chapter 4, we used the NDM as the first work to create a whole-brain predictive model of HD in vivo. A static, conserved WM network was assumed

in NDM construction as WM data from subjects in the Track-HD study was not available for our use. Prior work in the Track-HD cohort shows there are differences in WM organization in HD, which target the rich club (McColgan et al., 2015). Though our AD work in Chapter 2 suggests the WM network in HD is conserved, this assumption needs to be empirically tested for future model development.

Furthermore, evaluation of the NDM is HD was performed in a cross-sectional manner, because longitudinal data was not available to us. Our cross-sectional design was adequate to determine which seeding and transmission strategies were sufficient to recapitulate stereotyped patterns of HD atrophy. However, our model must be expanded to show it can reproduce longitudinal aspects of HD progression in a longitudinal study design.

Lastly, future work to expand the NDM in HD should include mathematically modeling the effect of genetic repeat length. A proliferation of work shows a significant association between the length of the trinucleotide CAG repeat and age of HD onset (Andrew et al., 1993; Chen and Wolynes, 2017; Duyao et al., 1993). Significant associations between the rate of striatal atrophy and mutation length have also been reported (Aylward et al., 2000). Hence, precise prediction of a subject's age of onset, with added granularity of how fast the brain will degenerate could offer significant clinical promise for the treatment of HD.

Treatment implications and future directions: Dynamics of structural networks

Though our study examining dynamics **of** structural networks in SZ did not model neurodegenerative aspects of the disease, the impact of the work is

not diminished. In Chapter 5, we showed the presence of an extended neurodevelopmental period of WM network reorganization, which was associated with gene expression. There is a wide body of work providing insight into specific genes that may be involved in the aetiology of SZ. For example, the Schizophrenia Working Group of the Psychiatric Genomics Consortium examined over 150,000 cases to show 128 significant independent gene associations, spanning 108 loci (Ripke et al., 2014). Similarly, a study of 418 subjects revealed novel deletions and duplications of genes that were highly linked to SZ (Walsh et al., 2008). Fewer studies examine associations between SZ neuroimaging biomarkers and genes (Chavarria-Siles et al., 2016; Terwisscha van Scheltinga et al., 2013).

However, much of this work consists of large GWAS studies that do not specifically link the relationship between the brain's local gene expression and structural architecture. Earlier this year, the relationship between local gene expression and connectome disconnectivity was established, as measured by fiber tract connectivity density (Romme et al., 2017). We extend prior reports as the first work utilizing multiple topological graph metrics to empirically evaluate the relationship between local gene expression and WM network organization. Treatment implications of our work are substantial. Discovery of candidate genes that may be linked specifically to structural network organization may one day elucidate the specific genes linked to the "split" (schizo) "mind" (phrenia) phenotype (Bleuler, 2010). It is our hope that discovery of such candidate genes will lead to treatment for the remediation of altered pathways, either in utero or in early development before disease onset.

Our work in Chapter 5 focused on the development of a network model to capture dynamics **of** structural networks in SZ. Going forward, the proposed

model must be validated. Unlike our studies in AD and HD, our SZ study had less than 100 subjects, which significantly limits model generalizability (Waller et al., 2017). Future work will validate our model in a significantly larger subset of clinically heterogeneous SZ subjects and ancestry-matched controls.

Further illumination of the relationship between structural network organization, gene expression and clinical severity is also critical. We did not have access to individual subject clinical profiles and were thus unable to build a more comprehensive model, which would illustrate clinical relevance. Inclusion of individual clinical profiles as well as inclusion of a less homogenous patient group into future models will shed light on potential SZ subtypes. It is well-documented that there exist subtypes of SZ, including schizoaffective, schizophreniform and schizotypal personality disorder, which show different clinical profiles, outcomes and neuroimaging biomarkers (Fenton et al., 1997; Takahashi et al., 2017; Weinberg et al., 2016). Expansion of the current work through validation and addition of clinical metrics will ultimately lead to the eventual construction of whole-brain predictive models of SZ. Such a model could lead to better characterization of subtypes and their associated WM network organization for differential diagnosis and targeted treatment for patients that may response to a specific drug class or type.

Conclusion

Understanding network organization is critical to elucidating higher order brain interactions. Though studies examining static network differences in neurodegenerative pathology have been carried out at discrete time points, models of how the brain changes with disease progression are lacking. In this thesis, we elucidated mechanisms of neurodegeneration through the

construction and evaluation of whole brain predictive models. Using Alzheimer's Disease and Huntington's Disease, we show that prion-like disease spread in neurodegeneration is mediated by intrinsic structural network architecture. Models of Schizophrenia also illustrate the importance of structural architecture, as we show ongoing structural network remodeling associated with gene expression into the third decade. This process appears to be more neurodevelopmental than neurodegenerative. Going forward, we suggest the possibility for the creation of an umbrella model of neurodegeneration, which is is rooted in intrinsic structural network architecture in the Network Diffusion Model. We also suggest future studies that can validate the proposed neurodevelopmental model in Schizophrenia. It is our hope that the work presented in the present thesis is the basis of future work that leads to practical, prognostic and diagnostic clinical tools for the prediction of neurodegeneration on the single-subject level.

REFERENCES

Abdelnour, F., Dayan, M., Devinsky, O., 2015. Estimating brain's functional graph from the structural graph's Laplacian. SPIE Opt.

Abdelnour, F., Mueller, S., Raj, A., 2015. Relating Cortical Atrophy in Temporal Lobe Epilepsy with Graph Diffusion-Based Network Models. PLoS Comput. Biol. 11, e1004564.

Abrahams, S., Goldstein, L.H., Suckling, J., Ng, V., Simmons, A., Chitnis, X., Atkins, L., Williams, S.C.R., Leigh, P.N., 2005. Frontotemporal white matter changes in amyotrophic lateral sclerosis. J. Neurol. 252, 321–331. doi:10.1007/s00415-005-0646-x

Amad, A., Cachia, A., Gorwood, P., Pins, D., Delmaire, C., Rolland, B., Mondino, M., Thomas, P., Jardri, R., 2014. The multimodal connectivity of the hippocampal complex in auditory and visual hallucinations. Mol. Psychiatry 19, 184–191. doi:10.1038/mp.2012.181

Andreasen, N., Minthon, L., Davidsson, P., Vanmechelen, E., Vanderstichele, H., Winblad, B., Blennow, K., 2001. Evaluation of CSF-tau and CSF-Abeta42 as diagnostic markers for Alzheimer disease in clinical practice. Arch. Neurol. 58, 373–9.

Andreasen, N., Sjögren, M., Blennow, K., 2003. CSF markers for Alzheimer's disease: total tau, phospho-tau and Abeta42. World J. Biol. Psychiatry 4, 147–55.

Andrew, S., Goldberg, Y., Kremer, B., Telenius, H., 1993. The relationship between trinucleotide (CAG) repeat length and clinical features of Huntington's disease. Nature.

Arbabshirani, M.R., Plis, S., Sui, J., Calhoun, V.D., 2017. Single subject prediction of brain disorders in neuroimaging: Promises and pitfalls. Neuroimage 145, 137–165. doi:10.1016/j.neuroimage.2016.02.079

Arrasate, M., Finkbeiner, S., 2012. Protein aggregates in Huntington's disease. Exp. Neurol. 238, 1–11. doi:10.1016/j.expneurol.2011.12.013

Ashe, P.C., Berry, M.D., Boulton, A.A., 2001. Schizophrenia, a neurodegenerative disorder with neurodevelopmental antecedents. Prog. Neuro-Psychopharmacology Biol. Psychiatry 25, 691–707. doi:10.1016/S0278-5846(01)00159-2

Attems, J., Thal, D.R., Jellinger, K.A., 2012. The relationship between subcortical tau pathology and Alzheimer's disease. Biochem. Soc. Trans. 40, 711–5.

Aylward, E.H., Codori, A.M., Rosenblatt, A., Sherr, M., Brandt, J., Stine, O.C., Barta, P.E., Pearlson, G.D., Ross, C.A., 2000. Rate of caudate atrophy in presymptomatic and symptomatic stages of Huntington's disease. Mov. Disord. 15, 552–560. doi:10.1002/1531-8257(200005)15:3<552::AID-MDS1020>3.0.CO;2-P

Bai, F., Shu, N., Yuan, Y., Shi, Y., Yu, H., Wu, D., Wang, J., Xia, M., He, Y., Zhang, Z., 2012. Topologically Convergent and Divergent Structural Connectivity Patterns between Patients with Remitted Geriatric Depression and Amnestic Mild Cognitive Impairment. J. Neurosci. 32.

Barnes, J., Carmichael, O.T., Leung, K.K., Schwarz, C., Ridgway, G.R., Bartlett, J.W., Malone, I.B., Schott, J.M., Rossor, M.N., Biessels, G.J., DeCarli, C., Fox, N.C., 2013. Vascular and Alzheimer's disease markers independently predict brain atrophy rate in Alzheimer's Disease Neuroimaging Initiative controls. Neurobiol. Aging 34, 1996–2002. doi:10.1016/j.neurobiolaging.2013.02.003

Bassett, D.S., Bullmore, E., Verchinski, B.A., Mattay, V.S., Weinberger, D.R., Meyer-Lindenberg, A., 2008. Hierarchical organization of human cortical networks in health and schizophrenia. J Neurosci 28, 9239–9248. doi:10.1523/JNEUROSCI.1929-08.2008

Bassett, D.S., Sporns, O., 2017. Network neuroscience. Nat. Neurosci. 20, 353–364. doi:10.1038/nn.4502

Becher, M.W., Kotzuk, J.A., Sharp, A.H., Davies, S.W., Bates, G.P., Price, D.L., Ross, C.A., 1998. Intranuclear Neuronal Inclusions in Huntington's Disease and Dentatorubral and Pallidoluysian Atrophy: Correlation between the Density of Inclusions andIT15CAG Triplet Repeat Length. Neurobiol. Dis. 4, 387–397. doi:10.1006/nbdi.1998.0168

Benes, F.M., Turtle, M., Khan, Y., Farol, P., 1994. Myelination of a key relay zone in the hippocampal formation occurs in the human brain during childhood, adolescence, and adulthood. Arch. Gen. Psychiatry 51, 477–84.

Bird, T., Knopman, D., VanSwieten, J., Rosso, S., Feldman, H., Tanabe, H., Graff-Raford, N., Geschwind, D., Verpillat, P., Hutton, M., 2003. Epidemiology and genetics of frontotemporal dementia/Pick's disease. Ann. Neurol. 54, S29–S31. doi:10.1002/ana.10572

Bleuler, E., 2010. [Dementia praecox or the group of schizophrenias]. Vertex 21, 394–400.

Braak, H., Braak, E., 1996. Evolution of the neuropathology of Alzheimer's disease. Acta Neurol. Scand. Suppl. 165, 3–12.

Braak, H., Braak, E., 1991. Neuropathological stageing of Alzheimer-related changes. Acta Neuropathol. 82, 239–59.

Brenner, S., 1974. The genetics of Caenorhabditis elegans. Genetics 77, 71–94.

Brettschneider, J., Tredici, K. Del, Lee, V., 2015. Spreading of pathology in neurodegenerative diseases: a focus on human studies. Nat. Rev.

Brundin, P., Melki, R., Kopito, R., 2010. Prion-like transmission of protein aggregates in neurodegenerative diseases. Nat. Rev. Mol. Cell Biol.

Bullmore, E., Sporns, O., 2009. Complex brain networks: graph theoretical analysis of structural and functional systems. Nat. Rev. Neurosci. 10, 186–198. doi:10.1038/nrn2575

Chavarria-Siles, I., White, T., de Leeuw, C., Goudriaan, A., Lips, E., Ehrlich, S., Turner, J.A., Calhoun, V.D., Gollub, R.L., Magnotta, V.A., Ho, B.-C., Smit, A.B., Verheijen, M.H.G., Posthuma, D., 2016. Myelination-related genes are associated with decreased white matter integrity in schizophrenia. Eur. J. Hum. Genet. 24, 381–6. doi:10.1038/ejhg.2015.120

Chen, M., Wolynes, P.G., 2017. Aggregation landscapes of Huntingtin exon 1 protein fragments and the critical repeat length for the onset of Huntington's disease. Proc. Natl. Acad. Sci. U. S. A. 114, 4406–4411. doi:10.1073/pnas.1702237114

Clavaguera, F., Bolmont, T., Crowther, R.A., Abramowski, D., Frank, S., Probst, A., Fraser, G., Stalder, A.K., Beibel, M., Staufenbiel, M., Jucker, M., Goedert, M., Tolnay, M., 2009. Transmission and spreading of tauopathy in transgenic mouse brain. Nat. Cell Biol. 11, 909–913. doi:10.1038/ncb1901

Daianu, M., Jahanshad, N., Nir, T.M., Jack, C.R., Weiner, M.W., Bernstein, M.A., Thompson, P.M., 2015. Rich club analysis in the Alzheimer's disease connectome reveals a relatively undisturbed structural core network. Hum. Brain Mapp. 36, 3087–3103. doi:10.1002/hbm.22830

Daianu, M., Jahanshad, N., Nir, T.M., Toga, A.W., Jack, C.R., Weiner, M.W., Thompson, for the Alzheimer's Disea, P.M., Alzheimer's Disease Neuroimaging Initiative, 2013. Breakdown of Brain Connectivity Between Normal Aging and Alzheimer's Disease: A Structural *k* -Core Network Analysis. Brain Connect. 3, 407–422. doi:10.1089/brain.2012.0137

Damoiseaux, J.S., Smith, S.M., Witter, M.P., Sanz-Arigita, E.J., Barkhof, F., Scheltens, P., Stam, C.J., Zarei, M., Rombouts, S.A.R.B., 2009. White matter tract integrity in aging and Alzheimer's disease. Hum. Brain Mapp. 30, 1051–1059. doi:10.1002/hbm.20563

Davies, S.W., Turmaine, M., Cozens, B.A., DiFiglia, M., Sharp, A.H., Ross, C.A., Scherzinger, E., Wanker, E.E., Mangiarini, L., Bates, G.P., 1997. Formation of neuronal intranuclear inclusions underlies the neurological dysfunction in mice transgenic for the HD mutation. Cell 90, 537–48.

de Calignon, A., Polydoro, M., Suárez-Calvet, M., William, C., Adamowicz, D.H., Kopeikina, K.J., Pitstick, R., Sahara, N., Ashe, K.H., Carlson, G. a., Spires-Jones, T.L., Hyman, B.T., 2012. Propagation of tau pathology in a model of early Alzheimer's disease. Neuron 73, 685–97. doi:10.1016/j.neuron.2011.11.033

de Haan, W., Pijnenburg, Y.A.L., Strijers, R.L.M., van der Made, Y., van der Flier, W.M., Scheltens, P., Stam, C.J., 2009. Functional neural network analysis in frontotemporal dementia and Alzheimer's disease using EEG and graph theory. BMC Neurosci. 10, 101. doi:10.1186/1471-2202-10-101

de la Monte, S.M., Vonsattel, J.-P., Richardson, E.P., 1988. Morphometric Demonstration of Atrophic Changes in the Cerebral Cortex, White Matter, and Neostriatum in Huntington's Disease. J. Neuropathol. Exp. Neurol. 47, 516–525. doi:10.1097/00005072-198809000-00003

Deco, G., Kringelbach, M., 2014. Great Expectations: Using Whole-Brain Computational Connectomics for Understanding Neuropsychiatric Disorders. Neuron 84, 892–905. doi:10.1016/j.neuron.2014.08.034

DeLisi, L.E., 1992. The Significance of Age of Onset for Schizophrenia. Schizophr. Bull. 18, 209–215. doi:10.1093/schbul/18.2.209

DeLisi, L.E., Sakuma, M., Tew, W., Kushner, M., Hoff, A.L., Grimson, R., 1997. Schizophrenia as a chronic active brain process: a study of progressive brain structural change subsequent to the onset of schizophrenia. Psychiatry Res. Neuroimaging 74, 129–140. doi:10.1016/S0925-4927(97)00012-7

Dickerson, B.C., Wolk, D.A., Alzheimer's Disease Neuroimaging Initiative, 2012. MRI cortical thickness biomarker predicts AD-like CSF and cognitive decline in normal adults. Neurology 78, 84–90. doi:10.1212/WNL.0b013e31823efc6c

Duyao, M., Ambrose, C., Myers, R., Novelletto, A., Persichetti, F., Frontali, M., Folstein, S., et al., 1993. Trinucleotide repeat length instability and age of onset in Huntington's disease. Nat. Genet. 4, 387–392. doi:10.1038/ng0893-387

Ewers, M., Insel, P., Jagust, W.J., Shaw, L., Trojanowski J, J.Q., Aisen, P., Petersen, R.C., Schuff, N., Weiner, M.W., 2012. CSF Biomarker and PIB-PET-Derived Beta-Amyloid Signature Predicts Metabolic, Gray Matter, and Cognitive Changes in Nondemented Subjects. Cereb. Cortex 22, 1993–2004. doi:10.1093/cercor/bhr271

Ewers, M., Mattsson, N., Minthon, L., Molinuevo, J.L., Antonell, A., Popp, J., Jessen, F., Herukka, S.-K., Soininen, H., Maetzler, W., Leyhe, T., Bürger, K., Taniguchi, M., Urakami, K., Lista, S., Dubois, B., Blennow, K., Hampel, H., 2015. CSF biomarkers for the differential diagnosis of Alzheimer's disease: A large-scale international multicenter study. Alzheimer's Dement. 11, 1306–1315. doi:10.1016/j.jalz.2014.12.006

Fenton, W., McGlashan, T., Victor, B., 1997. Symptoms, subtype, and suicidality in patients with schizophrenia spectrum disorders. Am. J.

Fischer, C.E., Ting, W.K.-C., Millikin, C.P., Ismail, Z., Schweizer, T.A., Alzheimer Disease Neuroimaging Initiative, 2016. Gray matter atrophy in patients with mild cognitive impairment/Alzheimer's disease over the course of developing delusions. Int. J. Geriatr. Psychiatry 31, 76–82. doi:10.1002/gps.4291

Fornito, A., Zalesky, A., Pantelis, C., Bullmore, E.T., 2012. Schizophrenia, neuroimaging and connectomics. Neuroimage 62, 2296–2314. doi:10.1016/j.neuroimage.2011.12.090

Fujino, J., Takahashi, H., Miyata, J., Sugihara, G., Kubota, M., Sasamoto, A., Fujiwara, H., Aso, T., Fukuyama, H., Murai, T., 2014. Impaired empathic abilities and reduced white matter integrity in schizophrenia. Prog. Neuro-Psychopharmacology Biol. Psychiatry 48, 117–123. doi:10.1016/j.pnpbp.2013.09.018

Guimera, R., Mossa, S., Turtschi, A., Amaral, L.A.N., 2005. The worldwide air transportation network: Anomalous centrality, community structure, and cities' global roles. Proc. Natl. Acad. Sci. 102, 7794–7799. doi:10.1073/pnas.0407994102

Gutekunst, C.-A., Li, S.-H., Yi, H., Mulroy, J.S., Kuemmerle, S., Jones, R., Rye, D., Ferrante, R.J., Hersch, S.M., Li, X.-J., 1999. Nuclear and Neuropil Aggregates in Huntington's Disease: Relationship to Neuropathology. J. Neurosci. 19.

Harper, P., 1992. The epidemiology of Huntington's disease. Hum. Genet. 89, 365–376. doi:10.1007/BF00194305

Harris, G.J., Pearlson, G.D., Peyser, C.E., Aylward, E.H., Roberts, J., Barta, P.E., Chase, G.A., Folstein, S.E., 1992. Putamen volume reduction on magnetic resonance imaging exceeds caudate changes in mild Huntington's disease. Ann. Neurol. 31, 69–75. doi:10.1002/ana.410310113

Hasan, M.K., Lee, W., Park, B., Han, K., 2012. Connectivity Analysis of Hippocampus in Alzheimer's Brain Using Probabilistic Tractography. pp. 521–528. doi:10.1007/978-3-642-24553-4_69

Heinemann, S.D., Posimo, J.M., Mason, D.M., Hutchison, D.F., Leak, R.K., 2016. Synergistic stress exacerbation in hippocampal neurons: Evidence favoring the dual-hit hypothesis of neurodegeneration. Hippocampus 26, 980–994. doi:10.1002/hipo.22580

Heller, E., 1981. The semiclassical way to molecular spectroscopy. Acc. Chem. Res.

Herrera, F., Tenreiro, S., Miller-Fleming, L., 2011. Visualization of cell-to-cell transmission of mutant huntingtin oligomers. PLOS Curr.

Hodgson, J.G., Agopyan, N., Gutekunst, C.-A., Leavitt, B.R., LePiane, F., Singaraja, R., Smith, D.J., Bissada, N., McCutcheon, K., Nasir, J., Jamot, L., Li, X.-J., Stevens, M.E., Rosemond, E., Roder, J.C., Phillips, A.G., Rubin, E.M., Hersch, S.M., Hayden, M.R., 1999. A YAC Mouse Model for Huntington?s Disease with Full-Length Mutant Huntingtin, Cytoplasmic Toxicity, and Selective Striatal Neurodegeneration. Neuron 23, 181–192. doi:10.1016/S0896-6273(00)80764-3

Holme, P., Saramäki, J., 2012. Temporal networks. Phys. Rep.

Huisman, M.H.B., de Jong, S.W., van Doormaal, P.T.C., Weinreich, S.S., Schelhaas, H.J., van der Kooi, A.J., de Visser, M., Veldink, J.H., van den Berg, L.H., 2011. Population based epidemiology of amyotrophic lateral sclerosis using capture-recapture methodology. J. Neurol. Neurosurg. Psychiatry 82, 1165–1170. doi:10.1136/jnnp.2011.244939

Hulstaert, F., Blennow, K., Ivanoiu, A., Schoonderwaldt, H.C., Riemenschneider, M., De Deyn, P.P., Bancher, C., Cras, P., Wiltfang, J., Mehta, P.D., Iqbal, K., Pottel, H., Vanmechelen, E., Vanderstichele, H., 1999. Improved discrimination of AD patients using beta-amyloid(1-42) and tau levels in CSF. Neurology 52, 1555–62.

Iba, M., Guo, J.L., McBride, J.D., Zhang, B., Trojanowski, J.Q., Lee, V.M.-Y., 2013. Synthetic Tau Fibrils Mediate Transmission of Neurofibrillary Tangles in a Transgenic Mouse Model of Alzheimer's-Like Tauopathy. J. Neurosci. 33.

Iba, M., McBride, J.D., Guo, J.L., Zhang, B., Trojanowski, J.Q., Lee, V.M.-Y., 2015. Tau pathology spread in PS19 tau transgenic mice following locus coeruleus (LC) injections of synthetic tau fibrils is determined by the LC's afferent and efferent connections. Acta Neuropathol. 130, 349–62.

Jack, C.R., Holtzman, D.M., 2013. Biomarker Modeling of Alzheimer's Disease. Neuron 80, 1347–1358. doi:10.1016/j.neuron.2013.12.003

Jack, C.R., Knopman, D.S., Jagust, W.J., Petersen, R.C., Weiner, M.W., Aisen, P.S., Shaw, L.M., Vemuri, P., Wiste, H.J., Weigand, S.D., Lesnick, T.G., Pankratz, V.S., Donohue, M.C., Trojanowski, J.Q., 2013. Tracking pathophysiological processes in Alzheimer's disease: an updated hypothetical model of dynamic biomarkers. Lancet Neurol. 12, 207–216. doi:10.1016/S1474-4422(12)70291-0

Jucker, M., Walker, L.C., 2013. Self-propagation of pathogenic protein aggregates in neurodegenerative diseases. Nature 501, 45–51. doi:10.1038/nature12481

Karran, E., Mercken, M., Strooper, B. De, 2011. The amyloid cascade hypothesis for Alzheimer's disease: an appraisal for the development of therapeutics. Nat. Rev. Drug Discov. 10, 698–712. doi:10.1038/nrd3505

Kim, Y.J., Yi, Y., Sapp, E., Wang, Y., Cuiffo, B., Kegel, K.B., Qin, Z.H., Aronin, N., DiFiglia, M., 2001. Caspase 3-cleaved N-terminal fragments of wild-type and mutant huntingtin are present in normal and Huntington's disease brains, associate with membranes, and undergo calpain-dependent proteolysis. Proc. Natl. Acad. Sci. U. S. A. 98, 12784–9. doi:10.1073/pnas.221451398

Kloppel, S., Draganski, B., Golding, C. V., Chu, C., Nagy, Z., Cook, P.A., Hicks, S.L., Kennard, C., Alexander, D.C., Parker, G.J.M., Tabrizi, S.J., Frackowiak, R.S.J., 2008. White matter connections reflect changes in voluntary-guided saccades in pre-symptomatic Huntington's disease. Brain 131, 196–204. doi:10.1093/brain/awm275

Kochunov, P., Glahn, D.C., Rowland, L.M., Olvera, R.L., Winkler, A., Yang, Y.H., Sampath, H., Carpenter, W.T., Duggirala, R., Curran, J., Blangero, J., Hong, L.E., 2013. Testing the hypothesis of accelerated cerebral white matter aging in schizophrenia and major depression. Biol Psychiatry 73, 482–491. doi:10.1016/j.biopsych.2012.10.002

Kochunov, P., Hong, L.E., 2014. Neurodevelopmental and neurodegenerative models of schizophrenia: white matter at the center stage. Schizophr Bull 40, 721–728. doi:10.1093/schbul/sbu070

Kuemmerle, S., Gutekunst, C.-A., Klein, A.M., Li, X.-J., Li, S.-H., Beal, M.F., Hersch, S.M., Ferrante, R.J., 1999. Huntingtin aggregates may not predict neuronal death in Huntington's disease. Ann. Neurol. 46, 842–849. doi:10.1002/1531-8249(199912)46:6<842::AID-ANA6>3.0.CO;2-O

Lee, S.-H., Coutu, J.-P., Wilkens, P., Yendiki, A., Rosas, H.D., Salat, D.H., 2015. Tract-based analysis of white matter degeneration in Alzheimer's disease. Neuroscience 301, 79–89. doi:10.1016/j.neuroscience.2015.05.049

Lee, V.M.-Y., Goedert, M., Trojanowski, J.Q., 2001. Neurodegenerative Tauopathies. Annu. Rev. Neurosci. 24, 1121–1159. doi:10.1146/annurev.neuro.24.1.1121

Liu, X., Lai, Y., Wang, X., Hao, C., Chen, L., Zhou, Z., Yu, X., Hong, N., 2014. A combined DTI and structural MRI study in medicated-na?ve chronic schizophrenia. Magn. Reson. Imaging 32, 1–8. doi:10.1016/j.mri.2013.08.004

Lo, C.-Y., Wang, P.-N., Chou, K.-H., Wang, J., He, Y., Lin, C.-P., 2010. Diffusion Tensor Tractography Reveals Abnormal Topological Organization in Structural Cortical Networks in Alzheimer's Disease. J. Neurosci. 30. doi:10.1523/JNEUROSCI.4136-10.2010

Marrakchi-Kacem, L., Delmaire, C., Guevara, P., Poupon, F., Lecomte, S., Tucholka, A., Roca, P., Yelnik, J., Durr, A., Mangin, J.-F., Leh?ricy, S., Poupon, C., 2013. Mapping Cortico-Striatal Connectivity onto the Cortical Surface: A New Tractography-Based Approach to Study Huntington Disease. PLoS One 8, e53135. doi:10.1371/journal.pone.0053135

Mattsson, N., Insel, P.S., Landau, S., Jagust, W., Donohue, M., Shaw, L.M., Trojanowski, J.Q., Zetterberg, H., Blennow, K., Weiner, M., 2014. Diagnostic accuracy of CSF Ab42 and florbetapir PET for Alzheimer's disease. Ann. Clin. Transl. Neurol. 1, 534–543. doi:10.1002/acn3.81

McColgan, P., Seunarine, K.K., Razi, A., Cole, J.H., Gregory, S., Durr, A., Roos, R.A.C., Stout, J.C., Landwehrmeyer, B., Scahill, R.I., Clark, C.A., Rees, G., Tabrizi, S.J., 2015. Selective vulnerability of Rich Club brain regions is an organizational principle of structural connectivity loss in Huntington?s disease. Brain 138, 3327–3344. doi:10.1093/brain/awv259

Mori, T., Ohnishi, T., Hashimoto, R., Nemoto, K., Moriguchi, Y., Noguchi, H., Nakabayashi, T., Hori, H., Harada, S., Saitoh, O., Matsuda, H., Kunugi, H., 2007. Progressive changes of white matter integrity in schizophrenia revealed by diffusion tensor imaging. Psychiatry Res 154, 133–145. doi:10.1016/j.pscychresns.2006.09.004

Neumann, M., Sampathu, D.M., Kwong, L.K., Truax, A.C., Micsenyi, M.C., Chou, T.T., Bruce, J., Schuck, T., Grossman, M., Clark, C.M., McCluskey, L.F., Miller, B.L., Masliah, E., Mackenzie, I.R., Feldman, H., Feiden, W., Kretzschmar, H.A., Trojanowski, J.Q., Lee, V.M.-Y., 2006. Ubiquitinated TDP-43 in Frontotemporal Lobar Degeneration and Amyotrophic Lateral Sclerosis. Science (80-.). 314, 130–133. doi:10.1126/science.1134108

Ng, A., Jordan, M., Weiss, Y., 2002. On spectral clustering: Analysis and an algorithm. Adv. neural Inf.

Nir, T.M., Jahanshad, N., Villalon-Reina, J.E., Toga, A.W., Jack, C.R., Weiner, M.W., Thompson, P.M., Alzheimer's Disease Neuroimaging Initiative (ADNI), 2013. Effectiveness of regional DTI measures in distinguishing Alzheimer's disease, MCI, and normal aging. NeuroImage Clin. 3, 180–195. doi:10.1016/j.nicl.2013.07.006

Novak, M.J.U., Seunarine, K.K., Gibbard, C.R., McColgan, P., Draganski, B., Friston, K., Clark, C.A., Tabrizi, S.J., 2015. Basal ganglia-cortical structural connectivity in Huntington's disease. Hum. Brain Mapp. 36, 1728–1740. doi:10.1002/hbm.22733

O'Donoghue, S., Holleran, L., Cannon, D.M., McDonald, C., 2017. Anatomical dysconnectivity in bipolar disorder compared with schizophrenia: A selective review of structural network analyses using diffusion MRI. J. Affect. Disord. 209, 217–228. doi:10.1016/j.jad.2016.11.015

Oh, S., Harris, J., Ng, L., Winslow, B., Cain, N., Mihalas, S., 2014. A mesoscale connectome of the mouse brain. Nature.

Ordway, J.M., Tallaksen-Greene, S., Gutekunst, C.-A., Bernstein, E.M., Cearley, J.A., Wiener, H.W., Dure, L.S., Lindsey, R., Hersch, S.M., Jope, R.S., Albin, R.., Detloff, P.J., 1997. Ectopically Expressed CAG Repeats Cause Intranuclear Inclusions and a Progressive Late Onset Neurological Phenotype in the Mouse. Cell 91, 753–763. doi:10.1016/S0092-8674(00)80464-X

Owen, J.P., Chang, Y.S., Mukherjee, P., 2015. Edge density imaging: Mapping the anatomic embedding of the structural connectome within the white matter of the human brain. Neuroimage 109, 402–417. doi:10.1016/j.neuroimage.2015.01.007

Owen, J.P., Wang, M.B., Mukherjee, P., 2016. Periventricular White Matter Is a Nexus for Network Connectivity in the Human Brain. Brain Connect. 6, 548–557. doi:10.1089/brain.2016.0431

Palop, J.J., Chin, J., Mucke, L., 2006. A network dysfunction perspective on neurodegenerative diseases. Nature 443, 768–73.

Pasternak, O., Westin, C.-F., Bouix, S., Seidman, L.J., Goldstein, J.M., Woo, T.-U.W., Petryshen, T.L., Mesholam-Gately, R.I., McCarley, R.W., Kikinis, R., Shenton, M.E., Kubicki, M., 2012. Excessive Extracellular Volume Reveals a Neurodegenerative Pattern in Schizophrenia Onset. J. Neurosci. 32.

Paulsen, J.S., Nopoulos, P.C., Aylward, E., Ross, C.A., Johnson, H., Magnotta, V.A., Juhl, A., Pierson, R.K., Mills, J., Langbehn, D., Nance, M., 2010. Striatal and white matter predictors of estimated diagnosis for Huntington disease. Brain Res. Bull. 82, 201–207. doi:10.1016/j.brainresbull.2010.04.003

Pettersson-Yeo, W., Allen, P., Benetti, S., McGuire, P., Mechelli, A., 2011. Dysconnectivity in schizophrenia: where are we now? Neurosci Biobehav Rev 35, 1110–1124. doi:10.1016/j.neubiorev.2010.11.004

Prescott, J.W., Guidon, A., Doraiswamy, P.M., Roy Choudhury, K., Liu, C., Petrella, J.R., Initiative, F. the A.D.N., 2014. The Alzheimer Structural Connectome: Changes in Cortical Network Topology with Increased Amyloid Plaque Burden. Radiology 273, 175–184. doi:10.1148/radiol.14132593

Price, J., Morris, J., 1999. Tangles and plaques in nondemented aging and" preclinical" Alzheimer's disease. Ann. Neurol.

Raj, A., Kuceyeski, A., Weiner, M., 2012. A Network Diffusion Model of Disease Progression in Dementia. Neuron 73, 1204–1215. doi:10.1016/j.neuron.2011.12.040

Raj, A., LoCastro, E., Kuceyeski, A., Tosun, D., Relkin, N., Weiner, M., 2015a. Network Diffusion Model of Progression Predicts Longitudinal Patterns of Atrophy and Metabolism in Alzheimer's Disease. Cell Rep. 10, 359–369. doi:10.1016/j.celrep.2014.12.034

Rao, J., Chiappelli, J., Kochunov, P., Regenold, W.T., Rapoport, S.I., Hong, L.E., 2015. Is schizophrenia a neurodegenerative disease? Evidence from age-related decline of brain-derived neurotrophic factor in the brains of schizophrenia patients and matched nonpsychiatric controls. Neurodegener. Dis. 15, 38–44. doi:10.1159/000369214

Rapoport, J.L., Giedd, J.N., Gogtay, N., 2012. Neurodevelopmental model of schizophrenia: update 2012. Mol. Psychiatry 17, 1228–1238. doi:10.1038/mp.2012.23

Redcay, E., Moran, J.M., Mavros, P.L., Tager-Flusberg, H., Gabrieli, J.D.E., Whitfield-Gabrieli, S., 2013. Intrinsic functional network organization in high-functioning adolescents with autism spectrum disorder. Front. Hum. Neurosci. 7, 573. doi:10.3389/fnhum.2013.00573

Reitz, C., Honig, L., Vonsattel, J.P., Tang, M.-X., Mayeux, R., 2009. Memory performance is related to amyloid and tau pathology in the hippocampus. J. Neurol. Neurosurg. Psychiatry 80, 715–721. doi:10.1136/jnnp.2008.154146

Ren, P.-H., Lauckner, J.E., Kachirskaia, I., Heuser, J.E., Melki, R., Kopito, R.R., 2009. Cytoplasmic penetration and persistent infection of mammalian cells by polyglutamine aggregates. Nat. Cell Biol. 11, 219–225. doi:10.1038/ncb1830

Ripke, S., Neale, B.M., Corvin, A., Walters, J.T.R., Farh, K.-H., Holmans, P.A., Lee, P., Bulik-Sullivan, et al., 2014. Biological insights from 108 schizophrenia-associated genetic loci. Nature 511, 421–427. doi:10.1038/nature13595

Romme, I.A.C., de Reus, M.A., Ophoff, R.A., Kahn, R.S., van den Heuvel, M.P., 2017. Connectome Disconnectivity and Cortical Gene Expression in Patients With Schizophrenia. Biol. Psychiatry 81, 495–502. doi:10.1016/j.biopsych.2016.07.012

Rosas, H.D., Tuch, D.S., Hevelone, N.D., Zaleta, A.K., Vangel, M., Hersch, S.M., Salat, D.H., 2006. Diffusion tensor imaging in presymptomatic and early Huntington's disease: Selective white matter pathology and its relationship to clinical measures. Mov. Disord. 21, 1317–1325. doi:10.1002/mds.20979

Rosén, C., Hansson, O., Blennow, K., Zetterberg, H., Rowe, C., McLean, C., Masters, C., Evin, G., Li, Q., Lovestone, S., Resnick, S., 2013. Fluid biomarkers in Alzheimer's disease – current concepts. Mol. Neurodegener. 8, 20. doi:10.1186/1750-1326-8-20

Rowley, J., Fonov, V., Wu, O., Eskildsen, S.F., Schoemaker, D., Wu, L., Mohades, S. ,et al., 2013. White Matter Abnormalities and Structural Hippocampal Disconnections in Amnestic Mild Cognitive Impairment and Alzheimer's Disease. PLoS One 8, e74776. doi:10.1371/journal.pone.0074776

Rüb, U., Del Tredici, K., Schultz, C., Thal, D.R., Braak, E., Braak, H., 2001. The autonomic higher order processing nuclei of the lower brain stem are among the early targets of the Alzheimer's disease-related cytoskeletal pathology. Acta Neuropathol. 101, 555–64.

Rubinov, M., Bullmore, E., 2013a. Fledgling pathoconnectomics of psychiatric disorders. Trends Cogn. Sci. 17, 641–647. doi:10.1016/j.tics.2013.10.007

Rubinov, M., Bullmore, E., 2013b. Schizophrenia and abnormal brain network hubs. Dialogues Clin. Neurosci. 15, 339–49.

Rubinov, M., Sporns, O., 2010. Complex network measures of brain connectivity: Uses and interpretations. Neuroimage 52, 1059–1069. doi:10.1016/j.neuroimage.2009.10.003

Saunders, A.M., Strittmatter, W.J., Schmechel, D., George-Hyslop, P.H., Pericak-Vance, M.A., Joo, S.H., Rosi, B.L., Gusella, J.F., Crapper-MacLachlan, D.R., Alberts, M.J., Hulette, C., Crain, B., Goldgaber, D., Roses, A.D., 1993. Association of apolipoprotein E allele epsilon 4 with late-onset familial and sporadic Alzheimer's disease. Neurology 43, 1467–72. doi:10.1212/WNL.43.8.1467

Savica, R., Grossardt, B.R., Bower, J.H., Boeve, B.F., Ahlskog, J.E., Rocca, W.A., 2013. Incidence of Dementia With Lewy Bodies and Parkinson Disease Dementia. JAMA Neurol. 70, 1396. doi:10.1001/jamaneurol.2013.3579

Schöll, M., Lockhart, S.N., Schonhaut, D.R., O'Neil, J.P., Janabi, M., Ossenkoppele, R., Baker, S.L., Vogel, J.W., Faria, J., Schwimmer, H.D., Rabinovici, G.D., Jagust, W.J., 2016. PET Imaging of Tau Deposition in the Aging Human Brain. Neuron 89, 971–982. doi:10.1016/j.neuron.2016.01.028

Schott, J., Bartlett, J., Fox, N., Barnes, J., 2010. Increased brain atrophy rates in cognitively normal older adults with low cerebrospinal fluid Aβ1-42. Ann. Neurol.

Schwarz, A.J., Yu, P., Miller, B.B., Shcherbinin, S., Dickson, J., Navitsky, M., Joshi, A.D., Devous, M.D., Mintun, M.S., 2016. Regional profiles of the candidate tau PET ligand 18F-AV-1451 recapitulate key features of Braak histopathological stages. Brain.

Seeley, W., 2017. Mapping Neurodegenerative Disease Onset and Progression. Cold Spring Harb. Perspect.

Seeley, W.W., Crawford, R.K., Zhou, J., Miller, B.L., Greicius, M.D., 2009. Neurodegenerative Diseases Target Large-Scale Human Brain Networks. Neuron 62, 42–52. doi:10.1016/j.neuron.2009.03.024

Shaw, L.M., Vanderstichele, H., Knapik-Czajka, M., Figurski, M., Coart, E., Blennow, K., Soares, H., Simon, A.J., Lewczuk, P., Dean, R.A., Siemers, E., Potter, W., Lee, V.M.-Y., Trojanowski, J.Q., Initiative, the A.D.N., 2011. Qualification of the analytical and clinical performance of CSF biomarker analyses in ADNI. Acta Neuropathol. 121, 597–609. doi:10.1007/s00401-011-0808-0

Spillantini, M., Crowther, R., Jakes, R., 1998. α-Synuclein in filamentous inclusions of Lewy bodies from Parkinson's disease and dementia with Lewy bodies. Proc.

Sporns, O., 2014. Contributions and challenges for network models in cognitive neuroscience. Nat. Neurosci. 17, 652–660. doi:10.1038/nn.3690

Sporns, O., 2012. Discovering the human connectome. MIT Press.

Sporns, O., Tononi, G., Kötter, R., O'Neill, M., Young, M., 2005. The Human Connectome: A Structural Description of the Human Brain. PLoS Comput. Biol. 1, e42. doi:10.1371/journal.pcbi.0010042

Stam, C.J., Reijneveld, J.C., 2007. Graph theoretical analysis of complex networks in the brain. Nonlinear Biomed. Phys. 1, 3. doi:10.1186/1753-4631-1-3

Starkstein, S.E., Brandt, J., Bylsma, F., Peyser, C., Folstein, M., Folstein, S.E., 1992. Neuropsychological correlates of brain atrophy in Huntington's disease: a magnetic resonance imaging study. Neuroradiology 34, 487–489. doi:10.1007/BF00598956

Stomrud, E., Hansson, O., Zetterberg, H., Blennow, K., Minthon, L., Londos, E., ST, D., 2010. Correlation of Longitudinal Cerebrospinal Fluid Biomarkers With Cognitive Decline in Healthy Older Adults. Arch. Neurol. 67, 87–95. doi:10.1001/archneurol.2009.316

Tabrizi, S., Langbehn, D., Leavitt, B., Roos, R., 2009. Biological and clinical manifestations of Huntington's disease in the longitudinal TRACK-HD study: cross-sectional analysis of baseline data. Lancet.

Tabrizi, S., Reilmann, R., Roos, R., Durr, A., 2012. Potential endpoints for clinical trials in premanifest and early Huntington's disease in the TRACK-HD study: analysis of 24 month observational data. Lancet.

Tabrizi, S., Scahill, R., Owen, G., Durr, A., Leavitt, B., 2013. Predictors of phenotypic progression and disease onset in premanifest and early-stage Huntington's disease in the TRACK-HD study: analysis of 36-month. Lancet.

Tabrizi, S.J., Scahill, R.I., Owen, G., Durr, A., Leavitt, B.R., Roos, R.A., Borowsky, B., Landwehrmeyer, B., Frost, C., Johnson, H., Craufurd, D., Reilmann, R., Stout, J.C., Langbehn, D.R., Surmeier, D.J., Obeso, J.A., Halliday, G.M., Pathogens, S., Manuscript, A., Goedert, M., Masuda-Suzukake, M., Falcon, B., Colosimo, C., Berardelli, A., Brundin, P., Melki, R., Kopito, R., Arrasate, M., Finkbeiner, S., Walsh, D., Selkoe, D., McColgan, P., Seunarine, K., Razi, A., Cole, J., Mattsson, N., Schott, J., Hardy, J., Turner, M., Grossman, M., Franks, K., Chuah, M., King, A., Brettschneider, J., Tredici, K. Del, Lee, V., Babcock, D.T., Ganetzky, B., 2016. Like prions: The propagation of aggregated tau and α-synuclein in neurodegeneration. Brain 18, 509–524. doi:10.1016/B978-0-12-381328-2.00018-3

Takahashi, T., Takayanagi, Y., Nishikawa, Y., Nakamura, M., Komori, Y., Furuichi, A., Kido, M., Sasabayashi, D., Noguchi, K., Suzuki, M., 2017. Brain neurodevelopmental markers related to the deficit subtype of schizophrenia. Psychiatry Res. Neuroimaging 266, 10–18. doi:10.1016/j.pscychresns.2017.05.007

Tan, Z., Dai, W., Erp, T. van, Overman, J., Demuro, A., 2015. Huntington's disease cerebrospinal fluid seeds aggregation of mutant huntingtin. Molecular.

Tapiola, T., Alafuzoff, I., Herukka, S.-K., Parkkinen, L., Hartikainen, P., Soininen, H., Pirttilä, T., 2009. Cerebrospinal Fluid β-Amyloid 42 and Tau Proteins as Biomarkers of Alzheimer-Type Pathologic Changes in the Brain. Arch. Neurol. 66, 382–9. doi:10.1001/archneurol.2008.596

Terwisscha van Scheltinga, A.F., Bakker, S.C., van Haren, N.E.M., Derks, E.M., Buizer-Voskamp, J.E., Boos, H.B.M., Cahn, W., Hulshoff Pol, H.E., Ripke, S., Ophoff, R.A., Kahn, R.S., 2013. Genetic Schizophrenia Risk Variants Jointly Modulate Total Brain and White Matter Volume. Biol. Psychiatry 73, 525–531. doi:10.1016/j.biopsych.2012.08.017

Thal, D.R., Rüb, U., Orantes, M., Braak, H., 2002. Phases of A beta-deposition in the human brain and its relevance for the development of AD. Neurology 58, 1791–800.

Tosun, D., Chen, Y.-F., Yu, P., Sundell, K.L., Suhy, J., Siemers, E., Schwarz, A.J., Weiner, M.W., 2016. Amyloid status imputed from a multimodal classifier including structural MRI distinguishes progressors from nonprogressors in a mild Alzheimer's disease clinical trial cohort. Alzheimer's Dement. 12, 977–986. doi:10.1016/j.jalz.2016.03.009

van den Heuvel, M.P., Mandl, R.C., Stam, C.J., Kahn, R.S., Hulshoff Pol, H.E., 2010. Aberrant frontal and temporal complex network structure in schizophrenia: a graph theoretical analysis. J Neurosci 30, 15915–15926. doi:10.1523/JNEUROSCI.2874-10.2010

van den Heuvel, M.P., Sporns, O., Collin, G., Scheewe, T., Mandl, R.C.W., Cahn, W., Go?i, J., Hulshoff Pol, H.E., Kahn, R.S., 2013. Abnormal Rich Club Organization and Functional Brain Dynamics in Schizophrenia. JAMA Psychiatry 70, 783. doi:10.1001/jamapsychiatry.2013.1328

Vonsattel, J.P., Myers, R.H., Stevens, T.J., Ferrante, R.J., Bird, E.D., Richardson, E.P., 1985. Neuropathological classification of Huntington's disease. J. Neuropathol. Exp. Neurol. 44, 559–77.

Waller, L., Walter, H., Kruschwitz, J.D., Reuter, L., Müller, S., Erk, S., Veer, I.M., 2017. Evaluating the replicability, specificity, and generalizability of connectome fingerprints. Neuroimage 158, 371–377. doi:10.1016/j.neuroimage.2017.07.016

Walsh, T., McClellan, J.M., McCarthy, S.E., Addington, A.M., Pierce, S.B., Cooper, G.M., Nord, A.S., Kusenda, M., Malhotra, D., Bhandari, A., Stray, S.M., Rippey, C.F., Roccanova, P., Makarov, V., Lakshmi, B., Findling, R.L., Sikich, L., Stromberg, T., Merriman, B., Gogtay, N., Butler, P., Eckstrand, K., Noory, L., Gochman, P., Long, R., Chen, Z., Davis, S., Baker, C., Eichler, E.E., Meltzer, P.S., Nelson, S.F., Singleton, A.B., Lee, M.K., Rapoport, J.L., King, M.-C., Sebat, J., 2008. Rare Structural Variants Disrupt Multiple Genes in Neurodevelopmental Pathways in Schizophrenia. Science (80-.). 320.

Wang, M.B., Owen, J.P., Mukherjee, P., Raj, A., Bukshpun, P., Vora, S., 2017. Brain network eigenmodes provide a robust and compact representation of the structural connectome in health and disease. PLOS Comput. Biol. 13, e1005550. doi:10.1371/journal.pcbi.1005550

Wang, Q., Su, T.P., Zhou, Y., Chou, K.H., Chen, I.Y., Jiang, T., Lin, C.P., 2012. Anatomical insights into disrupted small-world networks in schizophrenia. Neuroimage 59, 1085–1093. doi:10.1016/j.neuroimage.2011.09.035

Weinberg, D., Lenroot, R., Jacomb, I., Allen, K., 2016. Cognitive subtypes of schizophrenia characterized by differential brain volumetric reductions and cognitive decline. JAMA.

Wig, G.S., Schlaggar, B.L., Petersen, S.E., 2011. Concepts and principles in the analysis of brain networks. Ann. N. Y. Acad. Sci. 1224, 126–146. doi:10.1111/j.1749-6632.2010.05947.x

Young, A.L., Oxtoby, N.P., Daga, P., Cash, D.M., Fox, N.C., Ourselin, S., Schott, J.M., Alexander, D.C., 2014. A data-driven model of biomarker changes in sporadic Alzheimer's disease. Brain 137, 2564–2577. doi:10.1093/brain/awu176

Zhang, J., Peng, Q., Li, Q., Jahanshad, N., Hou, Z., Jiang, M., Masuda, N., Langbehn, D.R., Miller, M.I., Mori, S., Ross, C.A., Duan, W., 2010. Longitudinal characterization of brain atrophy of a Huntington's disease mouse model by automated morphological analyses of magnetic resonance images. Neuroimage 49, 2340–2351. doi:10.1016/j.neuroimage.2009.10.027

Zhou, J., Gennatas, E., Kramer, J., Miller, B., Seeley, W., Bangaru, S., Grzadzinski, R., Evans, A.C., Zang, Y.F., Castellanos, F.X., Milham, M.P., 2012. Predicting Regional Neurodegeneration from the Healthy Brain Functional Connectome. Neuron 73, 1216–1227. doi:10.1016/j.neuron.2012.03.004